



DIPLOMARBEIT

Titel der Diplomarbeit

Near Infrared Spectra of post-AGB Variables

angestrebter akademischer Grad

Magistra der Naturwissenschaften (Mag. rer. nat.)

Verfasserin:	Bakk. Marianne Jungwirth
Matrikel-Nummer:	a0202720
Studienrichtung:	Astronomie A066 861
Betreuer:	Dr. Thomas Lebzelter

Wien, November 2010

Widmung

*Und wusstest du, dass das Sternenlicht,
Kurz bevor es in den Himmel aufbricht,
Auf deiner Nase sitzt und lacht,
Dann erst springt es in die Nacht.*

(Die Nacht von Wir sind Helden)

*Diese Diplomarbeit ist meinem Ehemann Gerald Jungwirth gewidmet,
der mit mir nach den Sternen greift.*

Contents

1	Introduction	1
1.1	Stellar Evolution	1
1.1.1	Main Sequence	2
1.1.2	Red Giant Branch and Horizontal Branch	6
1.1.3	Asymptotic Giant Branch and TP-AGB	8
1.1.4	The post-AGB Phase	13
1.1.4.1	Binary post-AGB Evolution	20
1.1.5	Planetary Nebulae	22
1.1.6	White Dwarfs	23
1.1.7	Supernovae	24
1.1.8	Neutron Stars	26
1.1.9	Pulsars	26
1.1.10	Black Holes	26
2	Variable Stars	28
2.1	Groups of Variable Stars	28
2.1.1	RV Tauri Stars	29
2.1.2	SR Stars	35
3	Data	37
3.1	Observation	37
3.2	Sample	38
3.3	Data-Reduction	40
3.4	Line Identification	43
3.5	Line Measurements	43
3.6	Model Spectra	43
4	Results	44
4.1	V509 Cas	45
4.2	RW Cep	53
4.3	HD 143352	59
4.4	θ Her	63
4.5	AC Her	71

4.6	SX Her	83
4.7	89 Her	89
4.8	CX Lac	101
4.9	SX Lac	105
4.10	TT Oph	109
4.11	TX Oph	119
4.12	UZ Oph	125
4.13	AR Pup	131
4.14	R Sct	137
5	Summary	150
5.1	J Filter	151
5.2	H Filter	156
5.3	K Filter	162
	Appendix	174
A	Standard Stars	174
A.1	α Boo	175
A.2	9 Her	179
A.3	δ Oph	183
B	Comparison Stars	194
B.1	HD 148513	195
B.2	HD 210889	199
B.3	λ Peg	203
B.4	μ Peg	207
	Curriculum Vitae	212

Abstract

The aim of this master thesis is to have a closer look on the interesting topic of post-AGB stars. During the evolution of an intermediate mass star, different burning phases are observed: on the Main Sequence (MS), hydrogen is burning in the core. After that on the Red Giant Branch (RGB), hydrogen burning continues in an outer shell. On the tip of the RGB, the helium produced during the hydrogen burning ignites in the core. The stable helium-core-burning continues on the Horizontal Branch (HB) simultaneously with a hydrogen burning shell. When the helium in the core is exhausted, the star enters the Asymptotic Giant Branch (AGB) phase where helium burning continues in a shell. The star grows in radius and luminosity until the outer part is removed from the core by heavy mass loss. This is the start of the post-AGB phase which describes the path of a star off the AGB and to the planetary nebula (PN).

During the post-AGB phase a star loses mass due to a stellar wind. Gonzalez et al. (1997) estimate the mass loss rate of a dusty wind consisting of dust and gas to be $2 \times 10^{-6} M_{\odot} \text{ yr}^{-1}$, with a dust-to-gas ratio of 1% in mass. The dust is driven outward, where it surrounds the core and darkens the image of the star in the visible. The hot star in the center of the dust shell can make the planetary nebular glow after some time. The central star eventually becomes a white dwarf (WD).

Due to the evolutionary stage of post-AGB stars certain characteristics appear in the spectra of these objects. The low observed metallicities between $[\text{Fe}/\text{H}] = -0.2$ to -2.3 (Gonzalez et al., 1997) do not represent the initial composition of the star, they are a result of a depletion process (see Giridhar et al., 1998a). The different burning phases lead to an enhancement of C, N, O and S, as well as products of helium-burning and s-process elements. In some cases, P-Cygni line profiles were observed as well as spectral lines composed of an emission component with a superimposed central absorption component. Such line profiles indicate shell-like structures expected for stars during the post-AGB phase.

The spectra of this thesis lie in the near-infrared at wavelengths of $1 \mu\text{m}$ to $2.5 \mu\text{m}$ and show atomic lines in the shorter-wavelength areas as well as molecular features at longer wavelengths. The program stars are members of the group of variable stars of RV Tauri and SRd, the first group is thought to consist of post-AGB stars.

The data were obtained in the years 2000 and 2001 and were reduced with IRAF. The observations were corrected for dark count and bias as well as telluric features and sky background. The frames were normalized in the J and H filter to make a comparison with model spectra possible. The model spectra were produced using

a MARCS-code. Only models in the range between 4000 K and 5000 K with $\log g$ values between 0.00 and 0.75 were computed because post-AGB stars are expected to lie in that range.

The identification and measurement of the lines found in the stellar spectra were done with IRAF, using a Voigt profile to measure the equivalent widths because it matches both atomic lines and molecular features.

My aim was to search the stellar spectra for the characteristics described above to classify them as post-AGB objects. The next step was to find common properties within certain wavelength regions for an easier identification of such objects in the future.

Of the 14 program stars described in this thesis, seven (HD 143352, AC Her, 89 Her, TT Oph, TX Oph, UZ Oph, AR Pup) are very likely post-AGB stars (see *The Toruń catalogue of Galactic post-AGB and related objects* by Szczerba et al., 2007), four (RW Cep, SX Her, CX Lac, SX Lac) might be post-AGB candidates. The spectrum obtained from one star (V509 Cas) does not give any evidence for a post-AGB status, and two stars of the sample (θ Her, R Sct) might be no post-AGB stars. There are indications that θ Her belongs to the group of *hybrid giants*, while observations of R Sct suggest, that this star could still be in the TP-AGB phase.

Zusammenfassung

Das Ziel dieser Diplomarbeit ist es, das interessante Gebiet der Post-AGB Sterne etwas näher zu beleuchten. Während der Entwicklung eines Sterns mittlerer Masse kann man verschiedene Brennphasen beobachten: auf der Hauptreihe (MS) findet Wasserstoffbrennen im Kern statt. Dieses Wasserstoffbrennen setzt sich später auf dem Roten Riesen Ast (RGB) in einer Schale fort. Das durch das Wasserstoffbrennen erzeugte Helium im Kern zündet an der Spitze des RGB. Die folgende Phase auf dem Horizontalast (HB) ist durch stabiles Heliumbrennen im Kern und Wasserstoffbrennen in einer Schale gekennzeichnet. Wenn das Helium im Kern aufgebraucht ist, setzt sich das Heliumbrennen in einer Schale fort. Diesen Entwicklungsabschnitt nennt man Asymptotischen Riesenast (AGB). Der Stern bläht sich, während er zu höheren Leuchtkräften aufsteigt, immer weiter auf. Schlussendlich kommt es zu einem großen Massenverlust, der die Hülle vom brennenden Kern löst. Danach beginnt die Post-AGB Phase, in der sich ein Stern mittlerer Ausgangsmasse zu einem Planetarischen Nebel (PN) entwickelt.

Während der Post-AGB Phase verliert der Stern Masse in Form von Staub und Gas, die dann als Staubmantel um den Stern liegen und diesen im optischen Bereich verdunkelt. Der Massenverlust durch diesen Wind beläuft sich laut Gonzalez et al. (1997) auf $2 \times 10^{-6} M_{\odot} \text{ yr}^{-1}$, mit einem Massenverhältnis von Staub-zu-Gas von 1%. Der heiße Stern im Inneren des Staubmantels kann nach einiger Zeit den Planetarischen Nebel zum fluoreszieren bringen. Der Zentralstern wird letztendlich ein Weißer Zwerg.

Aufgrund ihrer Entwicklung werden bestimmte Besonderheiten in den Spektren von post-AGB Sternen erwartet. Die beobachteten niedrigen Metallizitäten zwischen $[\text{Fe}/\text{H}] = -0.2$ bis -2.3 (Gonzalez et al., 1997) sind das Ergebnis eines Abreicherungsprozesses (siehe Giridhar et al., 1998a) und repräsentieren nicht die Anfangsmetallizität. Da sie bereits mehrere Brennphasen durchlaufen haben, können Anreicherungen von C, N, O und S sowie Produkte aus dem Helium-Brennen nachgewiesen werden. Eine Erhöhung an s-Prozess Elementen wurde ebenfalls beobachtet. In manchen Sternspektren findet man auch so genannte P-Cygni Linienprofile und Spektrallinien mit einer Emissionskomponente, die von einer zentralen Absorptionskomponente überlagert wird. Solche Linienprofile sind ein Hinweis auf Schalen-Strukturen um den Stern, die bei Post-AGB Objekten erwartet werden.

Die Spektren, die dieser Arbeit zu Grunde liegen, wurden im Nahen Infraroten bei Wellenlängen zwischen $1 \mu\text{m}$ bis $2.5 \mu\text{m}$ aufgenommen und zeigen sowohl Atomlinien im kurzwelligeren Bereich als auch Moleküllinien in den längerwelligen Bereichen. Die Programmsterne sind Mitglieder der variablen Sterngruppen des Typs RV Tauri

und SRd, wobei gerade Sterne der ersten Gruppe als post-AGB Kandidaten in Frage kommen.

Die Daten aus den Jahren 2000 und 2001 wurden mit Hilfe des Programms IRAF reduziert und ausgewertet. Die Beobachtungen wurde dabei sowohl auf Dunkelstrom als auch auf atmosphärische Spektrallinien und Himmelshintergrund korrigiert und anschließend normiert, um den Vergleich mit Modellspektren zu erleichtern. Die Vergleichsmodelle wurden mittels MARCS-Code erstellt, wobei nur der Bereich zwischen 4000 K und 5000 K betrachtet wurde mit $\log g$ -Werten zwischen 0.00 und 0.75.

Das anschließende Identifizieren und Ausmessen der Linien fand auch in IRAF statt, wobei ein Voigt-Profil zum Messen der Äquivalenzbreiten gewählt wurde, da dieses am Besten sowohl für Atomlinien als auch Moleküllinien geeignet war.

Mein Ziel war es, in den Sternspektren nach den oben genannten Kriterien zu suchen und sie als Post-AGB Objekte zu klassifizieren. Als weiterer Schritt wurde nach Gemeinsamkeiten in den Wellenlängenbereichen gesucht, um die Identifikation dieser Objekte in Zukunft zu erleichtern.

Von den 14 Programmsternen, die in dieser Arbeit als post-AGB Objekte in Frage kommen, sind sieben (HD 143352, AC Her, 89 Her, TT Oph, TX Oph, UZ Oph, AR Pup) mit hoher Wahrscheinlichkeit post-AGB Sterne (siehe *The Toruń catalogue of Galactic post-AGB and related objects* von Szczerba et al., 2007), vier (RW Cep, SX Her, CX Lac, SX Lac) kommen als mögliche Kandidaten in Frage, über einen Stern (V509 Cas) kann ich aufgrund des beobachteten Spektrums keine Aussage treffen, und zwei Programmsterne (θ Her, R Sct) sind vermutlich keine post-AGB Sterne. Es gibt Hinweise, dass θ Her zur Gruppe der *hybrid giants* gehört, während Beobachtungen von R Sct die Vermutung nahelegen, dieser Stern könnte sich noch in der TP-AGB Phase befinden und noch nicht in der post-AGB Phase.

Chapter 1

Introduction

1.1 Stellar Evolution

Galaxies are composed of stars in different stages of their evolution. Dependent on their initial mass, stars take certain evolutionary paths during their lives and spend more or less time in specific phases. The division into different groups is based upon the initial mass of the star:

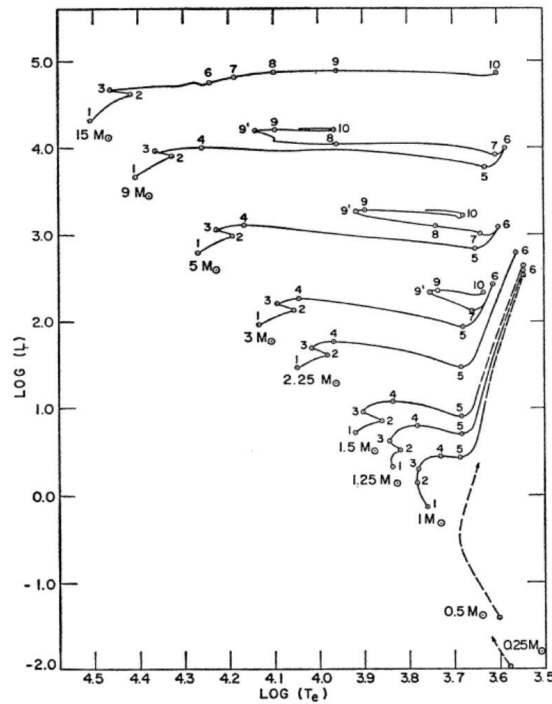


Figure 1.1: Evolutionary paths for metal-rich stars of different masses (Iben, 1967).

- **low-mass stars:** According to Herwig (2005), these stars have initial masses below $1.8 M_{\odot}$, experience a helium-core flash and end as White Dwarfs.
- **intermediate-mass stars:** Between 1.8 and $8-10 M_{\odot}$ stars also evolve into White Dwarfs like low-mass stars, but following a slightly different evolutionary

path, depending on their mass. Intermediate mass stars start helium burning without a helium-core flash.

- **massive stars:** Stars over $8\text{--}10 M_{\odot}$ end their lives as Neutron Stars or Black Holes.

A low-mass star of about $1 M_{\odot}$ experiences a rather long time, about 11×10^9 years, on the main sequence, before it moves on to the next stage of evolution. A star like our sun ends its life after approximately 12.4×10^9 years at a mass of about 0.54 to $0.58 M_{\odot}$ as a White Dwarf (Sackmann et al., 1993).

Intermediate-mass stars are comparable to low-mass stars in their evolution and their end, while high-mass stars face a completely different fate. Stars with initial masses above $8\text{--}10 M_{\odot}$ have short lives compared to lower-mass stars and become Supernovae after a core collapse. As one can see in Fig.1.1, the evolution of a $15 M_{\odot}$ star is faster, with only about 1×10^7 years on the main sequence and shorter timescales at the other evolutionary stages (Iben, 1967).

1.1.1 Main Sequence

When a star first ignites hydrogen in its center due to high pressure and temperature ($T_c = 5 \times 10^6$ K, Weigert et al., 2005), it appears in the so called Hertzsprung-Russell (HR) diagram (Rosenberg, 1911; Hertzsprung, 1911) on the Zero Age Main Sequence (ZAMS). The HR-diagram illustrates the evolution of stars using effective temperature and absolute luminosity as x- and y-axis. Fig.1.2 shows the evolution of a $5 M_{\odot}$ star from the beginning of the hydrogen burning in the core on.

The first phase is called the Main Sequence (MS) and is the longest and most stable phase in the whole stellar evolution.

Massive stars are hotter than low-mass stars, that is why massive stars are on the blue side of the MS in the HR-diagram and cooler stars on the red side. Massive stars are also more luminous than stars like e.g. the sun, they can be observed at far distances. Low-mass MS stars are more difficult to observe at greater distances. To describe the evolutionary paths of stars, one can use the relation between luminosity L , radius R and the effective temperature T_{eff} , as can be seen in the next formula (Unsöld & Baschek, 2002):

$$L = 4\pi R^2 \sigma T_{\text{eff}}^4 \quad (1.1)$$

As can be seen in Fig. 1.1, a star with $1 M_{\odot}$ first evolves a bit to the left and up, which can be translated to an increase in temperature and luminosity and a decrease in radius.

Two processes are responsible for the energy production during the MS phase:

pp-chain: The pp-chain fuses four protons into a ^4He atom. This reaction takes place at temperatures between 5 to 15×10^6 K. The energy gained by this reaction

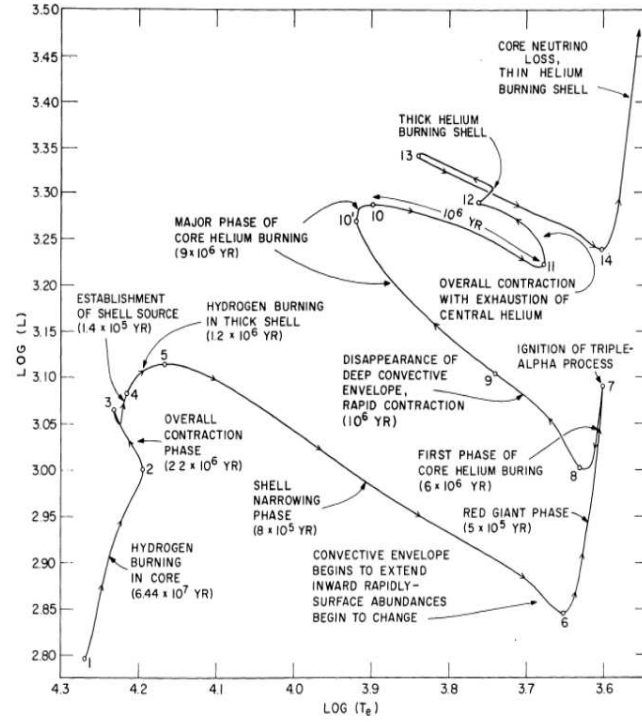
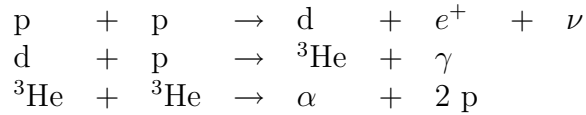


Figure 1.2: The evolution of a $5 M_{\odot}$ model star with Population I composition from Iben (1991).

is $6 \times 10^{14} \text{ J kg}^{-1}$, the highest amount of all fusion processes in the star.

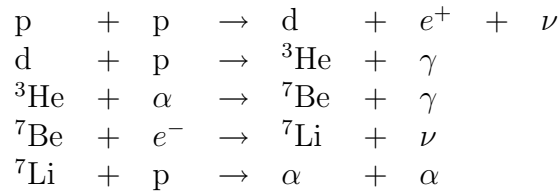
Two protons build a deuterium-nucleus, the following reactions can differ, the most significant path is (following *Astronomie und Astrophysik* by Weigert et al., 2005):

pp 1 chain:

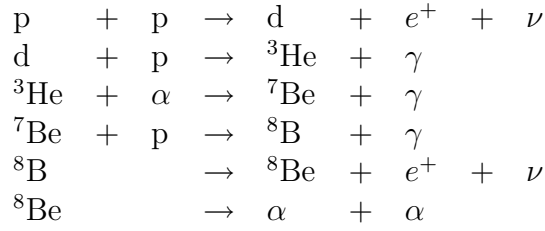


The pp 2 chain as well as the pp 3 differ from pp 1 after the first two reactions (following *Nuclear Physics of Stars* by Iliadis (2007)):

pp 2 chain:



pp3 chain:

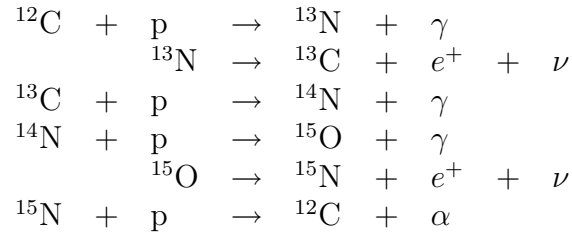


Explanation of the letters used: The α sign stands for the α -particle ${}^4\text{He}$, p for proton and d for deuteron. The capital letters represent the nuclei of the elements, e^+ describes a positron, e^- an electron, ν a neutrino and γ is the gamma quantum (light quantum).

CNO-cycle: The result is the same as in the pp-chain: to fuse four protons to one ${}^4\text{He}$ nucleus, but C, N, O and F function as catalysts. This reaction takes place at a higher temperature than the pp-chain, 1.5 to 3×10^7 K.

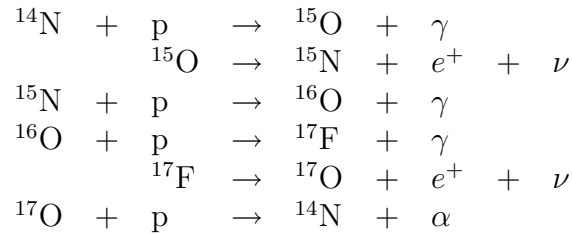
Four slightly different paths for this cycle are known, as summarized by Wiescher et al. (1999). The first CNO cycle is explained as follows:

CNO-1:



The last reaction can be replaced by ${}^{15}\text{N}(\text{p}, \gamma){}^{16}\text{O}$, leading to the second CNO cycle composed of the following reactions (Wiescher et al., 1999):

CNO-2:

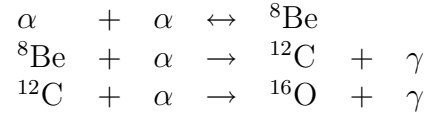


1.1.2 Red Giant Branch and Horizontal Branch

The hydrogen burning moves outward and continues in a shell above the helium core. The energy production in the shell is not as efficient as the core burning. To ignite helium, a temperature of at least 10^8 K is needed, and to get to that high temperatures, the inner part of the star starts to contract (Habing & Olofsson, 2003a). In the case of low-mass stars, the contraction goes as far as degeneracy of the helium core. The convective envelope reaches the inner part of the star and changes the surface abundances. This mixing process is called first dredge-up and enriches the surface with ^4He and the products of CN cycling, mainly ^{14}N and ^{13}C (Lattanzio & Wood, 2003).

The Red Giant Phase on the Red Giant Branch (RGB) is characterised by high luminosities and cool temperatures, as can be seen in the HR-diagram. These properties are caused by the expansion of the outer layers of the star, which leads to lower temperature and higher radius.

At the tip of the RGB helium ignites and a stable helium burning in the core develops on the Horizontal Branch (HB) simultaneously with a hydrogen burning shell. The triple- α -process fuses α -particles mostly into carbon and oxygen. The following reactions are the most common ones during the helium burning phase (Weigert et al., 2005):



Elements produced during this burning stage are mostly ^{12}C and ^{16}O , the relation of the produced elements is dependent on the initial mass of the star.

Low-mass stars with initial masses below $1.8 M_{\odot}$ experience the start of the core helium burning phase as a violent He-core flash due to the electron-degeneracy of the helium core. After that, the star continues a more quiet helium core burning on the so-called zero age horizontal branch (ZAHB) as explained by Herwig (2005). Stars above that mass limit start helium core burning in a less violent way and also continue to burn helium in a calm way while hydrogen keeps burning in a shell.

A phenomenon that was first observed in some metal-rich clusters, and after that for field stars, is called red clump (RC). In the H-R diagram of such clusters stars were not spread out over the whole range of the HB, but were clumped together at the reddest point of the HB. In older clusters like globular clusters in the Milky Way, a HB that extends into the very blue region of the HR-diagram can be observed, a so-called extreme-HB. The morphology of the HB depends on the metallicity of the stars (the cluster) and the age as well as a third parameter. This third parameter is up to now not fully understood, but a difference was observed for horizontal branches in clusters of approximately same age and metallicity and astronomers try to find a reason for this difference.

There are several candidates for this third parameter (Binney & Merrifield, 1998), like:

- **Variations in helium abundance:** The helium abundance can vary from cluster to cluster (Sandage & Wildey, 1967), but this difference is too small to have a significant effect on the horizontal branch.
- **Variations in other element abundances:** The CNO cycle uses C, N, and O as catalysts to fuse hydrogen into helium. If the abundances of these three catalysts are increased, the hydrogen-burning would be more efficient and the opacity would be affected. Although differences between clusters in the $[C+N+O/Fe]$ values (relative abundances of CNO to iron) were suspected, observations (Dickens et al., 1991) showed that between two clusters of comparable metallicity the $[C+N+O/Fe]$ values did not differ and therefore this theory does not approve as a solution for the third parameter problem.
- **Rotation:** The mass loss between the RGB and the HB has influence on the shape of the HB, so if there was a difference in mass loss between clusters, the morphology of the HB would be different. If a cluster consists of faster-rotating stars with less bound envelopes, one could expect a blue horizontal branch, because fast-rotating stars lose mass more easily (Suntzeff, 1981). This suggestion seems unlikely because no correlation was found between the rotation of stars on the HB and the HB color (Peterson et al., 1995).
- **Cluster density and concentration:** This theory is based upon an observational indicator that clusters with high star-concentration in the center show bluer HBs (Fusi Pecci et al., 1993). The spatial distribution of the stars in a cluster can therefore have an effect on the HB due to enhanced mass loss before the beginning of the HB-phase.

In a certain region of the HR-diagram, variable stars can be found which are pulsating, that means, they experience changes in luminosity and radial dimension. This part of the HR-diagram is called the instability-strip and a lot of different variable stars can be found there, but the instability-strip also crosses the MS and the WD region, as can be seen in Fig. 1.4 (Iben, 1991).

In later stages of stellar evolution, mass loss plays a significant role, but it is difficult to fully understand the mechanisms behind the mass loss phenomenon. In the case of red giant stars, the Reimers mass-loss law (Reimers, 1975)

$$\dot{M} = 4 \times 10^{-13} \eta_R \frac{LR}{M} \quad [M_{\odot}/yr] \quad (1.2)$$

is in good agreement with observations. Luminosity L , radius R and mass M used in this formula are in solar units and the η_R parameter measures between $1/3 < \eta_R < 3$.

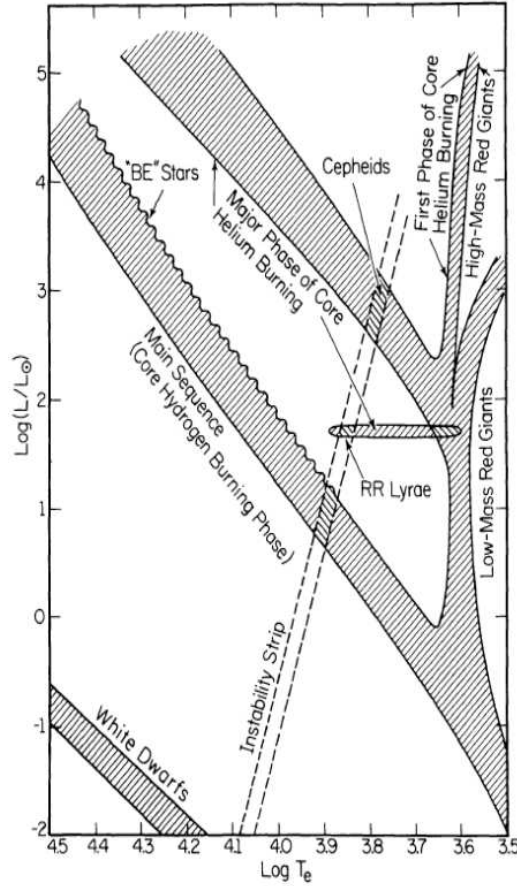


Figure 1.4: HR diagram of model stars of Population I composition during different phases of their evolution. The instability strip crosses the main sequence, the horizontal branch and the white dwarf region. Two groups of variable stars (RR Lyrae, Cepheids) are noted here (Iben, 1991).

1.1.3 Asymptotic Giant Branch and TP-AGB

When the helium in the core is exhausted, the helium burning continues in a shell and the star experiences another phase of contraction in the center. This contraction lasts until the core has a size of about 10^8 cm and a temperature of about 10^8 K, with a density of a White Dwarf. This leads to an increase in luminosity and the star evolves on to the Early AGB (E-AGB). During this stage, most of the energy is produced in the helium burning shell.

In the case of a more massive star (above $4 M_{\odot}$), He core burning is accompanied by hydrogen shell burning. When the helium in the core is exhausted, He burning in the shell leads to an expansion which extinguishes the hydrogen burning shell. The convective envelope then reaches into the no longer active hydrogen shell and mixes the produced elements up to the surface. This mixing episode is the second dredge-up and leads to an enrichment in ^4He , ^{12}C and ^{14}N while H gets mixed inward to the H-exhausted core (Lattanzio & Wood, 2003). After the second dredge-up, the hydrogen burning shell is reignited and the star moves again up the AGB.

The upper mass limit for AGB stars is set to be about $8 M_{\odot}$, that means the mass of

the core produced by helium burning is not high enough to enable carbon burning, so within the CO-core no nuclear burning takes place.

During the Asymptotic Giant Branch (AGB) phase, the star's interior can be divided into many different zones, where different chemical and physical conditions and processes can be found. To give the reader a better impression of the complexity of an AGB star, the schematic of the inner structure of such an object can be seen in Fig.1.5.

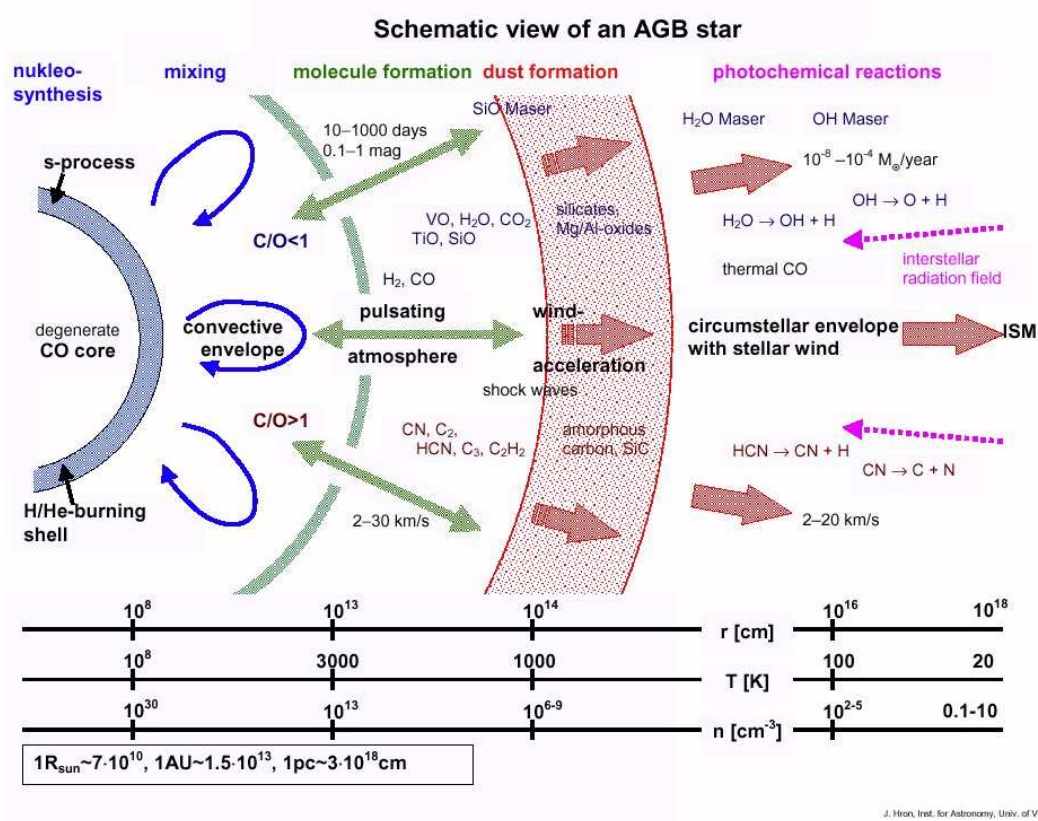


Figure 1.5: A schematic overview of an AGB star, drawn by J. Hron.

The schematic divides the AGB star roughly into five different parts with the following properties, convective zones and burning shells (Habing & Olofsson, 2003b):

- the hot and dense core, that later becomes the CO-White Dwarf, with the two burning shells where nucleosynthesis takes place;
- the convective stellar envelope above the H-burning shell, cooler and larger in radius than the core and less dense; in this region, the freshly produced elements get mixed up to the surface;
- the thin and warm dynamical atmosphere where formation of molecules is possible;

- the dust formation region where wind gets accelerated;
- the cool and very thin circumstellar envelope with stellar wind and photochemical reactions.

The star moves up on the AGB until it reaches a similar luminosity as the tip of the RGB, approximately $3000 L_{\odot}$. At this point, an alternate burning of the helium burning shell and the hydrogen burning shell takes place. A helium intershell region separates the two burning shells and is in radiative equilibrium (Busso et al., 1999). In the beginning the helium burning shell is inactive while the hydrogen burning shell is responsible for the energy production, leading to an increase in mass of the helium intershell as well as a rise in temperature and density. The resulting burning of the helium shell is rapid and called a thermal pulse, followed by a convective mixing of the envelope with the helium intershell region (Busso et al., 1999). This stage is called third dredge-up because it is the third dredge-up process in the life of an intermediate-mass star and the second one for a low-mass star (Habing & Olofsson, 2003b). The thermal pulses and the associated third dredge-up episodes are repeated many times and give this part of the AGB its name: thermally pulsing AGB or TP-AGB phase (Habing & Olofsson, 2003a).

The intershell region mostly consists of the products of the CNO cycle and triple- α reactions, ^4He (70-75%), ^{12}C (20-25%), few percent of ^{16}O and ^{22}Ne , a product of α -captures on the ^{14}N produced by the CNO cycle in the hydrogen burning shell (Lattanzio & Wood, 2003). A ^{13}C pocket is produced that can function as a neutron source for the s-process due to the $^{13}\text{C}(\alpha, n)^{16}\text{O}$ reaction, but the terms for the creation of such a pocket are not fully understood up to now.

The s-process describes the creation of heavier elements through slow neutron capture and β decay. Along the valley of stable nuclei, neutron capture creates elements heavier than ^{56}Fe until ^{209}Bi (Wallerstein et al., 1997). For example, ^{56}Fe captures neutrons until it reaches ^{59}Fe , then it gets transformed to ^{59}Co through β decay.

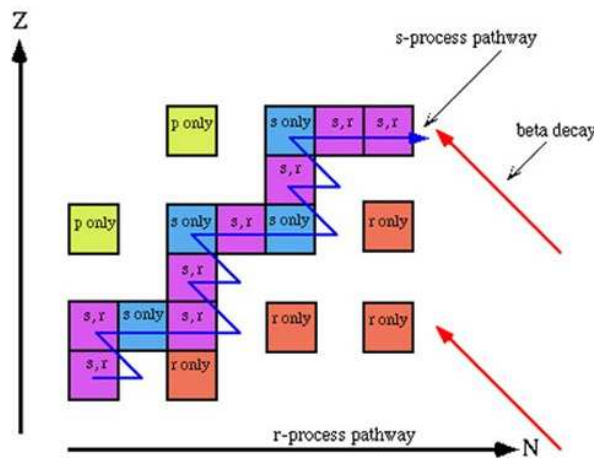


Figure 1.6: A scheme of the s-process and other processes known in stars. (Picture taken from <http://www4.nau.edu/meteorite>, copyright by J. H. Wittke & T. E. Bunch.)

An indicator for ongoing s-process and the presence of third dredge-up is the observation of the radioactive element technetium (^{99}Tc , with a half live time of 2×10^5 years) in the spectra of some TP-AGB stars (Lebzelter & Hron, 2003). The short living technetium is produced between the hydrogen and the helium burning shells by the s-process and then gets mixed up to the stellar surface within a few thermal pulses.

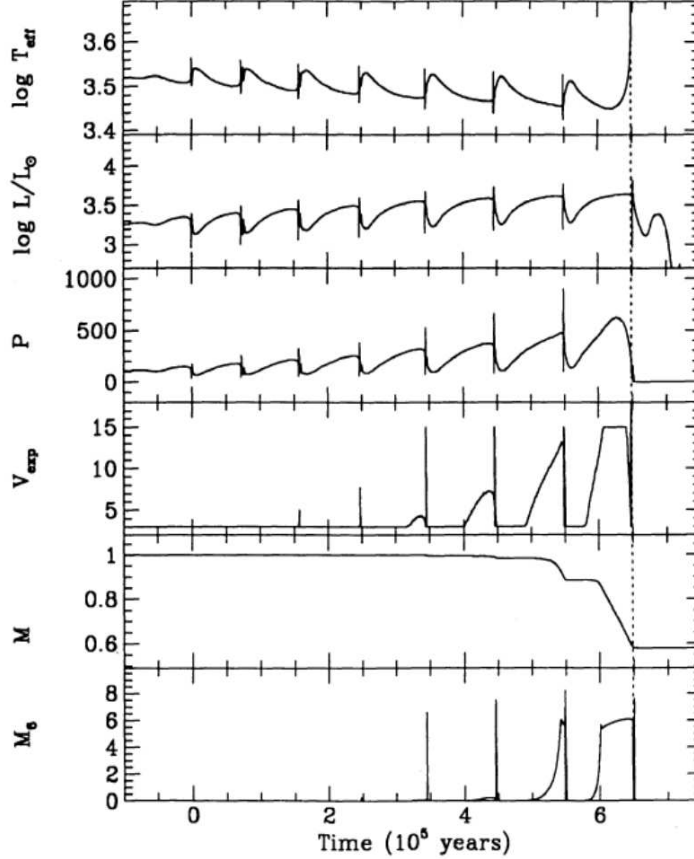


Figure 1.7: Change of effective temperature, luminosity, pulsation period P in days, stellar wind expansion velocity V_{exp} in km/s, total mass in M_{\odot} and mass-loss rate M_6 in units of $10^{-6} M_{\odot} \text{ yr}^{-1}$, during the TP-AGB phase (picture taken from Vassiliadis & Wood, 1993) for a star of $1.0 M_{\odot}$, $Y=0.25$ and $Z=0.008$. The start of the time line represents the first major thermal pulse, the dotted line symbolizes the end of the AGB phase.

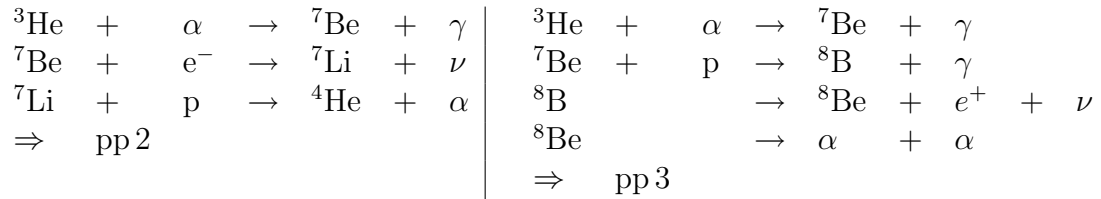
The third dredge-up episodes are responsible for the existence of carbon-rich stars: the newly produced carbon gets mixed up to the stellar surface and changes the abundance from $\text{C/O} < 1$ (oxygen-rich) to $\text{C/O} > 1$ (carbon-rich). Oxygen-rich stars are called M stars and their optical spectra are dominated by TiO bands, while C star spectra in the optical wavelength-range are dominated by C_2 and CN molecular features (Lattanzio & Wood, 2003). If a star is dominated by s-process elements, it is assigned to the group of S-stars. There are also configurations of MS or SC stars, with respect to the different ratios of oxygen, carbon and s-process elements seen in the spectra of stars. The average C/O-ratios (with noticeable scatter) found by Smith & Lambert (1990) for the different groups are: 0.41 for M-stars, 0.49 for MS, 0.57 for S, 0.95 for SC and 1.15 for C type stars. The s-process abundances

increase in the same way as the C/O-ratio.

The mass limit for the production of C-stars lies between $M_{MS} \sim 1.5 M_{\odot}$ and $\sim 4 M_{\odot}$ for a star with solar composition (Olofsson, 1999). A star with lower initial metallicity can be turned more easily into a carbon rich star even if it is of low initial mass.

The massive AGB-stars between 4.0 to 8.0 M_{\odot} (depending on metallicity) experience hot-bottom-burning (HBB), which is also called convective envelope burning, and describes a situation where the temperature at the bottom of the convective envelope is high enough ($T_{CE} > 50 \times 10^6$ K, Sackmann & Boothroyd, 1992) to enable nuclear burning (Lattanzio & Wood, 2003).

One effect of the HBB is the production of ${}^7\text{Li}$: the Cameron-Fowler mechanism (Cameron & Fowler, 1971) describes the process of ${}^7\text{Be}$ transport into outer and cooler layers where the electron capture necessary to produce ${}^7\text{Li}$ is possible. A short summary of the two different reaction paths possible during this process is (following Lattanzio & Wood, 2003):



This production of lithium during the helium shell flash stage can lead to the creation of super-rich lithium giants (Sackmann & Boothroyd, 1992), luminous red giants stars with high lithium abundance ($\log \epsilon({}^7\text{Li}) > 1$) that are more luminous than predicted by the core mass-luminosity relation (Paczyński, 1970).

The HBB is terminated by a decline in temperature at the base of the convective envelope due to a large decrease in envelope mass at rates of: $\dot{M} \sim 3 \times 10^{-5} M_{\odot}$ (Boothroyd & Sackmann, 1992).

The outer parts of an AGB star are often cool enough to enable the production of dust grains, but the temperature is not the only condition for dust production, also a high local density is needed. Normally, in the cooler parts of a star, the density is also lower, but in a pulsating atmosphere like in an AGB star, the shock waves will create something like a temporary reservoir of dense gas, making the formation of dust more efficient (Gustafsson & Höfner, 2003). Evidence for the existence of these dust grains is the spectral energy distribution of the AGB stars showing a second maximum at longer wavelengths, and emission features which can be assigned to certain dust species.

According to a stronger mass loss during the AGB phase, the Reimers law (Reimers, 1975) (formula 1.2) for red giants can not be simply applied to more evolved AGB stars. Bloeker (1995b) modified the models of shock-driven winds in the atmospheres of Mira-like stars calculated by Bowen (1988), who found out that the typical

mass-loss rates for AGB stars can only be represented properly with a combination of shock-driven winds and outer dust layers. The resulting formula

$$\dot{M}_{B1} = 4.83 \times 10^{-9} M_{ZAMS}^{-2.1} L^{2.7} \dot{M}_R \quad [M_{\odot}/yr] \quad (1.3)$$

was only used for stars with pulsational periods above 100 days in the fundamental mode P_0 , which was calculated based upon Ostlie & Cox (1986) as:

$$\log(P_0/d) = -1.92 - 0.73 \log M + 1.86 \log R \quad (1.4)$$

Stars with periods less than $P_0 < 100d$ can be sufficiently described with the Reimers law, the first term in formula 1.3, ($4.83 \times 10^{-9} M_{ZAMS}^{-9}$) creates a transition towards the law found by Bowen for the mass loss for his models above $P_0 = 100d$.

The AGB evolutionary stage is terminated by a superwind event, a significant mass loss ($10^{-7} - 10^{-4} M_{\odot} \text{ yr}^{-1}$, Van Winckel, 2003), that can occur several times in succession, see Fig.1.7, which leads to expanding dust and gas shells around the star.

1.1.4 The post-AGB Phase

During the post-AGB phase the circumstellar envelope expands and cools, revealing the central stellar remnant which is evolving to higher temperatures. The properties assumed for post-AGB stars (Oudmaijer et al., 1995) are spectral types between B to K and high luminosities (class I to III). A typical post-AGB star is expected to have luminosities around 10^3 to $10^4 L_{\odot}$ (Van Winckel, 2003). Post-AGB stars that just left the AGB are cool objects with low surface gravity (Waelkens & Waters, 2003) while more evolved stars can be found at higher temperatures in the HRD.

A lot of observations show thermal emission from cool dust in the infrared spectral energy distribution with a peak at $25 \mu\text{m}$, which can be assigned to circumstellar shells around the central star caused by the AGB wind, as well as hot circumstellar dust (about 1000 K) that peaks at $3\text{-}5 \mu\text{m}$ and is located closer to the star because it originated from a more recent mass loss during the post-AGB phase (Trams et al., 1989).

Another characteristic is an irregular variability in the light-curve and pulsations of the star (Waelkens & Waters, 2003). That leaves us with certain candidate groups of stars that fulfill the properties mentioned above: the RV Tauri stars and the SRd stars as well as a small group called R CrB stars (see Fig 1.8 for a comparison between a post-AGB candidate and R CrB itself). This work only deals with the first two groups, because only few R CrB type stars are known and their origin and evolution is still not clear. The extreme H-deficiency of R CrB stars points towards a non-standard evolution with the eventual removal of the entire hydrogen-rich envelope (Clayton, 1996). There are three possible theories to describe the origin of R CrB stars: evolution within a close binary system (Iben et al., 1996) with a low mass companion, the Final Helium Shell Flash (FF) scenario, where a white dwarf expands to the size of a supergiant by a final helium shell flash (Iben et al., 1983),

and the Double Degenerate (DD) model which suggests the creation of a R CrB star by merging of two white dwarfs (Schoenberner, 1986).

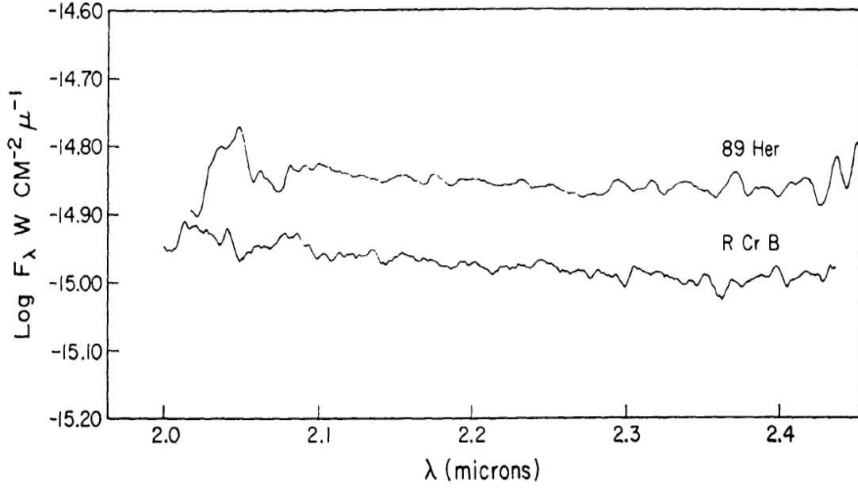


Figure 1.8: Comparison of the spectrum of the post-AGB candidate 89 Her with that of R CrB in the wavelength range from 2.0 to 2.5 μm (Gillett et al., 1970).

Trams et al. (1991) tried to identify low-mass post-AGB candidates in the literature by the following criteria:

- post-AGB stars should belong to Population II
- the circumstellar dust expected in this evolutionary phase should lead to an observable IR excess
- stars in the post-AGB phase should exhibit a photometrical and spectroscopical variability
- evidence for mass loss should be present in the spectra in the IR (hot dust) as well as in the optical wavelength range.

Based upon these criteria Trams et al. (1991) observed a sample of candidate post-AGB stars and divided them into three groups:

- Stars that have a large mass loss rate that leads to a great amount of hot dust ($T \sim 1000\text{ K}$)
- Stars with hot dust ($T \sim 1000\text{ K}$) produced by a large mass loss rate as well as cool dust ($T \sim 300\text{ K}$) as a remnant of the AGB wind
- Stars with cool dust ($T \sim 300\text{ K}$) mainly from the former AGB wind and a low mass loss rate

The post-AGB phase itself is rather short, about a few times 10^4 years, in the case of very massive objects it can be as short as ~ 30 years (Van Winckel, 2003). Bloeker (1995a) stated that the fading time scales during the post-AGB phase are influenced

by the different mass-loss histories on the AGB, for example if a star is more degenerated in the core due to a longer stay on the AGB, the fading will be faster, because a large amount of potential energy is used to increase the Fermi energy of the electrons. The three evolutionary tracks computed by Bloeker (1995a) (Fig. 1.9) show the evolution of a star based on the initial mass and the resulting final mass during the post-AGB phase towards the Planetary Nebula stage and the White Dwarf cooling sequence.

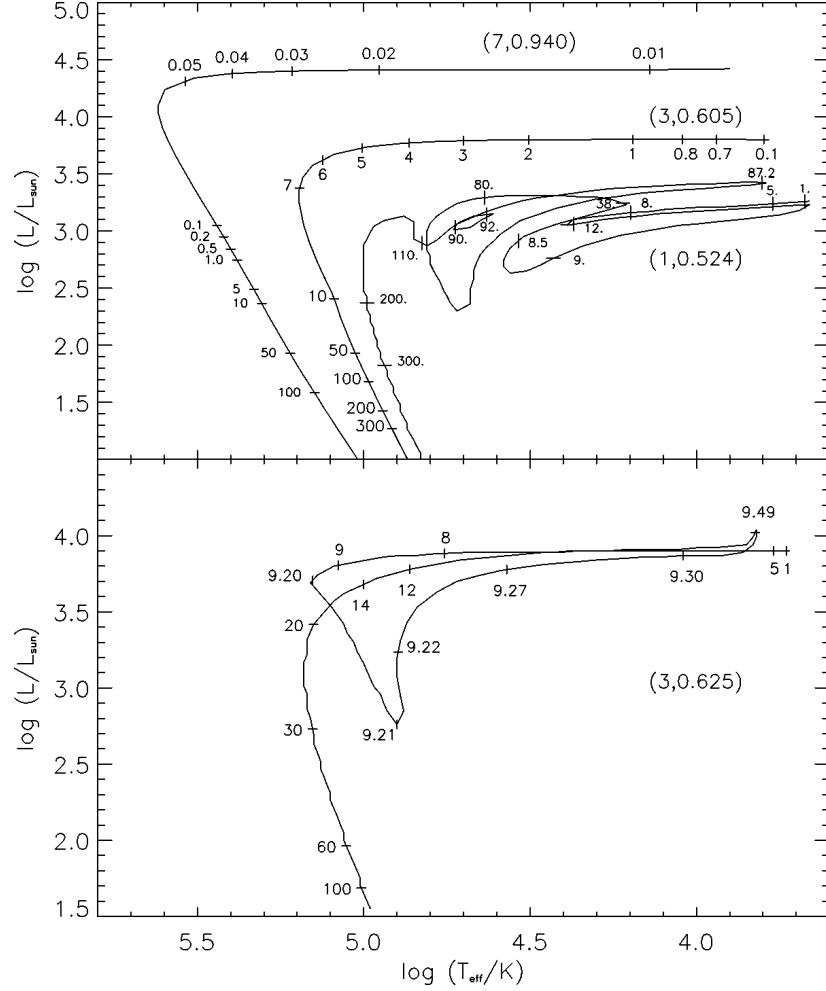


Figure 1.9: Evolutionary tracks from Bloeker (1995a) for stars of 1, 3 and $7 M_{\odot}$. Final masses are given next to the initial masses in the brackets. Time steps are in 10^3 years. The lower panel shows a "born-again"-AGB star scenario for a post-AGB evolution beginning close to the next thermal pulse.

Bloeker (1995a) calculated models for the decreasing mass loss that has been observed for post-AGB objects by using a relation between the decreasing radial pulsational period P_0 (see formula 1.4) and the mass loss rate he computed before (formula 1.3) towards the Reimers mass loss law (formula 1.2), which declines with T_{eff}^{-2} . The values for P_0 were 100 days for the starting of the decrease and 50 days for the reaching of the Reimers rate.

Another law was formulated for the part of the post-AGB phase that occurs above $T_{\text{eff}}=20\,000\text{ K}$:

$$\dot{M}_{CPN} = 1.29 \times 10^{-15} L^{1.86} \dot{M}_R \quad [M_{\odot}/yr] \quad (1.5)$$

This law gives a maximum mass loss rate of 1.5×10^{-8} to $2.1 \times 10^{-7} M_{\odot}/yr$ for a core mass (which can also be estimated as the final mass) of about 0.6 to $0.94 M_{\odot}$ during the horizontal part of the post-AGB evolution and strongly decreasing mass loss during the cooling sequence (Bloeker, 1995a).

Olofsson (2003) lists molecular species which were detected only in the circumstellar envelopes of post-AGB objects, namely CH, CH⁺, H₂, N₂H⁺, OCS, H₂CO, HC₄H, HC₆H, CH₃C₂H, CH₃C₄H, and C₆H₆.

The H₂ molecule is the most abundant one in post-AGB stars and is often found in emission as the $2.12 \mu\text{m}$ feature of shocked H₂ in the near-infrared, hinting towards an interaction between the remnant of the expanding circumstellar envelope of the AGB star and a faster post-AGB wind (Kastner et al., 1999).

In the beginning, a general enhancement in s-process elements was expected for post-AGB objects, but observations show that this is not the case. There are strongly s-process enhanced objects which are C-rich, and O-rich objects that show no such enhancement or even a deficiency of s-process elements (Waelkens & Waters, 2003).

In the mid-infrared region one can observe dust-features of post-AGB stars that can be divided into C-rich or O-rich chemistry.

In stars of O-rich chemistry, amorphous silicates are dominant with broad resonances at 10 and $18 \mu\text{m}$ (Molster et al., 1999). At 23.5, 27.5 and $33.5 \mu\text{m}$ the bands of crystalline silicates can be found (Waters et al., 1996), and in several cases the presence of crystalline H₂O ice near 43 and $60 \mu\text{m}$ was confirmed (Omont et al., 1990).

For C-rich stars the dust consists of amorphous carbon and SiC, the latter showing a resonance-feature at $11.2 \mu\text{m}$ (Goebel & Moseley, 1985). A broad and strong peak near $26 \mu\text{m}$ which is often called the $30 \mu\text{m}$ feature in the literature, can be assigned to MgS (Nuth et al., 1985). In cool post-AGB stars a feature at $20.3 \mu\text{m}$, also referred to as $21 \mu\text{m}$ feature, can be found which has been attributed to TiC (von Helden et al., 2000).

Post-AGB stars of C-rich chemistry show emission features at 3.3, 6.2, 7.7, 8.7, and $11.3 \mu\text{m}$, originating from polycyclic aromatic hydrocarbons (PAHs), which can only form above a temperature of 5000 - 6000 K (Allamandola et al., 1989). The high temperature needed for the creation of PAHs is the reason that PAHs can not be observed in C-rich AGB stars.

In one case bands of nanodiamonds have been identified at 3.43 and $3.53 \mu\text{m}$ (Guilloy et al., 1999).

The spectral energy distribution of these two post-AGB groups has the same double-peaked appearance and the metallicity spread is quite similar (Van Winckel, 2003).

Although the evolution of the star from O-rich and H-rich to C-rich and H-poor suggests that the dust of a C-rich object is C-rich itself, some exceptions are known, cases where the cool dust of a star is O-rich while the star is C-rich (Waelkens & Waters, 2003). These observations point to the assumption that the O-rich to C-rich chemical transformation may happen very rapidly.

The timescales for the post-AGB phase (a few times 10^4 years) and the thermal-pulse cycle (10^4 - 10^5 years) make it possible for some stars to experience a "late" or "very late" thermal pulse, the "late" occurs on the horizontal part of the post-AGB track, the "very late" on the White Dwarf cooling track (Iben, 1984).

These thermal pulses create the so-called born again AGB stars by bringing the stars back into the Red Giant region of the HR-diagram through a rapid inflation of the stellar envelope. According to this born again scenario, no photospheric hydrogen would survive, because it gets mixed into layers of higher temperature and burns rapidly. The resulting AGB-star continues to burn helium in a shell.

A very late thermal pulse scenario is suspected to be responsible for R CrB stars, which are C-rich objects with episodic dust formation events (Clayton, 1996).

Several observed low-mass low-luminosity protoplanetary nebulae (PPNe) show expansion velocities of their molecular envelopes that are very low (about 5 km/s) compared to those of high-luminosity objects (about 15 km/s). Alcolea & Bujarbal (1991) used this to identify possible progenitors of low-mass PPNe, based upon the assumption that the expansion velocity of the shell that was produced during the AGB wind will not change during the post-AGB phase. They deduce that RV Tauri variables also have low expansion velocities along with the chemical properties expected for evolved objects and therefore are evolutionary related to PPNe like the Red Rectangle or M2-9.

The Toruń catalogue of Galactic post-AGB and related objects by Szczerba et al. (2007) is a collection of 326 *very likely*, 107 *possible* and 64 *disqualified* post-AGB objects (state 1 October, 2006) that will be updated regularly. This on-line catalogue is based on the literature available at NASA's Astrophysics Data System and uses several different classification criteria to categorize the objects expected to be in the post-AGB phase. The observed properties of the two components, the star with its spectral type and luminosity class and the circumstellar envelope exhibiting infrared excess and spectral features due to dust or gas, are the foundation for the classification criteria.

The 326 *very likely* post-AGB objects are composed of the following classes (Szczerba et al., 2007):

- *IRASsel*: The majority, namely 115 stars, of the *very likely* post-AGB objects belong to this group of **IRAS selected sources**. A present circumstellar envelope blocks light from the star, therefore stars chosen upon this criterion are mostly optically faint. The IRAS colours are between those observed of AGB stars and planetary nebulae. Since there is no information on the star itself, it could also be a galaxy, an AGB star, a PN or a young stellar object, thus it is advisable to take another classification into account to properly identify the source as a post-AGB object.
- *hglsgl*: The 63 **high galactic latitude supergiants** are at $|b| > 15^\circ$ and expected to be low-mass stars at a later stage of stellar evolution. They show low metallicity as anticipated for Population II supergiants, and belong to spectral types K, G, F and A. Some stars within this class display extreme depletion of Fe-group elements, an indicator for past mass loss.

- *hglB*: 9 stars of the listed *very likely* post-AGB objects are **High Galactic latitude B-type supergiants**, with $|b| > 15^\circ$ and spectral type B as well as a chemical composition anticipated for post-AGB stars.
- *hotpAGB*: The 18 **hot post-AGB objects** included in the catalogue are supergiants with early-type spectral classes like A and B, appropriate post-AGB chemical compositions and lower Galactic latitudes ($|b| < 15^\circ$). In some cases, presumably the more massive sources, an IR-excess was observed.
- *IRexc*: Of this class of **Bright stars with infrared (IR) excess**, 34 candidate post-AGB objects were chosen. This classification uses observed strong far-IR excess as evidence for large mass loss (Parthasarathy & Pottasch, 1986), along with estimations of the dust mass. This selection criterion alone is not sufficient to clearly identify post-AGB stars.
- *UU Her*: **UU Her-type stars** are a small group within Population II supergiants that exhibit high radial velocities, pulsations with small amplitudes as well as a large IR excess produced by circumstellar dust. 13 UU Her stars are proposed as *very likely* post-AGB objects.
- *RV Tau*: The **RV Tau stars** are variable stars with alternating deep and shallow minima and a period of 30 to 150 days. They belong to spectral types F, G and K and often show IR excess. A high percentage of the known RV Tau stars are binaries. It is commonly expected that stars of this class are post-AGB objects, 99 of them are listed in the post-AGB catalogue.
- *R CrB*: 36 As mentioned above, the **R CrB stars** must have experienced some kind of event that removed the H-rich envelope and left the C-rich core. To account for their possible post-AGB nature, 36 R CrB stars are *very likely* post-AGB objects.
- *eHe*: **Extreme helium stars** are evolutionary related to R CrB stars and therefore are also possible post-AGB candidates, at least the authors assume that for 16 objects.
- *LTP*: 2 **Late Thermal Pulse objects** are also expected to be in their latest stages of evolution.
- *21 micron*: 12 **21 micron emission sources** are C-rich stars with enhanced s-process element abundances and a strong emission band at 21 microns. 12 of these objects are listed to be in the post-AGB phase.
- *refneb*: Within this class named **Reflection nebulosity**, 4 well known objects of post-AGB nature can be found, the Red Rectangle along with Minkowski Footprint, Egg Nebula and AFGL 618.

Objects that are expected to be *very likely* post-AGB stars have to at least fit one of the listed criteria and have more than 5 ADS references that confirm the post-AGB classification. If there are less than 5 papers in agreement with the post-AGB nature but one of the criteria above is satisfied, it is one of the 107 *possible* post-AGB objects up to now. For 64 objects, the assumption that they are post-AGB stars turned out to be doubtful according to different interpretations in the literature and

so they are *disqualified* (Szczerba et al., 2007).

The data of the 326 *very likely* post-AGB objects was then used for some general studies on the properties of post-AGB stars concerning the Galactic longitude and latitude as well as the most common spectral types of these objects.

Fig. 1.10 shows the Galactic longitude distribution of all 326 *very likely* objects (Szczerba et al., 2007) in the first panel, without helium stars (*R CrB*, *eHe* and *LTP*, 272 objects) in the second, and for planetary nebulae (1141), taken from the Strasbourg catalogue (Acker et al., 1992). The first two panels are quite similar, meaning that the helium star distribution is comparable to that of the other post-AGB objects, with most of the objects between $-60^\circ \leq l \leq +60^\circ$ and a higher concentration at the Galactic center. The third panel shows the majority of the PNe near the center. A reason for this difference to the post-AGB objects could be the nature of the objects, as PN can be detected even in the Galactic bulge due to the strong emission lines while this is not the case for post-AGB stars. Another possibility is the fact that low mass post-AGB objects might not be able to produce PN, so there will be more low-mass objects within the post-AGB class than in the PN (Szczerba et al., 2007).

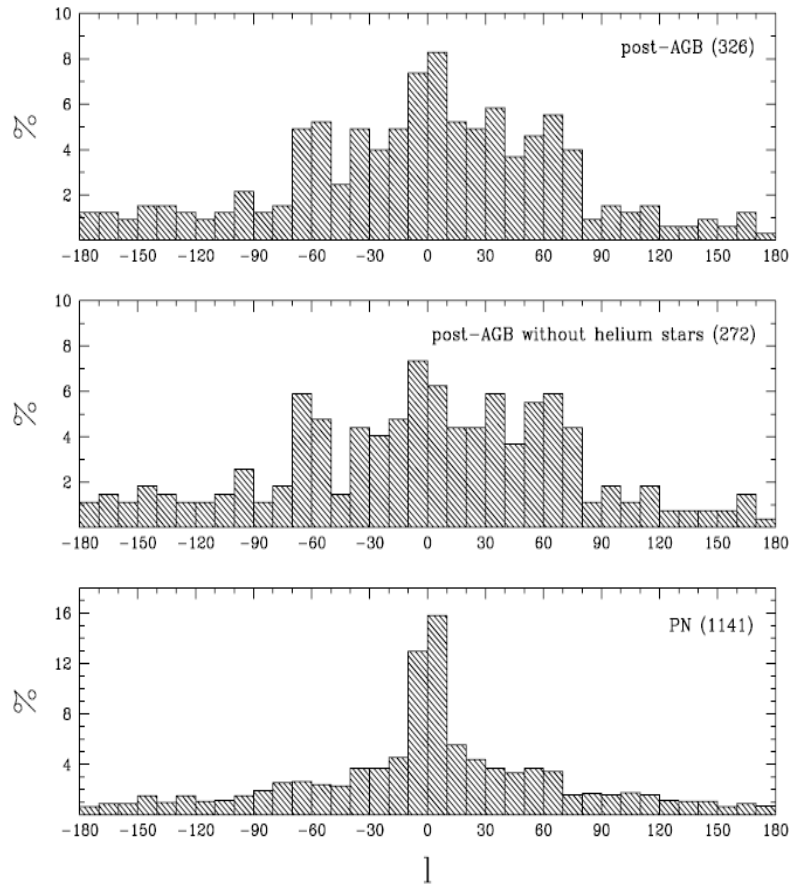


Figure 1.10: Galactic longitude distribution for all *very likely* post-AGB objects (first panel), post-AGB objects without helium stars (second panel) and for PN (Szczerba et al., 2007).

This can also be seen in Fig. 1.11, where the Galactic latitude distribution is plotted for post-AGB objects and PN. There are more post-AGB stars at high Galactic latitudes, presumably low-mass objects, than PN (Szczerba et al., 2007).

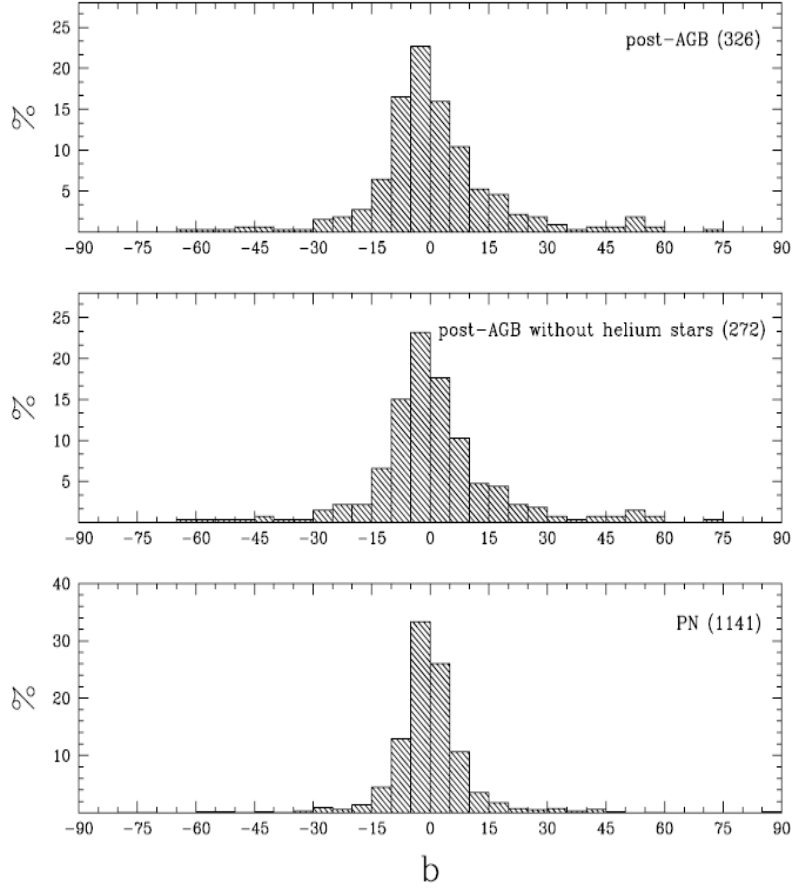


Figure 1.11: Galactic latitude distribution for all *very likely* post-AGB objects (first panel), post-AGB objects without helium stars (second panel) and for PN (third panel) (Szczerba et al., 2007).

The distribution of post-AGB objects throughout the spectral types (see Fig. 1.12) reveals an interesting gap at spectral type A (about 10 000 K). This gap is present in the sample of post-AGB objects at low Galactic latitudes as well as higher ones, regardless if the helium stars are included in the sample or not (Szczerba et al., 2007). This feature is not surprising if one takes into account the fast evolution rate during the post-AGB phase (Bloeker, 1995a).

1.1.4.1 Binary post-AGB Evolution

The shape of circumstellar envelopes of post-AGB objects and planetary nebulae could be explained if one assumes that these objects are binaries. In the cases of 89 Her and AC Her, both stars seem to have a lower mass companion (Waelkens & Waters, 2003). Szczerba et al. (2007) found 47 of their 326 *very likely* post-AGB objects to be confirmed binaries in the literature.

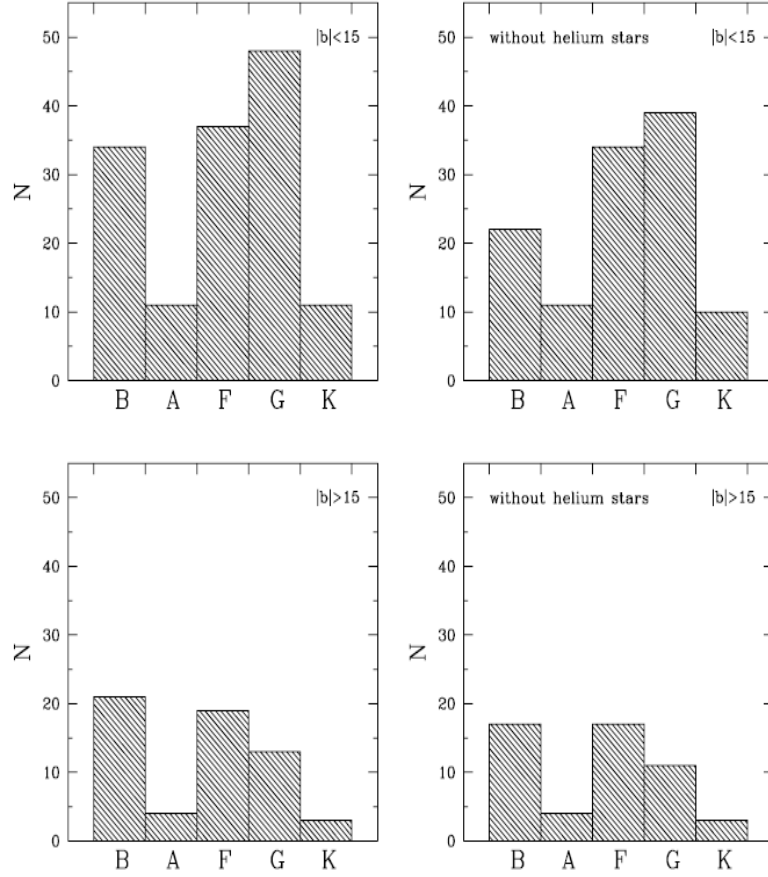


Figure 1.12: On the left side, the distribution of spectral types for *very likely* post-AGB objects at $|b| < 15^\circ$ (upper panel) and $|b| > 15^\circ$ (lower panel) and for *very likely* post-AGB objects without helium stars on the right side (Szczerba et al., 2007).

In Fig.1.13 the properties of the star AC Her are shown in more detail. The orbital period in days is 1194 with an eccentricity of 0.12 and a mass function of 0.25 (Van Winckel et al., 1998). The confirmation of the binarity based on radial velocity variations is shown in the left panel. On the right side the spectral energy distribution can be seen with a large IR excess caused by circumstellar dust.

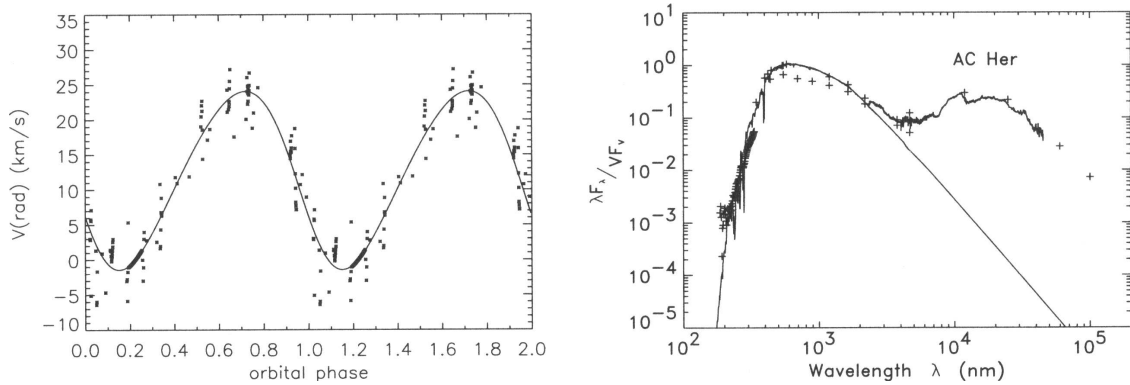


Figure 1.13: Properties of the binary AC Her. For further information see text (Habing & Olofsson, 2003a).

Some of the known post-AGB binaries show photospheric composition anomalies with extreme Fe, Mg, Ca, Si, and Cr deficiency combined with normal, almost solar abundances of C, N, O and S with respect to H (Mathis & Lamers, 1992), which are referred to as peculiar post-AGB stars (or pec-pAGBs). The effective temperatures of these pec-pAGB objects are between 6000 K to 7500 K with $\log g$ values between 1 and 2. An attempt was made by Mathis & Lamers (1992) to explain these anomalies by suggesting two different scenarios including the accretion of clean gas, which means that the elements that are underabundant have been depleted by dust. To achieve a photosphere without certain elements, a clean photosphere, one can use a companion in a binary system that accretes gas and so becomes the metal deficient pec-pAGB star, or a single star model that stopped the mass loss after a strong wind (superwind) and cleaned the gas of the dust grains by radiation pressure, leaving clean gas back to get reaccreted by the star itself. The binary scenario applies some restraints on the evolutionary status of the two companions, like both of them have to be on the AGB simultaneously, which make the single star model more likely.

Based upon the binary scenario of Mathis & Lamers (1992), Waters et al. (1992) proposed gas accretion from a circum-system disc in pec-pAGB binaries. This disc is created by dust, molecules and gas that were ejected during the AGB phase by one of the stars in the binary system, while the evolutionary status of the companion is not significant in this model. The post-AGB star can accret the clean gas from the circum-system disc during a timescale of the order of 10^3 years, which fits with the evolutionary time frame of a star evolving from the cool end of the AGB towards the hot end of the post-AGB (at $T_{\text{eff}}=7500$ K, Schoenberner, 1983). This scenario also accounts for the rather few pec-pAGB stars because the dimension of the binary system is a limiting factor: no circum-system disc will be created if the companions are too close, and if the system is too wide, the accretion of the post-AGB star will be too small to show a significant change in the photosphere (Waters et al., 1992).

The fact that depletion was found to have a stronger impact on the chemical composition of RV Tauri stars than dredge-up processes (see the series of papers by Giridhar et al. and Gonzalez et al. in the years 1994 to 2005), lead Van Winckel et al. (1999) to suggest that many RV Tauri stars of photometric class b could be binaries. Several observed properties can be explained with a binary system where circumstellar dust is stored, including the depletion mentioned above. Other indications for this theory are the shape of the spectral energy distributions as well as the weak microwave CO emission observed in some cases (Van Winckel et al., 1999).

1.1.5 Planetary Nebulae

A Planetary Nebula (PN) is the result of the circumstellar material surrounding the star being ionized by the hardened radiation field of the central star of spectral type O, which resembles the needed temperature to ionize the ejecta. If the post-AGB phase was too long, which would be the case for very low-mass (low-luminosity) objects, the circumstellar material would be too far away from the star by the time the central star reaches spectral type O, and so it would not be ionized and no PN could be observed (Waelkens & Waters, 2003).

Observations of central stars of PNe show that about 20% of them are hydrogen deficient, the others show solar-like compositions (Waelkens & Waters, 2003).

Although the mass loss during the AGB phase is believed to be spherical, PNe are not, they are observed to be mostly aspheric, often bipolar. Stanghellini et al. (2007) searched for PNe in the LMC and SMC to analyse their dust properties and possible correlations between chemical composition and shape. The authors were able to split the observed objects into two groups, CRD are PNe with carbonaceous dust while ORD show oxygen-rich dust in their spectra. Stanghellini et al. (2007) found symmetric morphology for the majority of the CRD objects and high asymmetries for ORD PNe.



Figure 1.14: X-Rays from the Cat's Eye Nebula (NGC 6543). Source: APOD ², Credit: X-ray: NASA/CXC/SAO; Optical: NASA/STScI

1.1.6 White Dwarfs

Low and intermediate mass stars up to masses of about 8 to 10 M_{\odot} are expected to become White Dwarfs (WD) in the end. During the previous stages of evolution, the star has suffered substantial mass loss. Therefore, WD can be found in a certain mass range. The upper mass limit for a WD was found by Chandrasekhar and is 1.4 M_{\odot} , but most of the White Dwarfs known have masses around 0.6 M_{\odot} . They are quite compact (approximately 10^3 km) and they are electron-degenerated due to the high compression, with densities around 10^8 to 10^{10} kg m⁻³ (Weigert et al., 2005).

²<http://antwrp.gsfc.nasa.gov/apod/archivepix.html>

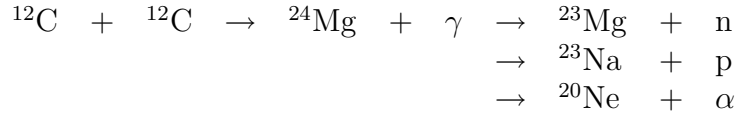
In very cool WD, a crystallization takes place, the ions in the star arrange themselves like a grid (Weigert et al., 2005). The WD moves in the HR-diagram from high luminosities to very low ones at a steady radius, and cools down slowly.

1.1.7 Supernovae

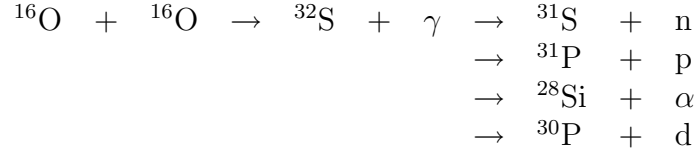
For completeness the fate of massive stars is also mentioned here, although they play no role for the area of post-AGB objects.

In massive stars, an onion-like structure can be found in the interior, with different burning phases layered above each other. The outermost layer of the star is unprocessed hydrogen, beneath that envelope, a hydrogen burning shell produces helium. After an intershell region, the helium burning shell fuses the ^4He nuclei into heavier elements, the basis for carbon-, oxygen- and silicon-burning.

At 5×10^8 to 1×10^9 K carbon burning starts, creating an excited ^{24}Mg nucleus, that could dissociate in different ways (Weigert et al., 2005):



At about 1.4×10^9 K, oxygen burning starts (Weigert et al., 2005):



As a result of the oxygen burning and the production of ^{28}Si , the silicon burning can start at about 2×10^9 K, with the most important outcome being (Weigert et al., 2005):



After the production of iron, nuclear fusion does not gain energy anymore.

Comparable to the s-process during the AGB-phase, the r-process can be found in SN. A great reservoir of neutrons leads to a rapid neutron capture, where isotopes are built that are containing many neutrons, before β decay sets in and continues until the valley of stable isotopes is reached.

During these burning stages, the central temperature rises up to several 10^9 K. The photons get energy-rich. In very high-mass stars pair production gets dominant, probably the heavier nuclei are getting disrupted again. In both cases, the center of the star becomes unstable. It keeps collapsing until the electrons are being pushed into the nuclei, creating a highly compressed core. The infalling material of the rest of the star upon this compact center bounces back again, building up shock waves that blow away the outer layers with about 10^4 km/s. The core that remains after the supernova explosion is a neutron star. The energy that is set free during a core collapse is around 10^{45} J, the maximum of the luminosity is about $10^{10} L_{\odot}$. A supernova explosion is one of the brightest and most spectacular events in the universe.

The rising of the luminosity can be explained by the increase of the surface, material that was blown away. The radioactive decay of short-lived elements is responsible for the lowering in light after some time. The high expansion velocity of the material ejected by the SN leads to a thinning of the gas, and due to the fact that these velocities are much higher than that of the surrounding interstellar medium, shockfronts are produced. So-called Supernova Remnants are beautiful glowing objects like the *Crab Nebula* (Fig.1.15) with interesting shapes and structures.

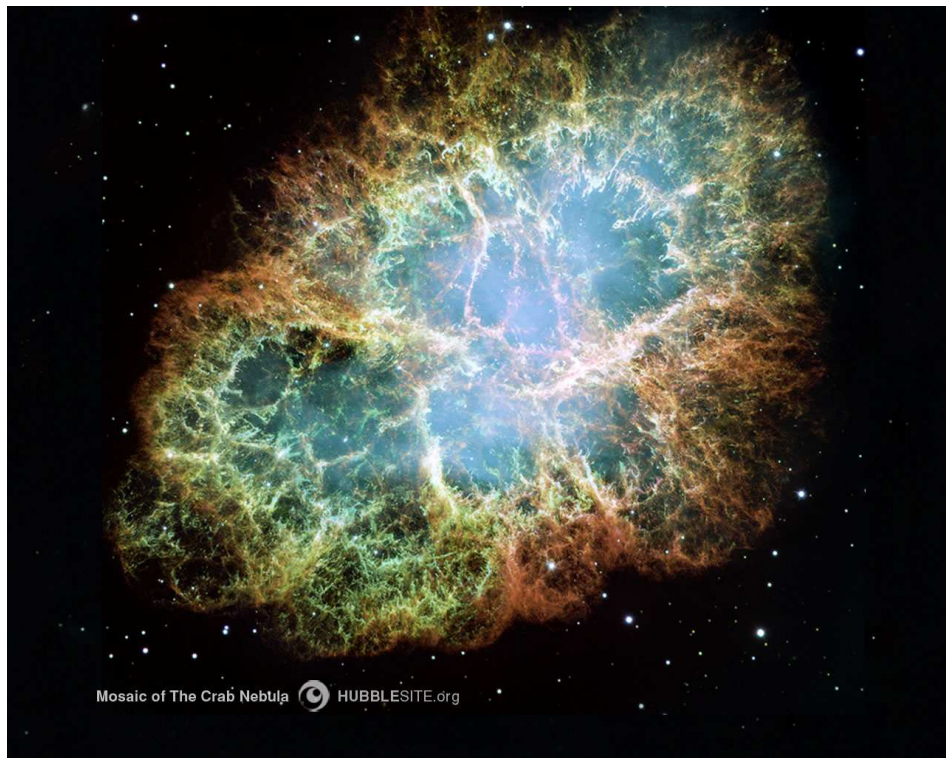


Figure 1.15: Crab Nebula Mosaic from HST. Source: APOD, Credit: NASA, ESA, J. Hester, A. Loll (ASU), Acknowledgement: Davide De Martin (Skyfactory)

Two distinct types of supernovae can be found, which have different origins. The separation into the groups is based on the observation of the luminosity and the spectroscopic properties.

Type Ia SNe exhibit a characteristic lightcurve with a steep rise and a slightly smoother decrease in luminosity after the maximum. In Type Ia SNe silicon-features

can be observed but no hydrogen, which points to a WD that has accreted mass of a companion in a binary system. When the accreted mass increases over the Chandrasekhar-limit, the WD blows away the outer layers in a supernova-explosion.

Type Ib, Ic SNe are a bit different. If the hydrogen-loss happened through effects like strong stellar wind of a massive star, which would be the case for Wolf-Rayet-Stars, they are filed to be Type Ib or Type Ic. No silicon features are found in the spectra of these stars.

Type II SNe show hydrogen in their spectrum near the maximum, the lightcurve is rather flat, no extreme maximum compared to a Type Ia SN. Progenitors for SNe of this group are massive supergiants of spectral type O (on the MS).

1.1.8 Neutron Stars

After a SN explosion, a small neutron star is left that is even more compact than a WD, with densities over $10^{18} \text{ kg m}^{-3}$. These objects are up to now not fully understood. Neutrons are partially arranged in grids, comparable to the electron-degenerated core of a WD, in other regions of the neutron star there could be some kind of neutron-liquid, while the outer layer of this star is composed of an ion-grid of atomic nuclei (Weigert et al., 2005). The upper mass limit for these stars is estimated to be somewhere between 1.5 to $3 M_{\odot}$. The initial mass of a neutron star is calculated to be roughly 10 to $40 M_{\odot}$.

1.1.9 Pulsars

Pulsars are neutron stars shortly after their formation. The neutron star is still very hot and is only visible as an X-ray source. The central star of the *Crab Nebula* mentioned before is the most famous pulsar known. The lightcurves are characterized by periods P between 1.5 ms and 4 s with duration of the pulse shorter than $0.1 P$, typically 5% of the period (Weigert et al., 2005). The reason for the observed periodicity appears to be rotation. The axis of the fast rotating magnetic field of the neutron star is not in line with the rotational axis of the star itself. If a relativistic electron or any other charged particle is accelerated by this fast rotating magnetic field it creates Synchrotron-radiation that emits in a restricted cone. The pulse of the neutron star is the result of the emitting cone pointing towards us. The rotation slows down with time, leading to longer periods, because the radiated energy is drawn from the rotation energy of the star.

1.1.10 Black Holes

In the two former cases of WD and Neutron Stars, degeneracy of some kind of particles can stop the collapse of the star, depending on the Chandrasekhar-mass-limit. If a star is entering the SN phase and the core is more massive than mentioned above, there is no way to stop the collapse. A black hole represents the most compact stellar remnant possible. The fact that such a high mass is compressed on such a

small radius results in a gravitational field strong enough that even light is not able to escape. The boundary of the event horizon is the so-called Schwarzschild-Radius:

$$r_s = \frac{2GM}{c^2} \tag{1.6}$$

If one takes the speed of light and estimates a mass of $3 M_\odot$, this leads to a Schwarzschild-Radius of about 9 km. The stellar remnant would disappear behind the event horizon, so the black hole itself cannot be seen, but some effects can be observed, like the influence of a BH on a nearby star, or the X-ray radiation of infalling matter. Initial stellar masses estimated for the creation of a black hole are above $40 M_\odot$ (Weigert et al., 2005).

Chapter 2

Variable Stars

As mentioned in the introduction, a star can experience variability during stellar evolution. The post-AGB phase is also accompanied by variability with a certain grade of irregularity, a more special property among the groups of variable stars.

2.1 Groups of Variable Stars

Some astronomers say, to some extent every star is variable. In fact there are many different ways a star can be labeled variable in its brightness. In *The General Catalogue of Variable Stars (GCVS)* by Samus et al. (1997), different groups of variable stars are described based upon the cause of the variability, like eruptive, pulsating or rotating variable stars, cataclysmic (explosive and novalike) variables and eclipsing binary systems.

In the late stages of stellar evolution, the stars begin to pulsate due to the mechanisms working in the star's interior. Therefore, the interesting group for this work is the group of Pulsating Variable Stars.

Pulsating Variable Stars can pulsate radially or nonradially, showing more or less periodic changes, expansion and contraction, of the stellar atmosphere. The pulsation type has influence on the shape of the star, as for radial pulsation, the star stays spherical and only changes in diameter, while in the nonradial case, the star shows a non-spherical shape with different zones of the star moving in- or outwards at the same time.

The group of pulsating variables can be subdivided into many different types, like the well known RR Lyrae stars, the Cepheids and others. Two types are of special interest for this thesis, the RV Tau variables and the SR variables.

2.1.1 RV Tauri Stars

The RV Tauri variables are radially pulsating supergiants with spectral types F to G at their maximum light and K to M at minimum. A basic characteristic of these stars is the shape of the light curve, a double wave with alternating primary and secondary minima (see Fig. 2.1) with periods of 50 and 150 days between two following deep minima (Preston et al., 1963). The primary and secondary minima can vary in depth, so that primary minima can become secondary and the other way round. This variation could be explained by two pulsational modes in the star, visualized by two sinusoidally varying functions (Gerasimovič, 1929), where the period of the second mode is twice that of the first mode. The depths of the secondary minima are more variable than that of the primary minima. The alternating deep and shallow minima mentioned above are also present in the colour curves, but with a time delay in respect to the light curve, the bluest colour is reached during the increase of the light curve, mostly after the secondary minimum (Pollard et al., 1996). Atmospheric shock waves are known to be present in RV Tauri stars. These shock waves are responsible for recombination emission lines that occur during rising light. The presence of these emission lines can lead to the very blue colours mentioned before (Pollard et al., 1996).

An attempt was made by Takeuti & Petersen (1983) to explain the pulsation characteristics of RV Tauri stars with the resonance hypothesis, which suggests a 2:1 resonance between the fundamental mode and the first overtone. However, the authors were not able to find a simple solution to the pulsational behaviour of RV Tauri stars with the resonance hypothesis. They stated that strong non-linear effects, for example a strongly enhanced first harmonic, could be the cause for the alternating deep and shallow minima.

While working on convection in RR Lyrae star models using a two dimensional numerical integration of the conservation equations of momentum, energy, and mass over several pulsation periods, Deupree & Hodson (1976) noticed in their models something they would expect for cooler and more luminous stars rather than RR Lyrae stars: convective motion is damped out every other period when the viscosity and diffusion terms are small and the convective velocities nearly sonic. This would lead to the alternating amplitudes known for RV Tauri variables.

The irregularities in RV Tauri stars also caused Aikawa & Bruegman (1987) to compute a hydrodynamic pulsation model with non-linear coupling between a pulsation driving mode and a strongly damped mode which was able to reproduce the characteristic variation of the light curve.

The work of Buchler & Kovacs (1987) aims to explain the alternating deep and shallow minima of RV Tauri stars with period doubling and a resulting chaotic behaviour.

The convention used to describe the phase of a RV Tauri star defines the primary (deep) minimum at phase 0.0 and the secondary (shallow) minimum at phase 0.5 (Pollard et al., 1996). RV Tauri stars with shorter periods are normally more regular than those with longer periods. RV Tauri stars are believed to be old-disk or halo-population low-mass supergiants of population II.

Such stars are expected to be in the evolutionary phase between the AGB and the planetary nebula phase. They are generally believed to be low-mass post-AGB ob-

jects which spent about 200 years in this variable RV Tauri state, but some of the known RV Tauri stars are "lazy" and might stay longer in this variable state, for example R Sct (Alcolea & Bujarrabal, 1991). These "lazy" RV Tauri stars show peculiarities in their envelopes like stronger molecular lines than observed in normal RV Tauri stars.

The assumption of RV Tauri stars being post-AGB objects seems to be confirmed by the relatively small number of RV Tauri stars, which would fit with the rather short (a few thousand years) evolution during the post-AGB phase (Pollard et al., 1996).

The *GCVS* divides the RV Tauri variables into two subtypes based upon their light curve:

- **RVa:** RV Tauri variables that do not vary in mean magnitude (like AC Her) and are single periodic. Pollard et al. (1996) observed very blue photometric colours of RVa stars during exceptionally deep minima.
- **RVb:** RV Tauri variables that vary in mean magnitude over a long period of 600 to 1500 days with amplitudes up to 2 mag in V (like RV Tau) on top of the short-term period of 50 to 150 days. This long-term variation is also present in the photometric colours. Both, the light and colour pulsational variations are weakened in some of the RVb stars at the minimum of the mean magnitude variation (Pollard et al., 1996).

It is difficult to find a model that is able to account for all the properties observed in RVb stars. An attempt was made to explain the RVb phenomenon by using a model of a dust-eclipsed RV Tauri star moving in a binary orbit (Fokin, 1994). The reddening of the colours and the decrease in light apply to this model, but other properties like the appearance of the reddest colours after and the weakening of the short-term variation at the light minimum of the long-term variation can not be explained by this model.

Pollard et al. (1996) adapted a model of Waelkens & Waters (1993) of binaries suggesting that they are interacting at some point during their orbit and that they are periodically eclipsed by a circumbinary dust-torus. This model is able to explain the periodic change in the long-term light and colour variations with mass ejection and the weakening of the pulsations at long-term minimum of the RV Tauri star with interaction. Depending on the strength of the interaction the observed properties would be more or less prominent.

A special feature often observed in RV Tauri stars is the presence of strong emission in the Balmer $H\alpha$ line throughout almost the whole pulsation cycle resulting from gas heated by shock waves propagating through the extended atmospheric layers where the $H\alpha$ line forms. Emission is also observed in metallic lines, and due to shockwaves passing through the photosphere, the profiles of the metallic absorption lines are sometimes doubled during phases 0.1 and 0.6 (Pollard et al., 1997) which can be interpreted either as two absorption components or as an emission component overlying a broad absorption line. The presence of TiO bands, which are stronger than expected for spectral types of RV Tauri stars, points towards special physical conditions that differ from normal stars (Pollard et al., 1997).

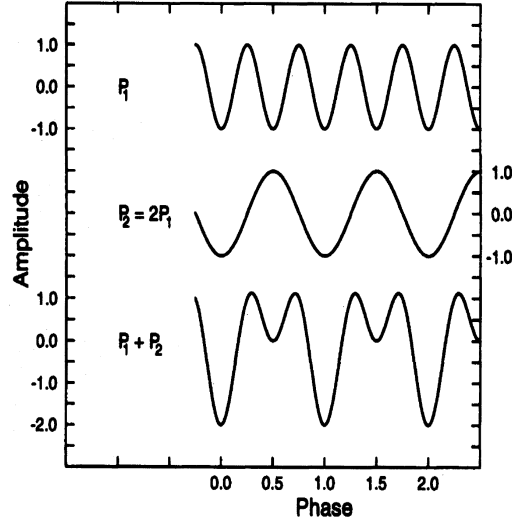


Figure 2.1: A characteristic lightcurve of a RV Tauri star reproduced by Pollard et al. (1996) using $P_2 = 2P_1$.

An additional subdivision done by Preston et al. (1963) considers the spectral properties of RV Tau stars:

- **RVA:** RV Tauri variables of spectral type G to K, that are metal-rich and sometimes show TiO bands at minimum light. This type exhibits irregularities in the strength of the CN bands (Preston et al., 1963). In UVB photometry, members of the RVA subgroup are redder than those of subgroup B.
- **RVB:** metal-poor RV Tauri variables having weak lines, showing evidence of CH and CN, and variations with light curve phase. Stars of this type are carbon-rich stars of type Fp(R) (Pollard et al., 1996). Short-period variables of this carbon-rich group are generally more stable in their pulsational behaviour than long-period variables (Pollard et al., 1996). The envelope dust temperatures observed for this group are cooler than those of subgroup A (Raveendran, 1989).
- **RVC:** Also metal-poor RV Tauri variables with weak lines and little to no CH or CN. This type is mostly found in globular clusters (Pollard et al., 1996).

DuPuy (1973) found a relation between period and luminosity for RV Tauri stars,

$$M_V = -5.3 + 0.021P^d \quad [\text{mag}] \quad (2.1)$$

but this result is based upon three RV Tauri stars which are confirmed members of a globular cluster, and they only have a period of about 60 to 90 days. Another difficulty with the period-luminosity relation of DuPuy is the fact that RV Tauri stars, which are found in globular clusters, often belong to the Preston RVC group, therefore it is questionable if the relation also fits the other Preston subgroups.

According to Joy (1952), the RV Tauri stars he observed showed low radial velocities ($|v_{rad}| < 70 \text{ km/s}$).

The RV Tauri stars show large radiation excesses in the mid- and far-infrared due to circumstellar shells (Alcolea & Bujarrabal, 1991), regardless whether the star is oxygen-rich or carbon-rich. This infrared excess can be modelled with one shell or with two adjacent shells, depending on the individual object (Alcolea & Bujarrabal, 1991).

For a "common" RV Tauri star (like R Sge, AC Her, see Fig. 2.2) a single-shell-model with a temperature $T_i \sim 500$ K at the inner radius of the dust shell with $R_i \sim 2 \times 10^{15}$ cm is sufficient enough to reproduce the IR flux observed. If one assumes an expansion velocity of gas and dust of 5 km/s, then the values correspond to a dust formation that stopped about 100 years ago.

For the peculiar or "lazy" objects, a model of two dust shells representing two different mass loss phases seems to be more appropriate (see Fig. 2.3), where the inner shell represents a small active mass loss and fits the observed dust emission at wavelengths under $30 \mu\text{m}$, while the outer shell corresponds to a higher mass loss rate in the past (Alcolea & Bujarrabal, 1991).

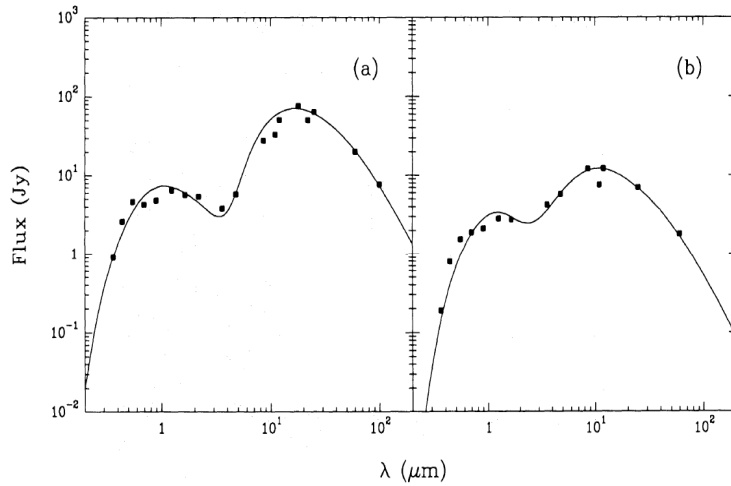


Figure 2.2: Comparison of a one-shell model (solid line) with observational data (dots) of the "common" RV Tauri variables (a) AC Her and (b) R Sge (Alcolea & Bujarrabal, 1991).

The fact that a lot of RV Tauri stars exhibit more than one dust shell leads to the assumption that mass loss is not a continuing process but a recurring one. Not at every pulsation dust is produced in recognisable amount, there are also quiet phases with insignificant dust formation (Alcolea & Bujarrabal, 1991).

There are objects with hot circumstellar dust as well as objects with cooler dust shells (Goldsmith et al., 1987). These shells may also undergo changes in their properties.

The silicate emission feature at $10 \mu\text{m}$ was found in carbon-rich stars as well as in oxygen-rich ones (Evans, 1985). RVb stars seem to be redder than RVa stars, which leads to the assumption that RVb stars exhibit in the inner regions denser dust shells than RVa stars, showing strong excess emission in the $1-3 \mu\text{m}$ band. This was

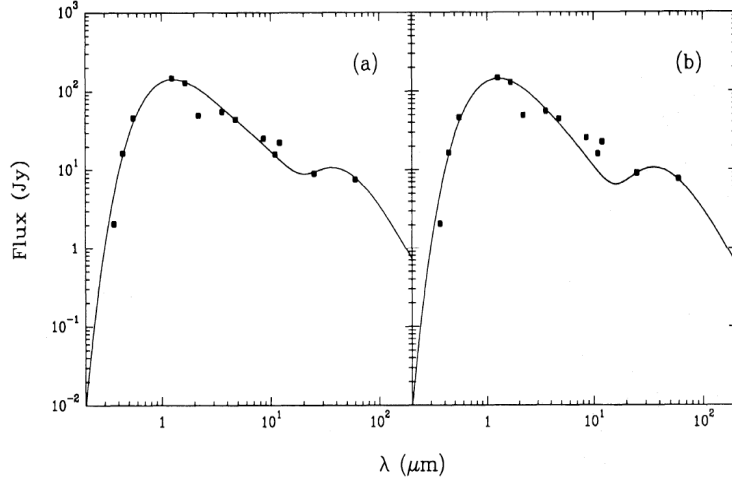


Figure 2.3: Comparison of a (a) two-shell model (solid line) and a (b) one-shell model with observational data (dots) of the "peculiar" RV Tauri variable R Sct (Alcolea & Bujarrabal, 1991).

confirmed by Raveendran (1989).

Evans (1985) suggested that the RVa and RVb groups might be consecutive evolutionary stages. The RVb stage could be the successive stage to the RVa stage, when the star moves to the hotter part of the HRD, also showing shorter periods and a drop in luminosity. The attempt to apply this thought to the RVA and RVB group based on the consideration of the dust shells exhibiting oxygen-rich components of the previous RVA stage in the RVB spectra is not recommendable due to the fact that RVB stars sometimes show metal deficiency and that there is a difference in space distribution between those two spectroscopic groups.

According to Raveendran (1989), the Preston-subgroups can also be detected while analyzing other properties of these stars, for example the inner shell temperature. Stars of the spectroscopic subgroup A can be found at higher temperatures, while those of type B are at temperatures lower than 450 K. Stars of group B also show larger $11 \mu\text{m}$ excesses for given excesses at $3 \mu\text{m}$.

Some astronomers compared the RV Tauri stars with other groups of variable stars, for example the so called R CrB variables, which also show an infrared excess, circumstellar shells, polarization changes and carbon enhancements (Evans, 1985). Also the comparison with Mira-variables is common, because Miras are known to be evolved stars on the cooler side of the HR-diagram. RV Tauri stars can be found at lower temperatures than oxygen- or carbon-rich Miras in the IRAS colour-colour diagram (Raveendran, 1989). An emission feature at $10 \mu\text{m}$ that was observed in spectra of several RV Tauri stars can be assigned to silicates, like in oxygen-rich Miras, but the emissivity indices of the silicate grains seem to be different. The reason for this might be the differences in temperature and luminosity of the two different types of stars.

The metallicity span of the RV Tauri stars is expected to range between $[\text{Fe}/\text{H}]=-2.3$ to $[\text{Fe}/\text{H}]=-0.2$ approximately (Gonzalez et al., 1997). The presence of some kind of wind will have influence on the chemical composition of the photosphere, as suggested by Gonzalez et al. (1997), who proposes that dust grain formation in the RV Tauri wind could lead to fractionation of elements and to abundance anomalies (see above).

Elements that condense into grains at high temperatures are often more depleted than elements with lower condensation temperatures. The pulsations in the atmosphere raise gas up into the inner regions of the circumstellar shell where dust grains condense and later the depleted gas falls back onto the star (Giridhar et al., 1998a). This dust-gas separation makes it difficult to observe indications for deep-mixing. Deep-mixing or extra-mixing describes a mechanism that enables a non-convective exchange between the envelope and hydrogen-burning zones (Busso et al., 2010). Changes in the photospheric CNO isotopic ratios are the result of deep-mixing episodes during the RGB and AGB.

The dust-gas separation and the conditions needed to create abundance anomalies in stars are described by Giridhar et al. (2005) in more detail:

The first constraint is some kind of dust-formation site near the star, for example a circumbinary or circumstellar disk or just wind. After the successful dust formation the dust grains must be separated and removed from the gas, probably by radiation pressure. In the end it is necessary for the mass of the accreted gas to exceed the envelope mass to dominate the photosphere.

The coolest RV Tauri stars have deep convective envelopes that might be the reason that the effects of dust-gas separation are diminished in these stars (Giridhar et al., 2005). This theory is supported by observations of RV Tauri stars of temperatures under $T_{\text{eff}} \sim 5000$ K which do not show any signs of dust-gas separation, independent of their metallicity.

The effect of element fractionation might be amplified by a binary companion as was observed for post-AGB A to F supergiants (Gonzalez et al., 1997). Some RV Tauri stars are known to be part of a binary system, but it is difficult to find evidence for a companion because the pulsations of the variable star could diminish the orbital radial velocity variations.

It is unlikely that all post-AGB objects had RV Tauri stars as progenitors, but it is likely that RV Tauri star eventually become post-AGB stars (Jura, 1986). There is reason to believe that RV Tauri variables left the AGB or RGB prematurely due to high mass loss that might be caused by a companion (Giridhar et al., 2000a).

2.1.2 SR Stars

The group of semiregular variables includes giants or supergiants of intermediate and late spectral types with a recognisable light curve period (Samus et al., 1997). This periodicity of about 20 to over 2000 days is sometimes interrupted or accompanied by irregularities that gave this group the designation *semiregular*. Usually the amplitudes of the light curves lie between 1 and 2 mag in V, but values of several hundredths to several magnitudes have also been observed. These stars belong to the old disc population. There is also a division into subgroups (see *The General Catalogue of Variable Stars (GCVS)* by Samus et al. (1997) for more information):

- **SRa:** Giants of spectral types M, C, S or Me, Ce, Se, which are comparable to Miras, only exhibiting smaller light amplitudes, less than 2.5 mag in V. Periods are between 35 to 1200 days with some variation in the lightcurve shapes and amplitudes.
- **SRb:** Stars of the same spectral types as SRa stars, but with irregularities and strong variations in periodicity. Mean cycle lengths for these stars are between 20 and 2300 days.
- **SRc:** These supergiants of spectral types M, C, S or Me, Ce, Se have rather long periods of 30 to several thousand days and light amplitudes of approximately 1 mag.
- **SRd:** This subgroup contains giants as well as supergiants of spectral classes F, G, or K. Some of them show emission lines in their spectra. Typical periods are between 30 to 1100 days with amplitudes of about 0.1 to 4 mag.

Only the subgroup of SRd variables is of interest in the search for post-AGB candidate objects, therefore the other subgroups are not discussed further.

The emission lines observed in the spectra of SRd stars could hint to shockfronts in the interior of the stars and the abundances are mostly those expected for stars in the latest stages of stellar evolution (Dawson & Patterson, 1982). SRd stars belong kinematically to the old disc or halo population and show metal abundances of about 5 to 30 times lower than the sun (Dawson & Patterson, 1982).

Giridhar et al. (1998b) confirmed that the low-mass SRd stars within their sample are generally metal-poor ($[\text{Fe}/\text{H}] \leq -1$) but evolved stars. The follow-up papers in this series dealt with additional SRd variables and their chemical composition and evolutionary status. One conclusion drawn in the second paper (Giridhar et al., 1999) was that the presence of element enrichment after the first dredge-up places this group of stars either on the tip of the RGB or on the AGB with luminosities greater than the RGB tip. If these stars were enriched in C and s-process elements, they would have experienced the third dredge-up and therefore be AGB stars, but no enrichment of this kind was found in the sample stars of Giridhar et al. (1999).

A relation between RV Tauri variables and SRd stars was suggested from a theoretical HRD of $\log g$ against $\log T_{\text{eff}}$ (see Fig. 2.4):

The SRd stars are placed at the cooler side of the observed RV Tauri stars. They could either be on the tip of the RGB or already on the AGB. During the post-AGB evolution, a star would move from lower to higher temperatures at constant luminosity. Therefore it is possible that SRd stars evolve into RV Tauri stars when they cross the Hertzsprung gap to higher temperatures (Giridhar et al., 1999).

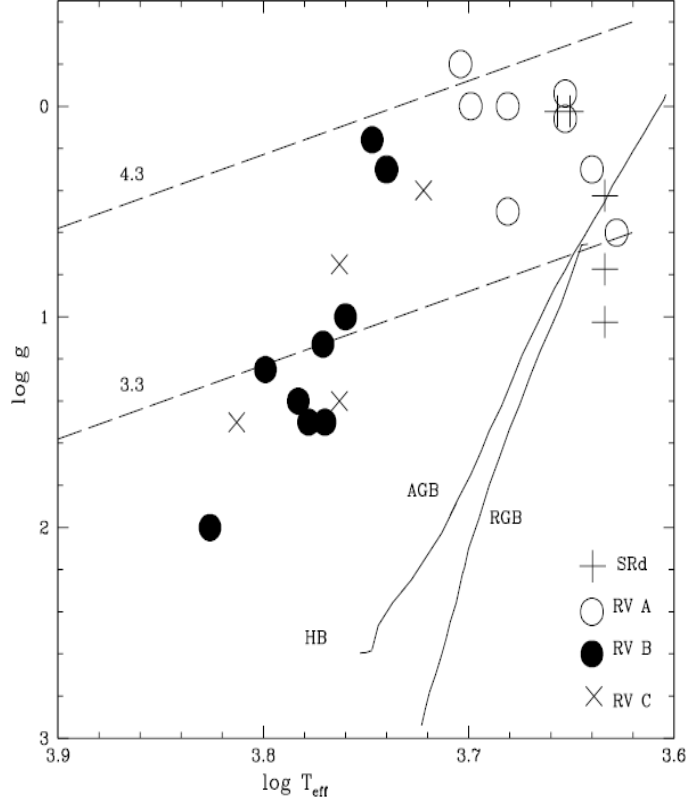


Figure 2.4: Figure taken from Giridhar et al. (1999): A sample of SRd and RV Tauri stars plotted into a theoretical HRD of $\log T_{\text{eff}}$ against $\log g$. The dashed lines symbolize a possible post-AGB evolution of a $0.8 M_{\odot}$ star at constant luminosity with $\log L/L_{\odot}=3.3$ (lower line, corresponds to an evolution off the RGB) and $\log L/L_{\odot}=4.3$ (upper line, evolution off the AGB). A theoretical isochron (10^{10} years, $Z=0.0004$) is plotted with RGB, HB and AGB.

The fact that there is no enrichment in s-process elements or carbon leads Giridhar et al. (2000b) to the assumption that SRd variables might not have experienced thermal pulses because they left the RGB or AGB too soon. The stellar pulsations observed in SRd stars as well as in RV Tauri variables could be responsible for heavy mass loss and an early departure from the AGB (Giridhar et al., 1999).

Chapter 3

Data

3.1 Observation

Joyce (1992) subdivided the infrared wavelength region into the near-infrared (1-5 μm), mid-infrared (5-25 μm), and far-infrared (25-350 μm). For this work spectra in the near-infrared were used, to be more precisely in the J,H and K filter (specific data see Table 3.1 below).

Post-AGB objects are normally cool stars on the red side of the HR-diagram, that means they show molecules in their spectra and, in some cases like AC Her, they also have dust shells. Those properties make post-AGB objects in the near-infrared so interesting.

	J	H	K	K*
Instrument	Phoenix	Phoenix	Phoenix	Phoenix
Observatory	KPNO	KPNO	KPNO	GSCP
Observer	Melendez	Hinkle, Lebzelter	Melendez	Lederer
Telescope	kp 4 m	kp 2.1 m	kp 4 m	gscp 8 m
Detector	ALAD256x1024	ALAD256x1024	ALAD256x1024	ALAD256x1024
Date Observation	14.03.2001	12.07.2000	14.03.2001	07.12.2006
Filter Position	4308 (6)	wn 6420 (12)	9232 (3)	4220 (5)
Wavelength Range	10803 - 10853 Å	15590 - 15660 Å	23059 - 23170 Å	23567 - 23665 Å

Table 3.1: The table shows important information concerning the observations.

3.2 Sample

The sample consists of SRd and RV Tauri stars as well as some standard stars for line identification (K- and M-stars) and some hot (A) stars as telluric standards. The stars were observed in the years 2000, 2001 and 2006 by different observers.

Table 3.2 shows the standard stars and what photometric band they were used for.

Star	RA [h ' "]	DEC [° ' "]	Spectral Type	J [mag]	H [mag]	K [mag]	
α Aql	19 59 47.0	+08 52 06.0	A7 V	0.31	0.10	0.10	J,K
α Boo	14 15 39.7	+19 10 56.7	K1.5 III	-2.25	-2.81	-2.91	J
α Cyg	20 41 25.9	+45 16 49.2	A2 Ia	1.14	0.90	1.01	H
9 Her	16 13 15.4	+05 01 15.9	K5 III	3.04	2.30	2.08	H
δ Oph	16 14 20.7	-03 41 39.6	M0.5 III	-0.13	-1.03	-1.17	H,J,K
Vega	18 36 56.3	+38 47 01.3	A0 V	-0.18	-0.03	0.13	J,K

Table 3.2: Stars used as telluric standards (early type stars) or for line identification (late type stars). The second column contains the right ascension, the third the declination. The spectral and luminosity type is given in column four, followed by the magnitudes measured in three near infrared bands (source: SIMBAD Astronomical Database, <http://simbad.u-strasbg.fr/simbad/>) and the observed wavelength ranges (see table 3.1 for further information).

Table 3.3 contains the sample stars with the classification found in the *GCVS* (Samus et al., 1997).

Star	GCVS Type	RA [h ' "]	DEC [° ' "]	Spectral Type	J [mag]	H [mag]	K [mag]	
V509 Cas	SRd	23 00 05.1	+56 56 43.4	G0 Iab	2.90	2.63	2.30	H
RW Cep	SRd	22 23 07.0	+55 57 47.6	K2	3.09	2.46	2.03	H
HD 143352	RV?	15 58 58.3	+26 08 04.6	F2	8.51	8.34	8.41	J
θ Her	—	17 56 15.2	+37 15 02.0	K1 IIa	1.73	1.06	1.00	J
AC Her	RVa	18 30 16.2	+21 52 00.6	F4 Ib	5.70	5.34	5.08	J,K
SX Her	SRd	16 07 27.3	+24 54 29.9	K2	5.54	5.02	4.64	H
89 Her	SRd	17 55 25.2	+26 02 60.0	F2 Ib	5.00	4.24	3.63	H
CX Lac	SRd	22 07 46.0	+40 06 26.7	K5	5.33	4.57	4.24	H
SX Lac	SRd	22 55 60.0	+35 11 44.7	M0	5.38	4.49	4.12	H
TT Oph	RVa	16 49 35.9	+03 37 54.1	F5	7.71	7.32	7.21	J,K
TX Oph	RVa	17 04 00.1	+04 59 00.8	G0	8.27	7.85	7.64	J
UZ Oph	RVa	17 21 59.3	+06 54 42.2	G2	8.43	7.94	7.79	J
AR Pup	RVb	08 03 01.7	-36 35 48.0	F0 Iab	7.89	6.82	5.29	K*
R Sct	RVa	18 47 29.0	-05 42 18.5	K0 Ib	2.82	2.37	2.16	J,K

Table 3.3: The stars are listed in the first column, the classification given in the *GCVS* (Samus et al., 1997) in the second. The next two columns show the right ascension and declination (for EQ 2000), followed by the spectral type and the luminosity class (where available). The next three columns display the magnitudes in three filters, the last column lists the wavelength ranges used for the observations in 2000, 2001 and 2006.

As one can see, the sample consists of stars of different luminosity classes, namely giants, intermediate giants and supergiants. Unfortunately, there are only three stars that were observed in two different wavelength ranges, for all other stars I only have observations in one wavelength setting. One can also see that some of the stars in this sample have spectral peculiarities mentioned in their classification.

The observations in the H-filter were done by Lebzelter and Hinkle in the year 2000; the K and J filter measurements were obtained by Melendez in 2001 (proposal by Lebzelter and Hinkle). The star AR Pup was observed by Lederer in the year 2006 also in the K band but in a slightly different wavelength range (23567-23665 Å), therefore, it is signed with K*.

To get a better insight on the spectral specialties of the RV Tau and SRd stars, normal stars were observed for comparison. Together with the stars for the line identification listed in the table of standard stars, a sample of comparison stars of various spectral types can be used.

Star	RA [h ' "]	DEC [° ' "]	Spectral Type	J [mag]	H [mag]	K [mag]	
α Boo	14 15 39.7	+19 10 56.7	K1.5 III	-2.25	-2.81	-2.91	J
HD 148513	16 28 34.0	+00 39 54.0	K4 III	2.97	2.35	2.14	H
HD 210889	22 12 47.8	+34 36 16.5	K2 III	3.51	3.00	2.79	H
9 Her	16 13 15.4	+05 01 15.9	K5 III	3.04	2.30	2.08	H
δ Oph	16 14 20.7	-03 41 39.6	M0.5 III	-0.13	-1.03	-1.17	H,J,K
λ Peg	22 46 31.9	+23 33 56.4	G8 Iab	2.03	1.46	1.51	H
μ Peg	22 50 00.2	+24 36 05.7	G8 III	1.70	1.24	1.18	H

Table 3.4: Stars without any specialties were used as comparison stars, to see the difference between the spectra of normal and variable stars within the same spectral class.

3.3 Data-Reduction

Data reduction was performed with IRAF by myself and in the case of AR Pup by Lederer.

The first step was to transfer the data from fits-format to .pix- and .imh-files. For data reduction I used flatfield-, dark- and science-frames. For the sample of stars observed in 2000, three science frames for each star were taken. For the 2001 sample, only a set of two frames for each star was available.

The dark frames were combined using the IRAF routine *darkcombine*. After that the flatfield frames were corrected for their darkcount and then also combined. Every filter has to have its own flatfield correction frame, because every filter has its own flatfield. An ideal flatfield-frame would be exposed homogeneously over the whole area, but in reality this is not the case, due to different effects like the Blaze-function of the spectrograph or inhomogeneous light sources. So the flatfield has to be normalized to eliminate these effects.

Only the flatfield-frames were corrected for dark-count, the science-frames have been treated differently. I was able to use the following method of sky subtraction because the spectra observed are not at the same position on the frame, they are shifted. In the case of the year-2000-observations, two science frames were summed up and then divided by 2 to get an average sky. To perform these operations, I used the IRAF task *imarith*. The resulting average sky frame is used to correct the third science frame. One does this for every science frame and then continues with the flatfield correction.

With *apall* the spectrum can be extracted, and one can see the spectral lines. An extracted spectrum without telluric correction and in pixel-scale can be seen in Fig 3.1.

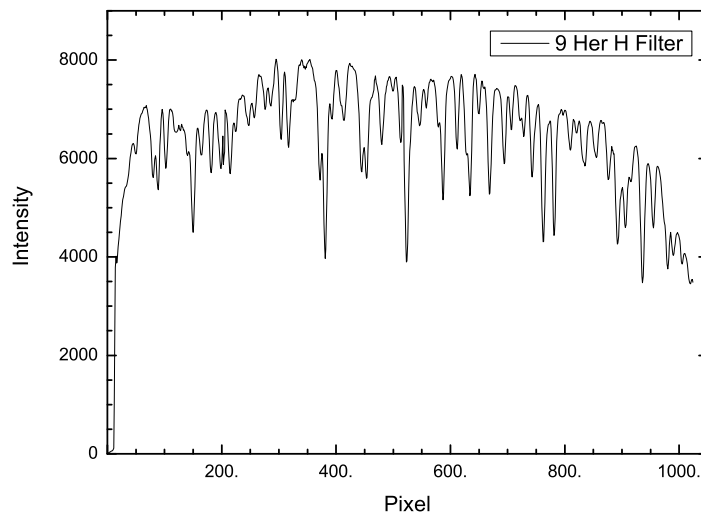


Figure 3.1: The spectrum of 9 Her in pixel-scale without telluric correction.

The star 9 Her was used as a calibration star, because it is not pulsating or in any other way special. To identify the lines in the spectrum, one needs an atlas to compare the features of the observations with confirmed lines of another star. In my case, the *Infrared Atlas of the Arcturus Spectrum, 0.9 - 5.3 microns* by Hinkle et al. (1995) was used to identify the lines, because Arcturus itself is a K2 giant star and has therefore a similar spectrum as 9 Her.

To calibrate the spectrum of 9 Her, I chose several significant lines from the atlas and assigned their position in angstrom manually with the IRAF task *identify*. This task can also be used to identify lines automatically by using a linelist-database, but in my case, there was no linelist available for the wavelength-region I needed, so I used about seven prominent lines to do the calibration of the spectrum. One has to keep in mind that the lines chosen should cover the whole wavelength range so that no errors occur due to missing lines at the beginning or the end of the stellar spectrum.

The 9 Her file was used afterwards to calibrate all the other H filter files. After the calibration, the three individual spectra of each star were combined so that only one spectrum was left for every single star observed in the H band. The same procedures mentioned above were used to correct the science frames taken in the other wavelength ranges.

Earth-based observations show lines in a stellar spectrum called *telluric lines* which originate from earth's atmosphere. They are always at the same position in wavelength and can therefore be used for wavelength calibration of the stellar spectrum regardless of the star's radial velocity.

A hot star, for example an A2-type star like α Cyg, is used as a telluric standard. The high temperature is the reason why these stars do not show lines in the infrared spectrum, so one only sees the telluric lines originating from the earth's atmosphere (see Fig. 3.2).

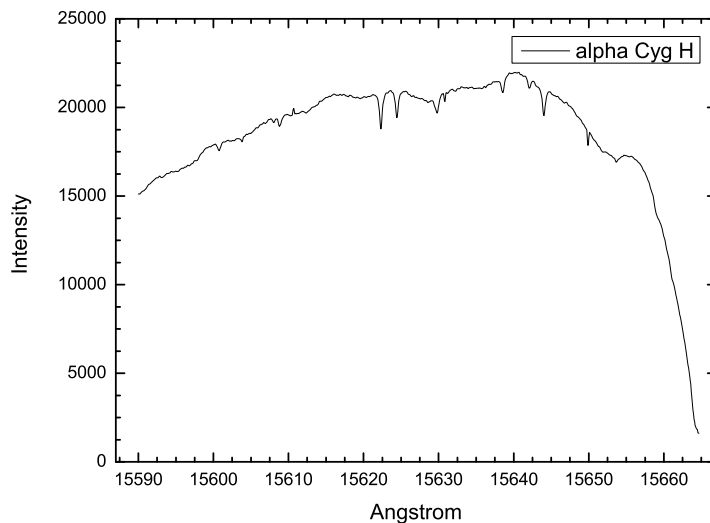


Figure 3.2: The spectrum of α Cyg was used for telluric correction.

The IRAF task *telluric* is convenient for telluric correction, because one has the opportunity to shift the telluric correction spectrum so that it fits the spectrum of the star to be corrected in the x-axis (wavelength) and also to chose the strength of the telluric lines. If this step is done properly, there are no more absorption lines of the earth's atmosphere present in the stellar spectrum, and the "curve" of the spectrum that originated from the instrument is also reduced to a minimum.

If this is not sufficient enough, as was the case for the H- and J-filter spectra, one can also use an artificial continuum (*pseudo continuum*) to normalize the flux and to get an even continuum (see Fig. 3.3).

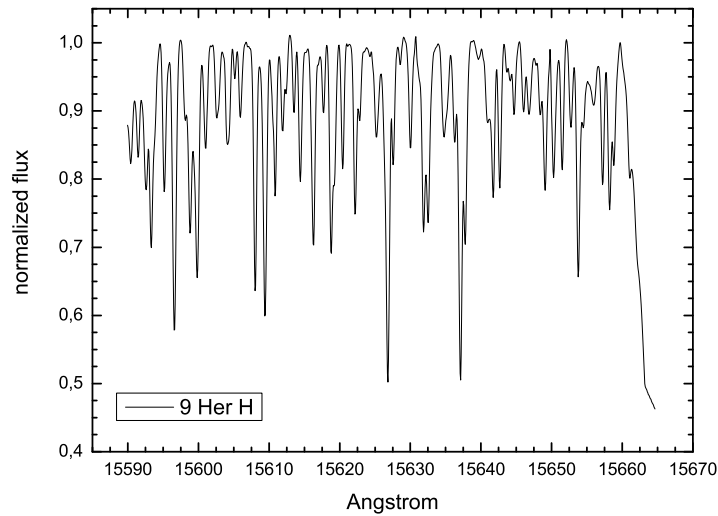


Figure 3.3: The finally reduced spectrum of 9 Her.

3.4 Line Identification

To identify the lines I wanted to measure later, I used again the *Infrared Atlas of the Arcturus Spectrum* by Hinkle et al. (1995), because in the electronic version there is also an appendix including the vacuum positions of the lines identified in the Arcturus spectrum. Not all lines present in the Arcturus spectrum were also found in the stellar spectra of the sample stars. Some stars also showed spectra with broadened lines (for example RW Cep, Section 4.2), and in these cases, it was quite difficult to identify lines or measure them.

3.5 Line Measurements

A Voigt-profile was used to measure both atomic and molecular lines. This decision was made after some comparison of measurements done with a Gaussian-, a Lorentz-, and a Voigt-profile within the IRAF environment. Molecular lines can be fitted best with a Gaussian-profile, but atomic lines are more pointed than those of molecular features and are therefore better resembled by a Lorentz- or Voigt-profile. Only one type of profile should be used throughout the measurements, so I chose the Voigt-profile because it fitted the atomic lines as well as those of molecular origin. There was no great deviation of the equivalent widths measured during the test between the three types of profiles.

As explained in section 3.3, most of the stellar spectra were normalized to a continuum, so the continuum used during the measurements was set to 1. In the case of the K-filter spectra, there was no continuum that could be used in the same way, so a value near the estimated continuum flux was chosen as the continuum. The values used will be given in the corresponding table listing the individual line measurements for each sample star.

3.6 Model Spectra

Models were computed by Michael T. Lederer, using the MARCS code (Gustafsson et al., 1975; Jorgensen et al., 1992). Temperatures between 4000 and 5000 K were used, and $\log g$ values between 0.00 and 0.75. The difference between the temperatures chosen was 100 K, between the $\log g$ values 0.25. No attempt was made to accurately fit the stellar parameters as the model spectra were only aimed for a general comparison of "normal" (hydrostatic) stars and the post-AGB objects of our sample. One can see in the *Results* section 4, that the models do not fit extremely well with the observations. That is due to errors in the temperature range, the $\log g$ values, microturbulence, metallicity and other causes.

Chapter 4

Results

In this chapter the results of this work will be presented and compared, as far as possible, to the literature.

For every single star, a spectrum was plotted using an IDL program written by Claudia Paladini. A table of identified, unblended lines, the measured equivalent widths and the difference from measured position to vacuum position (Hinkle et al., 1995) can be found adjacent to the plot. From the difference of the line positions, a radial velocity was estimated after taking the heliocentric movement into account.

P-Cygni line profile

Astronomers found a strange line profile in the spectrum of P-Cygni, that gave this peculiarity its name. Sometimes, one line of an atom or a molecule is split into an absorption component and an emission component. The position of the two components relative to each other give information on the movement of the halo.

If the emission component is redshifted relative to the absorption component, than it is a normal P-Cygni profile and indicates a strong outflow of matter from the star, e.g. an expanding halo. If it is the opposite way around and the absorption lines are redshifted relative to the emission lines, it is an invert P-Cygni profile and points toward an infall of material towards the star (see Fig.4.1).

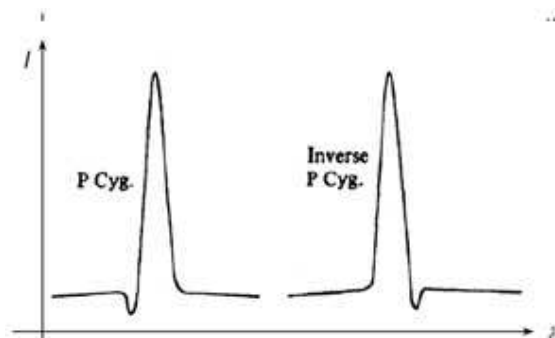


Figure 4.1: P-Cygni profile and inverse P-Cygni profile (Jaschek & Jaschek, 1990).

Another indicator for a shell around a star is an emission component with a central absorption (Trams et al., 1989).

4.1 V509 Cas

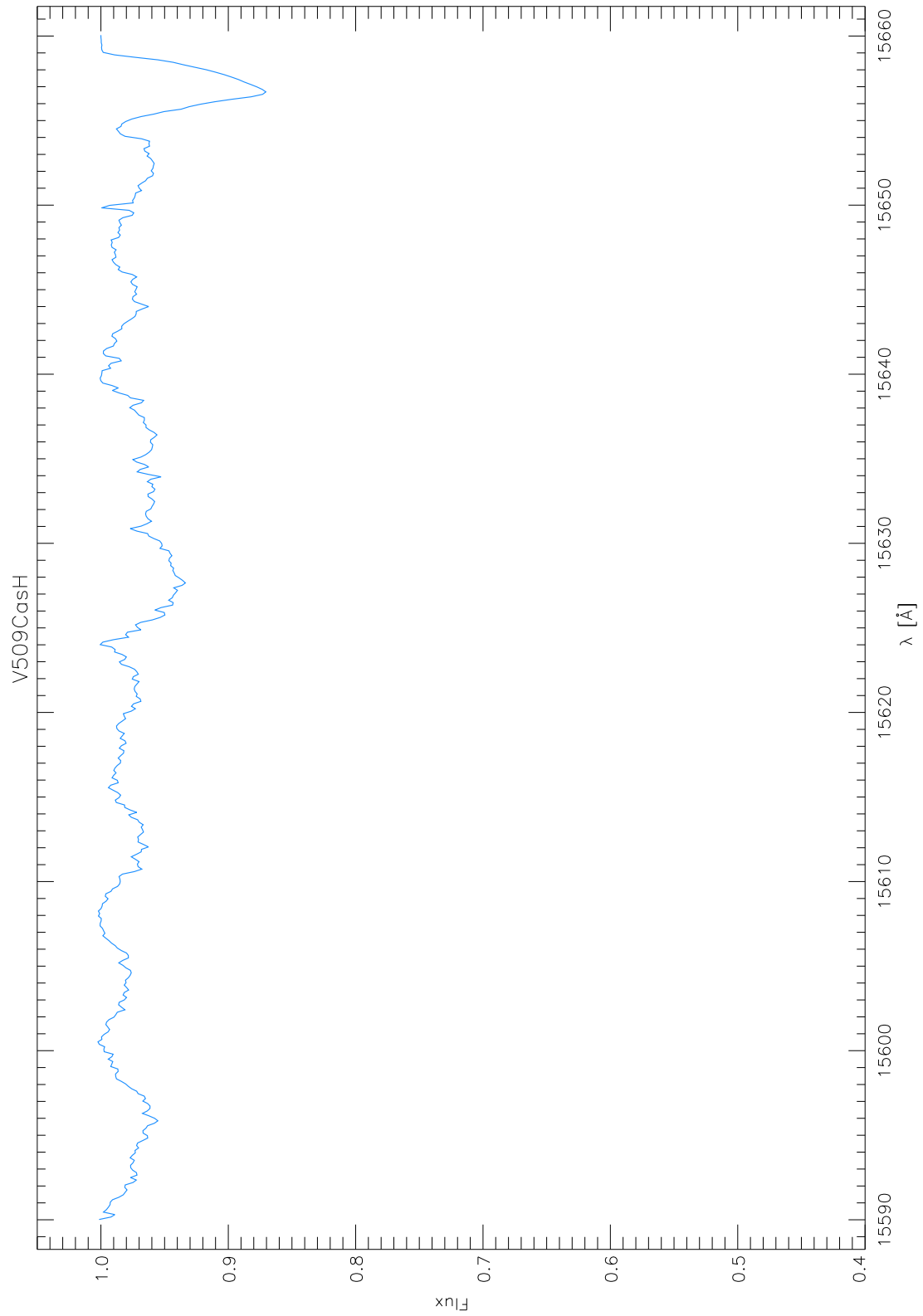


Figure 4.2: The spectrum of V509 Cas in the H-filter.

Analysis of the Spectrum

I was not able to identify or measure any lines in this spectrum after I subtracted the telluric lines. The feature at about 15657 Å was produced during data reduction. It originated from the continuum correction of the spectrum with an artificial continuum. This star appears to be too hot to show spectral lines in this wavelength range.

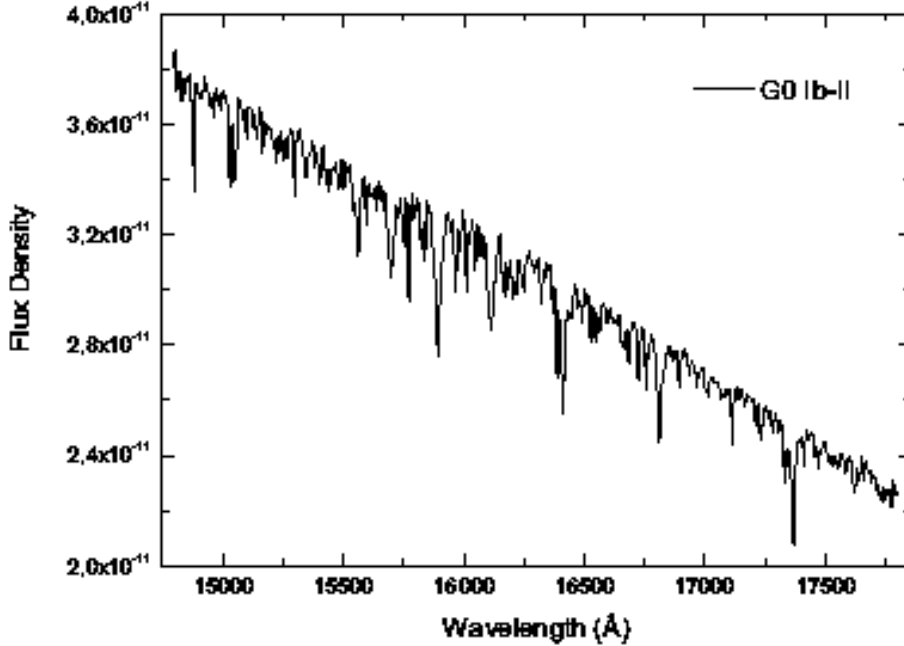


Figure 4.3: A Spectrum of the G0 Ib-II star HD 185018 in the H band (1.48 to 1.78 μm). Figure taken from the *IRTF* spectral library of cool stars by Rayner et al. (2009).

The spectrum of HD 185018 in Fig. 4.3 is similar in spectral type and comparable in luminosity class to V509 Cas, a G0 Ia star. As one can see, there are several Mg, Fe, and Si lines present in this wavelength range (Rayner et al., 2009), as expected for a star with the properties mentioned above.

The fact that this suspected SRd star shows no lines within this spectral region, while the other SRd stars in this sample show very strong and prominent lines, leads to the assumption that the SRd classification in the GCVS (Samus et al., 1997) might be questionable.

Another explanation could be based on the information found in the SIMBAD Astronomical Database (<http://simbad.u-strasbg.fr/simbad/>), which labels V509 Cas as a double or multiple star, so I assumed that probably a hot companion was observed and not the cool SRd star. This suggestion turned out to be rather unlikely, because the brightness ratio in this wavelength region would definitely favour the cool companion instead of the hot star.

Due to the lack of lines in the observed spectrum, no attempt was made to compare it to a model spectrum.

Literature

V509 Cas (or HR 8752), a double or multiple star, has a spectral type G0 Ia with a semi-period of 385 days. The first hints, that this star is not a "normal" star, were found by Sargent (1965), who observed blueshifted absorption and redshifted emission in the $H\alpha$ line as well as [N II] emission (6549 Å, 6583 Å). He concluded that these features might be assigned to an expanding shell with a temperature of about 10000 K and an electron density of about 10^6 cm^{-3} .

The P Cygni profile in the $H\alpha$ line and the presence of [N II] emission (6583 Å, 6549 Å) was confirmed by Luck (1975), who came to the same conclusion of a high-temperature, low-density shell or a chromosphere located around the star. Luck (1975) also suggested the presence of a low-temperature shell based upon the multiple structure of the Na D lines observed in his spectra, but could not prove whether they originate from a shell or from interstellar absorption. He also derived an effective temperature of $4000 \pm 300 \text{ K}$ and a $\log g$ value between 0.0 and -2.0 for this superluminous giant star and noted a general weakness of spectral features that could be caused by a very low gravity.

Lambert & Luck (1978) observed this star in the near infrared (6000 to 9000 Å) to get a better understanding of the variations found in the spectrum. In Fig. 4.4, four spectra taken between 1965 to 1976 are shown in the wavelength range of 6400 to 6450 Å with labeled metal lines in neutral and ionized stages. In the years 1950 to 1970, V509 Cas changed from spectral type G0 to G5, continuing its path through the HR-diagram to K in 1973 before it turned back to spectral type G0 in 1977. The change in spectral type is observable in Fig. 4.4 in the Fe I (6430.9 Å) and Fe II (6432.7 Å) lines. In November 1965 the Fe II line is stronger than the neutral iron line, as well as in October 1976, but in the two spectra taken in September 1969 and 1973, the opposite can be seen.

Another specialty in the spectrum of October 1976 noted by Lambert & Luck (1978) is the sudden absence of the Ca I line at 6449.8 Å while the Ca I line at 6439.1 Å is still present.

An attempt was also made by Lambert & Luck (1978) to explain the behaviour of V509 Cas as part of a binary system. If an optically thick wind is transferring mass to a main-sequence companion, than the late-type giant producing the wind would be hidden. The giant star would only be visible if the accretion would be disturbed.

Barden & Ramsey (1980) continued the research on V509 Cas after a hot (spectral type B1V) binary companion was confirmed by Stickland & Harmer (1978) through International Ultraviolet Explorer (IUE) spectra. Barden & Ramsey (1980) searched for changes in the emission lines near $H\alpha$ that occur within a timescale of days due to rapid effects within the shell and for variations on a timescale of months that could be caused by a hot companion that influences the shell.

There seems to be a trend that the mean equivalent widths from both red and blue emission features are decreasing on timescales of years, probably in association with the binary period. In addition to the long-time changes, Barden & Ramsey (1980) found changes within 48 hours of the Ca I line at 6572 Å and the blue $H\alpha$ emission component which origins remain unclear because they can not be explained by a shell influence caused by the binary companion.

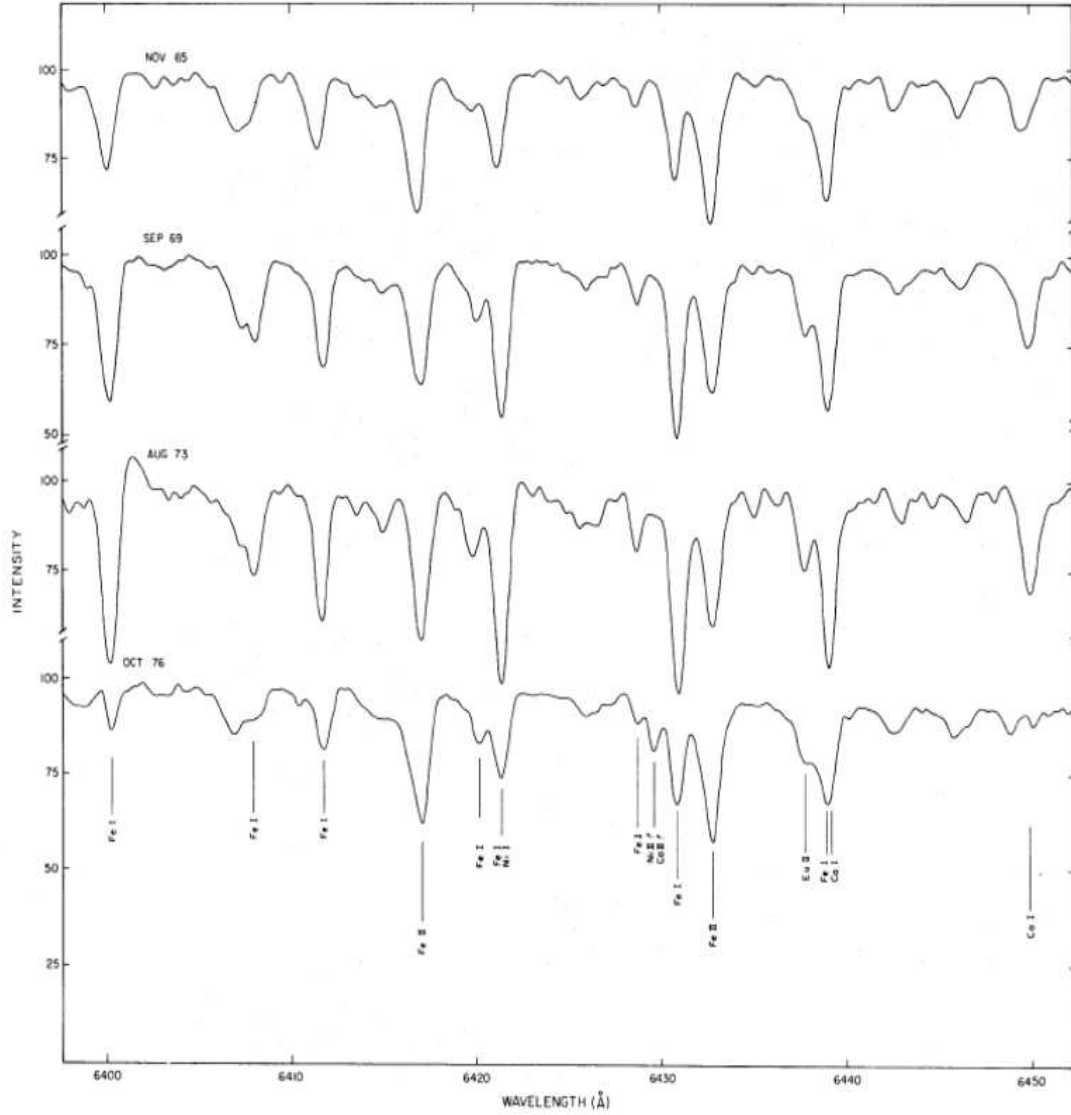


Figure 4.4: Changes in the spectrum of V509 Cas in the wavelength range of 6400 to 6450 Å. Figure was taken from Lambert & Luck (1978), who carried out the observations in November 1965, September 1969, August 1973 and October 1976.

Smolinski et al. (1982) concentrated their study on the spectral region around H α (6554 - 6566 Å), including the Ti II line at 6559.6 Å to get a better understanding of the strange behaviour of V509 Cas by measuring the radial velocities of the emission and absorption components and trying to assign them to certain parts of the star. The radial velocities they published are absolute. The radial velocity of the star lies between -44 km/s (Smolinski et al., 1982) and -58.3 km/s (Wilson, 1953).

Smolinski et al. (1982) reported the following four components to be of special interest for further investigation (see Fig. 4.5):

- A red emission component in H α with a radial velocity of -46 km/s is present during the whole time of observation and is assumed to originate from the H II region surrounding V509 Cas. A second red emission component at a velocity of -3 km/s could be caused by pulsation and/or binary nature, because it is changing in intensity.

- In spectra observed in 1979, blue emission was present in $H\alpha$. In the spectra of 1982, this emission is replaced by an absorption component with a velocity of -131 km/s .
- In the spectrum of September 27th, there are three absorption components in $H\alpha$, while on May 4th there are only two. Luck & Lambert (1981) found $H\alpha$ absorption features in two long period Cepheids (X Cyg, SV Vul) that are comparable in shape to the ones found by Smolinski et al. (1982) in V509 Cas.
- The two absorption components of the Ti II line seem to originate from the star (with a radial velocity of -44 km/s on May 4th, and -53 km/s on September 27th) and an expanding envelope (with a radial velocity of -102 km/s).

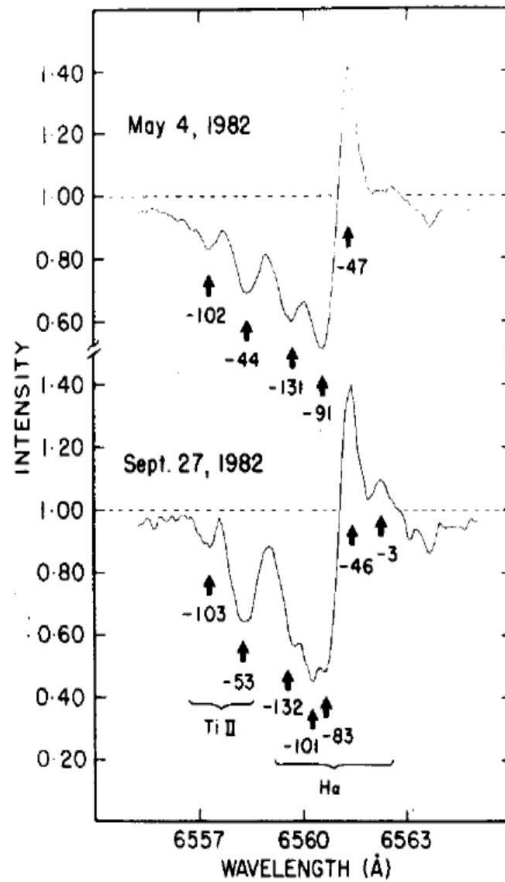


Figure 4.5: The $H\alpha$ region observed in 1982 by Smolinski et al. (1982). The continuum is indicated by a horizontal broken line. The values of the measured radial velocities are given in km/s (without correction for the stellar radial velocity).

According to a research of $H\alpha$ profiles in yellow supergiants (Arellano-Ferro, 1985), V509 Cas shows a complicated $H\alpha$ profile with red emission that changes significantly within a few months (see Fig. 4.6). This author also confirmed the findings of Barden & Ramsey (1980) concerning the change in strength of the red emission within months.

After extensive observation and analysis of hundreds of high dispersion spectra (6 and 10 \AA/mm), Smolinski et al. (1986) summarized their results of V509 Cas with a

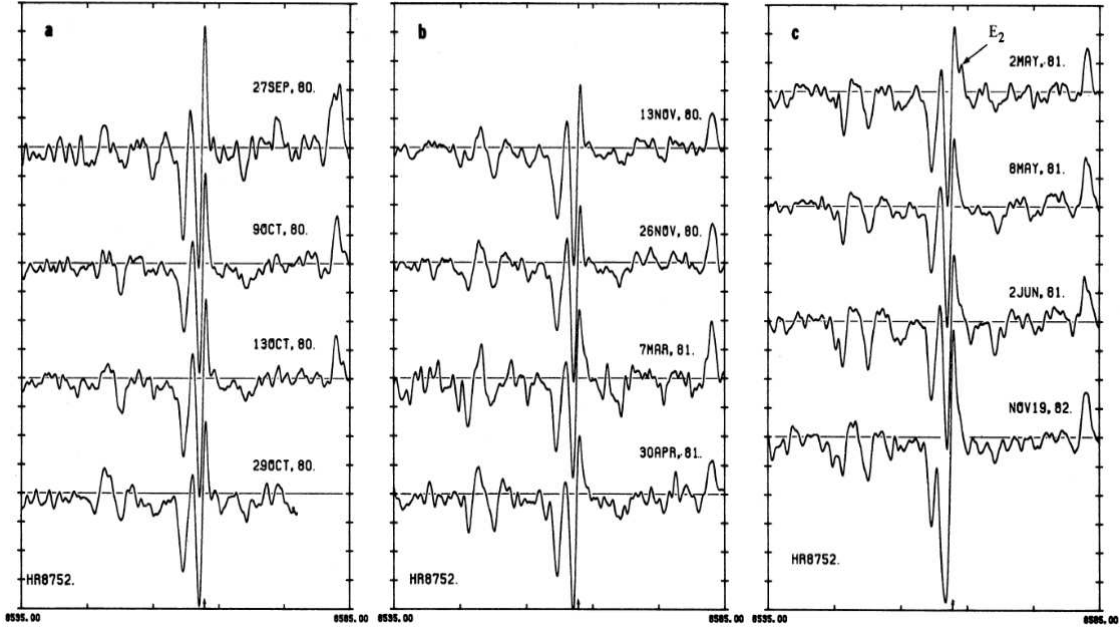


Figure 4.6: $H\alpha$ profiles for V509 Cas (Arellano-Ferro, 1985). The small arrow located on the x-axis indicates the rest-wavelength or $H\alpha$, the E_2 marker points out emission on the red wing of $H\alpha$ that could be caused by pulsation of the star or binarity.

model of a binary system (V509 Cas and a B1V-type star as proposed by Stickland & Harmer (1978) with a period of 620 days) within a common expanding, very active envelope. Smolinski et al. (1986) separated the expanding envelope into three different regions or shells with radial velocities (reduced in respect to the binary system) of about 35, 54 and 84 km/s. Depending on the time of observation, the three components can present themselves as absorption or emission features or they can disappear. The observations of Smolinski et al. (1977) and Sargent (1965) confirmed a H II region surrounding the envelope.

The last paper in the series of Smolinski et al. (1993) discussed the high dispersion spectra of the $H\alpha$ profile observed between 1970 to 1992. The authors found five characteristic shapes of emission and absorption components of the $H\alpha$ profile during this long-term study (see Fig. 4.7), which are described as follows:

- Profile A appeared five times during the 23 years of observation with an estimated duration of three months. This profile is composed of three emission and two absorption components.
- Profile B was observed six times with about ten months length and shows two emission components.
- Profile C only appeared twice with a duration of about four months and consists of two emission and three absorption components.
- Profile D was monitored five times within the period of the investigation with estimated lengths of eight months and represents a typical P Cygni profile of emission and absorption.

- Profile E was observed twice with an estimated length of three months and also shows a classical P Cygni profile with an additional absorption component to the emission and absorption present in Profile D.

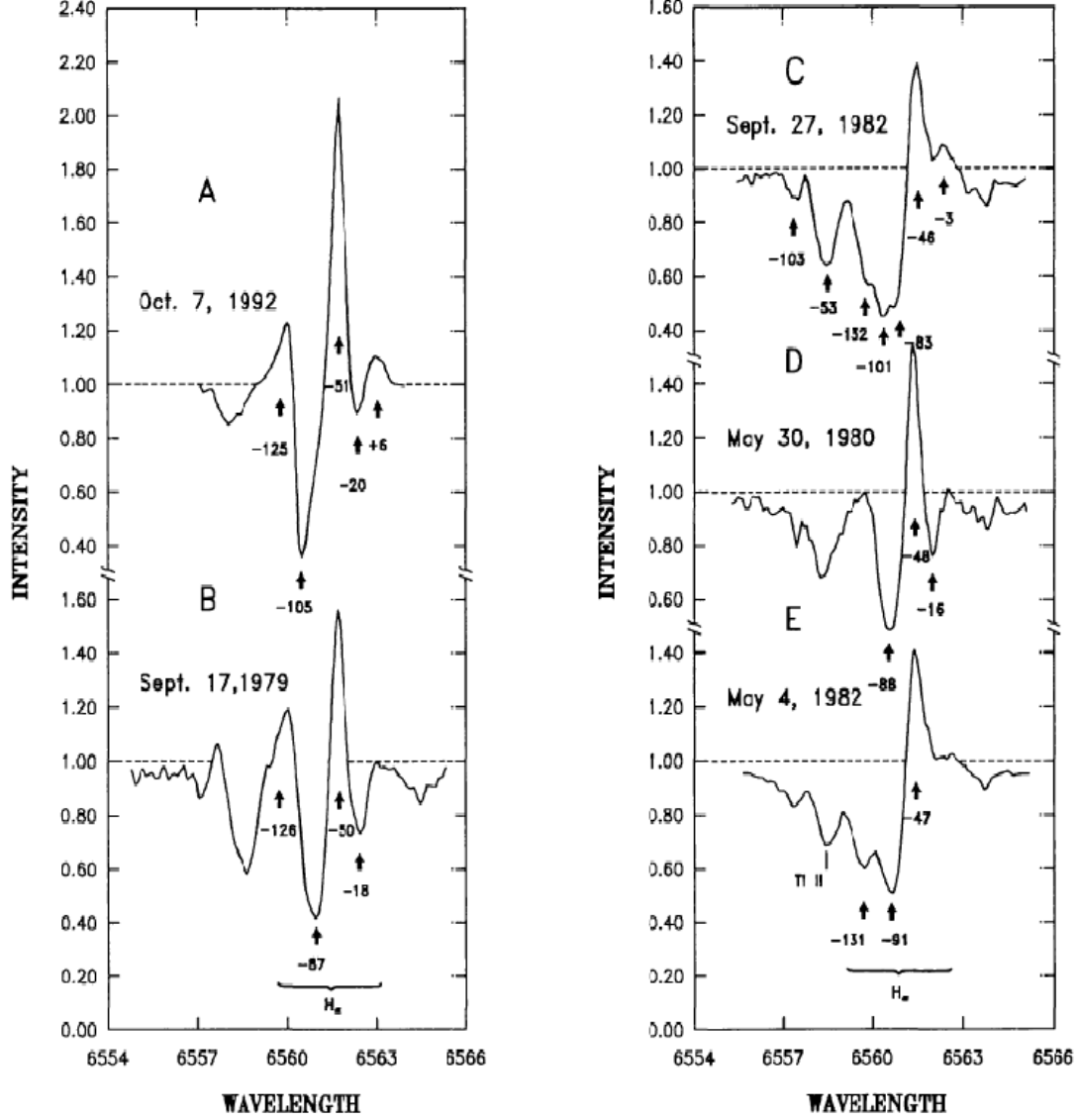


Figure 4.7: Typical $H\alpha$ profiles observed by Smolinski et al. (1993). The continuum levels are represented by horizontal broken lines and radial velocities measured at the respective dates of the observations are indicated. For further information see text.

Smolinski et al. (1993) stated that the P Cygni shape in the $H\alpha$ profile was present during the whole investigation between 1970 and 1992. They also separated the components upon their stable radial velocities into a feature at -13 km/s that can appear in emission or absorption, two emission components at -49 km/s and +6 km/s respectively, and an absorption component at -84 km/s which shows a systematic change.

It seems that this main absorption component of the P Cygni profile experiences an increase of radial velocity since 1970 (see Fig. 4.8), which might be related to an

enhanced mass loss in 1970 with eventual shell ejection and an acceleration of the expanding envelope or the stellar wind (Smolinski et al., 1993).

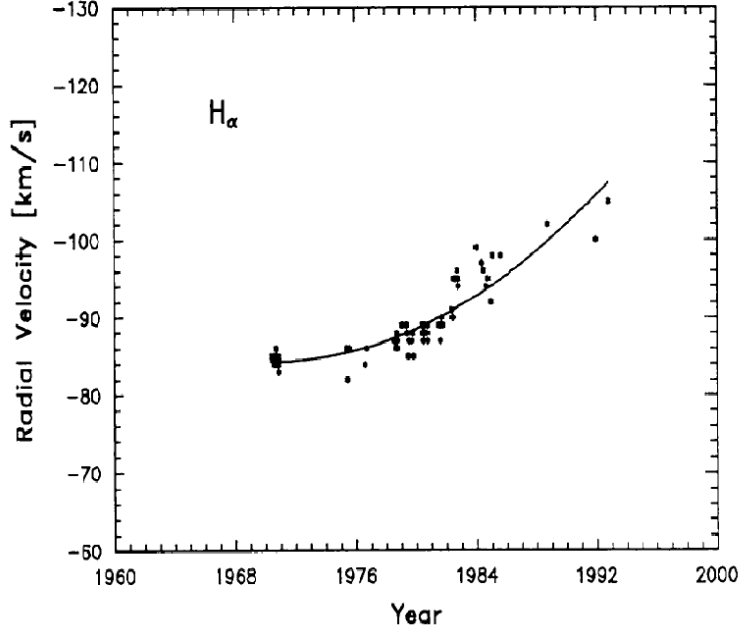


Figure 4.8: Increase of radial velocity of the main absorption component of the P Cygni profile between 1970 and 1992 (Smolinski et al., 1993). The line represents the second order fit to the data.

This theory is supported by de Jager & Nieuwenhuijzen (1997), who place the massive star V509 Cas (estimated initial mass above $30 M_{\odot}$) at an evolutionary phase from the red supergiants to the blue supergiants. During this phase the star passes the instability strip: the photosphere becomes unstable, which leads to a phase of increased mass loss. The timescales between such mass loss phases are rather short, two events have been observed for V509 Cas within 30 years, one in 1970 and one in 1980.

Yamamuro et al. (2007) observed V509 Cas from November 2002 to February 2004 with the intention to find proof for mass loss through time variations in the spectra. Unfortunately, the star was in a silent phase during that time, therefore no variation was detected.

4.2 RW Cep

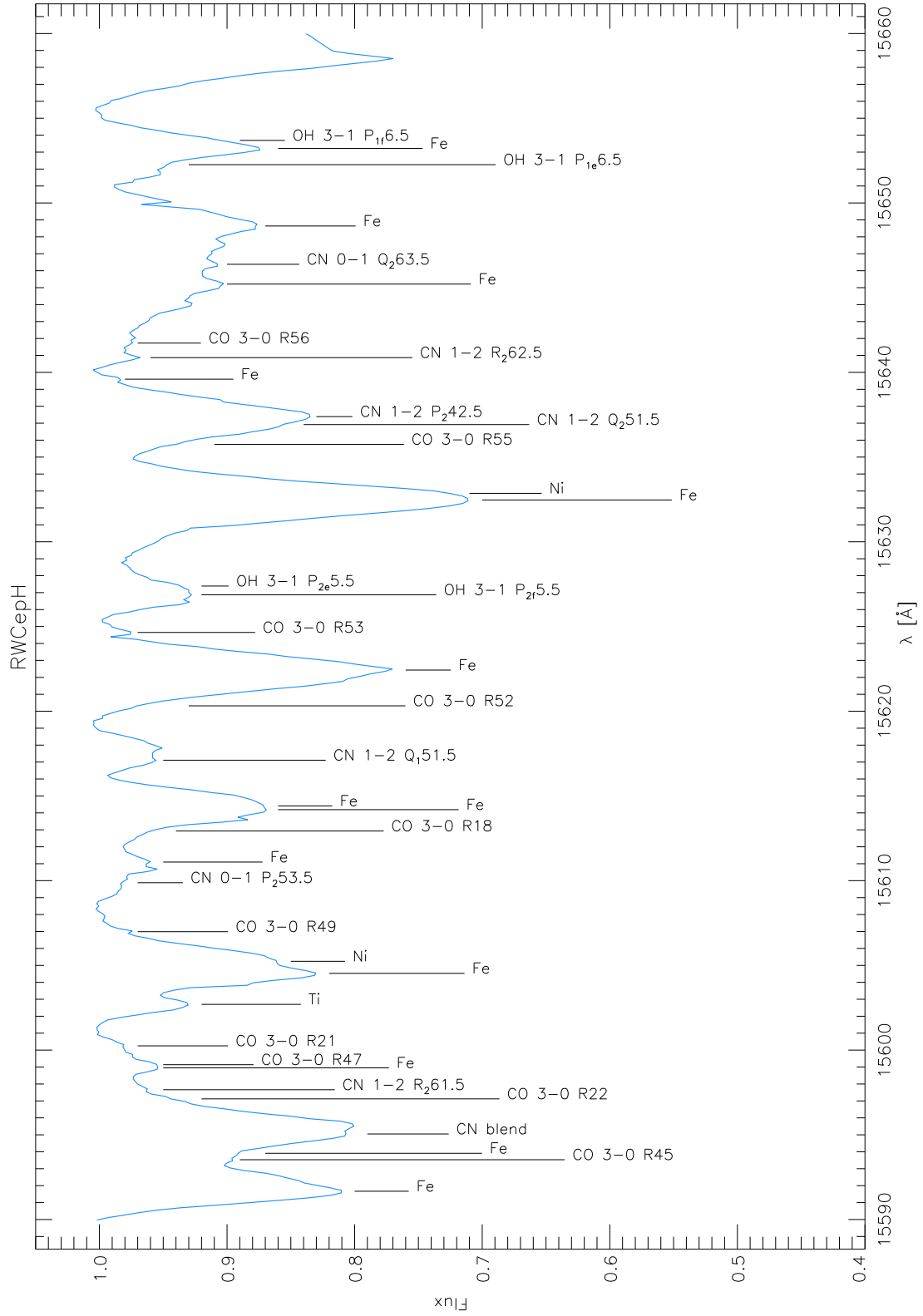


Figure 4.9: The spectrum of RW Cephei in the H-filter with identified and measured lines.

Wavelength [Å]	Atom/Molecule	EQW [mÅ]	Vacuum Pos.	Difference
15591.67	Fe	327.8	15595.75	4.08
15593.53	CO 3-0 R45	210.1	15597.17	3.64
15593.91	Fe	348.4	15598.01	4.10
15597.12	CO 3-0 R22	88.4	15601.61	4.49
15597.66	CN 1-2 $_{261.5}$	47.0	15601.99	4.33
15598.95	Fe	65.5	15603.13	4.18
15599.14	CO 3-0 R47	47.4	15603.52	4.38
15600.25	CO 3-0 R21	20.7	15605.00	4.75
15602.70	Ti	85.8	15607.11	4.41
15604.53	Fe	369.3	15608.48	3.95
15605.24	Ni	367.2	15609.92	4.68
15606.99	CO 3-0 R49	12.8	15610.97	3.98
15609.88	CN 0-1 P_2 53.5	98.3	15613.47	3.59
15611.10	Fe	70.4	15615.40	4.30
15612.93	CO 3-0 R18	65.5	15616.76	3.83
15614.19	Fe	286.6	15617.89	3.70
15614.41	Fe	280.2	15618.36	3.95
15617.11	CN 1-2 Q_1 51.5	46.7	15621.33	4.22
15620.32	CO 3-0 R52	24.9	15624.21	3.89
15622.43	Fe	776.6	15625.92	3.49
15624.65	CO 3-0 R53	17.6	15629.18	4.53
15626.87	OH 3-1 P_{2f} 5.5	198.0	15630.97	4.10
15627.39	OH 3-1 P_{2e} 5.5	58.5	15631.68	4.29
15632.47	Fe	927.1	15636.22	3.75
15632.86	Ni	710.1	15636.89	4.03
15635.75	CO 3-0 R55	111.6	15639.95	4.20
15636.92	CN 1-2 Q_2 51.5	282.3	15640.86	3.94
15637.39	CN 1-2 P_2 42.5	351.2	15641.80	4.41
15639.60	Fe	6.5	15643.75	4.15
15640.87	CN 1-2 R_2 62.5	30.0	15645.14	4.27
15641.73	CO 3-0 R56	29.7	15645.76	4.03
15645.21	Fe	257.7	15649.29	4.08
15646.38	CN 0-1 Q_2 63.5	232.2	15650.52	4.14
15648.64	Fe	398.1	15652.79	4.15
15652.26	OH 3-1 P_{1e} 6.5	121.9	15656.17	3.91
15653.22	Fe	290.8	15657.15	3.93
15653.69	OH 3-1 P_{1f} 6.5	154.2	15657.75	4.06

Table 4.1: The equivalent widths for the lines in Fig. 4.9 with the vacuum positions given by Hinkle et al. (1995). The mean difference between vacuum position and measured wavelength is 4.11 Å. The radial velocity derived from these measurements is -63.55 ± 5.43 km/s after heliocentric correction.

Analysis of the Spectrum

The lines are broadened due to macroturbulence, leading to blends of different adjacent lines, which made the identification and measurement of the different lines quite difficult. Compared to δ Oph (Fig. A.8) the OH-lines are very weak, atoms like Fe dominate the spectrum, as well as lines of the CN molecule.

A comparison of a model spectrum to the observed one was plotted (Fig. 4.10), with $T_{\text{eff}}=4700$ K, $\log g=0.75$ and macro turbulence $\zeta=18$ km/s.

The two Fe lines in the middle of the spectrum (at 15622.43 \AA and 15632.47 \AA) as well as the CN lines (CN 1-2 P₂42.5 and CN 1-2 Q₂51.5) seem to fit quite well. These lines seem to be more sensitive to temperature than to $\log g$. The Fe line at 15604.53 \AA appears to diminish in models with higher temperature, but is still present in the observed spectrum. Probably blending with other lines is responsible for this effect. The CO lines are mostly very weak and often blended with other lines. The missing lines in the observed spectrum in the region between 15605 \AA and 15610 \AA are presumably CO 3-0 R49 (identified, but weak) and CO 3-0 R19.

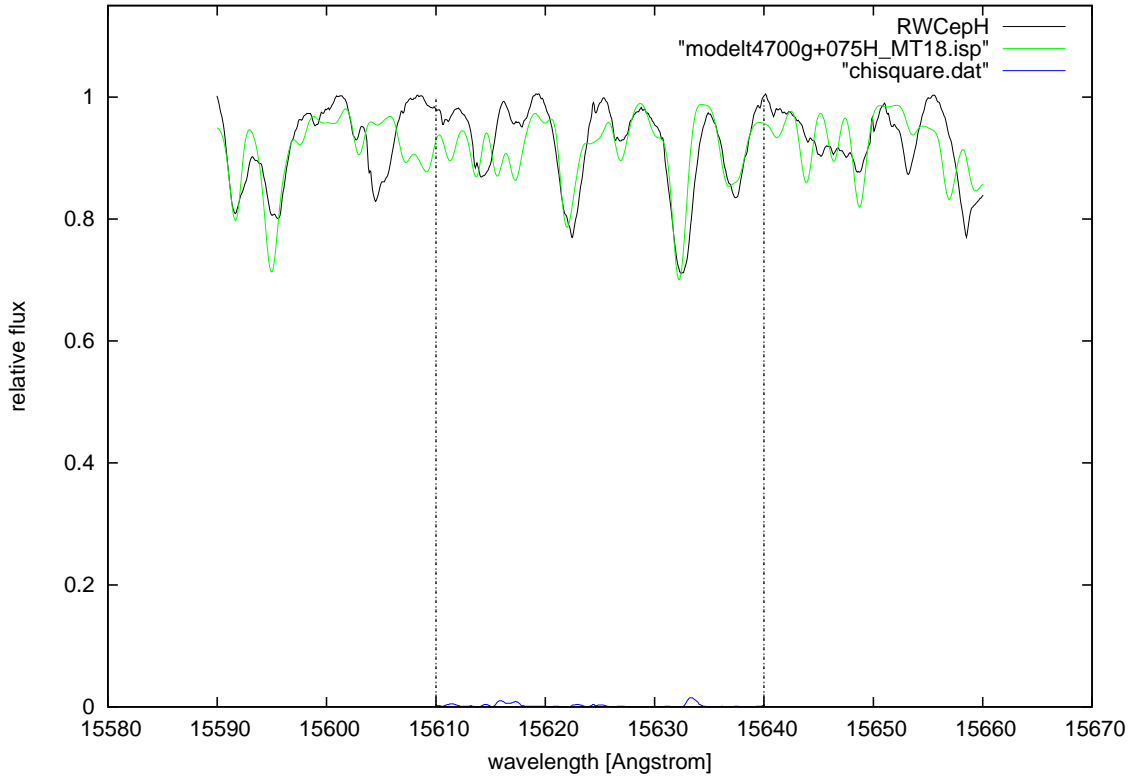


Figure 4.10: The star RW Cep overplotted by a MARCS model of 4700 K, $\log g=0.75$, and $\zeta=18$ km/s.

Literature

The *General Catalogue of Variable Stars* (Samus et al., 1997) lists the KOIa-0 star RW Cep as a SRd variable with a light minimum at 10.7 mag, a light maximum at 8.6 mag and a period of about 346 days. Percy & Kolin (2000) wanted to verify this statement but with their observations they could only prove that the period is about several hundred days and that this star experienced three irregular cycles within the Hipparcus light curve of 1200 days.

RW Cep impressed Merrill & Wilson (1956) with a very special spectrum showing absorption lines that are separated into a "shortward" and a "longward" component by a central maximum that can be interpreted as emission that is superposed on a broad absorption line. This very unsymmetrical appearance was reported for Ca I, Cr I, Mn I, Sr II, Fe I and Ti I. Many neutral metals, namely Fe I, Ti I, Ni I, Co I, V I, Mg I, Al I, and Sc I, show emission lines.

The observed spectrum could be explained if one assumes a star with three layers (Merrill & Wilson, 1956). The first layer, or *Reversing layer*, is responsible for the widening of absorption lines, probably due to turbulence. Above this layer, the *Chromosphere* creates emission features that appear either as bright lines or as the narrow maxima within the broad absorption line mentioned above. This layer might be moving outward at a small velocity. The last layer of this model star is an *Expanding shell*, where more narrow absorption lines are produced that are shifted about 20 km/s shortward from the center of the lines that are formed in the first layer.

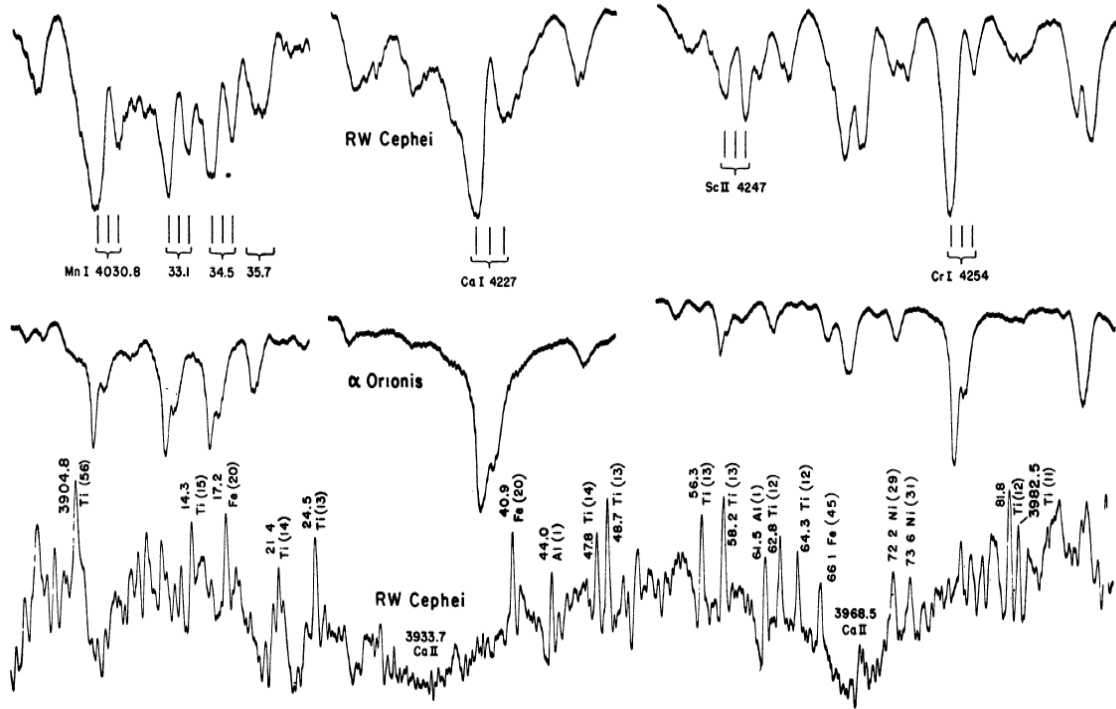


Figure 4.11: The upper and lower spectra are from RW Cep, the middle one is from α Ori (Merrill & Wilson, 1956). In the upper spectrum of RW Cep, one can see the broadened lines with the associated absorption and emission features.

Comparing the properties observed by Merrill & Wilson (1956) and the findings of this work, I can neither confirm nor deny the theory mentioned above. The spectral lines I analysed also show some kind of asymmetry, but there is no evidence for a superimposed emission component.

Gehrz & Woolf (1970) discovered an optically thin silicate emission in RW Cep, comparable to that observed in late M stars.

In the sample of Omont et al. (1993), RW Cep can also be found as a supergiant without an indication towards a post-AGB classification, however, the authors acknowledge that such an identification might be questionable. During their observations they did not detect CO, HCN or H₂O masers in this O-rich star that is positioned in region IIIa1 of the IRAS color-color diagram (van der Veen & Habing, 1988), where cool circumstellar envelopes are expected.

The work of Sylvester et al. (1998) deals with the search for silicate and hydrocarbon emission in the spectra of galactic M-type supergiants in the wavelength range from 7.5 to 13.3 μm . Within this spectral range one can find the so-called unidentified infrared (UIR) band, emission features at 11.3 and 8.7 μm that are assigned to carbon-rich dust like polycyclic aromatic hydrocarbons (PAH). The emission peak of the silicate feature observed in the spectrum of RW Cep is located at 10.1 μm and can be interpreted as evidence for mass loss. There is no evidence for UIR-band emission (see Fig. 4.12).

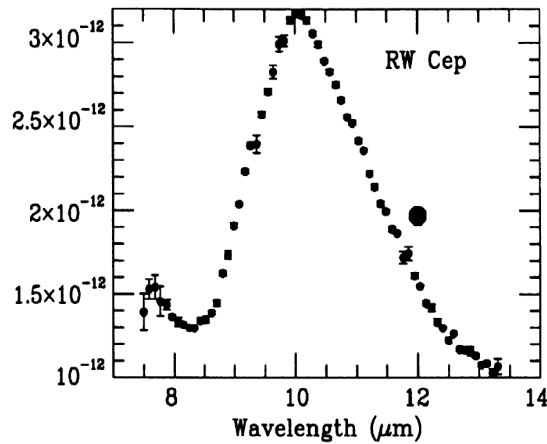


Figure 4.12: The silicate emission feature peak at 10.1 μm observed by Sylvester et al. (1998). The flux is given in $\text{W m}^{-2} \mu\text{m}^{-1}$.

Rayner et al. (2009) used spectra of RW Cep in *The Infrared Telescope Facility (IRTF) Spectral Library: Cool Stars* and found SiO emission at 4.00, 4.04, and 4.08 μm . The authors furthermore suggest a large NIR excess based upon the *JHK* colours observed and noticed sharp appearances of the first overtone bands of CO in the K band.

In Fig. 4.13 one can see the spectrum of RW Cep observed in the H band. Spectra of the I, Y, J, K, and L' band can be found within the *IRTF* (Rayner et al., 2009), I chose to show only the H band observations here because the observations presented in this thesis are in the same wavelength region.

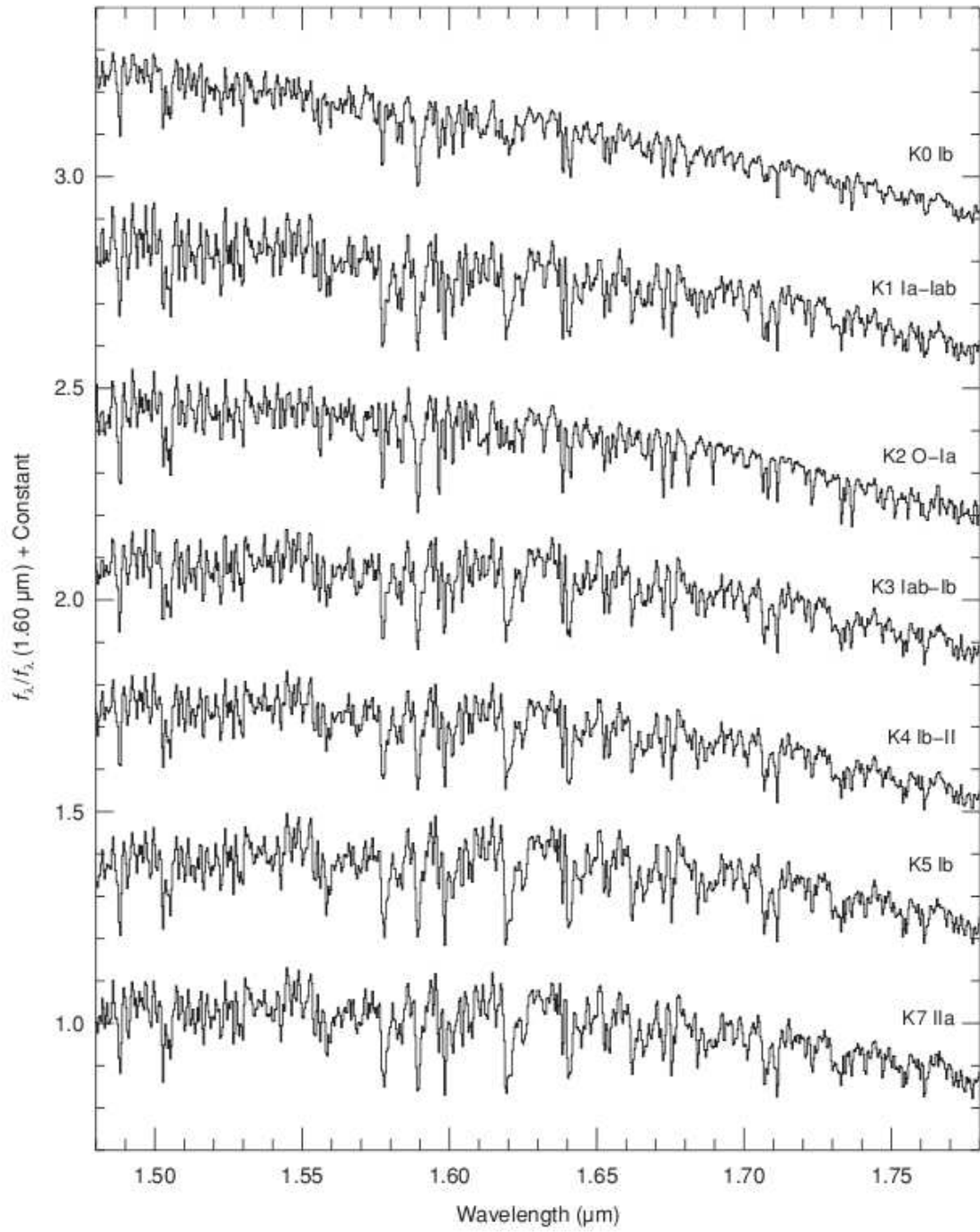


Figure 4.13: A series of spectra of K supergiant stars in the H band (1.48 to 1.78 μm). The spectrum of RW Cep is the third one labeled with K2 O-Ia. Figure taken from the *IRTF* spectral library of cool stars by Rayner et al. (2009).

4.3 HD 143352

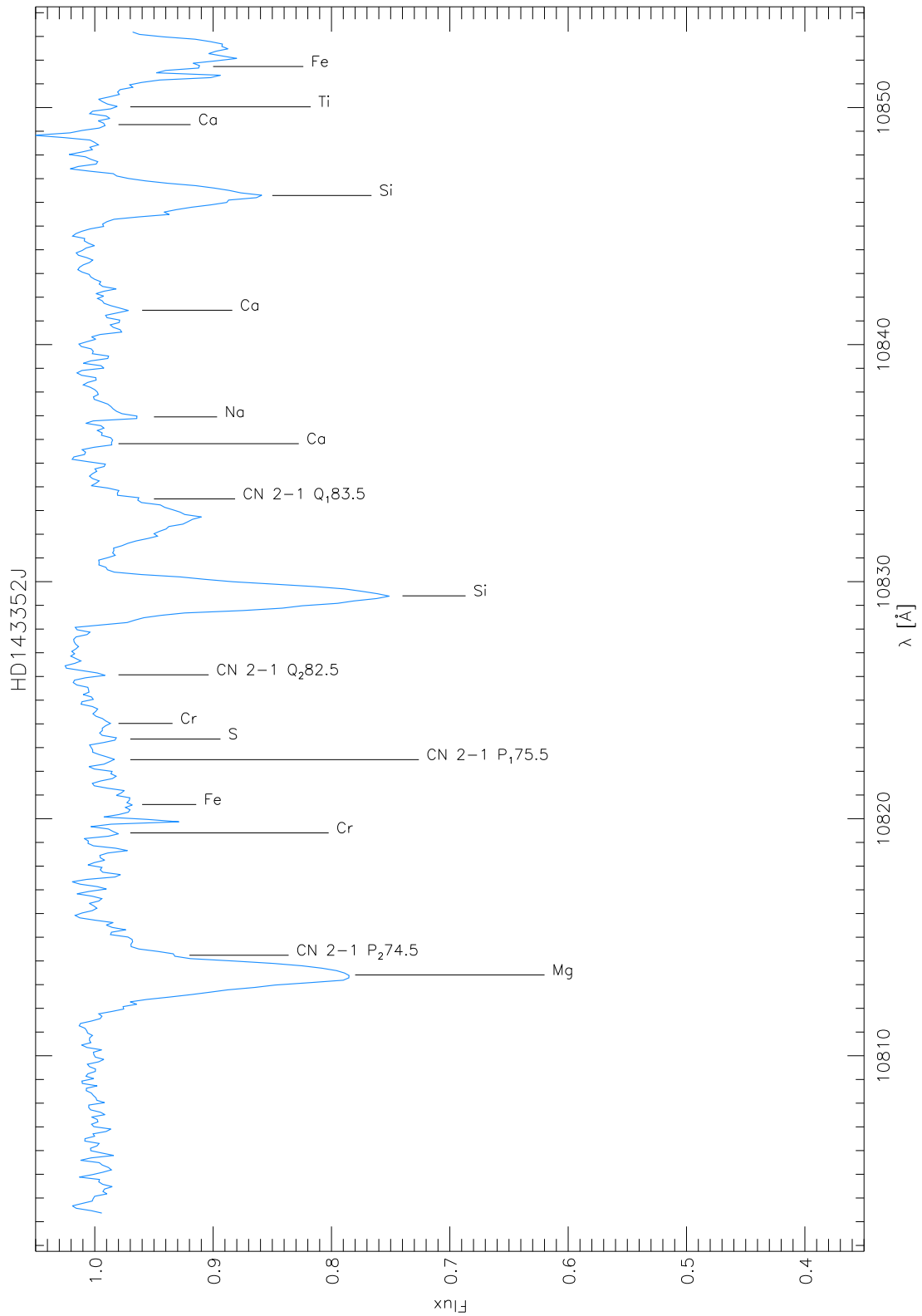


Figure 4.14: The spectrum of HD 143352 in the J-filter with identified and measured lines.

Wavelength [Å]	Atom/Molecule	EQW [mÅ]	Vacuum Pos.	Difference
10813.41	Mg	438.3	10814.05	0.64
10814.24	CN 2-1 P_2 74.5	39.2	10814.83	0.59
10819.40	Cr	10.2	10819.86	0.46
10820.60	Fe	28.2	10821.26	0.66
10822.49	CN 2-1 P_1 75.5	5.4	10823.43	0.94
10823.36	S	5.1	10824.17	0.81
10824.02	Cr	8.1	10824.58	0.56
10826.07	CN 2-1 Q_2 82.5	1.1	10826.84	0.77
10829.40	Si	311.8	10830.06	0.66
10833.49	CN 2-1 Q_1 83.5	12.4	10834.22	0.73
10835.82	Ca	3.4	10836.35	0.53
10836.95	Na	9.2	10837.84	0.89
10841.45	Ca	17.2	10841.94	0.49
10846.29	Si	160.7	10846.82	0.53
10849.28	Ca	2.9	10849.74	0.46
10850.03	Ti	7.1	10850.61	0.58
10851.73	Fe	51.5	10852.43	0.70

Table 4.2: The equivalent widths for the lines in Fig. 4.14 with the vacuum positions given by Hinkle et al. (1995). The mean difference between vacuum position and measured wavelength is 0.65 Å. The radial velocity derived from these measurements is -0.08 ± 3.88 km/s after heliocentric correction.

Analysis of the Spectrum

If one compares this star with the spectrum of δ Oph (Fig. A.6), the broadening of the atomic lines of Mg and Si in HD 143352 is obvious. Cr and Fe were difficult to identify due to the great number of "lines" near the continuum flux. The CN features appear equally broad like those of δ Oph. To account for this broadening of lines, a high macroturbulence of $\zeta=22$ km/s was used for the model spectrum. The S and Cr line at 10823.36 \AA and 10824.02 \AA , respectively, are overestimated in the model spectrum.

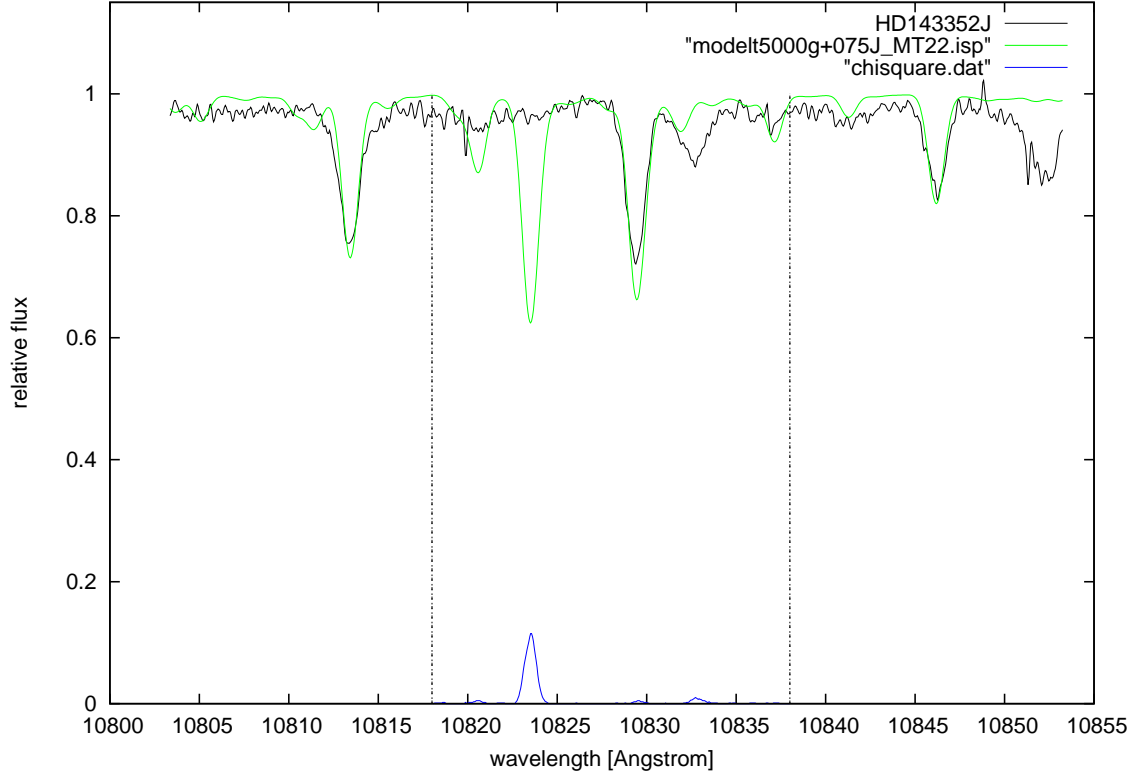


Figure 4.15: The star HD 143352 overplotted by a MARCS model of 5000 K, $\log g=0.75$, and $\zeta=22$ km/s.

Literature

There seems to be hardly any information available for this particular star (see Fig. 4.16), only one reference is listed in SIMBAD: *The Toruń catalogue of Galactic post-AGB and related objects* by Szczerba et al. (2007) filed it as a *very likely* post-AGB object based upon the satisfaction of two of their classification criteria (for more information see Chapter 1.1.4):

Post-AGB stars are often found within the group of high galactic latitude supergiants (hglsg) which are situated at $|b| > 15^\circ$. HD 143352 belongs to this group and is also classified as an RV Tauri star. As mentioned before, RV Tauri stars are commonly expected to be post-AGB objects, and there is no indication for HD 143352 to believe otherwise.

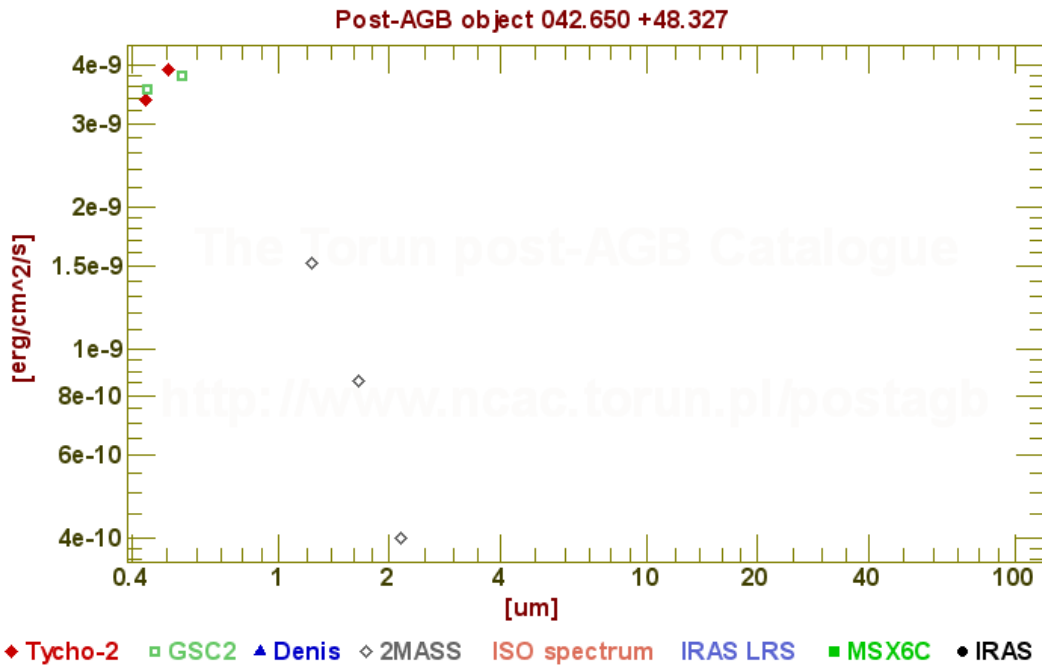


Figure 4.16: Measurements of the star HD 143352. This picture was taken from the online version of *The Toruń catalogue of Galactic post-AGB and related objects* by Szczerba et al. (2007).

4.4 θ Her

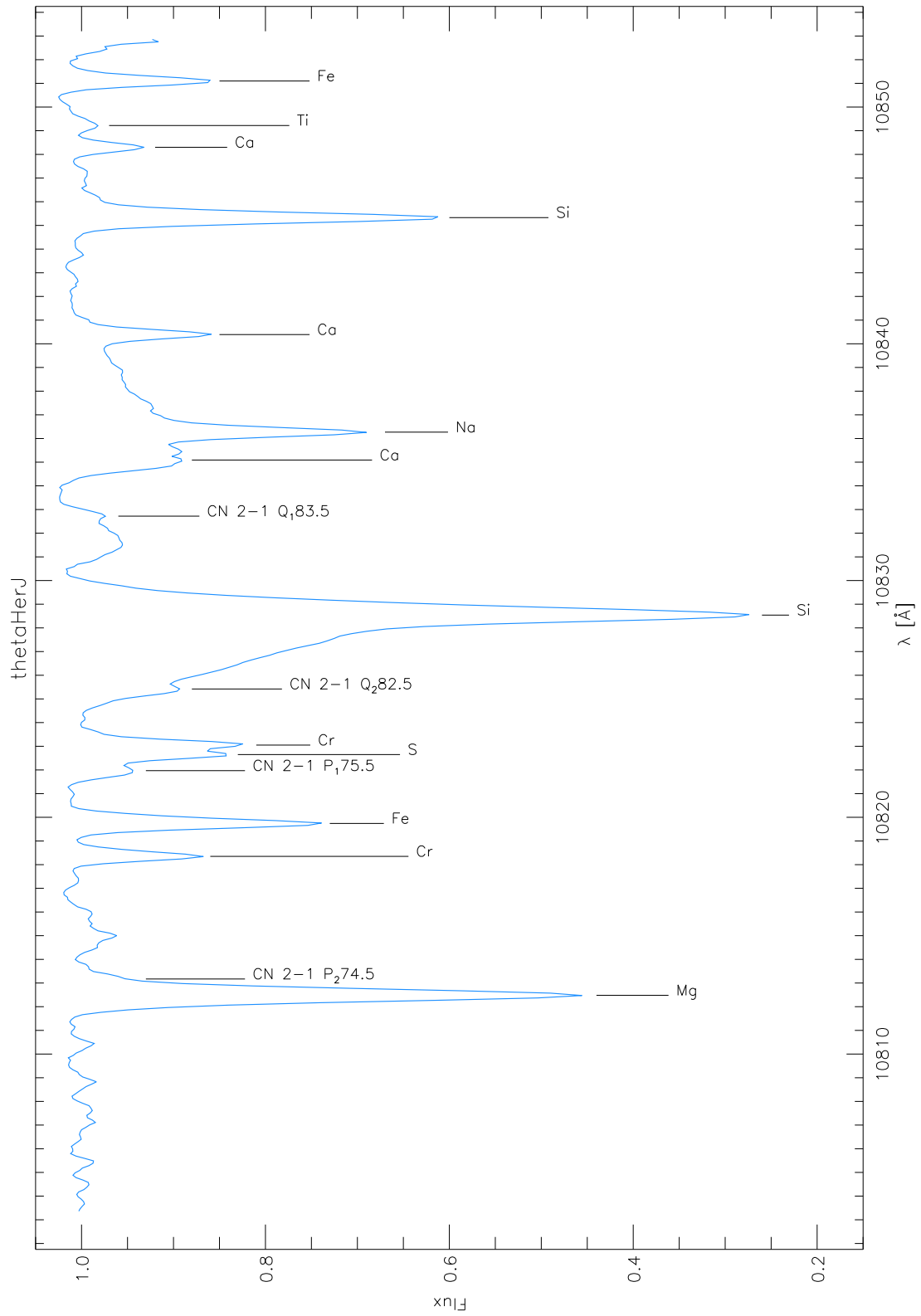


Figure 4.17: The spectrum of θ Herculis in the J-filter with identified and measured lines.

Wavelength [Å]	Atom/Molecule	EQW [mÅ]	Vacuum Pos.	Difference
10812.48	Mg	409.2	10814.05	1.57
10813.17	CN 2-1 P_2 74.5	25.2	10814.83	1.66
10818.35	Cr	87.0	10819.86	1.51
10819.74	Fe	152.6	10821.26	1.52
10821.97	CN 2-1 P_1 75.5	38.3	10823.43	1.46
10822.65	S	107.7	10824.17	1.52
10823.05	Cr	94.5	10824.58	1.53
10825.42	CN 2-1 Q_2 82.5	87.0	10826.84	1.42
10828.54	Si	1117.0	10830.06	1.52
10832.72	CN 2-1 Q_1 83.5	11.7	10834.22	1.50
10835.09	Ca	141.4	10836.35	1.26
10836.27	Na	278.2	10837.84	1.57
10840.39	Ca	81.5	10841.94	1.55
10845.33	Si	247.1	10846.82	1.49
10848.30	Ca	29.5	10849.74	1.44
10849.22	Ti	7.1	10850.61	1.39
10851.10	Fe	65.6	10852.43	1.33

Table 4.3: The equivalent widths for the lines in Fig. 4.17 with the vacuum positions given by Hinkle et al. (1995). The mean difference between vacuum position and measured wavelength is 1.48 Å. The radial velocity derived from these measurements is -26.34 ± 2.57 km/s after heliocentric correction.

Analysis of the Spectrum

I searched the literature for stellar parameters as a basis for my model calculations, and there are two different suggestions: a slightly cooler model ($T_{\text{eff}} \sim 4300$ K, $\log g \sim 1.4$, mean values taken from Williams (1971b) and McWilliam (1990)), and one with $T_{\text{eff}}=4690$ and $\log g=1.68$, published by Harper (1992). Both estimates suit my observations quite well, there is almost no difference between them concerning the most prominent lines. Eventually, I decided to base my model on the latter suggestion.

The most significant difference between this spectrum and the others taken in this filter is a strange shape between CN 2-1 Q₂62.5 and Si near 10823 Å. There is a decline towards the Si line that is not expected there. As this shape was seen in both of the exposures, it can be assumed that this is a real spectroscopic feature and not an artefact of the observation or the data reduction. Beside this speciality, the lines are broadened to a small extend, but the lines themselves and the strength of the lines is quite similar to the comparison stars. The S and Cr line at 10822.65 Å and 10823.05 Å, respectively, are overestimated in the model spectrum.

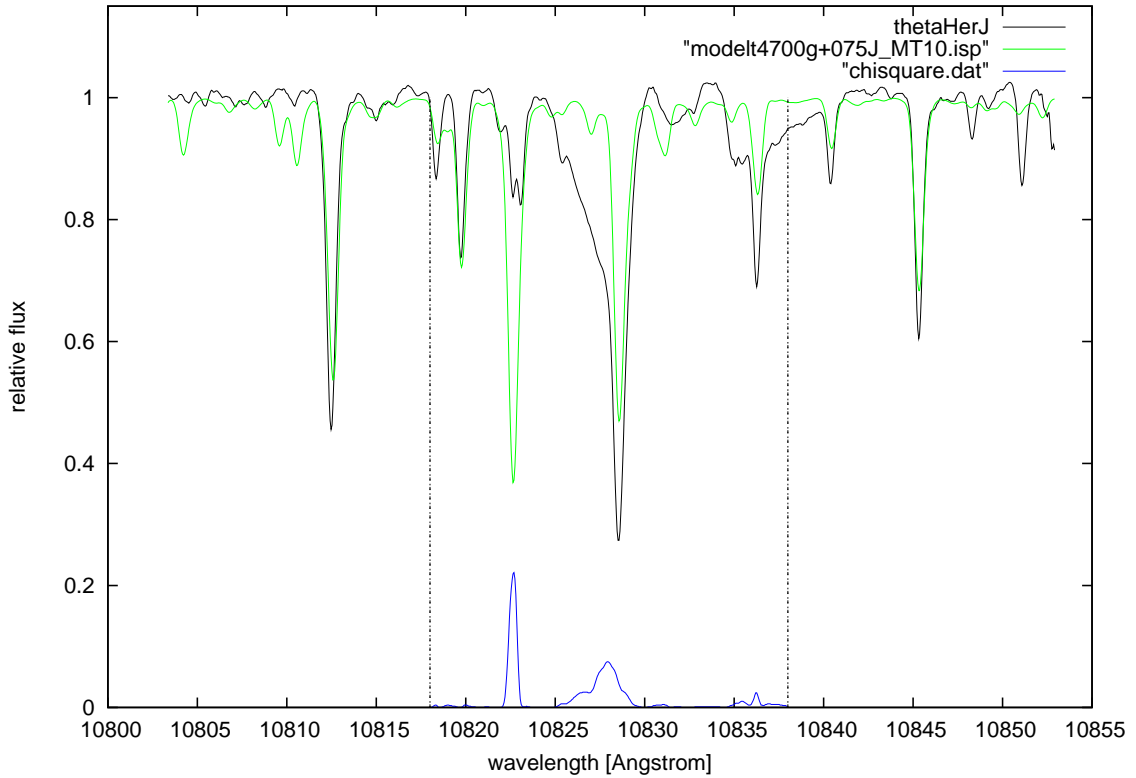


Figure 4.18: The star θ Her overplotted by a MARCS model of 4700 K, $\log g=0.75$ and $\zeta=10$ km/s.

Literature

The star θ Her is labeled as a variable star without further information about the variability type or class in the *General Catalogue of Variable Stars* (Samus et al., 1997).

According to an article published in the *Astronomical Journal* by Shapiro (1972), it was uncertain whether θ Her was a variable star or an eclipsing binary. The average radial velocity determined for this star was -28.0 km/s with small variations, leading to the assumption that this star is in fact a variable star and not an eclipsing binary, because the variations found were too small to be assigned to a binary period. The radial velocity I determined in this thesis, -26.34 km/s, is in good agreement with the value derived by Shapiro (1972).

A series of papers used narrow band observations to estimate elemental abundances of iron (Williams, 1971b), sodium and manganese (Williams, 1971a), calcium (Rego et al., 1972), and barium (Williams, 1975) in evolved stars, with the result being $[\text{Fe}/\text{H}]=0.25$, $[\text{Mn}/\text{H}]=0.14$, $[\text{Na}/\text{H}]=0.10$, $[\text{Ca}/\text{H}]=0.14$, and $[\text{Ba}/\text{H}]=0.71$ for θ Her. The stellar parameters derived during this series are: $T_{\text{eff}}=4364$ K, $\log g=1.6$. These values are in rather good agreement with McWilliam (1990), who calculated $T_{\text{eff}}=4330$ K, $\log g=1.28$, and $\xi=3.4$ km/s.

Another estimation of stellar parameters is given by Harper (1992), who found an effective temperature of 4690 K and surface gravity of $\log g=1.68$. He also estimated the radius and mass of θ Her to be $57 R_{\odot}$ and $5.7 M_{\odot}$.

The $\lambda 10830$ helium line has been observed in stars of spectral type G and K and is suspected to be produced in a hot chromosphere. Zirin (1976) observed this helium line in the spectra of θ Her over several years and found a possible period of five years between phases of emission (1966, 1971, and 1975). The author also reported strong CN bands and no other variation in the spectrum than the helium line emission. In the time between the observed emission features, only weak absorption was present (see Fig. 4.19).

The spectrum presented in this thesis shows the same spectral region as published by Zirin (1976). The $\lambda 10830$ helium line in the spectra taken by Zirin (1976) is placed to the right side of the Si line in June 1971 (see Fig 4.19, the last spectrum on the left). The spectrum I analysed has a similar structure, but the strange shaped feature is on the opposite side of Si, to the left. If it is the $\lambda 10830$ helium line, it must have been shifted to shorter wavelengths somehow.

Due to a composition of special emission and absorption lines, θ Her was included into the group of *hybrid giants*. These objects can be found in the vicinity of the Hertzsprung gap and are expected to be intermediate mass objects, B stars that evolved from the main sequence (Harper, 1992).

The observational properties of these hybrid atmosphere stars are double circumstellar absorption lines of Ca II and Mg II, composed of a high velocity feature at -70 to -130 km/s and a low velocity feature at -10 to -20 km/s, and emission lines that are assigned to low temperatures (O I, C I, etc.) as well as high temperatures (N V, C IV, C II) (Reimers, 1982).

θ Her

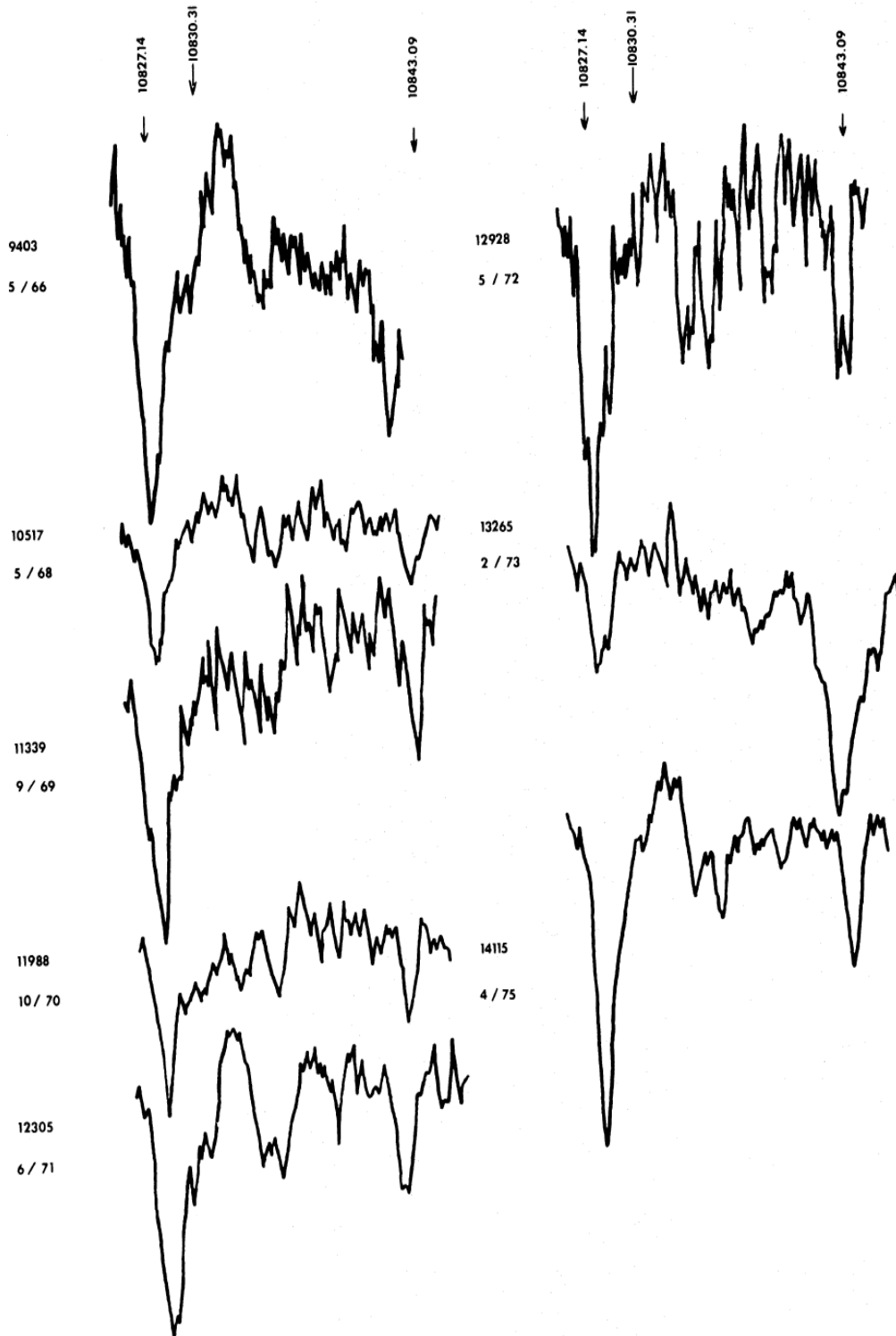


Figure 4.19: The $\lambda 10830$ helium line observed for over ten years (Zirin, 1976). Emission peaks are present in 1966 (first spectrum on the left side), 1971 (last spectrum left), and 1975 (last spectrum right). Weak emission can be seen in the spectra taken in 1968 (second spectrum left) and 1972 (first spectrum right). Absorption was observed in 1970 (fourth spectrum left).

This combination of a cool high-velocity wind and a solar-type transition region places the hybrid or chromosphere stars between hot objects with solar-like coronae and objects with cooler atmospheres (Drake et al., 1984b). Drake et al. (1984a) proposed a different solution for the low-velocity absorption components observed in the Mg II resonance lines (see Fig. 4.20) than circumstellar origin: the local interstellar medium (LISM).

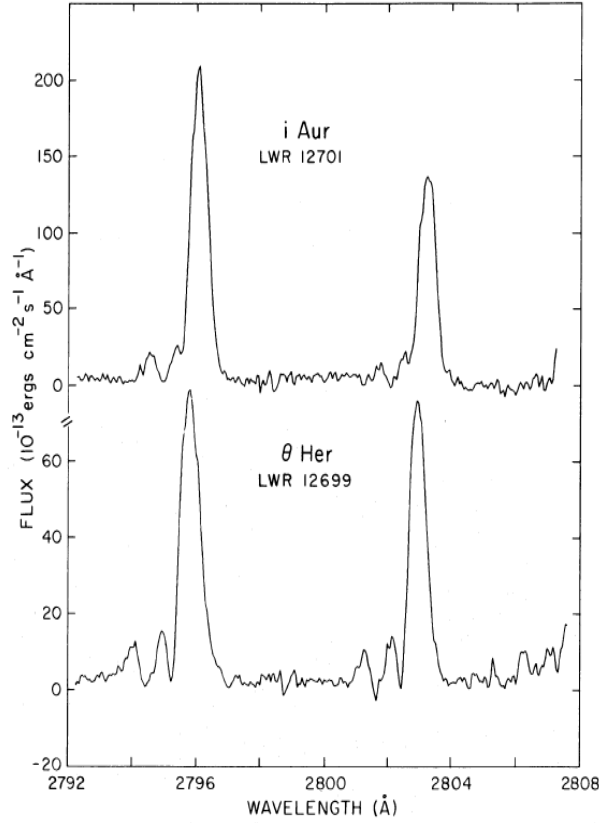


Figure 4.20: Line profiles of the Mg II resonance lines in θ Her observed by Hartmann et al. (1985).

The difference between the absorption lines produced by the high velocity outflow of the star and the LISM is high enough in radial velocity to separate them clearly. Therefore, the definition of hybrid stars has changed slightly to cool and luminous objects that show Mg II and/or Ca II absorption features as results of a high velocity wind as well as high-temperature lines like C IV $\lambda 1550$.

Ayres (2005) placed his sample of hybrid giants into a HRD (see Fig. 4.21), the lined area illustrates the Hertzsprung gap, the oval marks the clump of objects in their core-helium-burning-phase (like yellow giants of 1.5 - 3 M_{\odot}), the angular region displays stars with possible mass loss and cool winds.

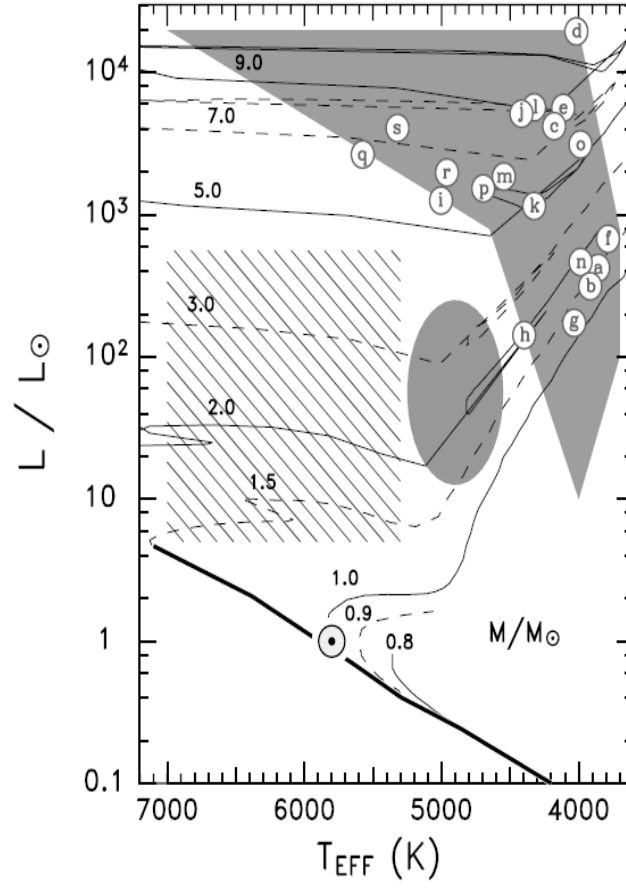


Figure 4.21: HRD of a sample of hybrid stars by Ayres (2005). θ Her is represented by m .

Considering the position of θ Her in the HRD, Ayres (2005) draw the conclusion that this star evolved from an O- or B-type main sequence progenitor to a high mass hybrid giant lately and therefore it must be a rather young (about 100 Myr) object.

4.5 AC Her

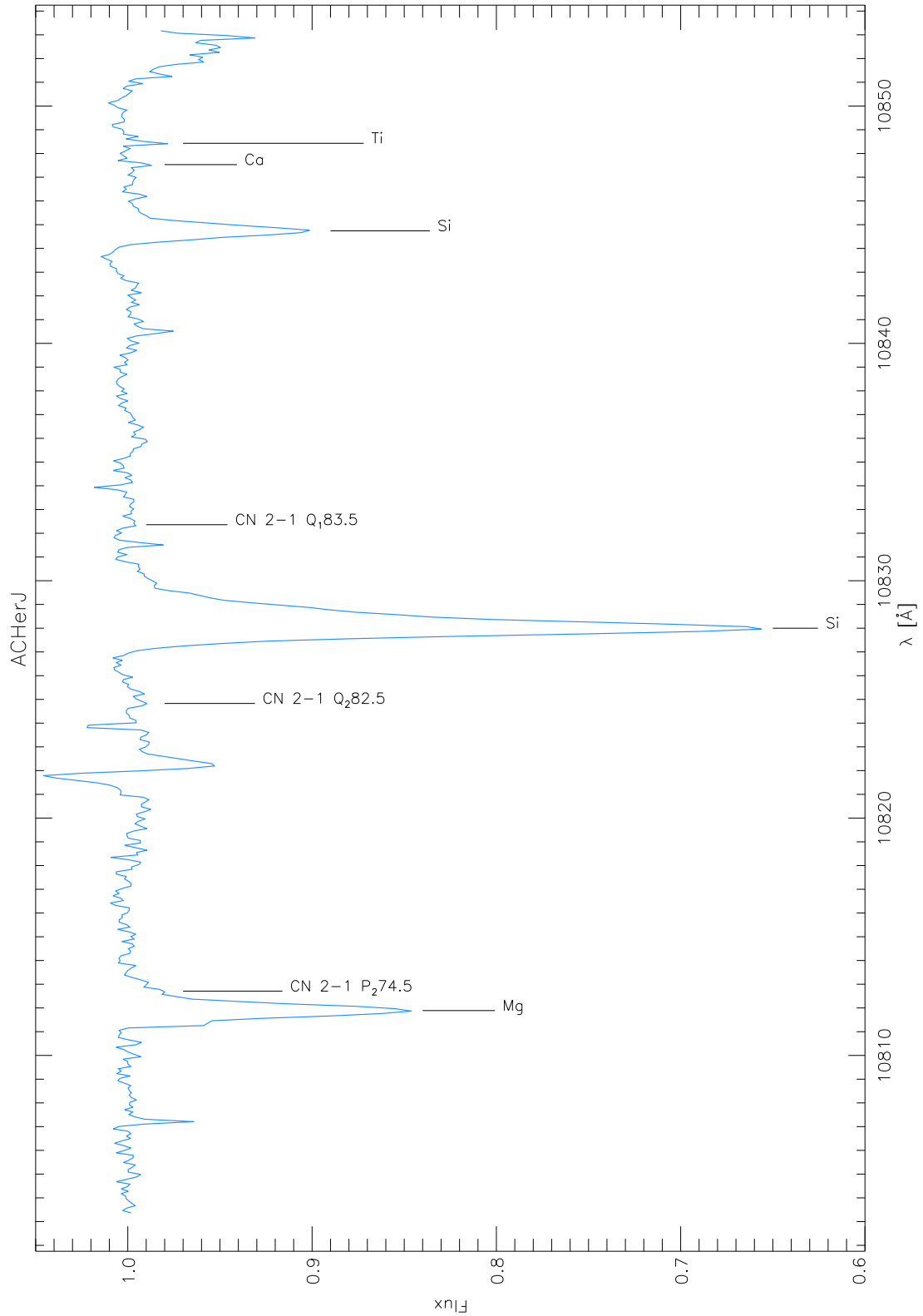


Figure 4.22: The spectrum of AC Herculis in the J-filter with identified and measured lines.

Wavelength [Å]	Atom/Molecule	EQW [mÅ]	Vacuum Pos.	Difference
10811.89	Mg	117.0	10814.05	2.16
10812.71	CN 2-1 P_2 74.5	8.4	10814.83	2.12
10824.83	CN 2-1 Q_2 82.5	3.2	10826.84	2.01
10828.00	Si	291.6	10830.06	2.06
10832.36	CN 2-1 Q_1 83.5	0.8	10834.22	1.86
10844.74	Si	72.7	10846.82	2.08
10847.53	Ca	2.2	10849.74	2.21
10848.43	Ti	5.2	10850.61	2.18

Table 4.4: The equivalent widths for the lines in Fig. 4.22 with the vacuum positions given by Hinkle et al. (1995). The mean difference between vacuum position and measured wavelength is 2.08 Å. The radial velocity derived from these measurements is -37.25 ± 2.91 km/s after heliocentric correction.

Analysis of the Spectrum

As can be seen in the table above, the atomic lines are quite strong. The emission feature with a P-Cygni-like profile at 10821 \AA could not be assigned to any atom or molecule with certainty. In comparison to the model spectrum, one can assume that this line shows a P-Cygni profile of either the S or Cr line. These two lines are overestimated in the model spectrum.

The feature on the red side of the strongest Si line could probably be the $\lambda 10830$ helium line. Comparable shapes were observed in the spectra of θ Her (see the work of Zirin (1976)).

In general the model spectrum seems to be too cold to fit the observed spectra. Values of the effective temperature vary between 4200 K to 7000 K, with the most common estimates of 6000 K.

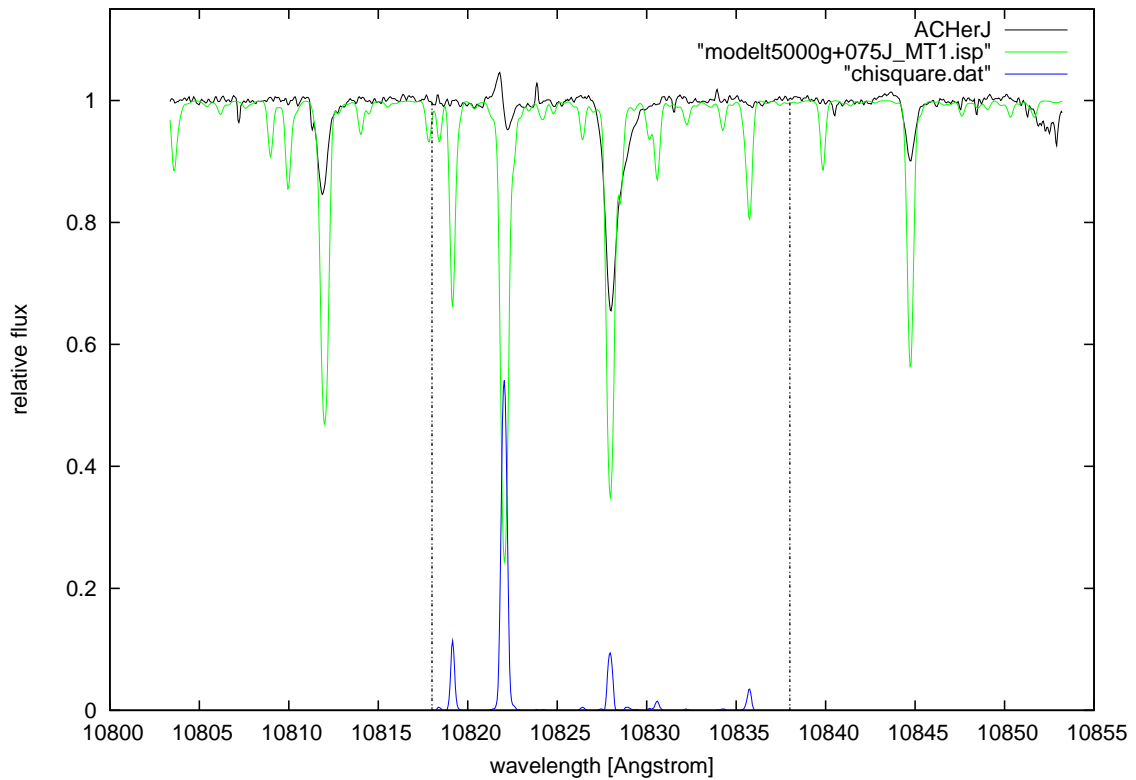


Figure 4.23: The star AC Her overplotted by a MARCS model of 5000 K, $\log g=0.75$ and $\zeta=1 \text{ km/s}$.

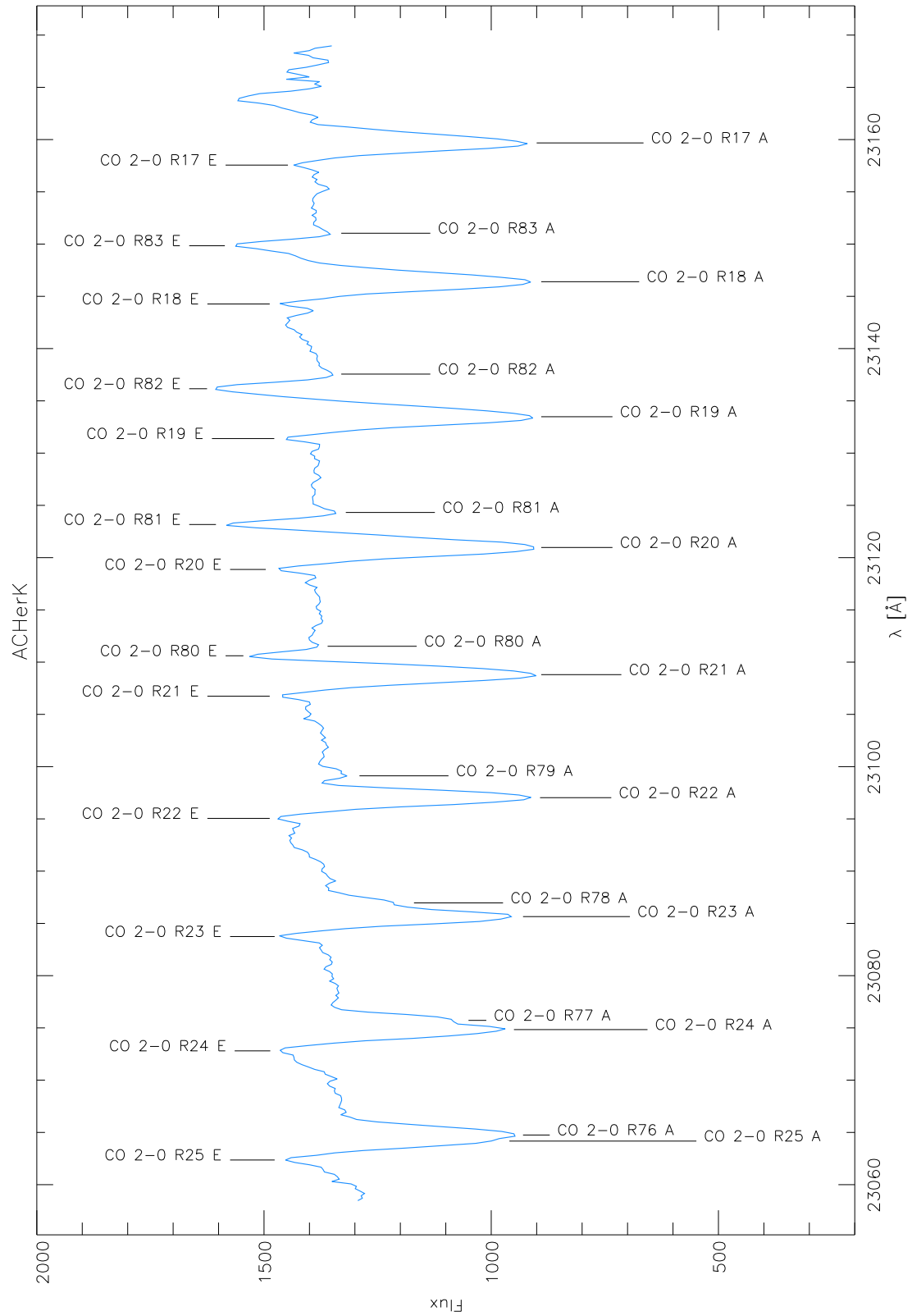


Figure 4.24: The spectrum of AC Herculis in the K-filter with identified and measured lines.

Wavelength [Å]	Atom/Molecule	EQW [mÅ]	Vacuum Pos.	Difference
23062.36	CO 2-0 R25 E	- 59.0	23067.89	5.53
23064.17	CO 2-0 R25 A	441.6	23067.89	3.72
23064.75	CO 2-0 R76 A	638.4	23069.24	4.49
23072.80	CO 2-0 R24 E	- 73.8	23078.41	5.61
23074.84	CO 2-0 R24 A	516.0	23078.41	3.57
23075.72	CO 2-0 R77 A	306.8	23080.18	4.46
23083.74	CO 2-0 R23 E	- 47.1	23089.34	5.60
23085.65	CO 2-0 R23 A	497.1	23089.34	3.69
23086.96	CO 2-0 R78 A	177.1	23091.57	4.61
23095.05	CO 2-0 R22 E	- 70.7	23100.67	5.62
23097.03	CO 2-0 R22 A	552.7	23100.67	3.64
23099.12	CO 2-0 R79 A	28.6	23103.40	4.28
23106.74	CO 2-0 R21 E	- 47.9	23112.40	5.66
23108.80	CO 2-0 R21 A	615.8	23112.40	3.60
23110.61	CO 2-0 R80 E	- 95.7	23115.67	5.06
23111.52	CO 2-0 R80 A	—	23115.67	4.15
23118.87	CO 2-0 R20 E	- 51.7	23124.54	5.67
23120.97	CO 2-0 R20 A	673.4	23124.54	3.57
23123.17	CO 2-0 R81 E	-141.9	23128.41	5.24
23124.32	CO 2-0 R81 A	13.7	23128.41	4.09
23131.39	CO 2-0 R19 E	- 36.0	23137.08	5.69
23133.48	CO 2-0 R19 A	672.2	23137.08	3.60
23136.16	CO 2-0 R82 E	-218.5	23141.59	5.43
23137.56	CO 2-0 R82 A	18.0	23141.59	4.03
23144.27	CO 2-0 R18 E	- 50.8	23150.03	5.76
23146.40	CO 2-0 R18 A	667.6	23150.03	3.63
23149.84	CO 2-0 R83 E	-158.5	23155.23	5.39
23151.04	CO 2-0 R83 A	8.7	23155.23	4.19
23157.56	CO 2-0 R17 E	- 40.3	23163.38	5.82
23159.68	CO 2-0 R17 A	625.1	23163.38	3.70

Table 4.5: The equivalent widths for the lines in Fig. 4.24 with the vacuum positions given by Hinkle et al. (1995). The mean differences between vacuum position and measured wavelength can be seen in Table 4.6. The radial velocity derived from the measurements in the J-band is -37.25 ± 2.91 km/s after heliocentric correction. Due to the splitting of the CO-lines, the more reliable radial velocity estimated from the J-band is given here.

Absorption	Diff. [Å]	RV [km/s]	Emission	Diff. [Å]	RV [km/s]
low-excitation	3.64	10.58 ± 0.69	low-excitation	5.66	-15.71 ± 1.07
high-excitation	4.29	2.12 ± 2.55	high-excitation	5.28	-10.75 ± 1.89
all	3.94	6.60 ± 4.60	all	5.54	-14.18 ± 2.67

Table 4.6: The mean radial velocities relative to the star for absorption and emission lines.

Analysis of the Spectrum

Due to the emission lines a continuum-fit like that used in the J-filter was not possible, so the spectrum presented here has an estimated continuum at 1375 counts. The position of the high-excitation lines used in the synthetic spectra of the K-band models turned out to be incorrect. The measurements were compared to the Arcturus-Atlas (Hinkle et al., 1995) and are therefore not affected by this problem.

In the K-filter, the high-excitation lines (CO 2-0 R76 to R83) as well as the low-excitation lines (CO 2-0 R17 to R25) are in absorption as well as in emission. In this case, the emission lines are blueshifted relative to the absorption component, which means an invert P-Cygni profile and matter falling onto the star.

At the blue end of the spectrum, the emission feature of the CO 2-0 R25 line is normally shaped, while the corresponding absorption feature is overlapped by the absorption component of the CO 2-0 R76 line. I suspect that the emission component of the latter is overlapped by the absorption line of the low-excitation line and therefore not measurable. Probably the emission line weakens the mentioned absorption line of R25. This might also be the case for the CO 2-0 R24/R77 and R23/R78 lines.

Further to the blue side of the spectrum, the emission components of the high-excitation lines become visible. In general, the absorption features of the high-excitation lines seem to be weaker than the emission features, while the absorption features of the low-excitation lines are stronger than the emission components.

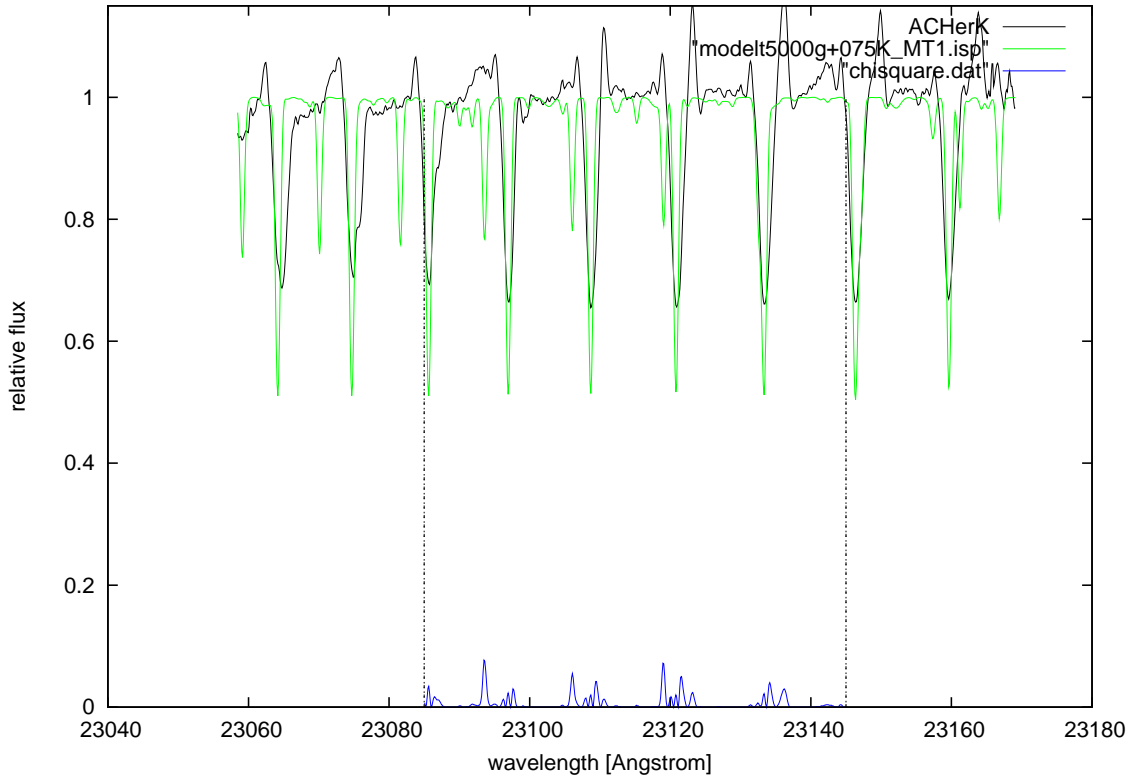


Figure 4.25: The star AC Her overplotted by a MARCS model of 5000 K, $\log g=0.75$ and $\zeta=1$ km/s.

Literature

AC Her is classified as a RVa star with a mean period of 75.462 days and a spectral type of F2pIb-K4e(CO,O). The maximum of the light curve in V lies at 6.85 mag, the minimum at 9.0 mag (Samus et al., 1997). Joy (1952) measured a mean radial velocity of about -30 km/sec. This star has a higher effective temperature than other known RV Tauri stars.

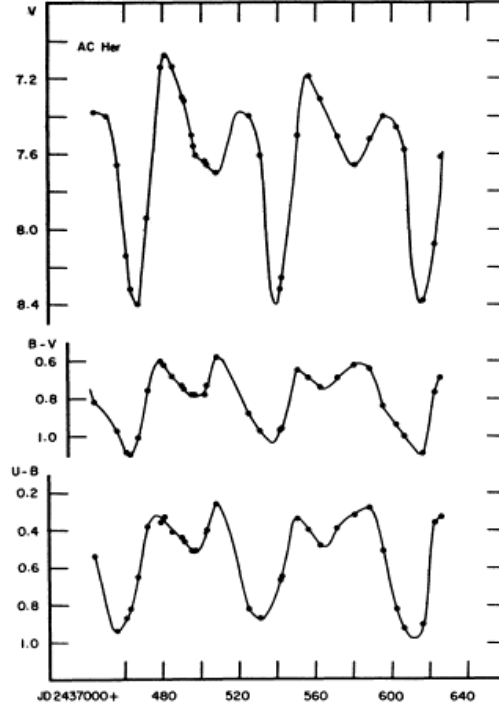


Figure 4.26: The light curve of the RV Tauri star AC Her in V, B-V and U-B (Preston et al., 1963).

Yoshioka (1979) did a curve-of-growth analysis of AC Herculis with the following results, as can be seen in Fig. 4.27: the iron-peak elements with even-even nuclei were found to be deficient by a factor of about 10 compared to the sun. Iron-peak elements with odd-even nuclei, such as V, Mn, and Co, and some lighter s-process elements, namely Sr, Y, and Zr, are a factor of 2 to 4 deficient compared to Fe. The heavier s-process element Ba and the r-process element Eu are deficient by a factor of 1.5 relative to Fe. The average of the α -process elements is overabundant by a factor of 2 compared to Fe, C and N by a factor of 6 and 18.

The carbon-rich AC Her, like many other RV Tauri stars, has a circumstellar dust shell that makes temperature estimates based on colour questionable. This shell might be the origin of CN and CH molecules, which could form in the cooler region above the photosphere. The kinematics of the atmosphere of this RV Tauri star is explained in Baird (1981) as a combination of two shock waves, one near primary minimum and one near secondary minimum. This second shock wave proceeds outwards while matter, which was ejected during previous pulsations, falls back on to the star.

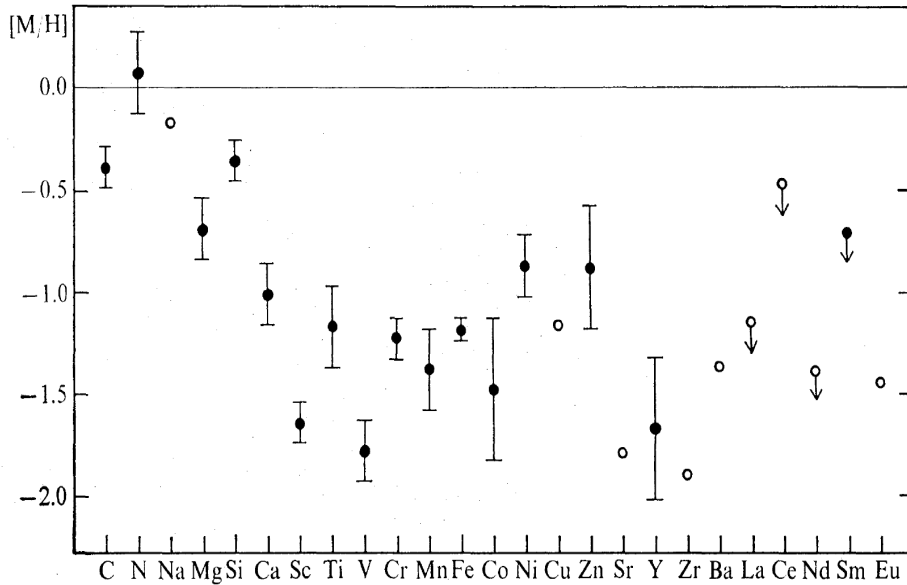


Figure 4.27: The chemical composition of AC Her relative to the sun, derived by Yoshioka (1979). Open circles represent results from only one line, filled circles represent results from two or more lines. The error bars give the maximum error due to the scatter of plots in the curve of growth. The arrows indicate that only an upper limit is obtained. Observations were done at secondary minimum.

Baird (1981) used an ATLAS 5 grid and MOOG to compute models of the atmosphere of AC Her at different phases and measured the theoretical equivalent widths to compare them with the observations and figure out the best parameters for T_{eff} , $\log g$ and Z . For these models, the author used the abundances of all metals excluding C, N and O, defining it as $Z_1 = 0.06 Z_{1\odot}$. The circumstellar reddening was determined to be $E(B-V) = +0.35 \pm 0.05$. At primary minimum, the temperature was determined to be 6000 K, with a $\log g$ value of 2.5, which is high, since this star is a supergiant. At secondary maximum, the best fitting model was computed using $T_{\text{eff}} = 7000$ K and $\log g = 1.5$. The result of the iron abundance given by the model atmospheres, $[\text{Fe}/\text{H}]_{\odot}^{\text{AC Her}} = -1.22$, is in agreement with the results found by Yoshioka (1979), as can be seen in Fig. 4.27. In the paper done by Baird (1981), the Z_1 elements discussed above have all been found depleted in the same way as Fe, with the exception of Co, Zn and Sr, which might be enhanced compared to iron. The values or upper limits found for C, N, and O were as follows: $\text{C} = 0.2 \text{ C}_{\odot}$, $\text{N} \leq 0.2 \text{ N}_{\odot}$, $\text{O} \leq 0.12 \text{ O}_{\odot}$. Baird (1981) also stated that their values are in good agreement with the ones published by Yoshioka (1979).

Evans (1985) observed a sample of RV Tauri stars, including AC Her, to get a better understanding of the circumstellar material and the light variations of these stars. He found a large radiation excess in AC Her, the amount of energy emitted in the long infrared is nearly as much as in the visible. Gehrz & Woolf (1970) found, that AC Her was displaying a strong emission feature at $11 \mu\text{m}$, but a weaker excess in the $3 \mu\text{m}$ region, suggesting that this observation might come from dust grains around the star. RV Tauri stars with a large excess at $3.4 \mu\text{m}$ have a greater amount of dust near the star, which leads to temperature estimations of a blackbody of 800 to 900 K, while in the case of AC Her, a value of 300 to 500 K for the dust grains and

4500 K for the star itself seems appropriate.

Although AC Her is reported to be carbon rich (RVB type), it does not exhibit the SiC emission at $11\,\mu\text{m}$ as expected for a carbon rich star, but it shows the $10\,\mu\text{m}$ silicate emission typical for oxygen-rich stars. The question is why a carbon rich star like AC Her shows silicate emission in the dust shells. The fact that AC Her shows large excesses at 12 and $25\,\mu\text{m}$ leads to the assumption that it has cooler shells than other stars of this group (Evans, 1985).

The work of Goldsmith et al. (1987) also included AC Her. They suggest a Planck mean absorption optical depth $\langle\tau\rangle$ of 0.11. Unlike the other sample stars used in their work, AC Her could not be fitted with a stellar continuum and a single dust shell. The optical spectrum could be fitted with a blackbody of 5680 K, while the near-IR data was good represented by a blackbody of 1800 K. A large excess in the N band leads to the assumption, that at least two distinct dust shells are present in the case of AC Her.

Raveendran (1989) does not share the opinion of the authors mentioned above. Raveendran did not find hot dust around AC Her and therefore is not convinced about the theory of sporadic dust formation. The author suggests a very cool dust shell (inner-shell temperature of 260 K), due to the low excess at near-infrared wavelengths and the observations in the far-infrared.

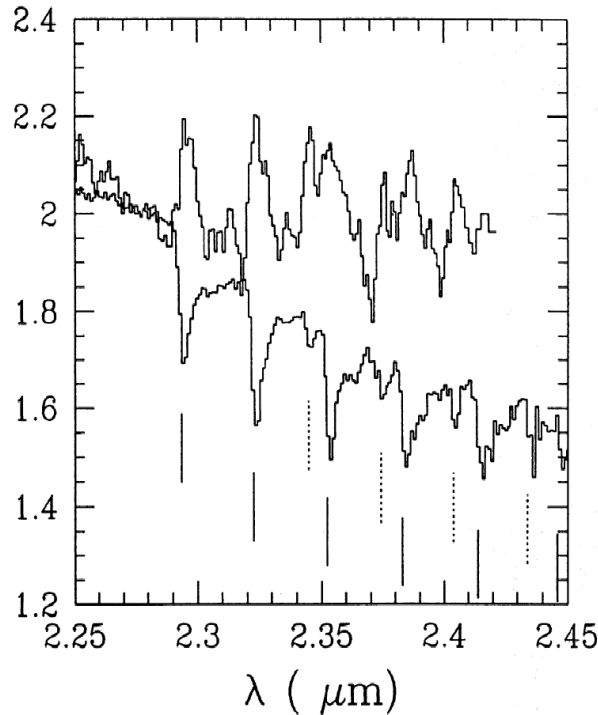


Figure 4.28: AC Her observed by Oudmaijer et al. (1995) in 1989 (upper spectrum) and 1992 (lower spectrum). Vertical lines indicate ^{12}CO band heads, vertical dotted lines ^{13}CO band heads. Flux is given in $\text{W m}^{-2} \mu\text{m}^{-1}$ in units of 10^{-12} .

The two spectra of AC Her obtained by Oudmaijer et al. (1995) in 1989 and 1992

show the same spectral range in the K band (see Fig 4.28). In the earlier spectrum, the ^{12}CO 2-0 and ^{13}CO 2-0 bands are in emission and equally strong. In the later spectrum, both bands are in absorption and the ^{13}CO band heads are weaker than the ones of ^{12}CO .

This variation of the CO lines seems to correlate with the pulsation period of the star. Emission of the CO overtone has been observed at minimum in V, a phase of contraction of the photosphere. After the second maximum in V, during the expanding phase of the star, the CO lines were in absorption. Oudmaijer et al. (1995) propose a model of mass outflow as the cause for these observations, suggesting the CO emission arises from an expanding detached shell.

Another theory, in which the emission is produced by interaction between the post-AGB wind and the wind produced at the end of the AGB-phase was dismissed by the authors due to the estimation that the CO emission originates from a region considerably smaller in radius than the inner boundary of the AGB dust shell (Oudmaijer et al., 1995).

In their search for abundance patterns in RV Tauri variables, Giridhar et al. (1998a) observed AC Her at two different pulsation phases, 0.70 and 0.47. During the 0.70 phase, two emission components of $\text{H}\alpha$ were observed that were separated by deep absorption as well as an asymmetry in $\text{H}\beta$. The second observation at 0.47 phase also exhibits this asymmetry in $\text{H}\beta$, but this time $\text{H}\alpha$ shows a P-Cygni-like structure with two absorption components. The stellar parameters derived from the observations are $T_{\text{eff}}=6000$ K, $\log g=1.25$, $\xi=4.2$ km/s, and $[\text{Fe}/\text{H}]=-1.4$ for phase 0.70, and $T_{\text{eff}}=5800$ K, $\log g=1.00$, $\xi=4.0$ km/s, and $[\text{Fe}/\text{H}]=-1.3$ for phase 0.47. The dust-gas separation reported for certain RV Tauri stars seems to be present in AC Her as well, being responsible for the underabundance of the high-temperature condensation elements Al, Ca, and Fe. Giridhar et al. (1998a) also noted no significant enrichment in s-process elements but an increase in carbon. The authors interpreted their findings with the following theory: that this star must have left the AGB before the third dredge-up occurred. Unfortunately, this theory does not explain the measured increase in carbon.

The theory of depletion of elements was also confirmed by Van Winckel et al. (1998), who noticed a deficiency in s-process elements that have high dust condensation temperatures. The authors also proposed a circumstellar dust shell with O-rich crystalline silicates and large dust grains indicated by strong millimeter continuum flux. They also confirmed that a binarity of AC Her fits with the suggestion of a long-lived circumbinary disc where the dust is stored (Van Winckel et al., 1998).

This disc was part of the investigation of Jura et al. (2000), who used Long Wavelength Spectrometer (LWS) data to determine the geometry of the dust around the binary system of AC Her. The observations of two peaks at $18.7 \mu\text{m}$ that are aligned more or less north-south (see Fig. 4.29) can be explained by two theories: an edge-on ring or a bipolar outflow.

Jura et al. (2000) argue that it is more likely an edge-on ring we see, because the current mass loss of AC Her is rather low for a bipolar outflow. This ring of material has a radius of about 300 AU and is composed of dust particles of the size of 200

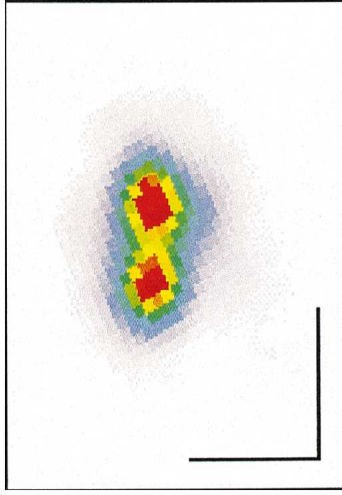


Figure 4.29: The $18.7\ \mu\text{m}$ image of AC Her by Jura et al. (2000), north is on top, east is on the left. The two spots have a north-south alignment.

μm to smaller than $1\ \mu\text{m}$, according to the mid-IR radiation.

In agreement with Jura et al. (2000), Gielen et al. (2007) found evidence for a circumbinary dusty disc around AC Her that seems to be in hydrostatic equilibrium. The unevolved companion is expected to have a mass of $1.1\ M_{\odot}$. The dust composition is magnesium rich with crystalline features that indicate cool temperatures in the outer parts of the disc.

4.6 SX Her

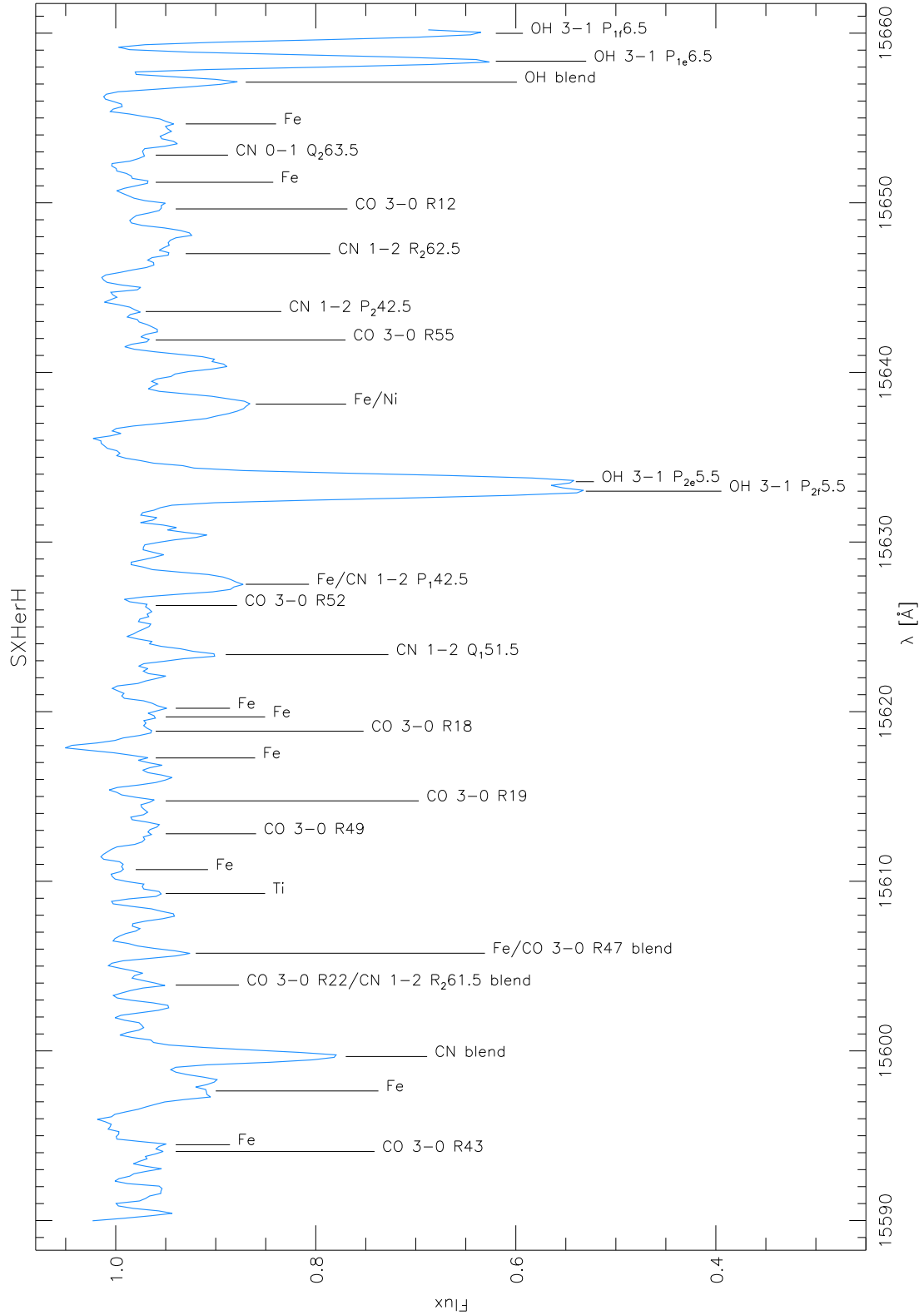


Figure 4.30: The spectrum of SX Herculis in the H-filter with identified and measured lines.

Wavelength [Å]	Atom/Molecule	EQW [mÅ]	Vacuum Pos.	Difference
15594.07	CO 3-0 R43	51.4	15591.91	-2.16
15594.47	Fe	20.8	15592.52	-1.95
15597.64	Fe	126.0	15595.75	-1.89
15609.28	Ti	37.4	15607.11	-2.17
15610.69	Fe	2.4	15608.48	-2.21
15612.80	CO 3-0 R49	39.8	15610.97	-1.83
15614.74	CO 3-0 R19	18.8	15612.58	-2.16
15617.27	Fe	10.7	15615.40	-1.87
15618.85	CO 3-0 R18	25.4	15616.76	-2.09
15619.69	Fe	35.7	15617.89	-1.80
15620.20	Fe	54.1	15618.36	-1.84
15623.36	CN 1-2 Q_1 51.5	116.3	15621.33	-2.03
15626.26	CO 3-0 R52	14.0	15624.21	-2.05
15633.00	OH 3-1 P_{2f} 5.5	481.9	15630.97	-2.03
15633.56	OH 3-1 P_{2e} 5.5	501.0	15631.68	-1.88
15641.91	CO 3-0 R55	33.1	15639.95	-1.96
15643.59	CN 1-2 P_2 42.5	17.6	15641.80	-1.79
15647.00	CN 1-2 R_2 62.5	46.3	15645.14	-1.86
15649.64	CO 3-0 R12	48.0	15647.46	-2.18
15651.21	Fe	26.2	15649.29	-1.92
15652.81	CN 0-1 Q_2 63.5	22.5	15650.52	-2.29
15654.65	Fe	67.2	15652.79	-1.86
15658.35	OH 3-1 P_{1e} 6.5	294.1	15656.17	-2.18
15659.99	OH 3-1 P_{1f} 6.5	317.4	15657.75	-2.24

Table 4.7: The equivalent widths for the lines in Fig. 4.30 with the vacuum positions given by Hinkle et al. (1995). The mean difference between vacuum position and measured wavelength is -2.01 Å. The radial velocity derived from these measurements is 20.99 ± 2.96 km/s after heliocentric correction.

Analysis of the Spectrum

This spectrum shows very strong OH lines, while CO lines or Fe are significantly weaker. The metallic lines of the atoms (like Fe or Ni) are difficult to identify, they are mostly blended with other lines and weaker than usual. Normally, most of the C and O would be bound in CO molecules, but in this case, there is almost no CO detectable, but the OH lines are the most dominant features in the spectrum. The few identified CN lines are very weak compared to the strong OH lines at 15633 \AA and 15633.56 \AA . Due to this fact, one can say, that this star is an oxygen-rich SRd variable, which has never been carbon-rich.

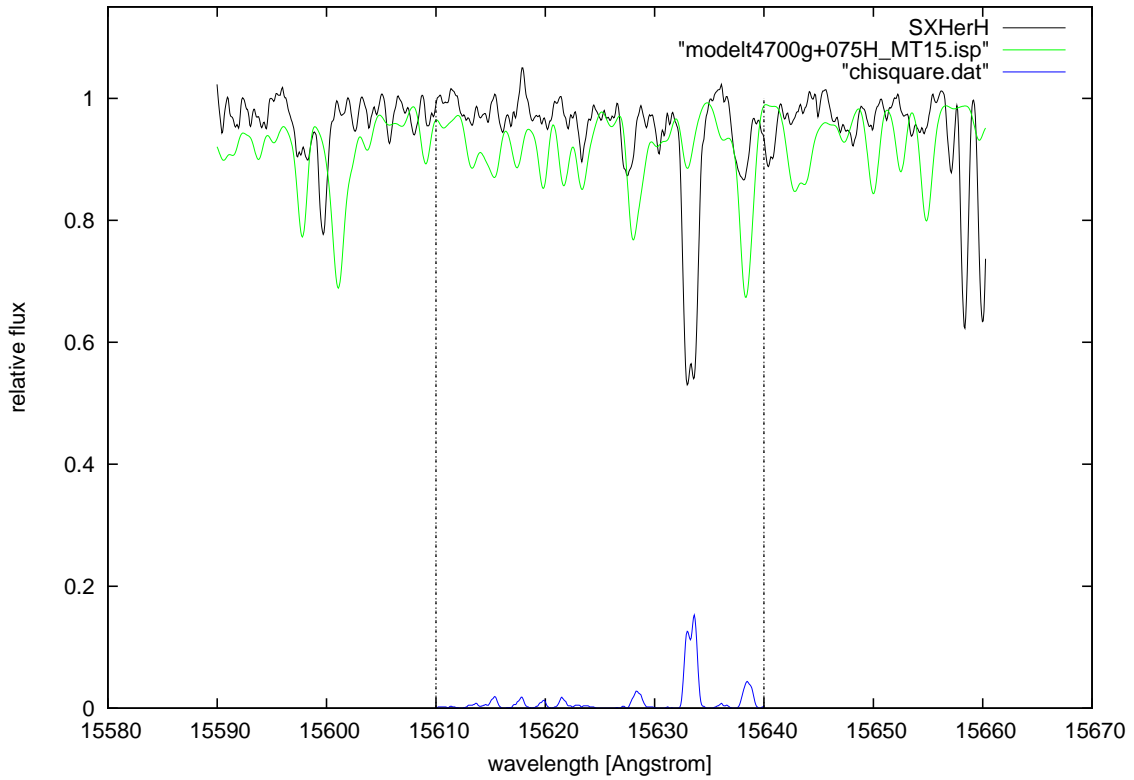


Figure 4.31: The star SX Her overplotted by a MARCS model of 4700 K, $\log g=0.75$ and $\zeta=15 \text{ km/s}$.

Literature

SX Her is an SRd variable with a period of 102.9 days and a spectral type of G3ep to K0 (M3) according to *The General Catalogue of Variable Stars (GCVS)* by Samus et al. (1997). The maximum of the light curve is at 8.6 mag and the minimum at 10.9 mag (photographic magnitudes). The low $[\text{Fe}/\text{H}]$ -ratio ($[\text{Fe}/\text{H}]=-1.8$) found by Preston & Wallerstein (1963) could explain the lack of metallic lines in the spectrum.

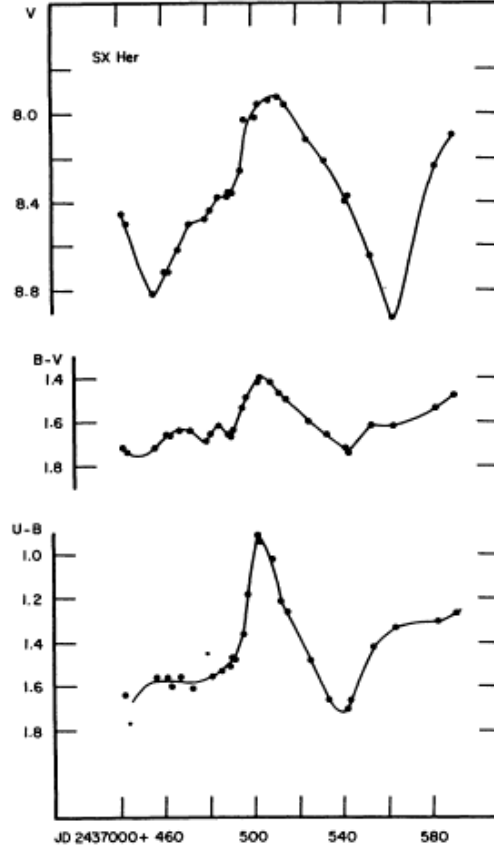


Figure 4.32: The light curve of the SRd variable star SX Her in V, B-V and U-B (Preston et al., 1963).

Radial-velocity measurements were done by Preston & Wallerstein (1963), who measured values between 9.2 to 19.7 km/s. The upper boundary is in good agreement with a radial velocity of 20.0 km/s found by Wilson (1953), as well as with the measurement of 20.99 km/s derived in this thesis.

The variation in radial-velocity found by Preston & Wallerstein (1963) could be compared to the one found in cepheids, but it is smaller in range. The authors observed strong Balmer emission lines in their spectra, which vary in intensity. They took this effect for evidence that the material generating the metallic absorption is above the origin of the hydrogen emission.

Concerning the near-infrared excess observed in a lot of RV Tauri stars, this SRd variable seems to show no such excess (Evans, 1985).

In their attempt to create a spectrophotometric atlas for RV Tauri variables, Cardelli & Howell (1989) also included the metal-poor SRd variable SX Her into their sample (see Fig. 4.33 together with Z Sex). The authors stated that the SRd variables, like

SX Her, show different spectra than their observed RV Tauri A type stars, so these two groups can be separated easily.

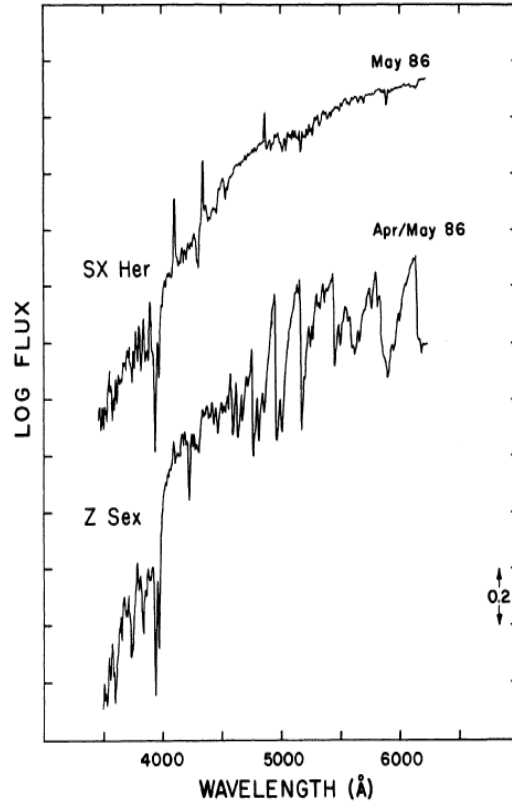


Figure 4.33: Spectrophotometric data for the SRd variable SX Her and the peculiar red giant Z Sex (Cardelli & Howell, 1989). The flux is given in $\text{ergs cm}^{-2}\text{s}^{-1}\text{Å}^{-1}$.

Percy & Kolin (2000) used Hipparcos photometry to analyse and detect changes in the period of SRd stars. A parabolic shape of the (O-C) diagram of the star means a linear change in period. For SX Her, they found a period of 102.9 days (see Fig. 4.34) and a linear change in the period of 0.0175 days/year (see Fig. 4.35).

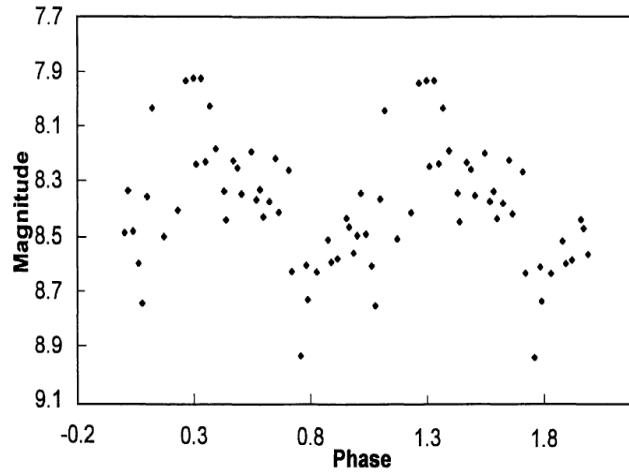


Figure 4.34: The phase curve of SX Her with a period of 102.9 days found by Percy & Kolin (2000).

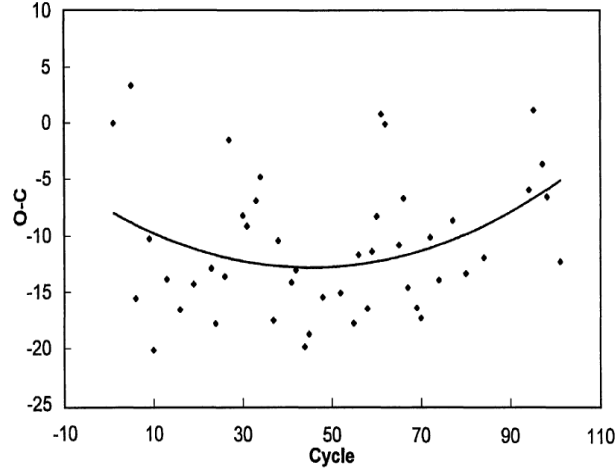


Figure 4.35: The (O-C) diagram for SX Her using the period mentioned above (Percy & Kolin, 2000).

The semiregularity of the light curves of certain stars is not fully understood (see Fig. 4.36), so Buchler et al. (2004) tried a different approach for an explanation by searching for low-dimensional chaos in the pulsation dynamics of these stars. If pulsation modes interact on a nonlinear basis, the result can be seen in the light curve as irregular pulsation.

An attempt to solve the problem of the semiregular light curve of SX Her with a three-dimensional reconstruction did fail. The pulsational dynamics of SX Her seem to be more complex than expected, for example with asymmetric bursts in the light curve. Buchler et al. (2004) suggest to use a higher dimensional phase space, probably $d=6$, to get satisfactory results.

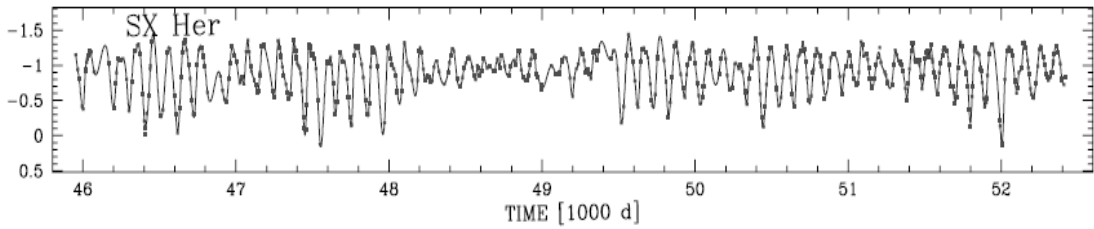


Figure 4.36: The observations (dots) and fits (lines) of the light curve of SX Her (Percy & Kolin, 2000). The data have been smoothed, and binned and averaged over 10 days.

4.7 89 Her

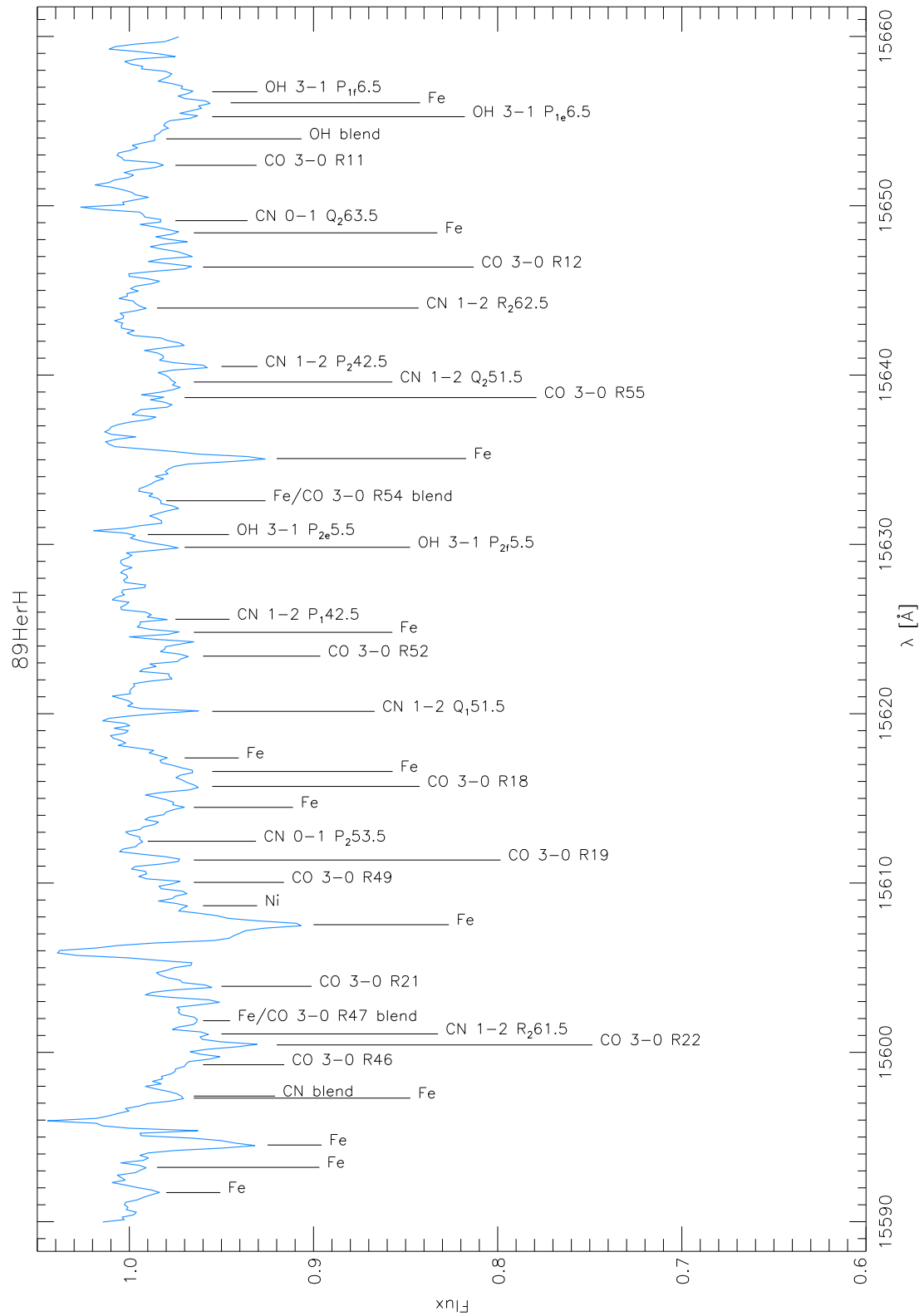


Figure 4.37: The spectrum of 89Herculis in the H-filter with identified and measured lines.

Wavelength [Å]	Atom/Molecule	EQW [mÅ]	Vacuum Pos.	Difference
15591.72	Fe	11.8	15592.52	0.80
15593.21	Fe	4.6	15594.31	1.10
15594.53	Fe	40.5	15595.75	1.22
15597.30	Fe	17.8	15598.01	0.71
15599.27	CO 3-0 R46	33.6	15600.21	0.94
15600.44	CO 3-0 R22	71.9	15601.61	1.17
15601.09	CN 1-2 R_2 61.5	36.0	15601.99	0.90
15603.90	CO 3-0 R21	36.4	15605.00	1.10
15607.54	Fe	122.0	15608.48	0.94
15608.66	Ni	15.3	15609.92	1.26
15610.04	CO 3-0 R49	11.4	15610.97	0.93
15611.36	CO 3-0 R19	16.4	15612.58	1.22
15612.47	CN 0-1 P_2 53.5	2.6	15613.47	1.00
15614.47	Fe	26.8	15615.40	0.93
15615.71	CO 3-0 R18	31.4	15616.76	1.05
15616.59	Fe	50.8	15617.89	1.30
15617.39	Fe	18.8	15618.36	0.97
15620.14	CN 1-2 Q_1 51.5	9.8	15621.33	1.19
15623.40	CO 3-0 R52	23.9	15624.21	0.81
15624.81	Fe	10.7	15625.92	1.11
15625.58	CN 1-2 P_1 42.5	5.7	15626.71	1.13
15629.83	OH 3-1 P_2 _f 5.5	16.0	15630.97	1.14
15630.58	OH 3-1 P_2 _e 5.5	1.1	15631.68	1.10
15635.07	Fe	59.3	15636.22	1.15
15638.67	CO 3-0 R55	5.6	15639.95	1.28
15639.59	CN 1-2 Q_2 51.5	32.8	15640.86	1.27
15640.51	CN 1-2 P_2 42.5	32.2	15641.80	1.29
15643.96	CN 1-2 R_2 62.5	2.8	15645.14	1.18
15646.38	CO 3-0 R12	17.3	15647.46	1.08
15648.40	Fe	33.7	15649.29	0.89
15649.12	CN 0-1 Q_2 63.5	6.6	15650.52	1.40
15652.39	CO 3-0 R11	9.2	15653.50	1.11
15655.26	OH 3-1 P_1 _e 6.5	29.2	15656.17	0.91
15656.08	Fe	40.9	15657.15	1.07
15656.73	OH 3-1 P_1 _f 6.5	42.9	15657.75	1.02

Table 4.8: The equivalent widths for the lines in Fig. 4.37 with the vacuum positions given by Hinkle et al. (1995). The mean difference between vacuum position and measured wavelength is 1.08 Å. The radial velocity derived from these measurements is -28.03 ± 3.04 km/s after heliocentric correction.

Analysis of the Spectrum

The spectrum of 89 Her (HR 6685) seems to be quite difficult to interpret, with no dominant feature like expected from the comparison stars. Some of the lines seem to be in emission, but it was difficult to fit a continuum through the spectrum in the first place, so it could probably be an effect of the data reduction as well. Neither CO nor OH lines are very prominent, in fact the metal lines seem to be the strongest in this part of the spectrum.

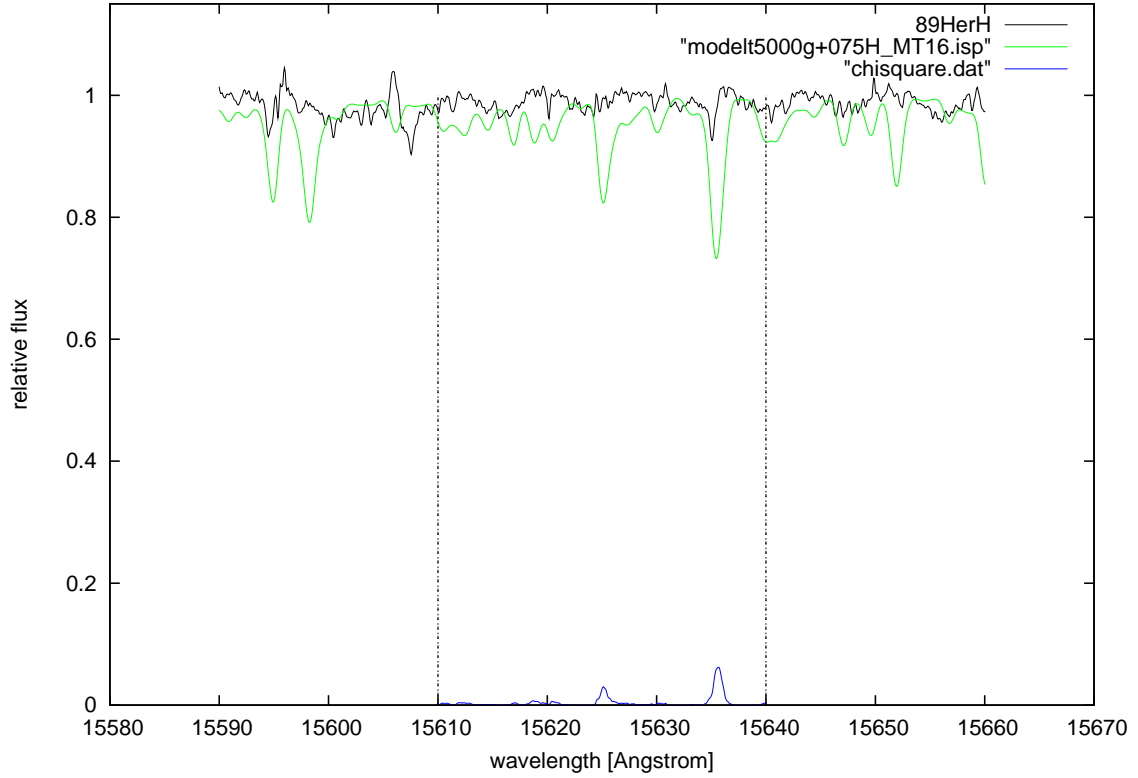


Figure 4.38: The star 89 Her overplotted by a MARCS model of 5000 K, $\log g=0.75$ and $\zeta=16$ km/s.

Literature

In the beginning 89 Her was expected to have a normal Population I abundance and therefore be a young supergiant (about 10^7 yr) that got thrown out of the galactic plane towards its current location in the halo (Searle et al., 1963). Additionally an infrared excess was observed (Gillett et al., 1970), that was interpreted as a circumstellar shell containing solid material that radiates in the infrared with temperatures of about 200 to 600 K. The stated binary nature of 89 Her (Arellano Ferro, 1984) was confirmed by Waters et al. (1993) with an orbital period of 288.4 days. The light variation of this star can be described by a semi-period of 63 days (Arellano-Ferro, 1985). Wilson (1953) derived a radial velocity of -28.5 km/s, which is comparative the measurement of -28.03 km/s derived in this thesis.

The theory of a young, Population I star was not supported by Fernie (1981), who suggested that this star was in fact a halo-type object and that it had to be older than expected. He also stated that the variations in light and colour are sometimes quite regular but there are times where the regularity is replaced by unexpected fluctuations.

Arellano-Ferro (1985) also observed 89 Her within a wavelength-range of 5300 to 6700 Å to analyse the changes in the H α profiles. He found a P-Cygni profile that lasted during the whole month of observation, with the blue-shifted absorption component being shifted at a velocity of about -30 km/s to the photosphere and the red-shifted emission component about 40 km/s.

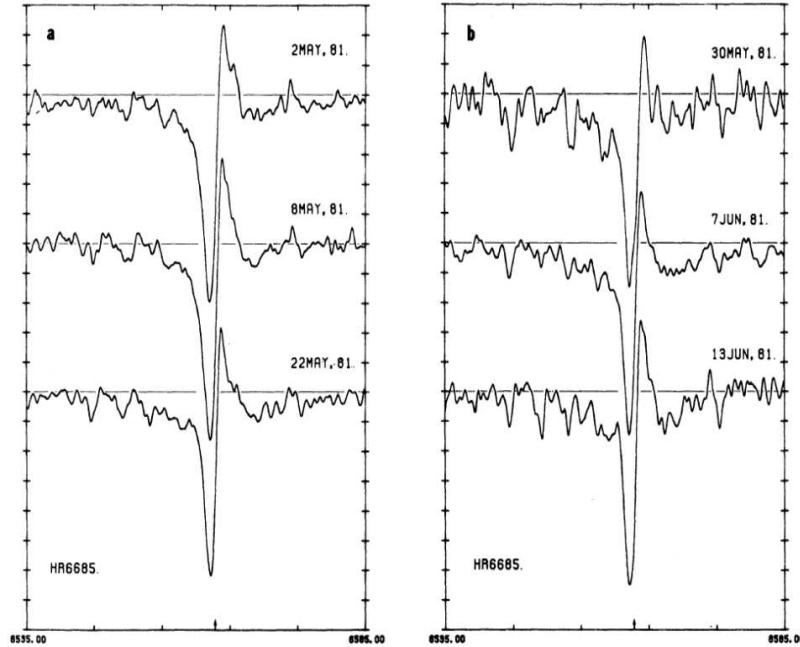


Figure 4.39: H α profile changes observed by Arellano-Ferro (1985).

Parthasarathy & Pottasch (1986) found the similarity of the light amplitude and the radial velocity variations between 89 Her and Cepheids, but 89 Her and other post-AGB candidates show a switching of pulsation modes which was not observed in Cepheid stars. The IRAS infrared spectrum of 89 Her shows the silicate emission feature at $10 \mu\text{m}$, with a maximum flux at $12 \mu\text{m}$. The parameters found by

Parthasarathy & Pottasch (1986) for 89 Her include the temperature of the star (about 7000 K), the dust temperature (500 K), an estimated radius of $130 R_{\odot}$ and the mass of the emitting dust being $M_d = 2.0 \times 10^{-7} M_{\odot}$. This amount of dust is rather small, so one may assume that the mass loss phase of this star has just begun, or that the ejected matter has not jet cooled down enough to form dust.

In a search for stars within the pre-planetary nebula phase Likkell et al. (1987) also observed 89 Her and detected CO emission that points to a cool circumstellar envelope. 89 Her was one of the warmest objects discussed in their paper and it showed silicate emission at $10 \mu\text{m}$. Likkell et al. (1987) confirmed the theory of previous observers like Parthasarathy & Pottasch (1986), that this star might be a post-AGB star.

89 Her was later counted to a group of stars called UU Her, yellow semi-regular variables which are located at high galactic latitudes, showing F type spectra similar to those of supergiant with strong FeII and SiII lines. An infrared excess and a P Cygni profile with emission component and a line profile variation of $H \alpha$ was observed by Giridhar (1988) (see Fig. 4.40), who suggested an extended atmosphere or a circumstellar shell due to their observations.

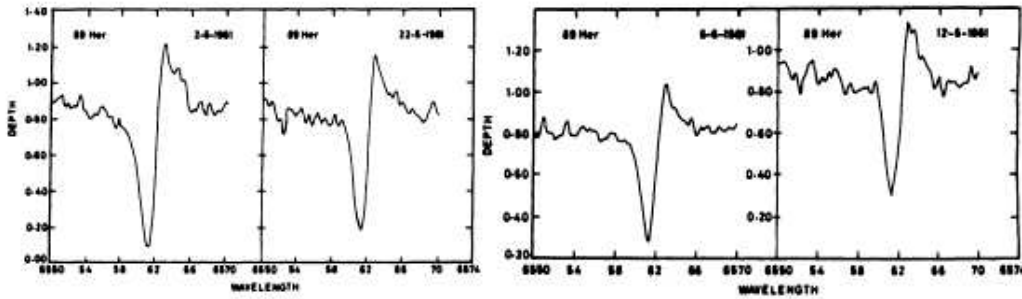


Figure 4.40: $H \alpha$ line profile variation of 89 Her (Giridhar, 1988).

Giridhar (1988) derived the following atmospheric parameters for 89 Her: $T_{\text{eff}} = 6000 \text{ K}$, $\log g = 0.5$, $\xi = 4.5 \text{ km/s}$. The abundances of Si, S, Ca and Fe are almost solar, while Al seems overabundant.

Another analysis of this star was done by Luck et al. (1990) with slightly different results: The photometric analysis gave $T_{\text{eff}} = 6400 \text{ K}$ and $\log g = 1.2$ while the spectroscopic parameters are $T_{\text{eff}} = 6500 \text{ to } 6600 \text{ K}$, $\log g = 0.3 \text{ to } 0.8$, $\xi = 4.3 \text{ km/s}$, $\zeta = 12 \text{ km/s}$. 89 Her seems to be metal-poor, there is no evidence for s-process enhancement in the spectra analysed by Luck et al. (1990). Heavy elements, including elements from Y to Eu, are not enriched.

Trams et al. (1991) files 89 Her as a suspected post-AGB star in their research for post-AGB candidates. 89 Her is one of the stars they observed that showed evidence for hot dust ($T \sim 1000 \text{ K}$) as well as cool dust ($T \sim 200 \text{ K}$) in the spectrum and has a Population II abundance. The estimated mass loss rate is about $10^{-7} \text{ to } 10^{-8} M_{\odot}/\text{yr}$ (Trams et al., 1989).

The binary nature of 89 Her led Waters et al. (1993) to another explanation of the features observed in the spectra than the object being a post-AGB star. The authors detected emission lines from Cr, Ti and Fe that were observed before by other astronomers (see Sargent & Osmer (1969), and Climenhaga et al. (1987)) and suggested that they are formed in a circum-system disc. They compared a Kurucz (1979) model to their observational UV and optical data and found the best fit at $T_{\text{eff}} = 6500$ K and $\log g = 1.0$ without any extinction ($E(B-V) = 0$) (see Fig. 4.41). They also estimated a stellar radius R_* of 43 solar radii for an evolved star like 89 Her with a luminosity of presumably $3000 L_{\odot}$.

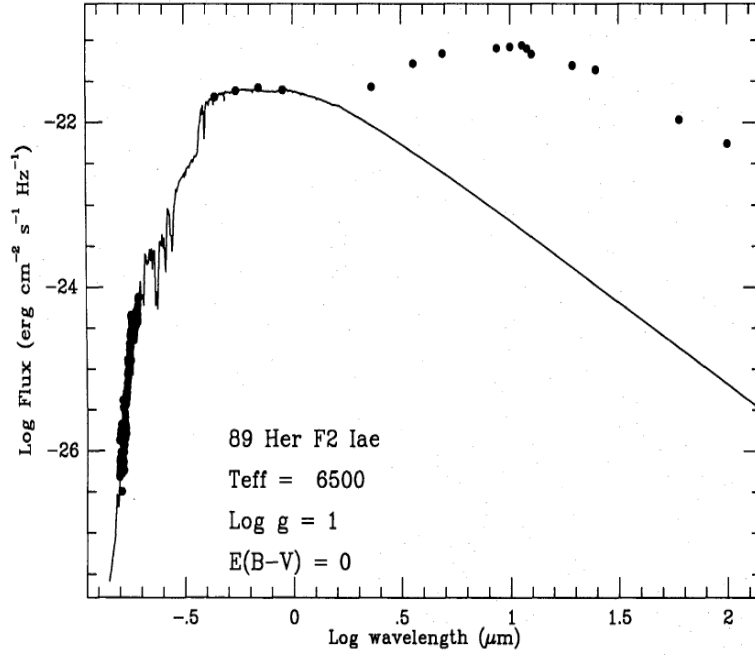


Figure 4.41: Comparison of observational data with a Kurucz (1979) model gave a best fit at $T_{\text{eff}} = 6500$ K and $\log g = 1.0$ (Waters et al., 1993).

An optically thin dust model was fitted to the IR excess of 89 Her to estimate the properties of the dust surrounding the star. The best fit was obtained with a model of a spherically symmetric dust envelope with an inner radius r_i of $40 R_*$ and an outer radius r_o of $5000 R_*$.

With a temperature of about 960 K at r_i (Waters et al., 1993), the dust must have been ejected from the star recently. Using two different methods (velocity of the outflow in $H\alpha$ $v_{H\alpha} = 150$ km/s, and expansion velocity derived from CO observations $v_{CO} = 4.6$ km/s), the authors tried to estimate the travel time of the dust from the ejection until it reaches the inner radius of the shell, with the results being 92 days from the first method and 8.2 years from the second. In both cases the timeframes are very short compared to the estimated evolutionary timescale of a post-AGB star with 500 to 5000 years, making it impossible for the shell to be made of material that was blown away during the AGB mass loss phase.

Alcolea & Bujarrabal (1991) were facing the same problem and tried to solve it with two shells instead of just one. The first outer shell was produced during a phase of higher mass loss in the past and the second inner shell represents a recent or ongoing

mass loss that is significantly smaller.

The timescales calculated for the formation of the observed outer shells may be related to the time of departure from the AGB. In the case of 89 Her, the formation started about 50 years ago, while the PPN Red Rectangle and M2-9 left the AGB about 130 years and 690 years ago, respectively (Alcolea & Bujarrabal, 1991). The very short timescale for 89 Her seems to indicate a faster evolution of this object compared to the expected evolutionary timescale of RV Tauri stars. This rapid evolution could be triggered by a higher ongoing mass-loss.

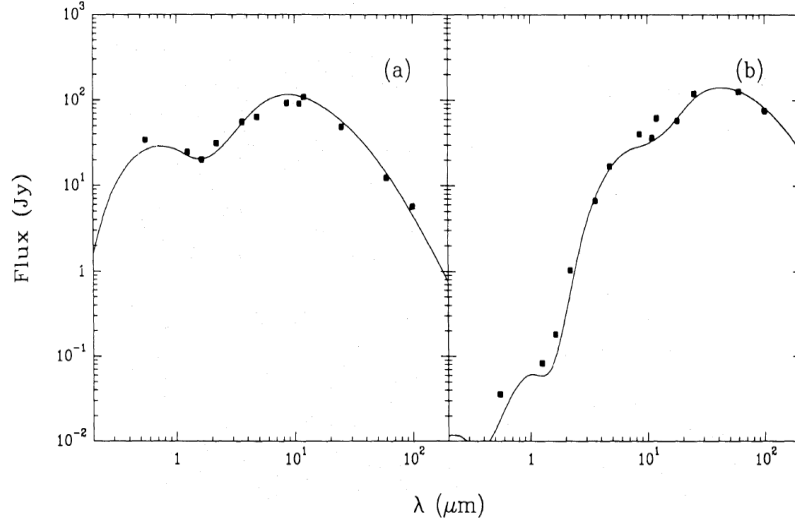


Figure 4.42: Comparison of a two-shell model (solid line) with observational data (dots) of (a) the semi-regular variable 89 Her and (b) the PPN M2-9 (Alcolea & Bujarrabal, 1991).

A specialty of the spectral lines observed are narrow CO lines (Likkell et al. (1987) and Alcolea et al. (1993), see Fig. 4.43), indicating a wind velocity of just 4 km/s if one assumes a spherically symmetric shell. This expansion velocity is in agreement with Alcolea & Bujarrabal (1991), who used this low expansion velocity as a means to identify low-mass protoplanetary nebulae like 89 Her.

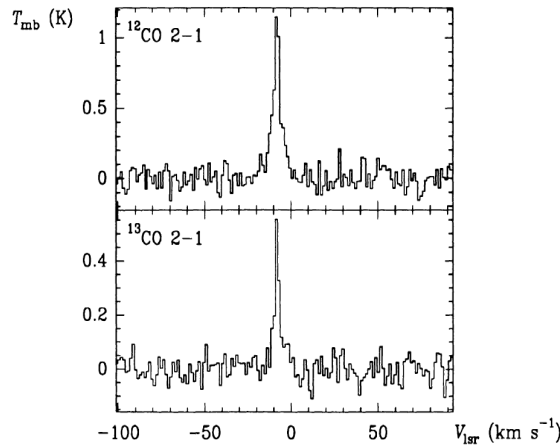


Figure 4.43: The narrow J=2-1 lines of ^{12}CO and ^{13}CO (Alcolea et al., 1993).

The fact that there seems to be low to no extinction towards 89 Her led Waters et al. (1993) to a different model for this binary system: a dust ring instead of a spherically symmetrical shell which is not positioned between the primary star (89 Her) and the line of sight. The geometric model (see Fig. 4.44) is composed of a circum-system disc around a wide binary system and an inclination angle under 90 degrees, no line broadening due to the expansion velocity of the AGB wind would be observed.

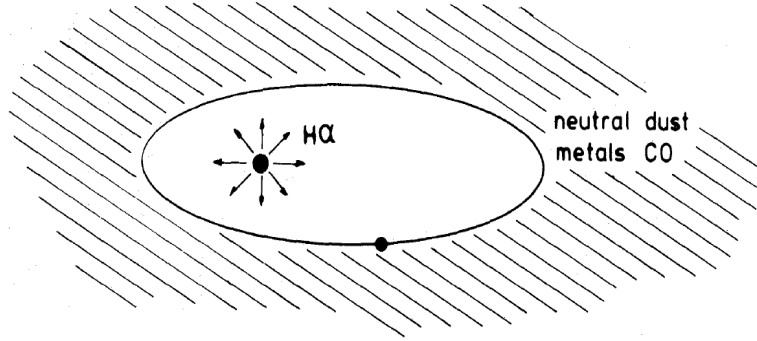


Figure 4.44: Model of a circum-system disc of warm dust, neutral metals and CO around a wide binary system (Waters et al., 1993).

In this model, the central star (89 Her) ejects mass in a spherically symmetric shell which can expand without hindrance at the polar regions while in the orbital plane it will reach the disc and be slowed down. The emission lines observed might originate from the collision of this wind with the disc. The star is rather close to the inner radius of the disc, which causes the warm dust observed, but giving no indication of the evolutionary stage of the star (Waters et al., 1993).

It is well known that PNe and PPNe often show axisymmetric shapes caused by the interaction of the post-AGB outflow with the surrounding matter of the AGB wind. Based upon this knowledge, Bujarrabal et al. (2007) used high-resolution interferometry CO observations to answer the question of the shape of the nebula around 89 Her. The CO maps give information about the structure of the hot dust that causes the near-IR excess as well as the cool dust, with large grains that are responsible for the far-IR flux.

The observations (see Fig. 4.45) showed two different components, a compact clump in the center that seems to be a rotating Keplerian disk, and an extended and expanding structure that might have the shape of an hour-glass with a slight inclination towards the observer (Bujarrabal et al., 2007).

Based upon Hipparcos, the distance from the sun to the binary 89 Her is about 1 kpc, leading to a calculated total size of $\sim 1.5 \times 10^{17}$ cm of the extended component and less than $\sim 5 \times 10^{15}$ cm of the central compact component. Furthermore the masses and expansion velocities were derived for both components: $\sim 3 \times 10^{-3} M_{\odot}$ and ~ 7 km/s for the extended structure, and $\sim 10^{-2} M_{\odot}$ and ~ 5 km/s for the central clump.

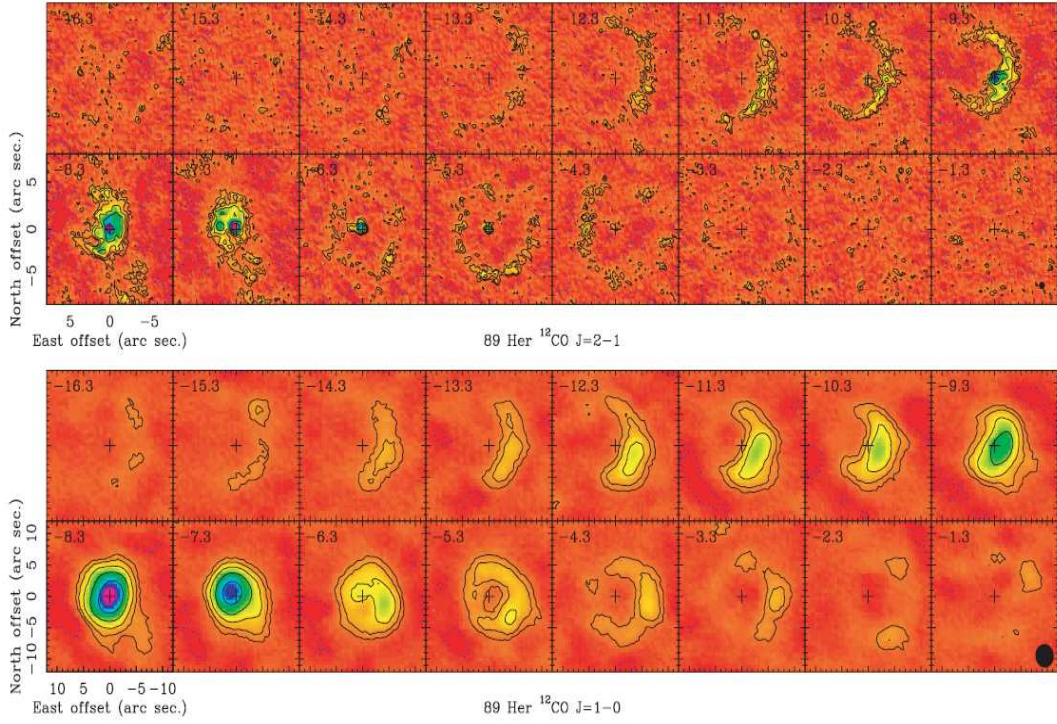


Figure 4.45: ^{12}CO J=2-1 (upper panels) and J=1-0 (lower panels) channel maps observed by Bujarrabal et al. (2007). The contours are separated by a factor of 2, the first contours being 15 and 30 mJy respectively. The numbers in the upper left corner of each panel gives the LSR velocity in km/s for the center. The beam half-intensity sizes is indicated as black ellipses in the last panels.

Bujarrabal et al. (2007) tried to reproduce the observational data of the expanding hour-glass-like structure with a rather simple model with thin walls and an inclination angle of the symmetry axis of the nebula of $\sim 15^\circ$ towards the line of sight (see Fig. 4.47). The calculated maps (see Fig. 4.46) reproduce the observations quite well.

Based upon the model assumptions, one can estimate the masses of the binary stars: $\sim 0.6 M_\odot$ for the primary and $\sim 0.35 M_\odot$ for the companion, that is expected to be a low-mass main sequence dwarf. The calculated semi-major axis of this model is 0.31 AU, meaning that the dusty disk is circumbinary.

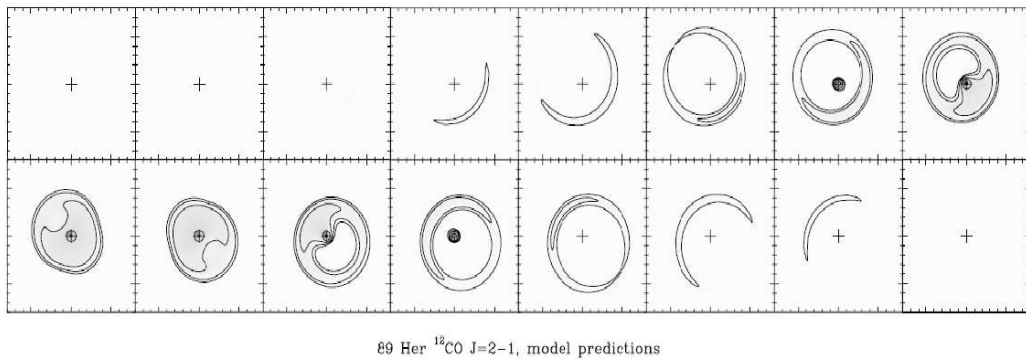


Figure 4.46: The predicted maps for the ^{12}CO J=2-1 line emission, with the same units and contours as used in Fig. 4.45 (Bujarrabal et al., 2007).

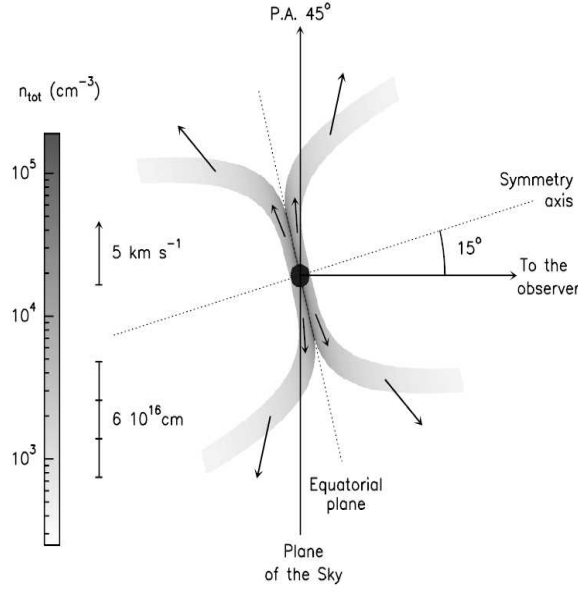


Figure 4.47: The model used by Bujarrabal et al. (2007) to calculate the nebula around 89 Her. One can see the geometric design as well as the density and velocity distribution for the extended component, while only limits were used for the compact central component (black circle).

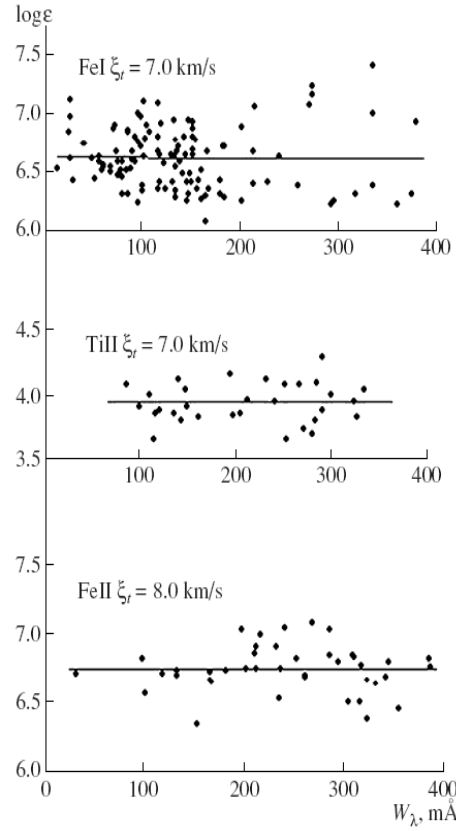


Figure 4.48: Equivalent widths (W_λ) against elemental abundances of iron and titanium derived from measured FeI, TiII and FeII lines for $\xi_t=7$ km/s (FeI and TiII) and $\xi_t=8$ km/s (FeII) (Khalilov et al., 2008).

A study of the atmospheric parameters as well as the elemental abundances of 89 Her was done by Khalilov et al. (2008), who derived an effective temperature of $T_{\text{eff}} = 6300 \pm 150$ K and gravity of $\log g = 0.5 \pm 0.2$.

To determine the microturbulence velocity ξ_t , the authors used lines that are observable in great number over a wide spectral range, so they chose the lines of neutral and ionized iron (FeI and FeII), and ionized titanium (TiII). The results were $\xi_t = 7.0$ km/s for FeI and TiII, and $\xi_t = 8.0$ km/s for FeII (see Fig. 4.48).

A model atmosphere was used with $T_{\text{eff}} = 6300$ K, $\log g = 0.5$ and $\xi_t = 7.5$ km/s (Khalilov et al., 2008) to derive the abundances of several elements and compare them to the solar values.

As can be seen in Fig. 4.49, the computed abundances of 89 Her are depleted relative to the solar composition, with the exception of Na, which is slightly overabundant. A majority of the elements (Ca, Sc, Mn, Fe, Co, Zr, Ba, La, Ce, Nd, Sm, and Gd) is underabundant compared to their solar values by about $\Delta \log \epsilon(\text{El}) = -1.0$ dex.

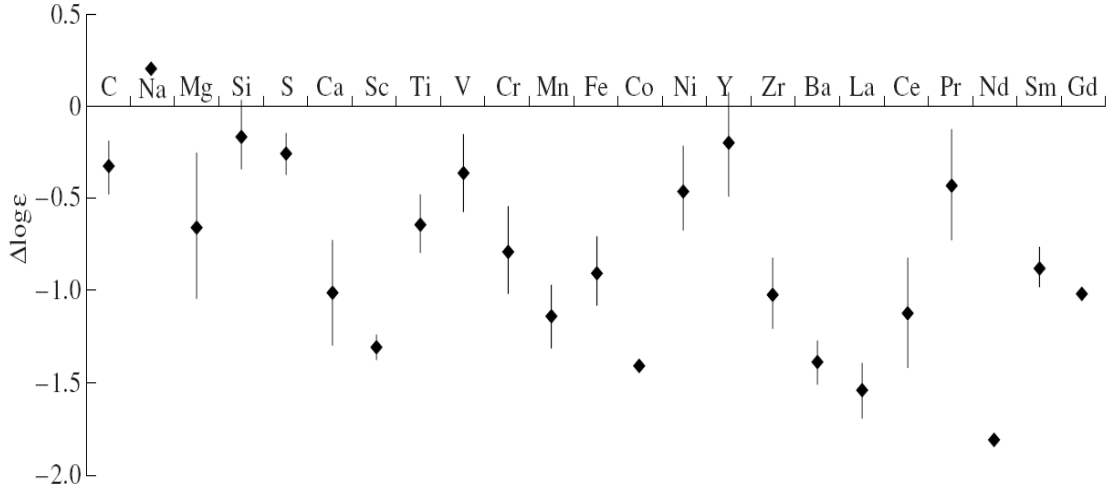


Figure 4.49: Elemental abundances of 89 Her compared to solar composition (Khalilov et al., 2008).

4.8 CX Lac

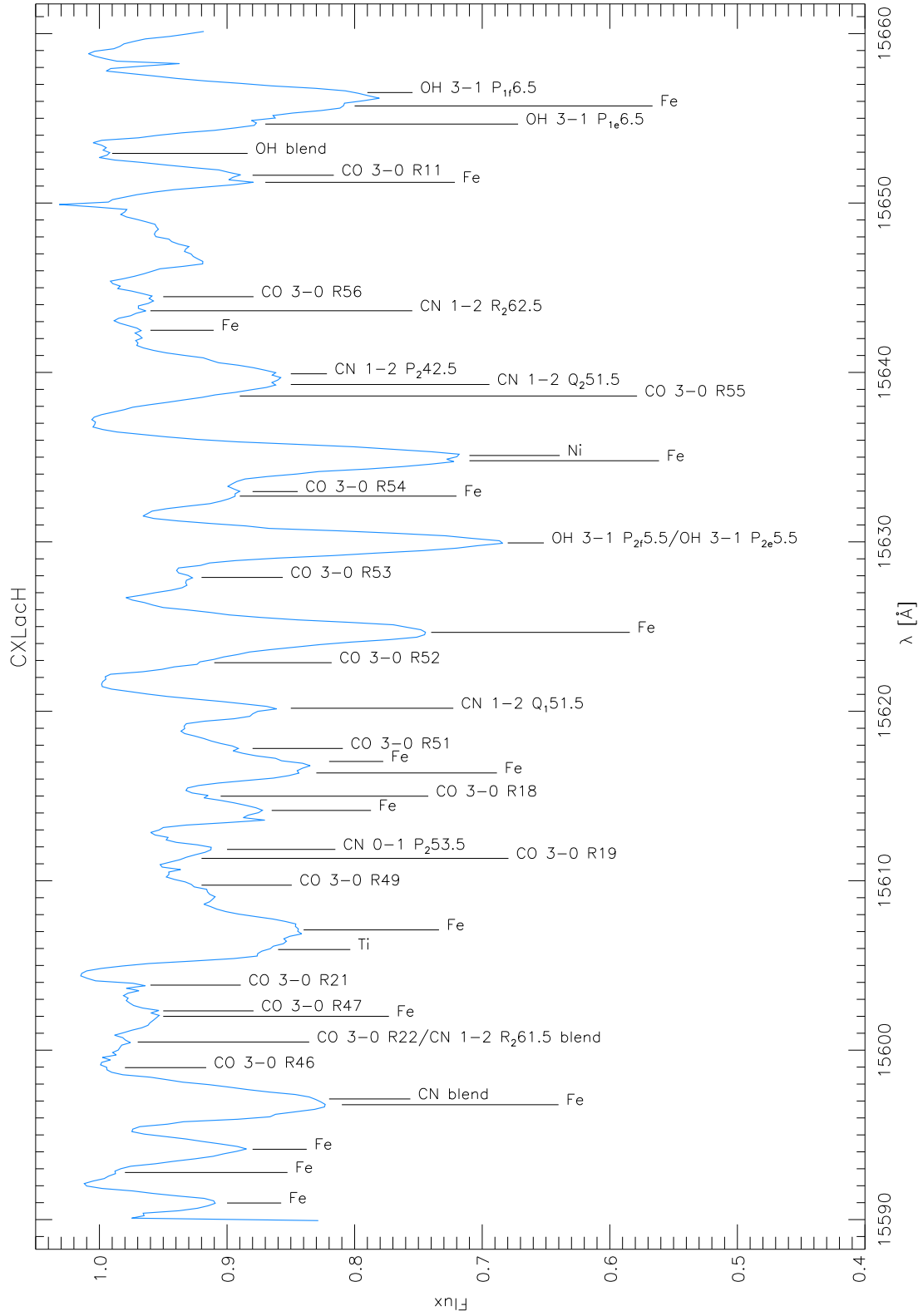


Figure 4.50: The spectrum of CX Lac in the H-filter with identified and measured lines.

Wavelength [Å]	Atom/Molecule	EQW [mÅ]	Vacuum Pos.	Difference
15590.98	Fe	119.6	15592.52	1.54
15592.78	Fe	9.2	15594.31	1.53
15594.15	Fe	246.3	15595.75	1.60
15596.78	Fe	359.9	15598.01	1.23
15598.97	CO 3-0 R46	1.7	15600.21	1.24
15602.00	Fe	50.4	15603.13	1.13
15602.32	CO 3-0 R47	41.9	15603.52	1.20
15603.84	CO 3-0 R21	11.0	15605.00	1.16
15605.94	Ti	206.3	15607.11	1.17
15607.10	Fe	467.2	15608.48	1.38
15609.74	CO 3-0 R49	98.1	15610.97	1.23
15611.32	CO 3-0 R19	114.0	15612.58	1.26
15611.85	CN 0-1 P_2 53.5	114.4	15613.47	1.62
15614.15	Fe	242.7	15615.40	1.25
15614.99	CO 3-0 R18	122.1	15616.76	1.77
15616.36	Fe	345.0	15617.89	1.53
15617.04	Fe	372.6	15618.36	1.32
15617.81	CO 3-0 R51	260.7	15619.52	1.71
15620.18	CN 1-2 Q_1 51.5	241.5	15621.33	1.15
15622.87	CO 3-0 R52	112.0	15624.21	1.34
15624.66	Fe	853.4	15625.92	1.26
15627.90	CO 3-0 R53	131.9	15629.18	1.28
15632.70	Fe	216.4	15633.89	1.19
15632.97	CO 3-0 R54	264.5	15634.42	1.45
15634.79	Fe	699.9	15636.22	1.43
15635.10	Ni	423.5	15636.89	1.79
15638.61	CO 3-0 R55	117.3	15639.95	1.34
15639.29	CN 1-2 Q_2 51.5	352.4	15640.86	1.57
15639.92	CN 1-2 P_2 42.5	366.8	15641.80	1.88
15642.49	Fe	43.8	15643.75	1.26
15643.64	CN 1-2 R_2 62.5	20.8	15645.14	1.50
15644.47	CO 3-0 R56	52.3	15645.76	1.29
15651.22	Fe	156.2	15652.79	1.57
15651.64	CO 3-0 R11	192.9	15653.50	1.86
15654.66	OH 3-1 P_{1e} 6.5	193.5	15656.17	1.51
15655.73	Fe	394.8	15657.15	1.42
15656.52	OH 3-1 P_{1f} 6.5	362.3	15657.75	1.23

Table 4.9: The equivalent widths for the lines in Fig. 4.50 with the vacuum positions given by Hinkle et al. (1995). The mean difference between vacuum position and measured wavelength is 1.41 Å. The radial velocity derived from these measurements is -9.45 ± 4.01 km/s after heliocentric correction.

Analysis of the Spectrum

The lines of CX Lac in the H-filter are broadened and a lot of them are blended with other lines, which made the measurements a bit tricky. Metal lines are the strongest features, CN and OH lines seem to be weaker.

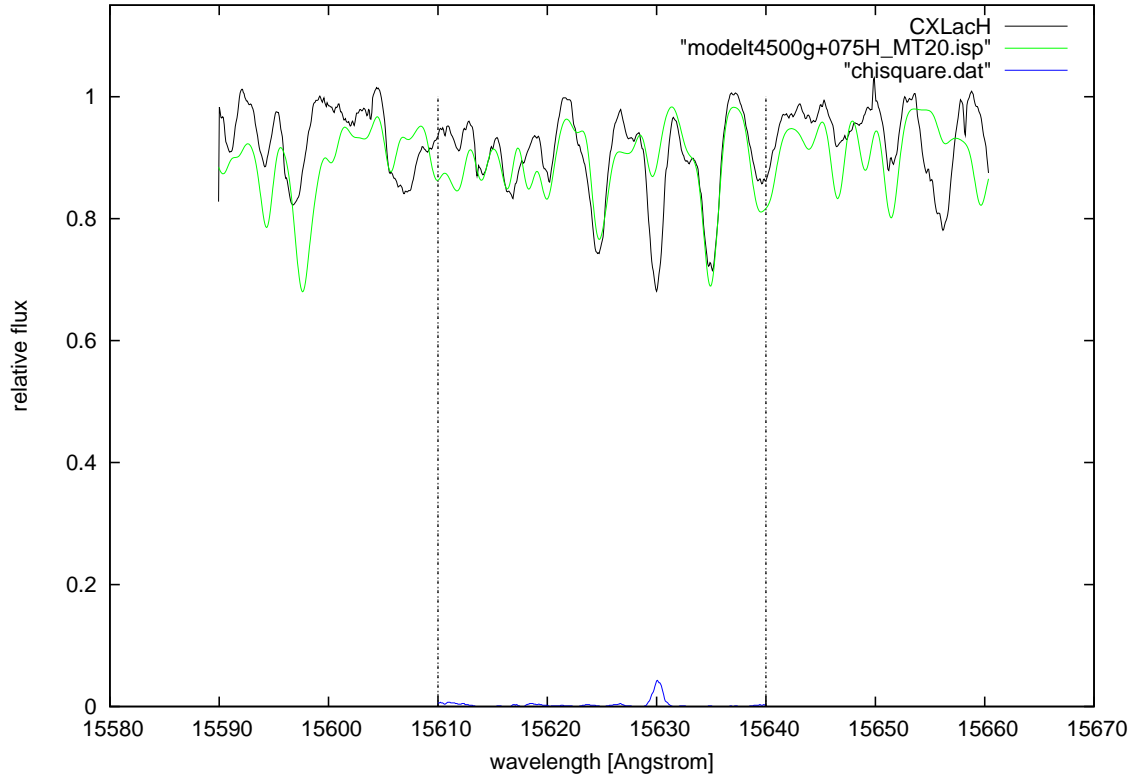


Figure 4.51: The star CX Lac overplotted by a MARCS model of 4500 K, $\log g=0.75$ and $\zeta=20$ km/s.

Literature

Unfortunately, only a few things about CX Lac can be found in the literature. The first one to mention this star was Morgenroth (1939), who stated an irregular lightcurve.

Feast et al. (1972) observed 120 M type SR variables, including CX Lac and SX Lac, to find out more about the kinematics of semiregular variables in the solar neighbourhood. The measurements were done with absorption lines as well as emission lines, whenever possible. In the case of CX Lac and SX Lac, no emission lines were present, so only the absorption lines were measured. The authors were not able to confirm the presence of TiO bands with certainty.

The values of the radial velocity found by Feast et al. (1972) for CX Lac were between +7 km/s to -17 km/s with a mean value of -4 km/s. The radial velocity of -9.45 km/s measured by me is a bit lower than the mean value but does fit quite good into the range given by Feast et al. (1972).

A paper called *Accurate Positions for 38 Variables in a $5^\circ \times 5^\circ$ Field around BL Lac* (Shokin & Samus, 1997) confirmed the variability of CX Lac.

4.9 SX Lac

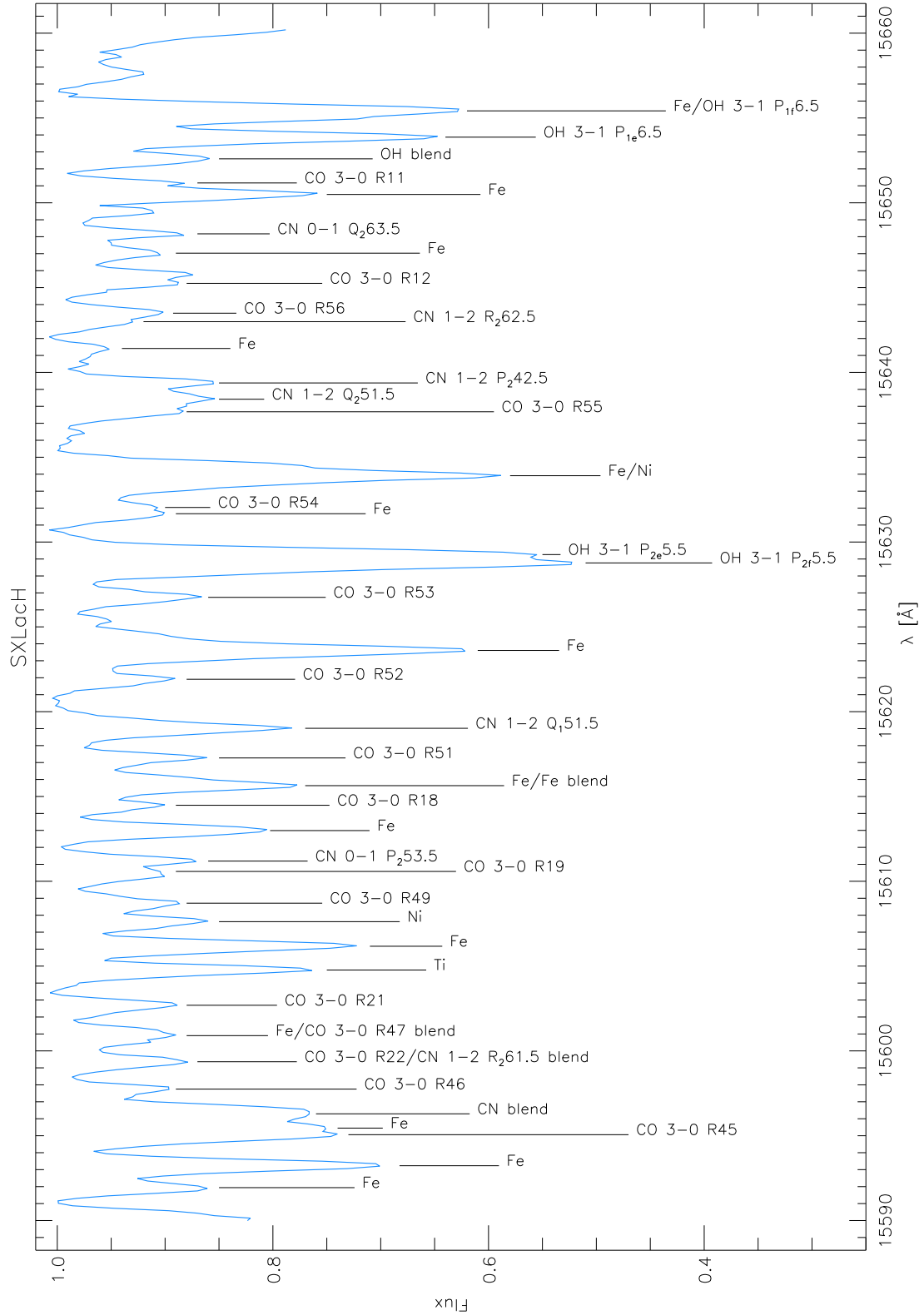


Figure 4.52: The spectrum of SX Lacertae in the H-filter with identified and measured lines.

Wavelength [Å]	Atom/Molecule	EQW [mÅ]	Vacuum Pos.	Difference
15591.94	Fe	122.6	15594.31	2.37
15593.23	Fe	319.2	15595.75	2.52
15595.06	CO 3-0 R45	331.4	15597.17	2.11
15595.45	Fe	726.0	15598.01	2.56
15597.75	CO 3-0 R46	75.4	15600.21	2.46
15602.69	CO 3-0 R21	121.0	15605.00	2.31
15604.77	Ti	224.4	15607.11	2.34
15606.17	Fe	294.4	15608.48	2.31
15607.62	Ni	195.4	15609.92	2.30
15608.71	CO 3-0 R49	111.4	15610.97	2.26
15610.58	CO 3-0 R19	120.1	15612.58	2.00
15611.19	CN 0-1 P_2 53.5	120.5	15613.47	2.28
15612.99	Fe	173.2	15615.40	2.41
15614.48	CO 3-0 R18	115.3	15616.76	2.28
15617.27	CO 3-0 R51	152.5	15619.52	2.25
15619.02	CN 1-2 Q_1 51.5	277.8	15621.33	2.31
15621.91	CO 3-0 R52	126.4	15624.21	2.30
15623.61	Fe	541.9	15625.92	2.31
15626.74	CO 3-0 R53	191.2	15629.18	2.44
15628.77	OH 3-1 P_{2f} 5.5	672.4	15630.97	2.20
15629.26	OH 3-1 P_{2e} 5.5	398.7	15631.68	2.42
15631.67	Fe	97.5	15633.89	2.22
15632.04	CO 3-0 R54	123.6	15634.42	2.38
15637.68	CO 3-0 R55	139.7	15639.95	2.27
15638.42	CN 1-2 Q_2 51.5	205.1	15640.86	2.44
15639.38	CN 1-2 P_2 42.5	120.9	15641.80	2.42
15641.41	Fe	54.5	15643.75	2.34
15642.99	CN 1-2 R_2 62.5	81.9	15645.14	2.15
15643.49	CO 3-0 R56	87.1	15645.76	2.27
15645.25	CO 3-0 R12	81.5	15647.46	2.21
15647.03	Fe	143.7	15649.29	2.26
15648.17	CN 0-1 Q_2 63.5	96.0	15650.52	2.35
15650.49	Fe	209.1	15652.79	2.30
15651.17	CO 3-0 R11	81.0	15653.50	2.33
15653.87	OH 3-1 P_{1e} 6.5	420.9	15656.17	2.30

Table 4.10: The equivalent widths for the lines in Fig.4.52 with the vacuum positions given by Hinkle et al. (1995). The mean difference between vacuum position and measured wavelength is 2.31 Å. The radial velocity derived from these measurements is -22.58 ± 2.09 km/s after heliocentric correction.

Analysis of the Spectrum

The spectrum of SX Lac was very similar to the comparison spectra I used of δ Oph and 9 Her. The two OH lines at approximately 15629 Å are the strongest features, followed by atomic lines. I was not able to find a model that could fit the strength of the OH lines. Even the cool model with 4000 K did not reach down to the center of the absorption lines, while other lines were too strong compared to the observations. Therefore, I chose a model with a higher temperature, to fit the CO lines better without considering the OH lines too much.

The shapes of the lines are not broadened and are therefore relatively easy to measure, because there are not too many blends in this spectrum. CN appears to be normally abundant compared to the two comparison stars.

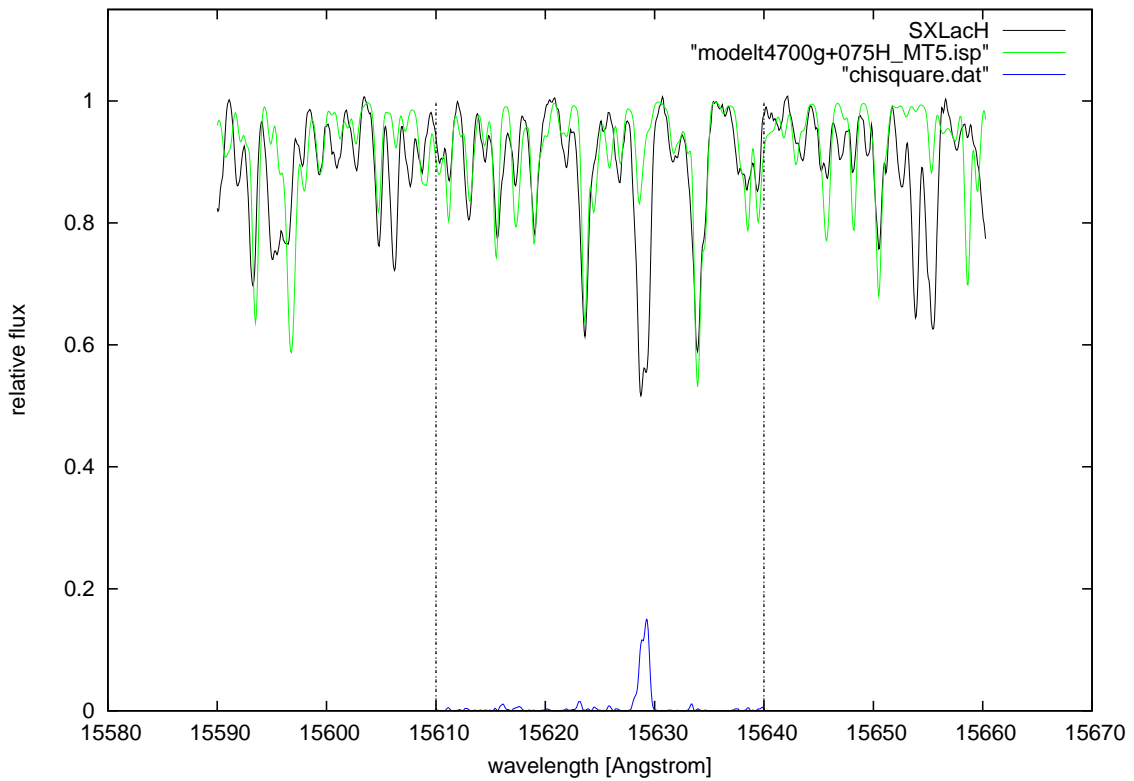


Figure 4.53: The star SX Lac overplotted by a MARCS model of 4700 K, $\log g=0.75$ and $\zeta=5$ km/s.

Literature

As mentioned for the star CX Lac, the SR variable SX Lac was also included in the work of Feast et al. (1972). In this case as well as in the case of CX Lac, the TiO bands could not be identified with certainty.

The spectrum of the star did not show any emission lines, so Feast et al. (1972) did only use absorption lines for radial velocity measurements. The values found were between -25 km/s to -12 km/s with a resulting mean value of about -18 km/s. The radial velocity of -22.58 km/s published in this thesis does fit well into the boundaries given by Feast et al. (1972).

Percy & Kolin (2000) used Hipparcos photometry to determine the period of the SRd star SX Lac to be 197 days. That result is in agreement with the stated *GCVS* (Samus et al., 1997) period of about 190 days.

In the *Pulkovo compilation of radial velocities for 35495 stars in a common system* (Gontcharov, 2006), SX Lac was listed with a mean radial velocity of about -18.0 km/s.

4.10 TT Oph

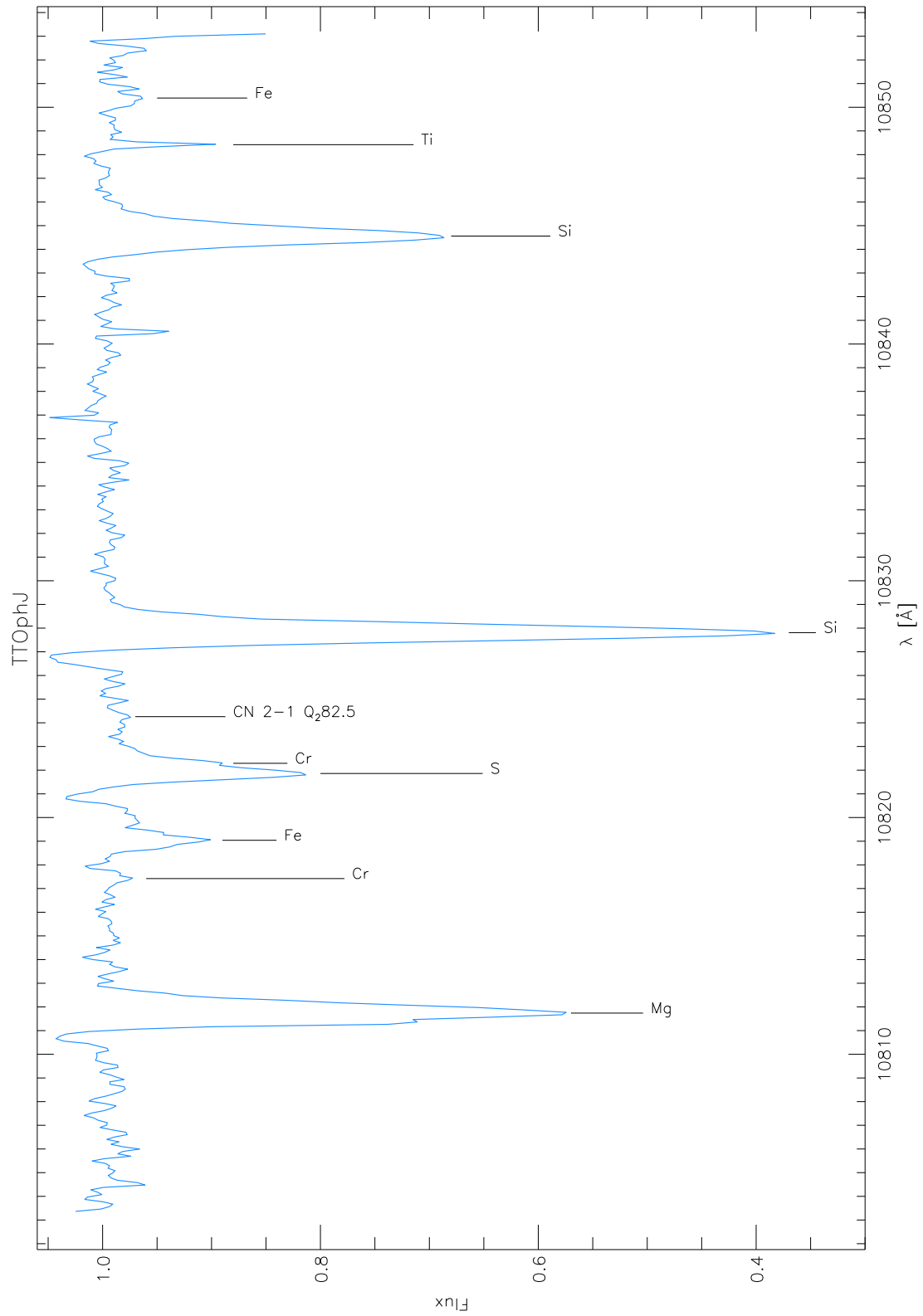


Figure 4.54: The spectrum of TT Ophiuchi in the J-filter with identified and measured lines.

Wavelength [Å]	Atom/Molecule	EQW [mÅ]	Vacuum Pos.	Difference
10811.74	Mg	383.4	10814.05	2.31
10817.42	Cr	13.5	10819.86	2.44
10819.04	Fe	73.6	10821.26	2.22
10821.86	S	120.9	10824.17	2.31
10822.29	Cr	87.6	10824.58	2.29
10824.26	CN 2-1 Q_2	15.4	10826.84	2.58
10827.81	Si	497.2	10830.06	2.25
10844.56	Si	290.4	10846.82	2.26
10848.42	Ti	21.6	10850.61	2.19
10850.39	Fe	25.4	10852.43	2.04

Table 4.11: The equivalent widths for the lines in Fig.4.54 with the vacuum positions given by Hinkle et al. (1995). The mean difference between vacuum position and measured wavelength is 2.29 Å. The radial velocity derived from these measurements is -36.81 ± 3.79 km/s after heliocentric correction.

Analysis of the Spectrum

The spectrum of TT Oph in the J-filter shows strong Mg, Si and Ti lines. The Fe lines are comparable to those of the standard stars used for line identification, but the Cr lines are weaker, and I was not able to identify the expected Ca lines as well as Na. The S and Cr line at 10821.86 Å and 10822.29 Å, respectively, are overestimated in the model spectrum.

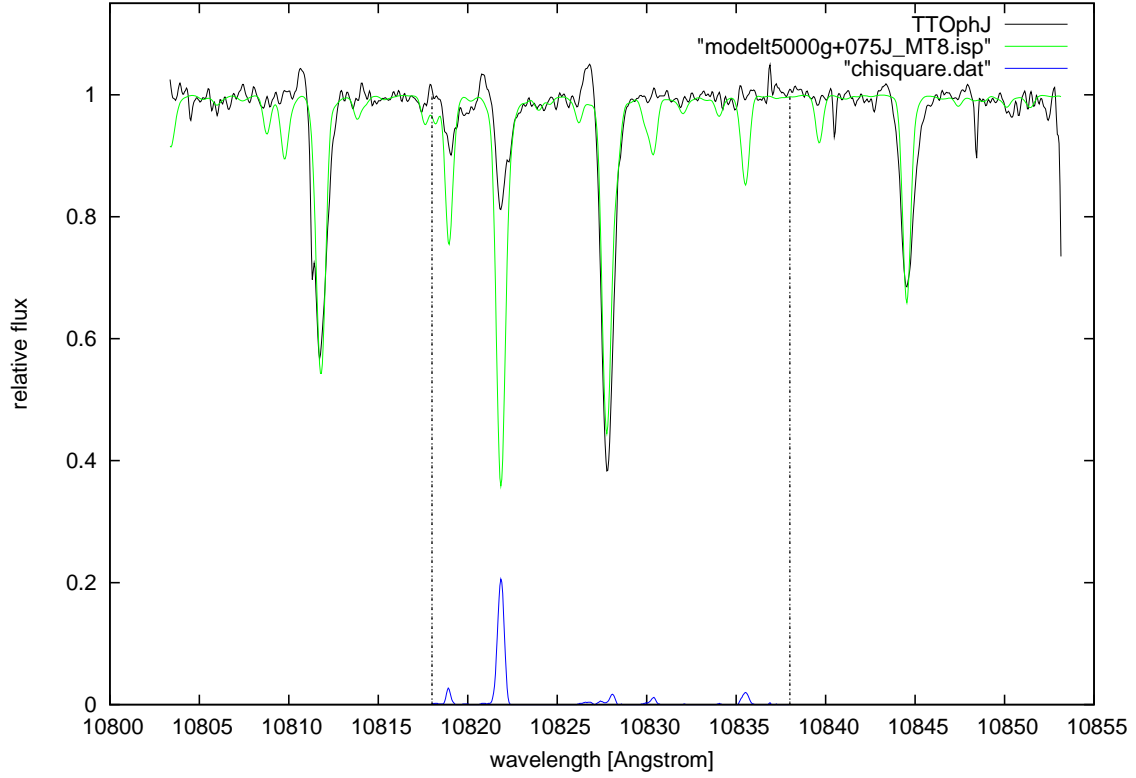


Figure 4.55: The star TT Oph overplotted by a MARCS model of 5000 K, $\log g=0.75$ and $\zeta=8$ km/s.

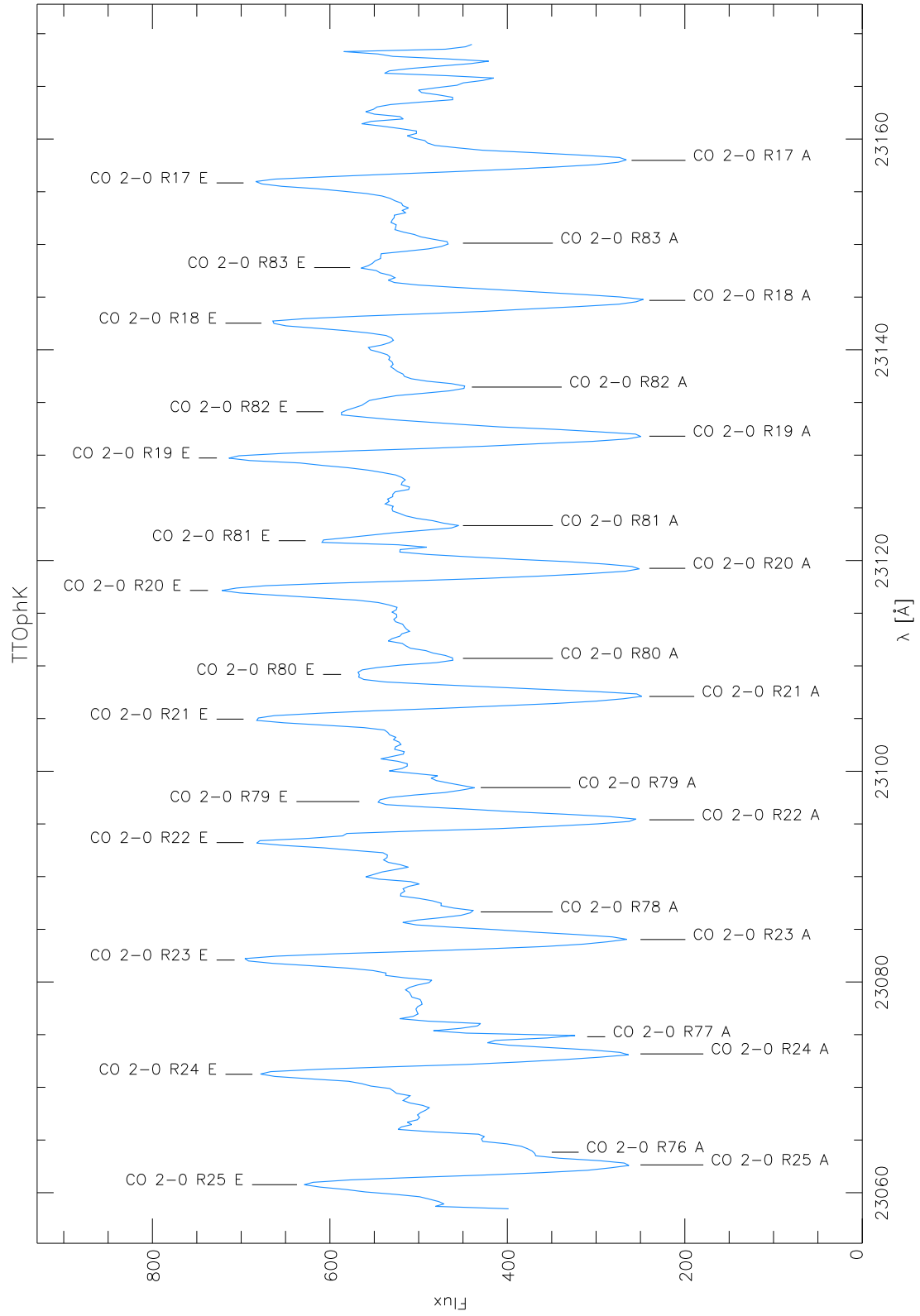


Figure 4.56: The spectrum of TT Ophiuchi in the K-filter with identified and measured lines.

Wavelength [Å]	Atom/Molecule	EQW [mÅ]	Vacuum Pos.	Difference
23060.76	CO 2-0 R25 E	-216.4	23067.89	7.13
23062.64	CO 2-0 R25 A	905.5	23067.89	5.25
23063.84	CO 2-0 R76 A	851.8	23069.24	5.40
23071.24	CO 2-0 R24 E	-338.3	23078.41	7.17
23073.17	CO 2-0 R24 A	833.3	23078.41	5.24
23074.80	CO 2-0 R77 A	347.5	23080.18	5.38
23082.08	CO 2-0 R23 E	-425.3	23089.34	7.26
23084.03	CO 2-0 R23 A	839.0	23089.34	5.31
23086.65	CO 2-0 R78 A	211.0	23091.57	4.92
23093.23	CO 2-0 R22 E	-493.4	23100.67	7.44
23095.39	CO 2-0 R22 A	805.7	23100.67	5.28
23097.12	CO 2-0 R79 E	- 33.9	23103.40	6.28
23098.45	CO 2-0 R79 A	186.2	23103.40	4.95
23104.95	CO 2-0 R21 E	-388.6	23112.40	7.45
23107.10	CO 2-0 R21 A	946.7	23112.40	5.30
23109.19	CO 2-0 R80 E	-125.9	23115.67	6.48
23110.71	CO 2-0 R80 A	172.6	23115.67	4.96
23117.16	CO 2-0 R20 E	-544.0	23124.54	7.38
23119.26	CO 2-0 R20 A	938.1	23124.54	5.28
23121.88	CO 2-0 R81 E	-196.3	23128.41	6.53
23123.31	CO 2-0 R81 A	193.0	23128.41	5.10
23129.73	CO 2-0 R19 E	-427.9	23137.08	7.35
23131.80	CO 2-0 R19 A	903.7	23137.08	5.28
23134.12	CO 2-0 R82 E	-304.0	23141.59	7.47
23136.46	CO 2-0 R82 A	160.1	23141.59	5.13
23142.53	CO 2-0 R18 E	-356.3	23150.03	7.50
23144.69	CO 2-0 R18 A	985.8	23150.03	5.34
23147.80	CO 2-0 R83 E	- 85.4	23155.23	7.43
23150.12	CO 2-0 R83 A	138.9	23155.23	5.11
23155.84	CO 2-0 R17 E	-416.0	23163.38	7.54
23157.98	CO 2-0 R17 A	874.9	23163.38	5.40

Table 4.12: The equivalent widths for the lines in Fig. 4.56 with the vacuum positions given by Hinkle et al. (1995). The mean differences between vacuum position and measured wavelength can be seen in Table 4.13. The radial velocity derived from the measurements in the J-band is -36.81 ± 3.79 km/s after heliocentric correction. Due to the splitting of the CO-lines, the more reliable radial velocity estimated from the J-band is given here.

Absorption	Diff. [Å]	RV [km/s]	Emission	Diff. [Å]	RV [km/s]
low-excitation	5.30	10.38 ± 0.60	low-excitation	7.36	-16.34 ± 1.76
high-excitation	5.12	12.70 ± 2.25	high-excitation	6.84	$- 9.60 \pm 6.57$
all	5.21	11.47 ± 1.98	all	7.17	-13.93 ± 5.28

Table 4.13: The mean radial velocities relative to the star for absorption and emission lines.

Analysis of the Spectrum

The continuum of this spectrum was estimated at about 523/524 in flux counts. The position of the high-excitation lines used in the synthetic spectra of the K-band models turned out to be incorrect. The measurements were compared to the Arcturus-Atlas (Hinkle et al., 1995) and are therefore not affected by this problem.

This spectrum shows again an invert P-Cygni profile like the K-band spectrum of AC Her, with the emission components of the lines blueshifted relative to the absorption components. Most of the high-excitation lines and all of the low-excitation lines show emission as well as absorption, the low-excitation lines have stronger lines both in emission and absorption than the high-excitation lines, but in both cases, the absorption component is the stronger one. All lines are quite broad.

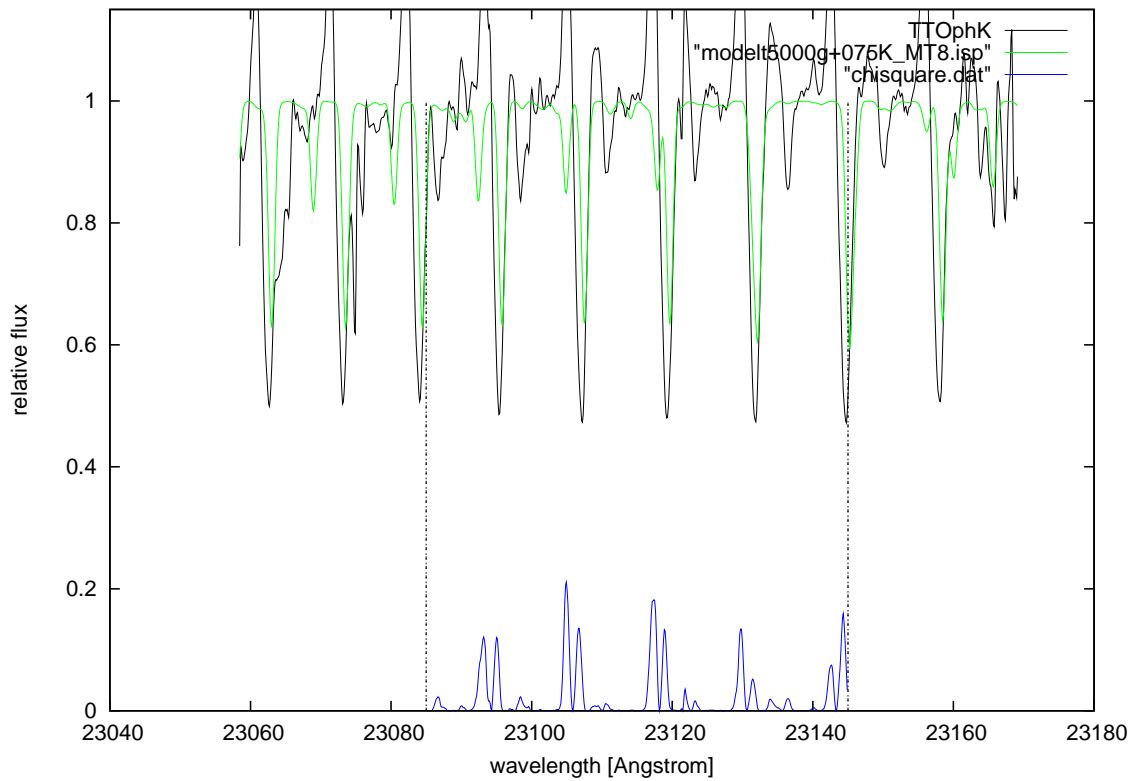


Figure 4.57: The star TT Oph overplotted by a MARCS model of 5000 K, $\log g=0.75$ and $\zeta=8$ km/s.

Literature

This star of the RVa subgroup has a period of 61.08 days with minimum light at 10.84 mag and maximum at 9.45 mag, and $[\text{Fe}/\text{H}]=-0.5$. The light and color variations are observed to be quite regular and symmetrical, but they can significantly change in amplitude from cycle to cycle (DuPuy et al., 1983). The spectral type is G2e-K0 according to *The General Catalogue of Variable Stars (GCVS)* by Samus et al. (1997).

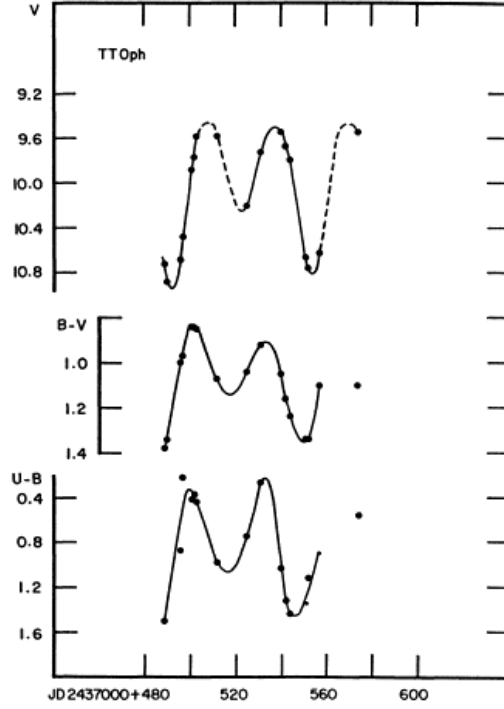


Figure 4.58: The light curve of the RV Tauri variable TT Oph in V, B-V and U-B (Preston et al., 1963).

TT Oph was filed to the Preston subtype A by Dawson (1979), although no TiO bands were observed at any phase, only Balmer emission during rising light was reported, which is unusual because normally the two features are correlated. This Balmer emission was confirmed by Wahlgren et al. (1984), who used IDS spectra taken with the 1.8 m Perkins telescope.

The stellar parameters T_{eff} , M_v , and $\log g$ were derived from photometry and used to make an estimation about the mass of the star (Dawson, 1979): T_{eff} between 4420 to 5470 K, $\log g$ about 1.77. Goldsmith et al. (1987) calculated the temperature for this star to be 5050 K, they also found no evidence for a dust shell around TT Oph.

Cardelli & Howell (1989) worked on a spectrophotometric atlas of RV Tauri variables with respect to their Preston type (Preston et al., 1963) that included several objects which are discussed in this thesis.

The RVa Preston type A star TT Oph was observed three times (see Fig. 4.59), the most interesting result being the data from May 87, where Balmer-line emission is

present in a phase near secondary light maximum.

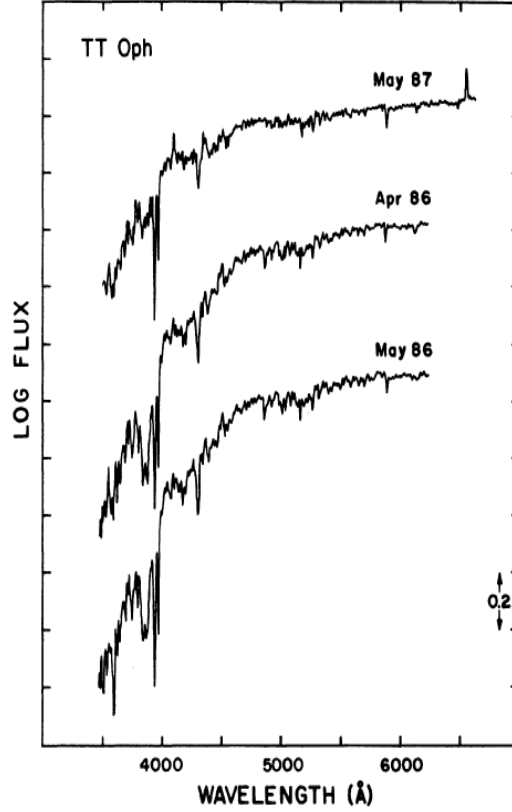


Figure 4.59: Spectrophotometric data for TT Oph (Cardelli & Howell, 1989). The flux is given in $\text{ergs cm}^{-2}\text{s}^{-1}\text{\AA}^{-1}$.

In the work of Wahlgren (1992), an attempt was made to determine the metallicity of selected RV Tauri variables by using moderate resolution spectra and synthetic spectra. The data obtained for TT Oph on five different nights between June 1984 and June 1985 showed varying hydrogen emission from strong $\text{H}\alpha$ emission as well as strong $\text{H}\beta, \gamma$ and δ emission to weak $\text{H}\beta$ and γ absorption. Fig. 4.60 shows the $\text{H}\alpha$ emission observed in the spectrum of TT Oph as well as in three other stars, TX Oph, UZ Oph and RV Tau.

The atmospheric parameters derived by Wahlgren (1992) for the synthetic spectrum of TT Oph are 5000 K for the effective temperature (T_{eff}), a $\log g$ value of 1.500 and a velocity parameter v_t of 6 km/s. The photometric estimation of the $[\text{Fe}/\text{H}]$ ratio of -0.66 by Dawson (1979) does not differ much from the value obtained by Wahlgren (1992), who found $[\text{Fe}/\text{H}] = -0.80$ with his synthetic model approach.

Giridhar et al. (2000a) also used a synthetic model for an abundance analysis of TT Oph. The stellar parameters for this model were derived from FeI and FeII-line analyses and are as follows: $T_{\text{eff}} = 4800$ K, $\log g = 0.5$ and microturbulence $\xi_t = 4.3$ km/s. The estimated $[\text{Fe}/\text{H}]$ ratio is -0.8, which is in good agreement with the values mentioned above by Wahlgren (1992) and Dawson (1979).

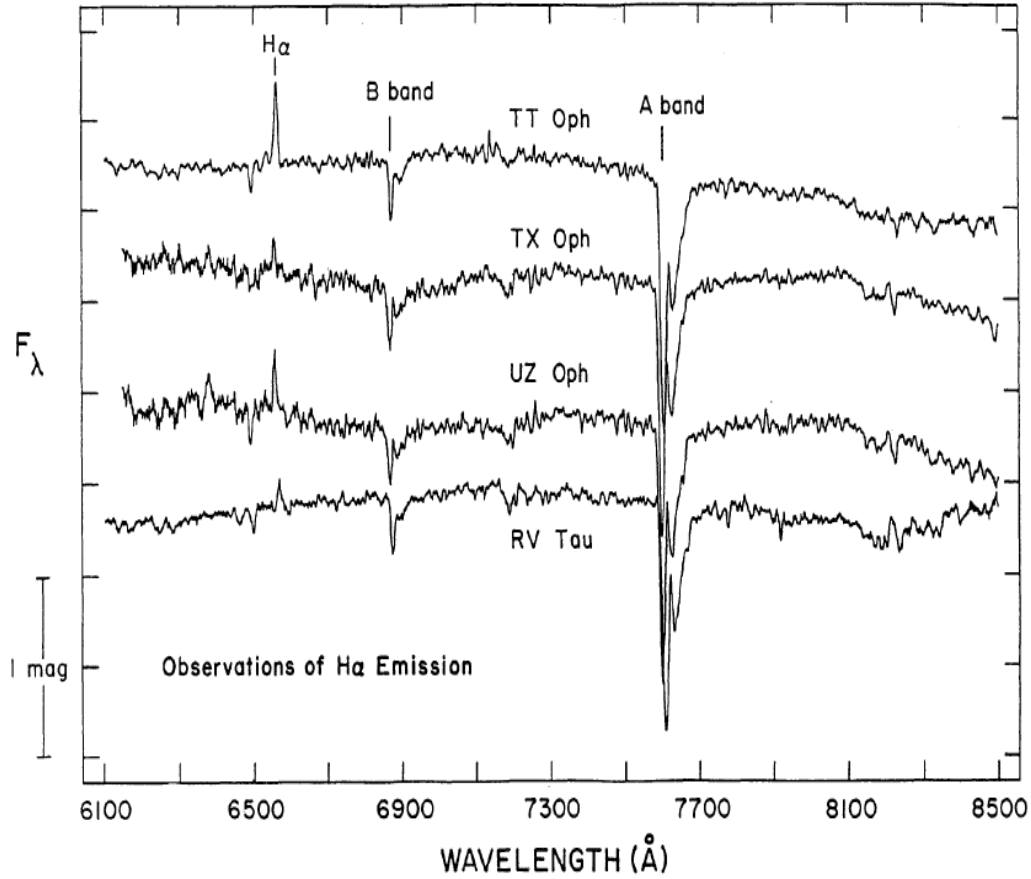


Figure 4.60: The four stars observed by Wahlgren (1992), which showed H α emission in their spectra. At this epoch, TT Oph also exhibits H β and H γ emission.

In general, the elemental abundances of TT Oph are quite similar to that expected for a normal star of same metallicity. In the case of Ca, Sc, and Ti, and for the heavier elements Y, Ce, Pr, Nd, and Sm, an underabundance was noticed (Giridhar et al., 2000a).

In *The Toruń catalogue of Galactic post-AGB and related objects* by Szczerba et al. (2007), TT Oph can be found in the group of *very likely* post-AGB object. The two reasons for the post-AGB classification are the facts that this star is a high galactic latitude supergiant and a confirmed RV Tauri star (see Chapter 1.1.4 to learn more about the selection criteria for post-AGB objects within this catalogue).

4.11 TX Oph

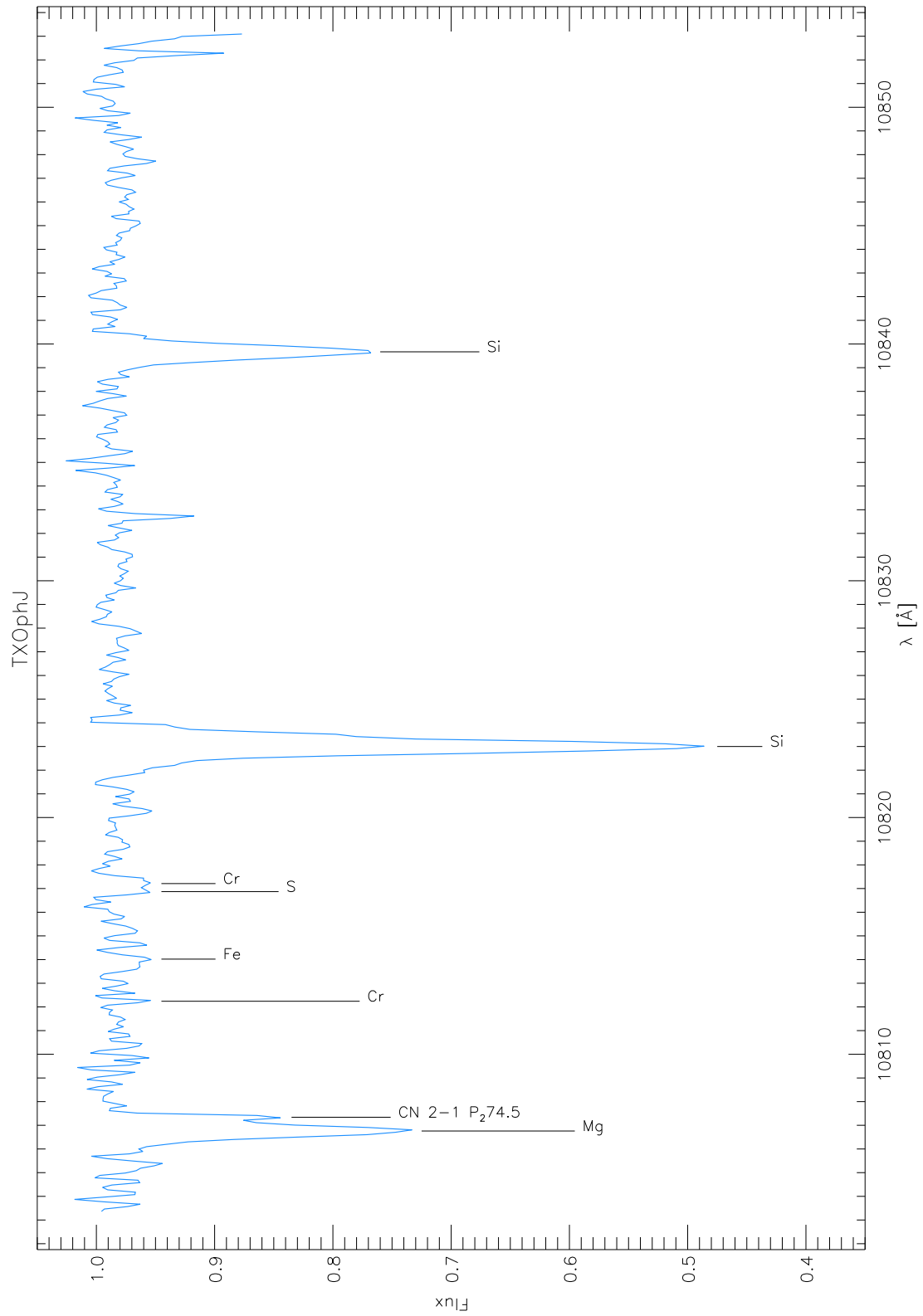


Figure 4.61: The spectrum of TX Ophiuchi in the J-filter with identified and measured lines.

Wavelength [Å]	Atom/Molecule	EQW [mÅ]	Vacuum Pos.	Difference
10806.76	Mg	184.5	10814.05	7.29
10807.34	CN 2-1 P_2	74.5	10814.83	7.49
10812.24	Cr	13.6	10819.86	7.62
10814.02	Fe	24.4	10821.26	7.24
10816.87	S	16.0	10824.17	7.30
10817.21	Cr	35.1	10824.58	7.37
10823.00	Si	381.5	10830.06	7.06
10839.67	Si	249.0	10846.82	7.15

Table 4.14: The equivalent widths for the lines in Fig.4.61 with the vacuum positions given by Hinkle et al. (1995). The mean difference between vacuum position and measured wavelength is 7.31 Å. The radial velocity derived from these measurements is -176.07 ± 4.65 km/s after heliocentric correction.

Analysis of the Spectrum

This spectrum seems very turbulent with only few prominent lines in it. The Si lines are the strongest by far, Mg, normally equally strong in the comparison stars, is weaker in this case. I was unable to identify the three Ca lines expected in this spectral region as well as most of the other lines, including a second Fe line and four additional CN lines. The S and Cr line at 10816.87 Å and 10817.21 Å, respectively, are overestimated in the model spectrum.

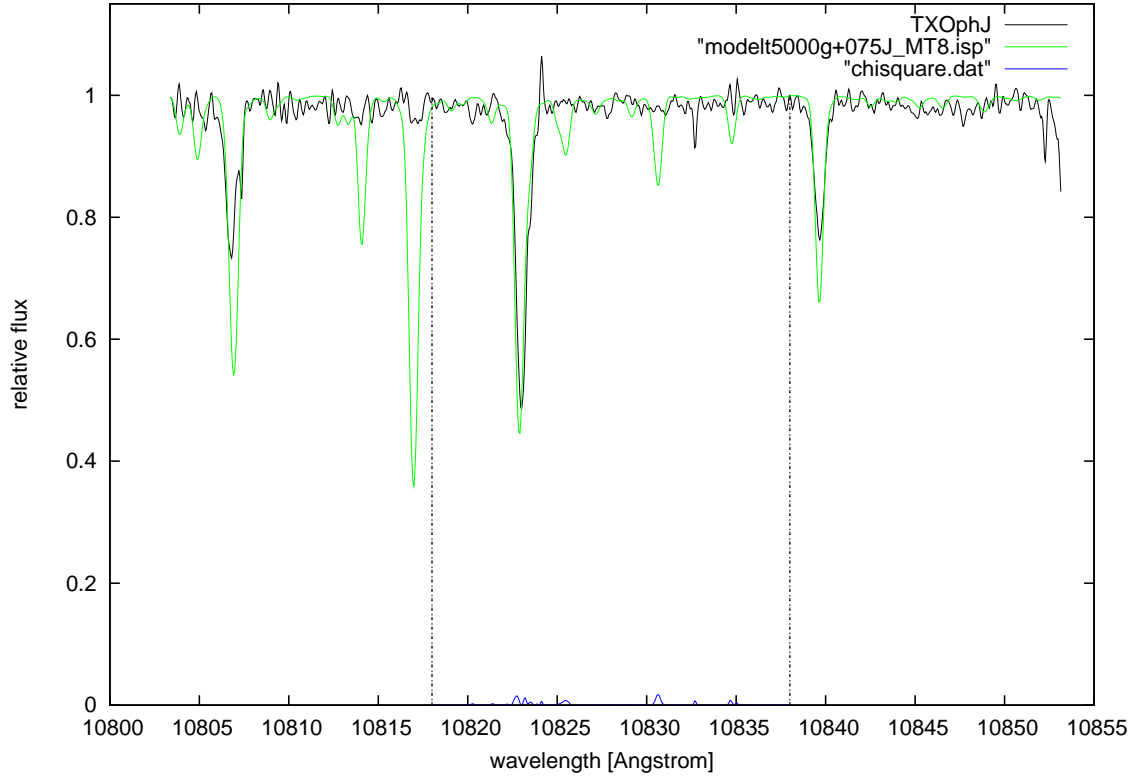


Figure 4.62: The star TX Oph overplotted by a MARCS model of 5000 K, $\log g=0.75$ and $\zeta=8$ km/s.

Literature

TX Oph is a variable star of the RVa-type with a spectral class of F5e-G6e and a period of 135 days (Samus et al., 1997). The light curve shows a minimum at 11.4 mag and a maximum at 9.7 mag in V.

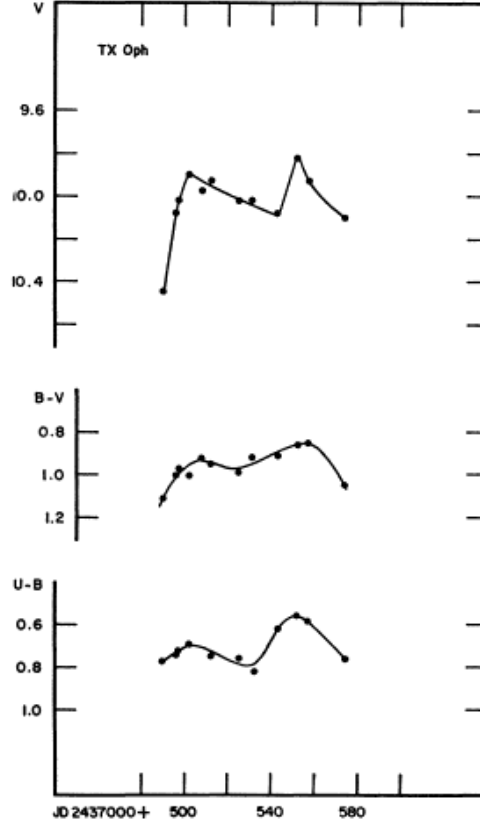


Figure 4.63: The light curve of the RV Tauri star TX Oph in V, B-V and U-B (Preston et al., 1963).

Wahlgren et al. (1984) found evidence for Balmer emission in the spectra they obtained from TX Oph.

The observations done by Goldsmith et al. (1987) suggest a single dust shell around TX Oph with a temperature of 970 K. The central star has a temperature of 5570 K. The Planck mean absorption optical depth $\langle \tau \rangle$ in the dust shell was calculated to be 0.06.

This RVa Preston type A (Preston et al., 1963) star was observed twice by Cardelli & Howell (1989), who noticed weak CN absorption lines and only slight differences between the two spectra (see Fig. 4.64).

The warm RV Tauri variable TX Oph was observed three times by Wahlgren (1992) between May 1984 and June 1985, who noticed fairly strong H α emission at his first observation that was absent two weeks later at his second observation. The last spectrum obtained in June 1985 revealed H γ central emission. To derive the metallicity of this RV Tauri variable, a synthetic spectrum was fitted to the observed spectrum (see Fig. 4.65). The best fitting synthetic spectrum gave the following atmospheric

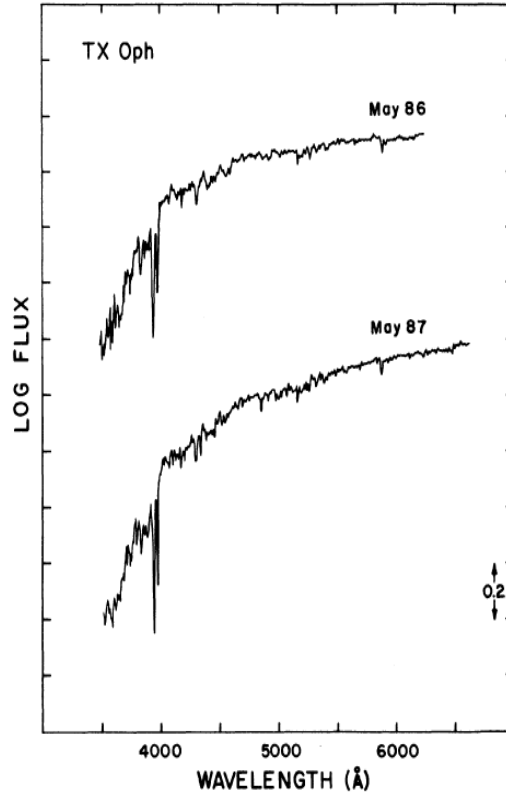


Figure 4.64: Spectrophotometric observations of TX Oph (Cardelli & Howell, 1989), the flux is given in $\text{ergs cm}^{-2}\text{s}^{-1}\text{\AA}^{-1}$.

parameters: $T_{\text{eff}}=5750\text{ K}$, $\log g=1.125$, velocity parameter $v_t=5\text{ km/s}$. The resulting metallicity of $[\text{Fe}/\text{H}]=-0.80$ is not in disagreement with the value found by Dawson (1979), who found $[\text{Fe}/\text{H}]=-0.68$ out of photometric data.

In part VI of their series of papers, Giridhar et al. (2005) made abundance analyses of field RV Tauri stars, including TX Oph (see Fig. 4.66). The parameters for the model used were derived from the analyses of Fe-lines (FeI and FeII) and gave $T_{\text{eff}}=5000\text{ K}$, $\log g=0.5$, $\xi_t=4.9\text{ km/s}$ and $[\text{Fe}/\text{H}]=-1.2$ for this specific star.

Giridhar et al. (2005) also measured a radial velocity of -166 km/s , which, together with the iron abundance, leads to the assumption that TX Oph belongs to the Galactic thick disc. Compared to this value, the radial velocity I derived in this thesis, -176.07 km/s , is higher. I only had few strong lines to use for my measurements, probably this or pulsation is the reason for the difference of the two velocities.

The element abundances of $[\text{Na}/\text{Fe}]$, $[\text{Zn}/\text{Fe}]$ and $[\text{Al}/\text{Fe}]$ estimated by Giridhar et al. (2005) are similar to that of a normal star with the same metallicity, not so for Ca, Sc and Ti, which are underabundant compared to a normal star of $[\text{Fe}/\text{H}]=-1.2$.

Based upon some of the papers presented above, *The Toruń catalogue of Galactic post-AGB and related objects* by Szczerba et al. (2007) filed TX Oph as a *very likely* post-AGB object because it is a high galactic latitude supergiant and a confirmed RV Tauri star (see Chapter 1.1.4 for more information about the selection criteria of post-AGB objects).

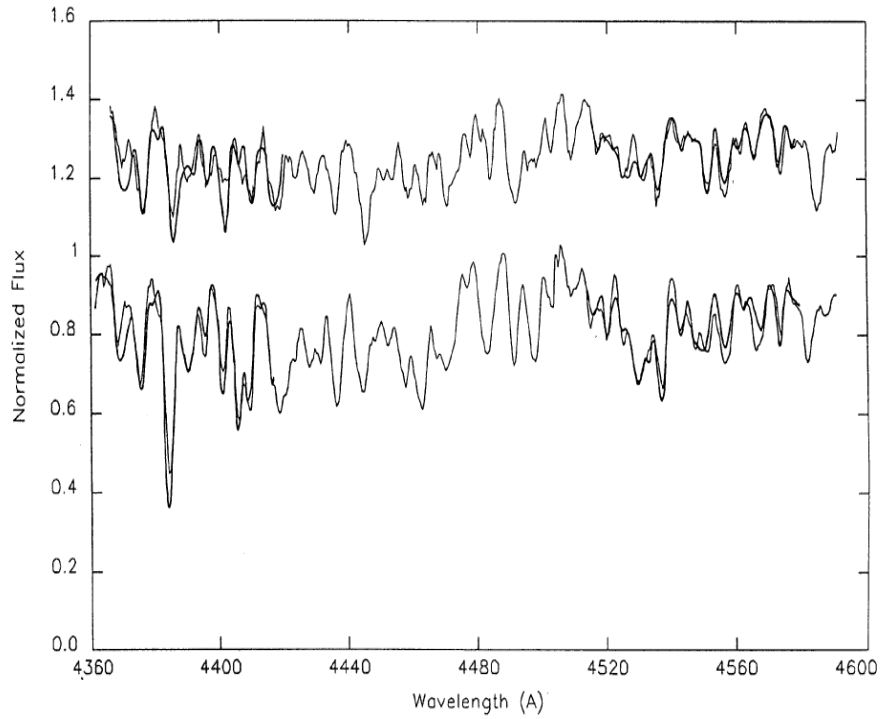


Figure 4.65: Comparison of the observed spectra (thin lines) of the warm variable TX Oph (upper spectrum) and the cool variable V564 Oph (lower spectrum), with the synthetic spectra (thick lines) computed by Wahlgren (1992).

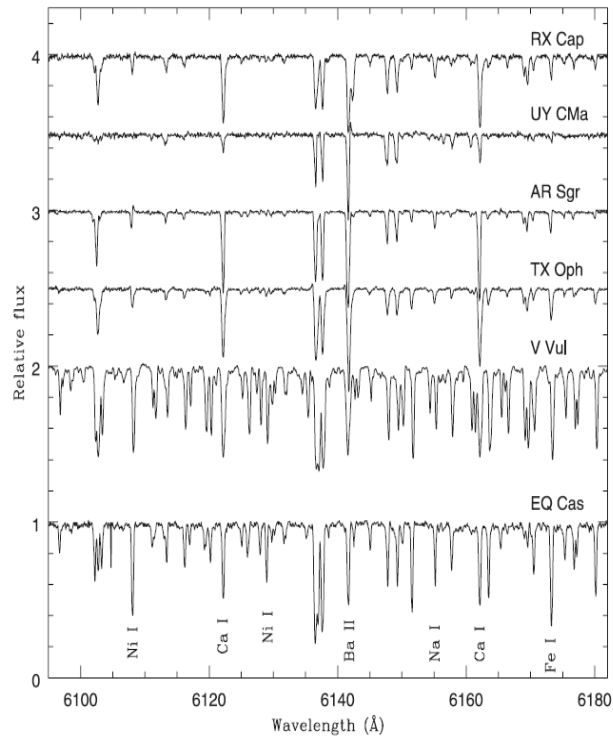


Figure 4.66: A representative sample of RV Tauri stars observed by Giridhar et al. (2005). The spectra are presented in descending order of temperature.

4.12 UZ Oph

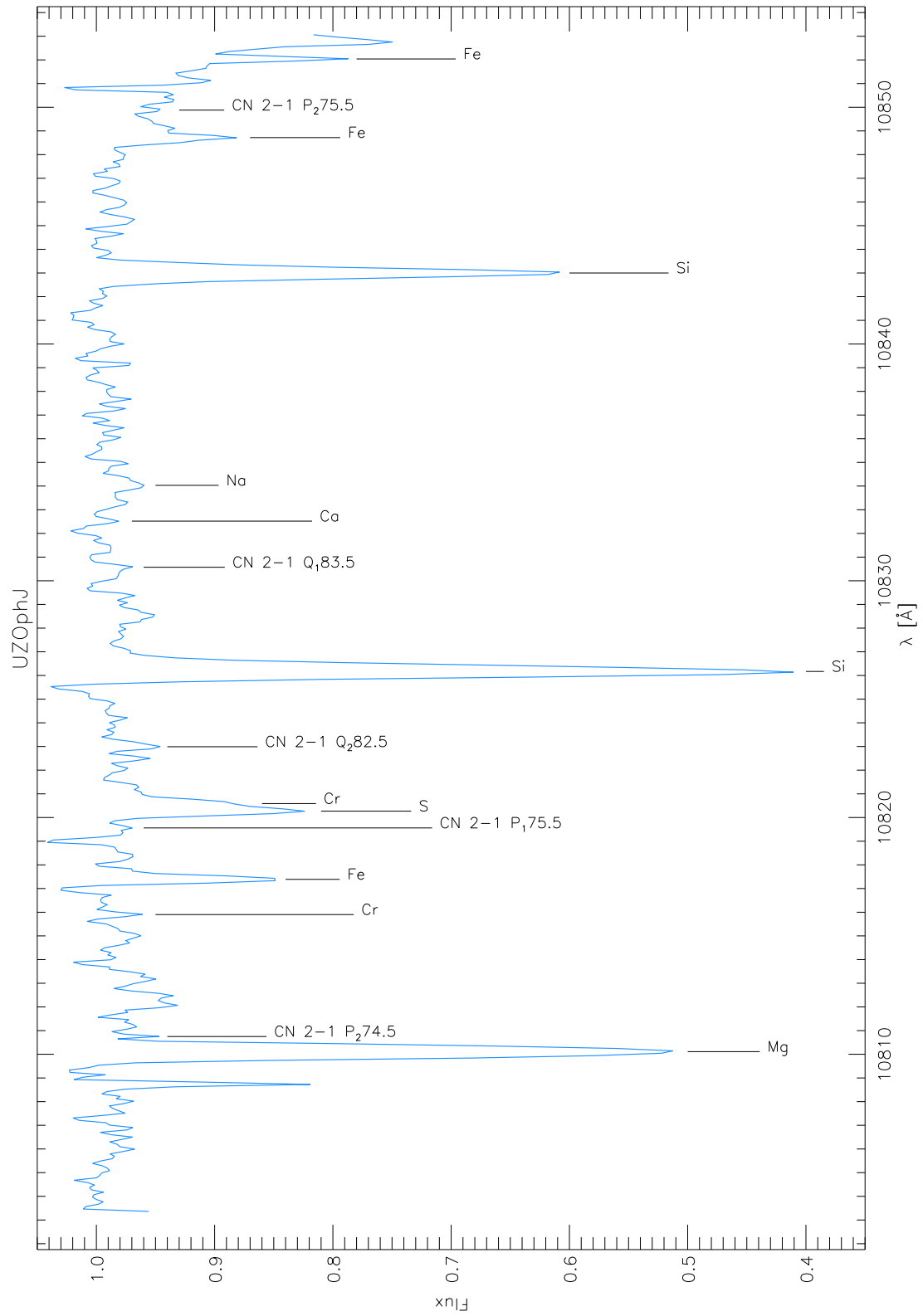


Figure 4.67: The spectrum of UZ Ophiuchi in the J-filter with identified and measured lines.

Wavelength [Å]	Atom/Molecule	EQW [mÅ]	Vacuum Pos.	Difference
10810.11	Mg	342.4	10814.05	3.94
10810.75	CN 2-1 P_2 74.5	9.9	10814.83	4.08
10815.90	Cr	8.7	10819.86	3.96
10817.39	Fe	66.3	10821.26	3.87
10819.56	CN 2-1 P_1 75.5	9.4	10823.43	3.87
10820.27	S	85.2	10824.17	3.90
10820.59	Cr	62.7	10824.58	3.99
10822.99	CN 2-1 Q_2 82.5	24.2	10826.84	3.85
10826.17	Si	357.5	10830.06	3.89
10830.57	CN 2-1 Q_1 83.5	7.9	10834.22	3.65
10832.52	Ca	4.1	10836.35	3.83
10834.03	Na	23.4	10837.84	3.81
10843.00	Si	257.4	10846.82	3.82
10848.72	Fe	69.0	10852.43	3.71
10849.88	CN 2-1 P_2 75.5	30.6	10853.76	3.88
10852.04	Fe	102.9	10855.95	3.91

Table 4.15: The equivalent widths for the lines in Fig.4.67 with the vacuum positions given by Hinkle et al. (1995). The mean difference between vacuum position and measured wavelength is 3.87 Å. The radial velocity derived from these measurements is -81.13 ± 2.74 km/s after heliocentric correction.

Analysis of the Spectrum

The lines observed in this spectrum are quite narrow and pointy, with the strongest ones being Si and Mg. Both Cr lines are visible, as well as all of the CN lines expected. Ca and Na are very weak, I was not able to identify all of the Ca lines normally present in this wavelength. The S and Cr line at 10820.27 Å and 10820.59 Å, respectively, are overestimated in the model spectrum.

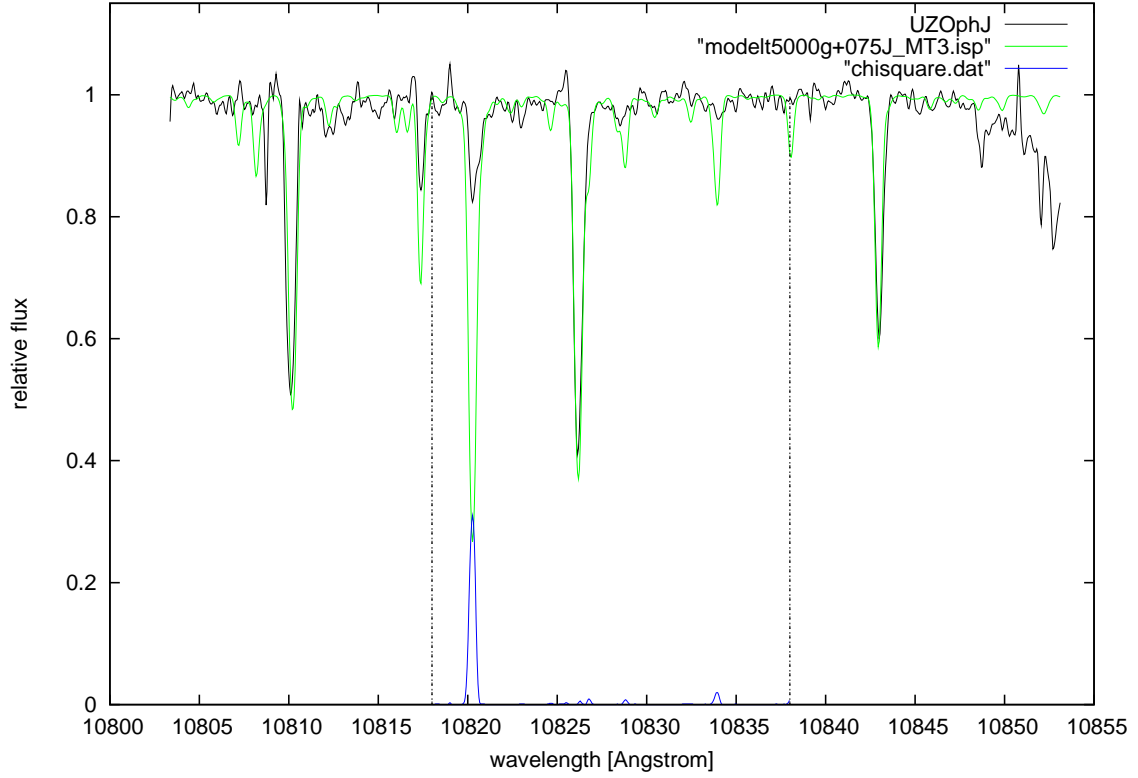


Figure 4.68: The star UZ Oph overplotted by a MARCS model of 5000 K, $\log g=0.75$ and $\zeta=3$ km/s.

Literature

According to *The General Catalogue of Variable Stars (GCVS)* by Samus et al. (1997), this star of the RVa-type has a period of 87.44 days with a maximum at 9.93 mag and a minimum at 11.50 mag in V. The spectral class assigned to this star is G2e-G8(M2).

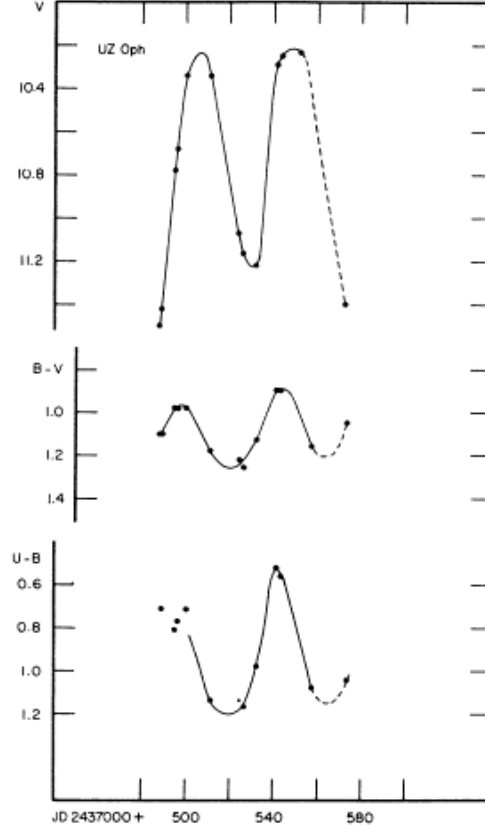


Figure 4.69: The light curve of the RV Tauri variable star UZ Oph in V, B-V and U-B (Preston et al., 1963).

Wahlgren et al. (1984) stated that this star also shows Balmer emission, like TT Oph, TX Oph and RV Tau. This has been confirmed by the observations done by Cardelli & Howell (1989), who found emission in all hydrogen Balmer lines in May 86 during a phase of rising light after the secondary minimum (see Fig. 4.70).

This star was also included in the sample observed by Goldsmith et al. (1987), who calculated a temperature of 4000 K and no dust shell around UZ Oph.

The observations of Wahlgren (1992) showed strong $H\alpha$ emission on May 24, 1984. This emission was absent a few weeks later on June 8. A possible $H\beta$ central emission was detected one year later on June 10, that was followed by a fairly strong $H\beta$ and $H\gamma$ emission on June 21. These observations were compared to a synthetic model spectrum to derive the metallicity and the atmospheric parameters of UZ Oph. The results are $T_{\text{eff}}=5750$ K, $\log g=0.750$, $\xi=8$ km/s and $[\text{Fe}/\text{H}]=-0.50$. The last value of the metallicity does not differ too much from the one derived by Dawson (1979), $[\text{Fe}/\text{H}]=-0.77$, who used photometric means.

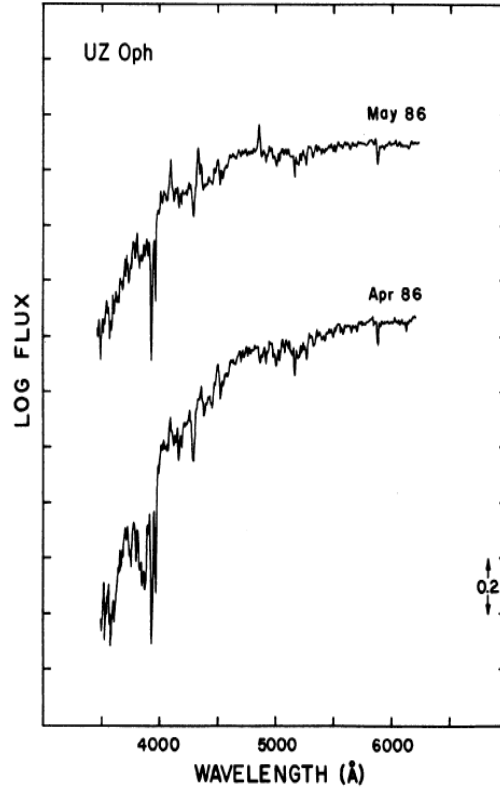


Figure 4.70: Spectrophotometric data for the RVa Preston type A (Preston et al., 1963) star UZ Oph observed by Cardelli & Howell (1989). Log flux is given in $\text{ergs cm}^{-2}\text{s}^{-1}\text{\AA}^{-1}$.

Within the work of Giridhar et al. (2005), UZ Oph was observed twice, first on July 13, 2001 and second on June 30, 2002. The measured radial velocity of the first observation was -95 km/s , the second was in good agreement with -90 km/s . Based upon these radial velocities, one can assume that UZ Oph belongs to the Galactic thick disk. The radial velocity derived in this thesis is comparative with a value of -81.13 km/s .

Both data sets were used to create a model of this star by analysing the FeI and FeII lines. The spectrum obtained on July 13, 2001 was best described by a model of $T_{\text{eff}}=5000 \text{ K}$, $\log g=0.5$, $\xi=3.6 \text{ km/s}$ and $[\text{Fe}/\text{H}]=-0.7$. The best fit model of the second observation on June 30, 2002 gave $T_{\text{eff}}=4800 \text{ K}$, $\log g=0.0$, $\xi=3.6 \text{ km/s}$ and $[\text{Fe}/\text{H}]=-0.8$. To derive the elemental abundances only the spectrum of 2002 was used, because there was not too much difference between the two observations (Giridhar et al., 2005). The results of the abundance analysis showed a composition quite similar to that of a normal star with the same metallicity. Only the heavy elements Y, La, Ba, Ce, Nd, Sm, and Eu are underabundant compared to the expected initial composition.

The Toruń catalogue of Galactic post-AGB and related objects by Szczerba et al. (2007) filed UZ Oph as a *very likely* post-AGB object because it is a high galactic latitude supergiant and a confirmed RV Tauri star (see Chapter 1.1.4).

4.13 AR Pup

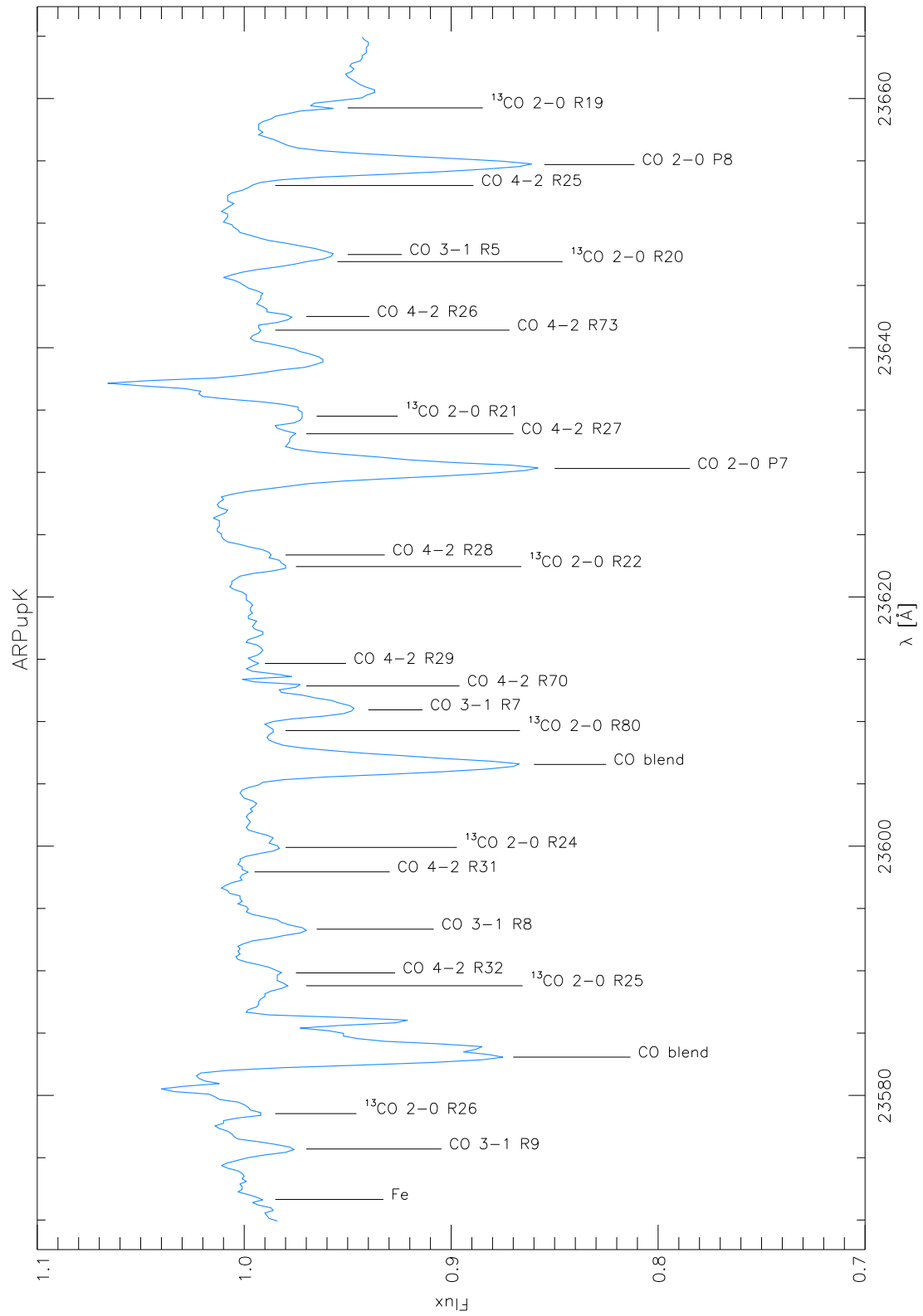


Figure 4.71: The spectrum of AR Puppis in the K-filter with identified and measured lines.

Wavelength [Å]	Atom/Molecule	EQW [mÅ]	Vacuum Pos.	Difference
23571.65	Fe	5.5	23573.10	1.45
23575.70	CO 3-1 R9	22.9	23577.15	1.45
23578.54	¹³ CO 2-0 R26	4.6	23579.92	1.38
23588.80	¹³ CO 2-0 R25	35.1	23590.27	1.47
23589.83	CO 4-2 R32	32.0	23591.38	1.55
23593.34	CO 3-1 R8	62.1	23594.42	1.08
23597.94	CO 4-2 R31	0.3	23599.11	1.17
23599.90	¹³ CO 2-0 R24	17.5	23601.03	1.13
23609.28	¹³ CO 2-0 R80	37.9	23610.26	0.98
23610.94	CO 3-1 R7	80.3	23612.10	1.16
23612.86	CO 4-2 R70	14.6	23614.06	1.20
23614.67	CO 4-2 R29	5.6	23615.82	1.15
23622.44	¹³ CO 2-0 R22	19.7	23623.71	1.27
23623.37	CO 4-2 R28	14.6	23624.81	1.44
23630.31	CO 2-0 P7	319.1	23631.25	0.94
23633.10	CO 4-2 R27	24.4	23634.23	1.13
23634.51	¹³ CO 2-0 R21	58.7	23635.64	1.13
23641.41	CO 4-2 R73	12.0	23642.89	1.48
23642.51	CO 4-2 R26	15.4	23644.05	1.54
23646.91	¹³ CO 2-0 R20	28.1	23647.97	1.06
23647.48	CO 3-1 R5	125.5	23648.75	1.27
23653.02	CO 4-2 R25	1.4	23654.31	1.29
23654.70	CO 2-0 P8	255.7	23655.46	0.76
23659.25	¹³ CO 2-0 R19	42.9	23660.69	1.44

Table 4.16: The equivalent widths for the lines in Fig.4.71 with the vacuum positions given by Hinkle et al. (1995). The mean difference between vacuum position and measured wavelength is 1.25 Å. The radial velocity derived from these measurements is -15.83 ± 2.58 km/s without heliocentric correction. I was not able to readout the heliocentric velocity of the observation date.

Analysis of the Spectrum

AR Pup is the only star in my sample observed in a different K-bandwidth. Therefore, the only comparison spectrum was the *Infrared Atlas of the Arcturus Spectrum* by Hinkle et al. (1995). The lines are broadened in the spectrum of AR Pup, leading to blending of lines. There seems to be some emission present, two lines namely, the CO 4-2 R66 and ^{13}CO 2-0 R81 line. I was not able to identify the prominent emission feature at 23635 Å. It is possible that this feature is artificial, but I am not in the possession of the original data. The data reduction for this star was performed by Michael Lederer.

The CO blends are among the strongest lines, followed by CO 2-0 P7 and P8. The weakest lines are the ^{13}CO 2-0 lines, which leaves the question, if the emission feature assigned to the ^{13}CO 2-0 R81 line is really an emission feature or just a very weak feature near the continuum.

The observations compared to a model spectrum (Fig. 4.72) suggest a higher temperature for this star than 5000 K, but these are the highest values I used for my model spectra. Gonzalez et al. (1997) found an effective temperature $T_{\text{eff}}=6000$ K and $\log g=1.5$, which seems to be more appropriate.

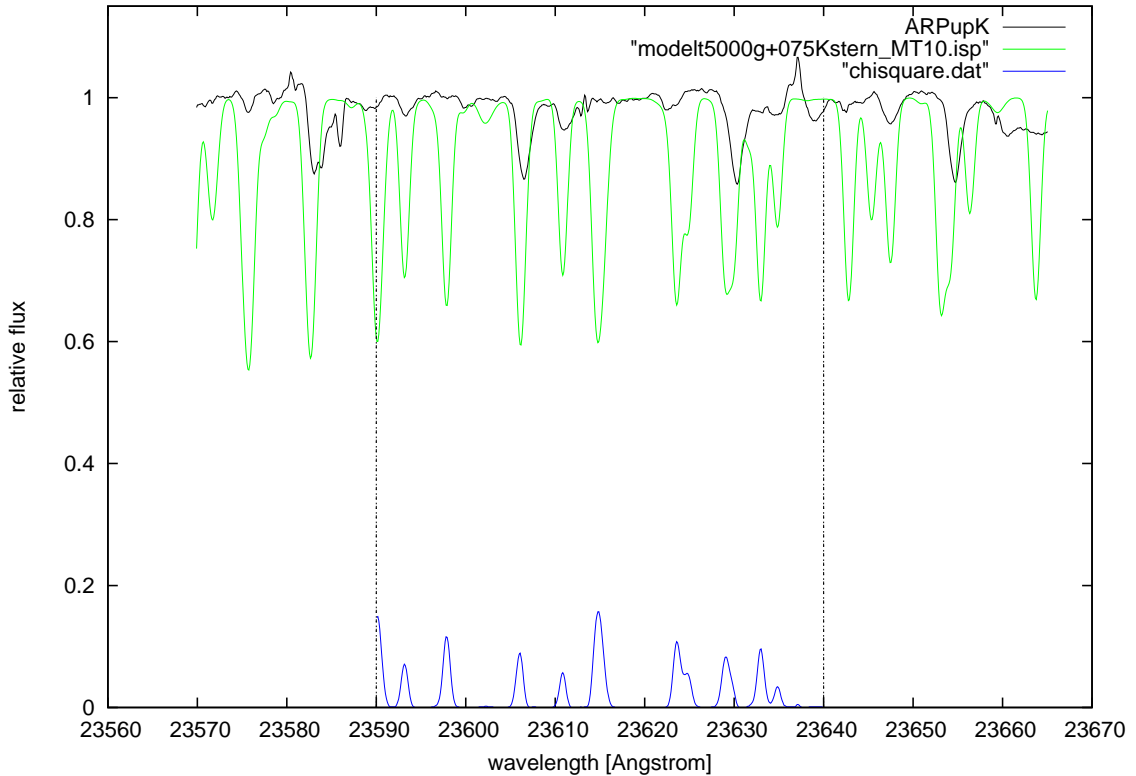


Figure 4.72: The star AR Pup overplotted by a MARCS model of 5000 K, $\log g=0.75$ and $\zeta=10$ km/s.

Literature

AR Pup was assigned to the RV Tauri photometric subclass b (Gehrz & Ney, 1972) and the Preston type B (Evans, 1985). As one can see in Fig. 4.73, this star shows a very strong H α emission feature (Pollard et al., 1997) without doubling, the peak in strength of the H α emission after first and second minima reflects the two shock waves expected to pass through the star during every variability cycle.

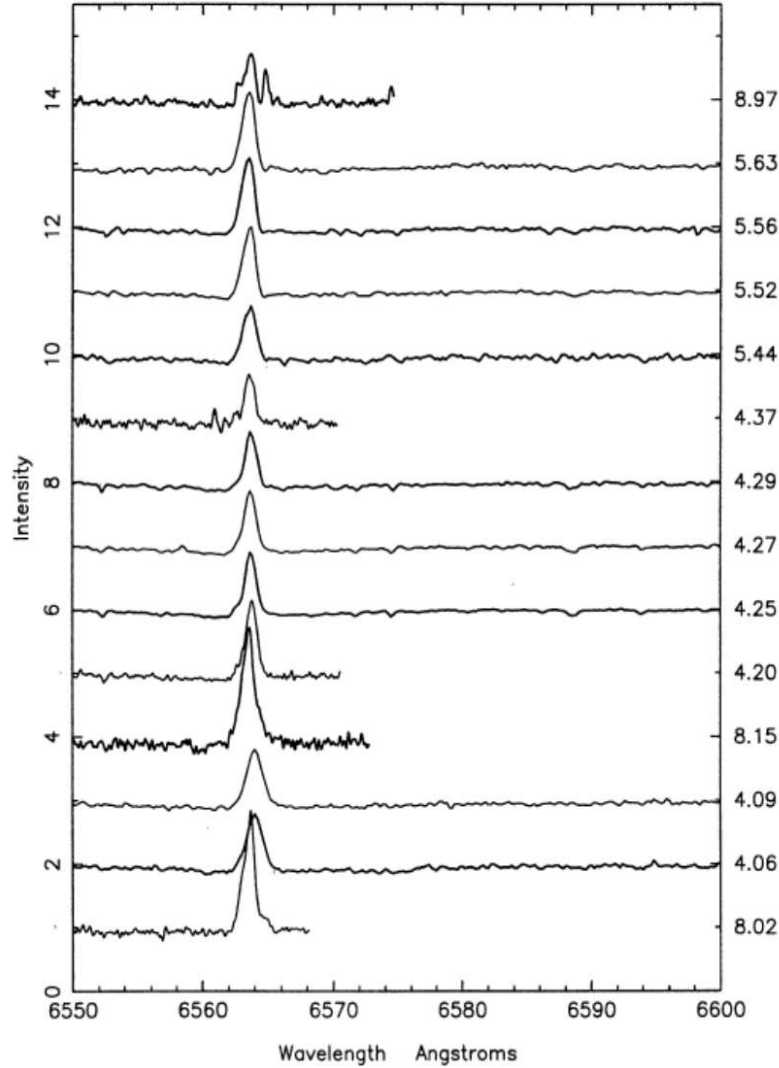


Figure 4.73: MJUO and MSSSO spectra of AR Pup taken from Pollard et al. (1997). The spectra are stacked in phase sequence (cycle number and phase can be found on the right side next to each spectrum) and show the region around the H α line.

AR Pup shows a very strong infrared excess. Although AR Pup is classified as a carbon rich star, it only shows the silicate emission at 10 μ m but not the SiC emission at 11 μ m as expected for a carbon rich star (Evans, 1985).

The temperature of the dust shell at the inner boundary, where the dust grains start condensing, was calculated by Raveendran (1989) to be 450 K. Infrared excess has been reported in the range of 12-25 μ m as well as the presence of hydrogen emission

in the Balmer lines during the larger part of the pulsation cycle with increase in strength during rising light (Gonzalez et al., 1997).

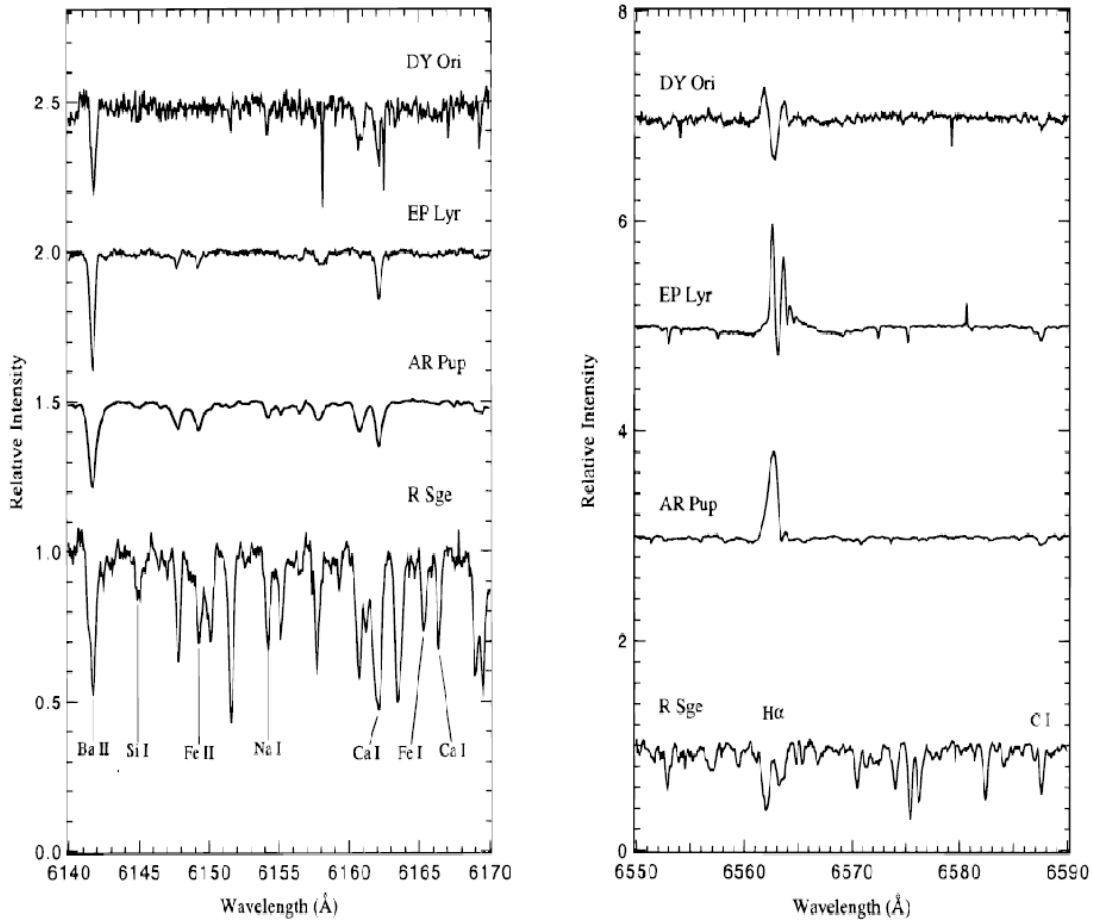


Figure 4.74: Spectra of the sample stars used in the work of Gonzalez et al. (1997). The identified lines are marked and named.

The atmospheric parameters calculated by Gonzalez et al. (1997) are $T_{\text{eff}}=6000$ K, $\log g=1.5$, $\xi_t=2.0$ km/s, and $[\text{Fe}/\text{H}]=-0.87$. If one compares the spectrum of AR Pup to another variable star, α Per, which has an effective temperature of $T_{\text{eff}}=6200$ K, one notices that Fe I as well as Ni I are rather weak in AR Pup (see Fig. 4.75).

AR Pup is a *very likely* post-AGB object according to *The Toruń catalogue of Galactic post-AGB and related objects* by Szczerba et al. (2007). This classification is based upon the RV Tauri nature of this star.

Van Winckel et al. (1999) investigated the variability of the linear polarization observed in AR Pup. Linear polarization is caused by dust scattering and has been found at most of the RV Tauri stars, but not as high as in AR Pup (up to $\sim 14\%$ in U). The authors reported a connection between the variation of the polarization and the light curve: a light maximum is accompanied by a maximum in polarization, and a polarization minimum follows shortly after light minimum. Van Winckel et al. (1999) narrowed the cause for this behaviour down to a local origin, so it can not

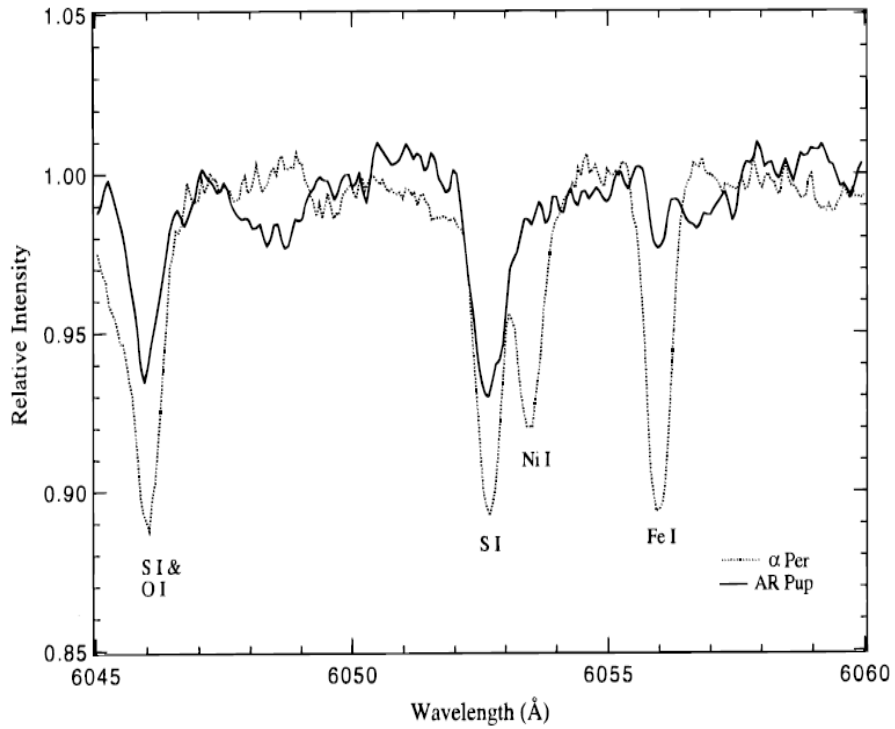


Figure 4.75: Comparison between the spectra of AR Pup and α Per Gonzalez et al. (1997).

be produced by the extended circumstellar envelope. The scenario suggested by the authors is an alignment of freshly produced non-spherical grains that are responsible for the observed polarization through selective absorption and scattering. The production of the grains takes place during an increase of polarization, while the decrease is linked to a destruction or slow dispersal of the grains.

4.14 R Sct

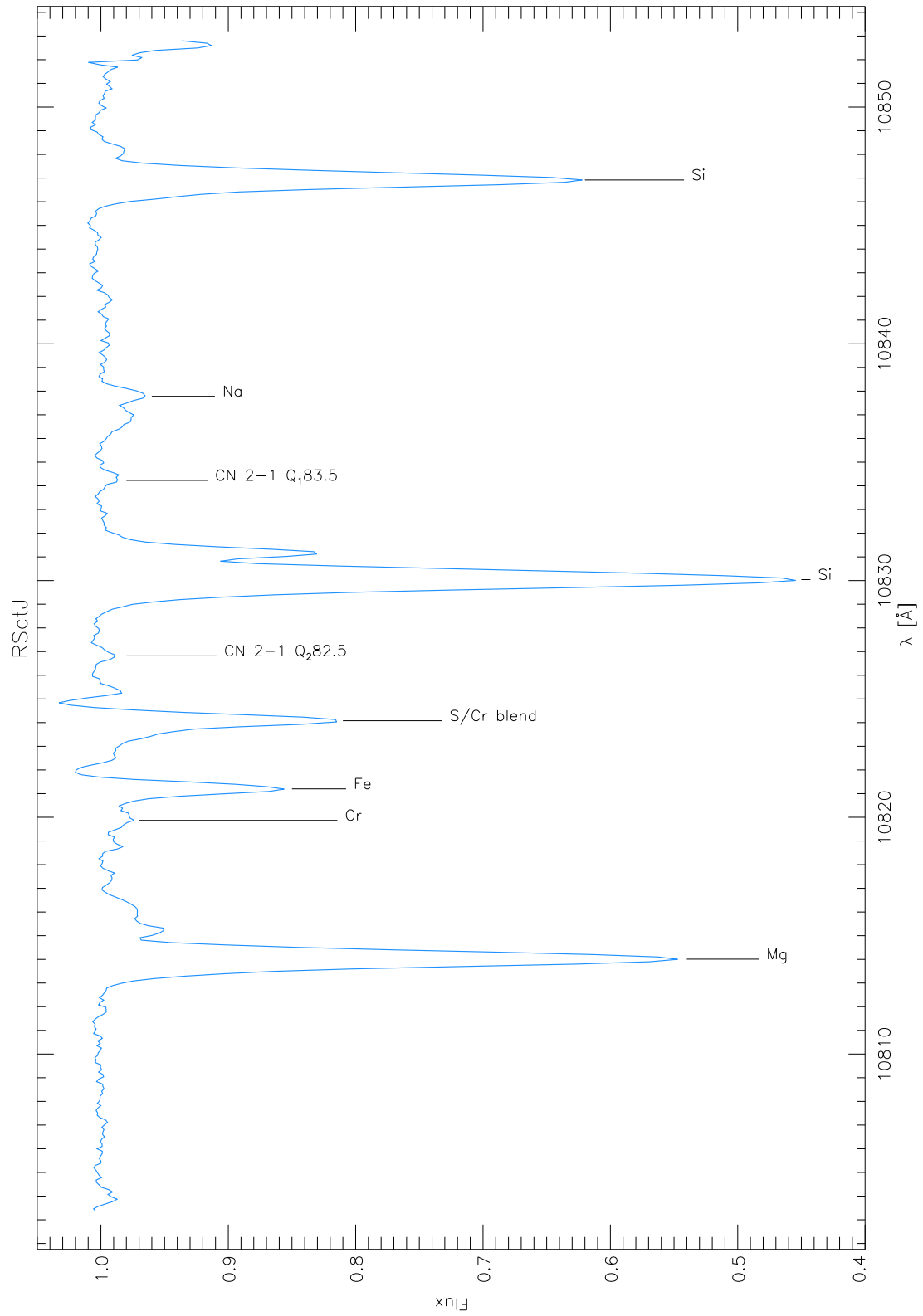


Figure 4.76: The spectrum of R Scuti in the J-filter with identified and measured lines.

Wavelength [Å]	Atom/Molecule	EQW [mÅ]	Vacuum Pos.	Difference
10814.01	Mg	412.8	10814.05	0.04
10819.87	Cr	15.6	10819.86	-0.01
10821.20	Fe	85.2	10821.26	0.06
10826.82	CN 2-1 Q_2 82.5	4.2	10826.84	0.02
10830.04	Si	560.7	10830.06	0.02
10834.23	CN 2-1 Q_1 83.5	4.4	10834.22	-0.01
10837.78	Na	30.9	10837.84	0.06
10846.92	Si	339.6	10846.82	-0.10

Table 4.17: The equivalent widths for the lines in Fig.4.76 with the vacuum positions given by Hinkle et al. (1995). The mean difference between vacuum position and measured wavelength is 0.01 Å. The radial velocity derived from these measurements is 26.96 ± 1.35 km/s after heliocentric correction.

Analysis of the Spectrum

The spectrum of R Sct in this wavelength region is not very spectacular. The Mg and Si lines are the strongest, followed by the Fe line at 10821 Å. The Cr lines are either very weak or blended, the CN lines as well. Ca seems not to be present in this spectrum. As one can see, a lot of lines present in the model are not observed in the stellar spectrum. The S/Cr blend at about 10824 Å is much stronger in the model than observed.

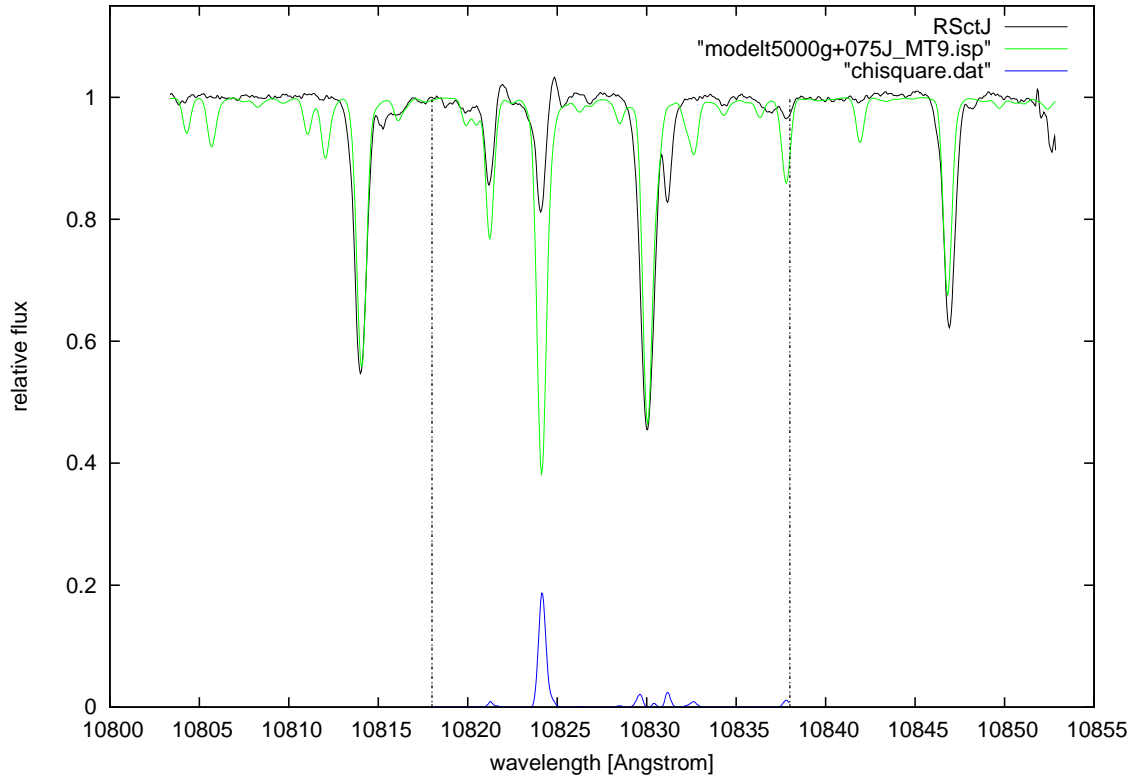


Figure 4.77: The star R Sct overplotted by a MARCS model of 5000 K, $\log g=0.75$ and $\zeta=9$ km/s.

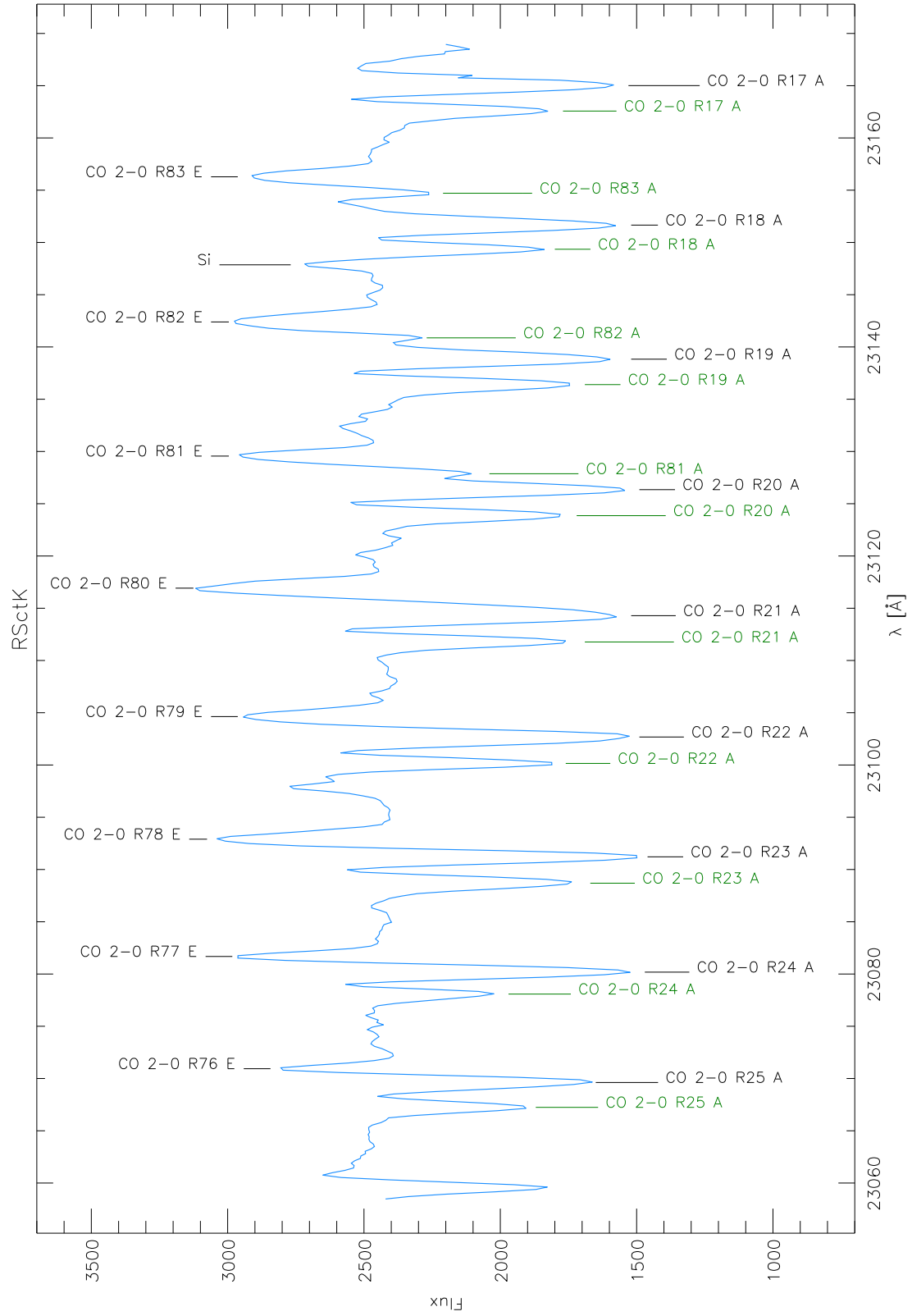


Figure 4.78: The spectrum of R Scuti in the K-filter with identified and measured lines.

Wavelength [Å]	Atom/Molecule	EQW [mÅ]	Vacuum Pos.	Difference
23067.24	CO 2-0 R25 A	303.6	23067.89	0.65
23069.62	CO 2-0 R25 A	459.9	23067.89	-1.73
23070.94	CO 2-0 R76 E	- 95.8	23069.24	-1.70
23078.08	CO 2-0 R24 A	199.5	23078.41	0.33
23080.18	CO 2-0 R24 A	510.6	23078.41	-1.77
23081.68	CO 2-0 R77 E	-182.3	23080.18	-1.50
23088.69	CO 2-0 R23 A	448.8	23089.34	0.65
23091.21	CO 2-0 R23 A	580.6	23089.34	-1.87
23092.90	CO 2-0 R78 E	-293.0	23091.57	-1.33
23100.15	CO 2-0 R22 A	308.6	23100.67	0.52
23102.68	CO 2-0 R22 A	879.7	23100.67	-2.01
23104.63	CO 2-0 R79 E	-248.5	23103.40	-1.23
23111.77	CO 2-0 R21 A	377.5	23112.40	0.63
23114.29	CO 2-0 R21 A	708.1	23112.40	-1.89
23116.92	CO 2-0 R80 E	-364.5	23115.67	-1.25
23123.86	CO 2-0 R20 A	419.6	23124.54	0.68
23126.35	CO 2-0 R20 A	613.2	23124.54	-1.81
23127.87	CO 2-0 R81 A	162.3	23128.41	0.54
23129.56	CO 2-0 R81 E	-243.8	23128.41	-1.15
23136.40	CO 2-0 R19 A	479.2	23137.08	0.68
23138.83	CO 2-0 R19 A	620.0	23137.08	-1.75
23140.87	CO 2-0 R82 A	59.1	23141.59	0.72
23142.39	CO 2-0 R82 E	-337.2	23141.59	-0.80
23147.86	Si	- 66.0	23147.94	0.08
23149.35	CO 2-0 R18 A	311.5	23150.03	0.68
23151.66	CO 2-0 R18 A	580.0	23150.03	-1.63
23154.71	CO 2-0 R83 A	71.9	23155.23	0.52
23156.28	CO 2-0 R83 E	-253.7	23155.23	-1.05
23162.57	CO 2-0 R17 A	386.1	23163.38	0.81
23165.01	CO 2-0 R17 A	588.2	23163.38	-1.63

Table 4.18: The equivalent widths for the lines in Fig. 4.78 with the vacuum positions given by Hinkle et al. (1995). The mean differences between vacuum position and measured wavelength can be seen in Table 4.19. The radial velocity derived from the measurements in the J-band is 26.96 ± 1.35 km/s after heliocentric correction. Due to the splitting of the CO-lines, the more reliable radial velocity estimated from the J-band is given here.

Black	Diff. [Å]	RV [km/s]	Green	Diff. [Å]	RV [km/s]
low-excitation A	-1.79	0.00 ± 1.51	low-excitation A	0.63	-31.30 ± 1.63
high-excitation E	-1.25	-6.96 ± 3.32	high-excitation A	0.59	-30.89 ± 1.17
all	-1.54	-3.28 ± 4.30	all	0.62	-31.20 ± 1.54

Table 4.19: The mean radial velocities relative to the star for the different components of the spectrum.

Analysis of the Spectrum

The continuum for this spectrum was estimated to be at 2500 in flux counts. The position of the high-excitation lines used in the synthetic spectra of the K-band models turned out to be incorrect. The measurements were compared to the Arcturus-Atlas (Hinkle et al., 1995) and are therefore not affected by this problem.

The K-filter spectrum of R Sct shows a very interesting structure. The green labeled features are assigned to a component or a shell that seems to have no emission lines, which means it has not experienced any kind of shock lately that could lead to emission features. Not all of the lines of the green labeled part can be seen, because the black labeled lines are overlapping some of them.

The black labeled features in this spectrum belong to another component of the star. In this part of the star, all the high-excitation lines are in emission without any absorption component, while the low-excitation lines are without an emission part. Si seems to be in emission as well, but at a completely different velocity than the CO lines.

The lines labeled in green are blueshifted, which points to an outflow of material. The whole appearance of the spectrum leads to the assumption that R Sct is composed of several different components at different velocities.

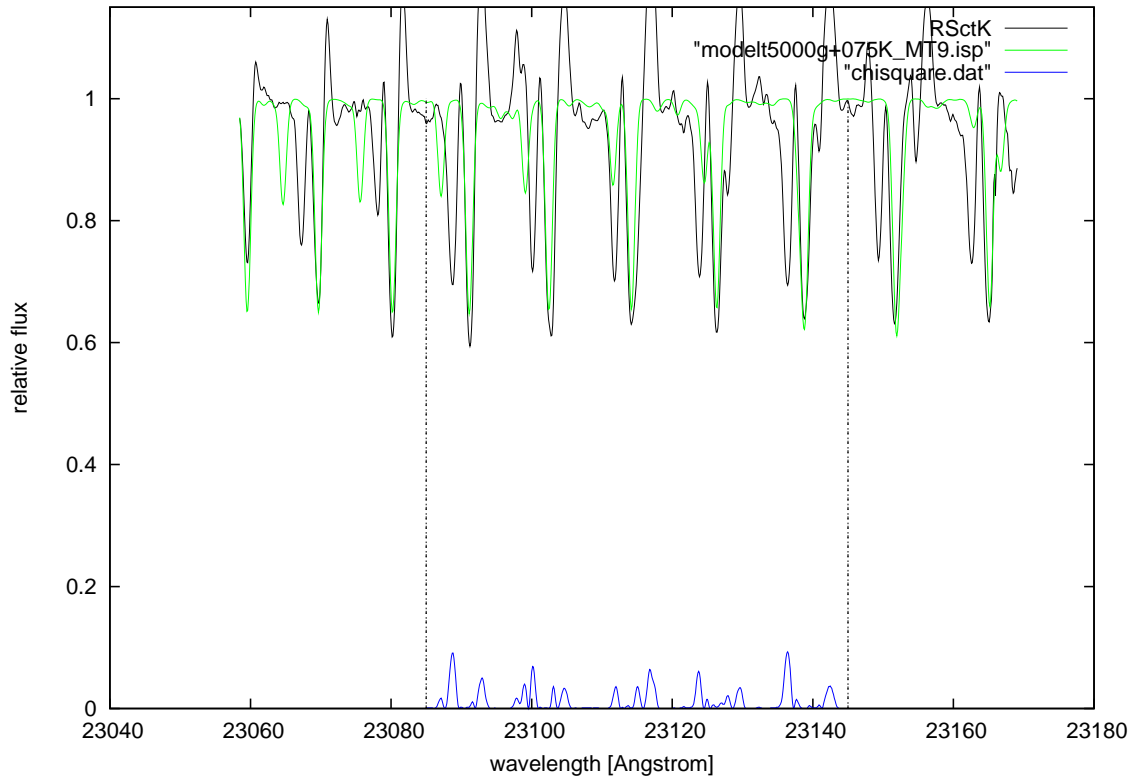


Figure 4.79: The star R Sct overplotted by a MARCS model of 5000 K, $\log g=0.75$ and $\zeta=9$ km/s.

Literature

The light variation of R Sct is irregular over an extended period of time and the alternation of minima, which is one of the three major criteria for identifying RV Tauri stars, exists only as a statistical regularity (Preston et al., 1963). The spectral class of this RVa star is found to be G0Iae-K2p(M3)Ibe (Samus et al., 1997), with a period of 146.5 days, and with its minimum light at 8.6 mag and its maximum at 4.2 mag. Based on near-infrared observations and the resulting absorption velocity curves of atoms in R Sct, and in combination with the outcome of the AAVSO light curve, Mozurkewich et al. (1987) proposed a period of 142 days.

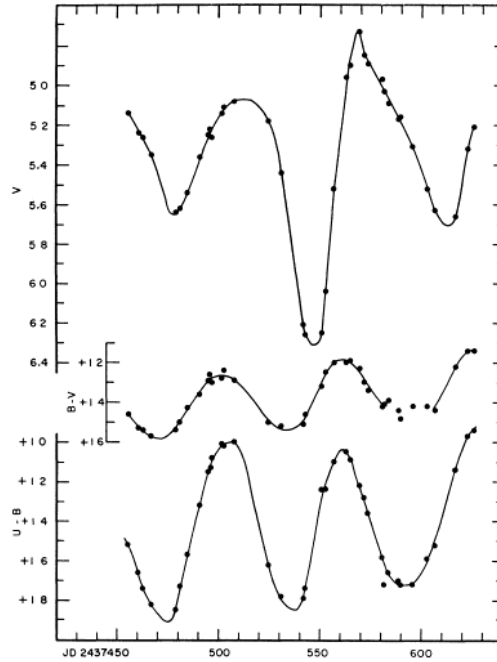


Figure 4.80: The light curve of the variable star R Sct in V, B-V and U-B (Preston, 1962).

Atmospheric parameters were derived by Luck (1981) with the following results: $T_{\text{eff}}=4400$ K, $\log g=0.0$ and microturbulent velocity=4.0 km/s. The [Fe/H] relation differs between -0.4 (Preston, 1962) and -0.9 (Luck, 1981), the latter also observed the s-process-elements to be significantly deficient (see Fig. 4.81 for the abundances found in that paper). Luck also found this star to be hydrogen-deficient, suggesting that this might be due to the evolutionary stage. An evolved star would have experienced mass loss or some kind of mixing process that would lead to a lower abundance of hydrogen at the outer part of the star. Such a scenario could change the surface ratios of metals to hydrogen, while the ratio of metals to iron would not be affected.

Preston (1962) also observed hydrogen emission and line doubling in the spectrum of R Sct at phases near maximum light, while at deep minimum, TiO is present in the spectrum. These strong TiO lines and CN lines were also confirmed by Pollard et al. (1997) at light minima. Line doubling was observed for Fe I lines and can be caused by shock waves passing through the part of the stellar atmosphere where these lines

originate (Pollard et al., 1997). Lines which form in deeper layers of the star would be affected first by the pulsation that moves outward while the shock fronts related to the pulsation will have less influence on them (Pollard et al., 1997). The emission components of the Ti I lines show a P Cygni-type profile that turns into an inverse P Cygni profile, leading to the assumption that expanding and infalling layers are present in the atmosphere of the star at the same time (Pollard et al., 1997).

Preston (1962) assumed a radial velocity of about 43.8 km/s. The $H\alpha$ emission is strongest after the primary light minima and the secondary light minima, this corresponds to two shock waves that are produced during a whole light-cycle (Pollard et al., 1997). In general it seems that the deeper and more regular the pulsations are, the stronger the $H\alpha$ emission (McLaughlin, 1939). R Sct shows a smaller infrared excess in the 11 μ m region (11.3 μ m and 12 μ m) (Evans, 1985) as well as in the 3 μ m region comparative other RV Tauri stars. There is also a small excess reported at 25 μ m and a larger one at 60 μ m.

The temperature calculated from photometry done by Goldsmith et al. (1987) is 4200 K. They also found no evidence for circumstellar dust in the spectrum, at least no hot dust over 500 K. Probably there is a cool dust shell around, that could not be detected. Raveendran (1989) also noted that this star seems to be a very peculiar object of this group of stars. It has the longest period observed within the RV Tauri group, does not exhibit the 10 μ m feature and is probably the most irregular RV Tauri star known (McLaughlin, 1932).

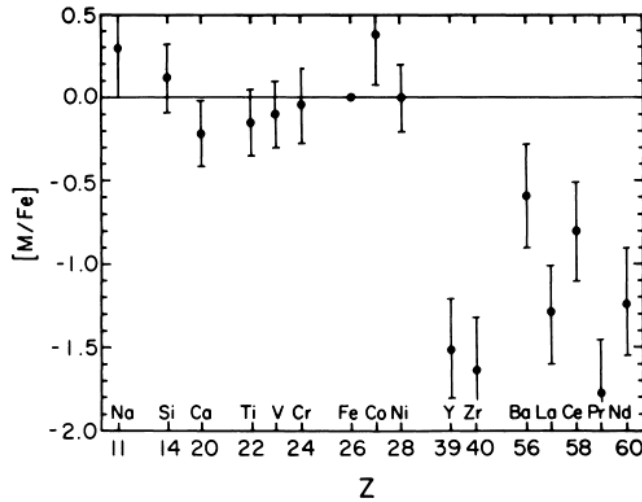


Figure 4.81: The abundances determined by Luck (1981) with respect to Fe. S-Process elements are significantly deficient.

A detailed analysis of the stellar atmosphere of R Scuti was done by Mozurkewich et al. (1987) using high resolution 2 μ m spectrograms (see Fig. 4.82). They identified lines originating from the neutral atoms of H, Ti, Si, S, Ca, Na, Mg with excitation energies between 1.7 and 8 eV and dominant molecular lines of CO (first-overtone bands), OH (first-overtone bands), and H₂O.

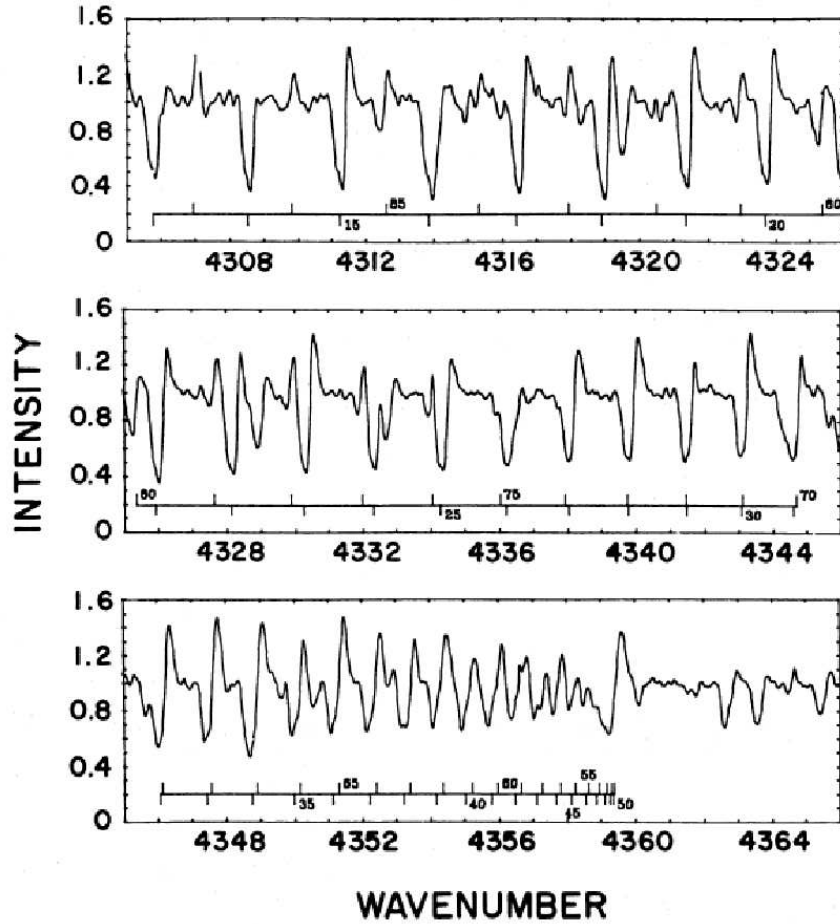


Figure 4.82: One of the spectra observed by Mozurkewich et al. (1987) with marked CO-lines. Part of the wavelength region (between 4315 and 4337 cm^{-1}) shown here was also covered by the spectrum of R Sct in the K filter in this work.

The unblended CO lines were split up into three groups, the low-J lines with $J < 25$, the mid-J lines with $28 < J < 50$, and the high-J lines with $J > 75$ (Mozurkewich et al., 1987). These averaged line profiles of the different excitation energies are shown in Fig.4.83. The change of the lines in shape and velocity during the different phases will not be described in detail here, only the results of this research will be presented in this work. Although the light curve observed seems to be quite irregular, the atomic absorption velocity curve is regular. This can be explained by the fact that above the photosphere the temperature is low enough to enable the formation of molecules. Small differences in temperature can have a significant effect on the opacity and the visible light curve. CO lines, which form higher in the atmosphere, can show larger irregularities in their velocity curves between periods due to opacity variations.

Mozurkewich et al. (1987) concluded a heliocentric mean velocity of 37 km/s . They also assume that the CO lines originate in the cooler layers of the upper atmosphere. The dominant CO feature is caused by material falling toward the star at a velocity of 20 km/s . The CO emission lines are formed when a shock front moves through the CO region every pulsation cycle and heats up the material. An extended envelope around the star should be responsible for the atomic emission, according to

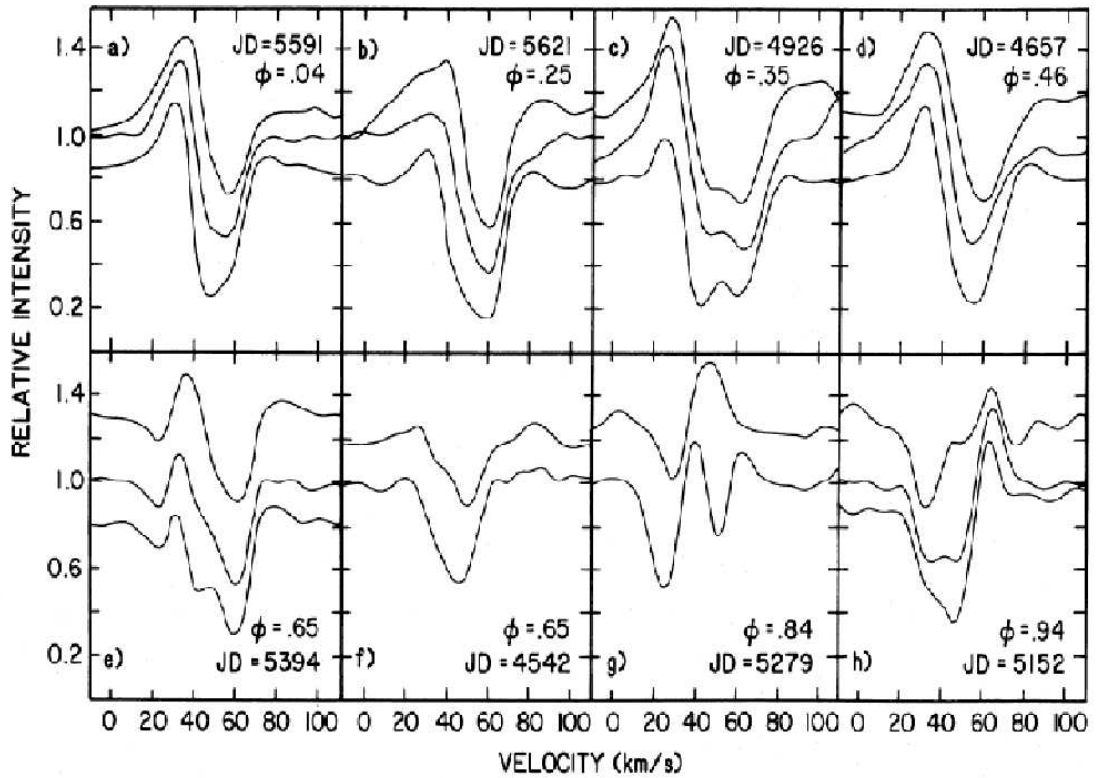


Figure 4.83: Averaged CO line profiles, starting at deep minimum light (0 phase) and continuing with increasing phase. The lines at the bottom in each panel average 0.05, the middle ones 0.2 and the lines on top 0.4 eV. In panel f) energies are 0.1 and 0.4 eV, in panel g) 0.5 and 1.7 eV for the bottom and the top lines (Mozurkewich et al., 1987).

Mozurkewich et al. (1987), but the authors were not quite sure about this last result.

Comparing the observed CO profiles of Mozurkewich et al. (1987) with the ones published in this thesis, the one at phase 0.84 (see Fig. 4.83, panel g) is probably the profile with the most similarities in shape, but with opposite velocities, meaning that mass is driven outward. The heliocentric radial velocities I derived are different in the two bandwidths: in the J-band, I found a velocity of 26.96 km/s, while the K-band measurements give values between 47.06 to 50.34 km/s, depending on the lines used.

Within the transition from AGB to PN (~ 1000 years), the estimated timescale for the RV Tauri phase is expected to be ~ 200 years (Alcolea & Bujarrabal, 1991). However, there are some RV Tauri stars that seem to linger in this variable state. R Sct seems to belong to these "lazy" objects that show peculiar envelope properties like higher molecular abundances than those of common RV Tauri stars. The continuum emission of a common RV Tauri star is dominated by a large mid- and far-IR excess combined with a lower one in the near-IR, that indicate thick envelopes of dust around the stars. The continuum emission of lazy objects like R Sct show a lower mid-IR excess and a stronger emission at wavelengths greater than $50 \mu\text{m}$. The attempt of Alcolea & Bujarrabal (1991) to explain the observations with a one-shell model failed, because the model did not fit the emission at wavelengths smaller

than $30 \mu\text{m}$. To solve this problem, a second inner shell, representing an ongoing low mass loss, was added to the outer shell that was produced by a mass loss phase in the past, i.e. the AGB wind (see Fig. 4.84). For the lazy RV Tauri star R Sct, this high mass loss event happened about 2000 years ago, this means that this star stayed in the variable state much longer than expected.

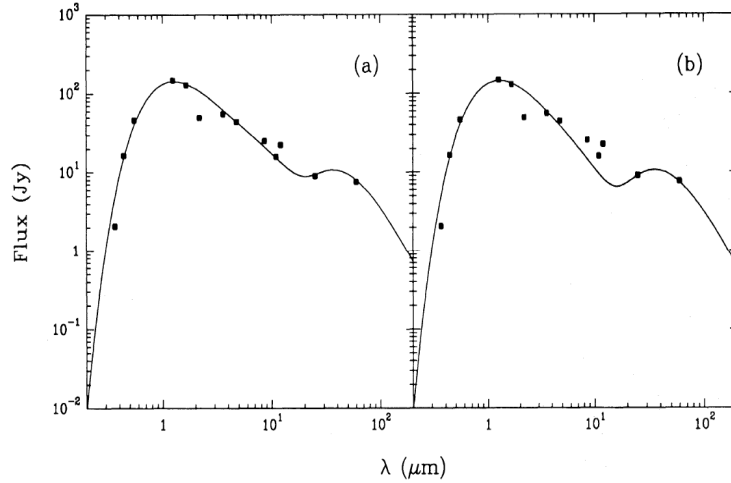


Figure 4.84: Comparison of a (a) two-shell model (solid line) and a (b) one-shell model with observational data (dots) of the "peculiar" RV Tauri variable R Sct (Alcolea & Bujarrabal, 1991).

Alcolea & Bujarrabal (1991) observed the following molecules in R Sct: CO, CS, SiO, HC_3N , HCO^+ and HCN. Compared to other star within their sample, the authors stated that R Sct has a higher CO emission and molecular abundance than observed in common RV Tauri variables. The presence of SiO indicates ongoing low mass loss because it has been proposed by Bujarrabal et al. (1989) that this molecule can only be found in regions where dust is not yet formed.

The work of Matsuura et al. (2002) confirmed the findings of Mozurkewich et al. (1987), who observed CO, H_2O and OH molecules, and present additional SiO and CO_2 bands (see Fig. 4.85). The three molecules H_2O , CO_2 , and SiO require a cooler region than the photosphere of the star to be stable, preferably an extended atmosphere. The presence of TiO absorption lines could also be assigned to the existence of such an extended atmosphere.

The structure of the H_2O lines, absorption features superimposed on emission features, suggests a cooler spherical extended shell responsible for absorption, and a warmer layer as origin for emission. The velocity profiles of the observed molecules in the extended atmosphere can be rather complicated and vary over time due to pulsation (Matsuura et al., 2002). Above this extended atmosphere lies the circumstellar envelope that expands with an approximately constant velocity.

The lazy status of R Sct proposed by Alcolea & Bujarrabal (1991) was based on the time that had elapsed since the last large mass loss phase, about 2000 years. Consid-

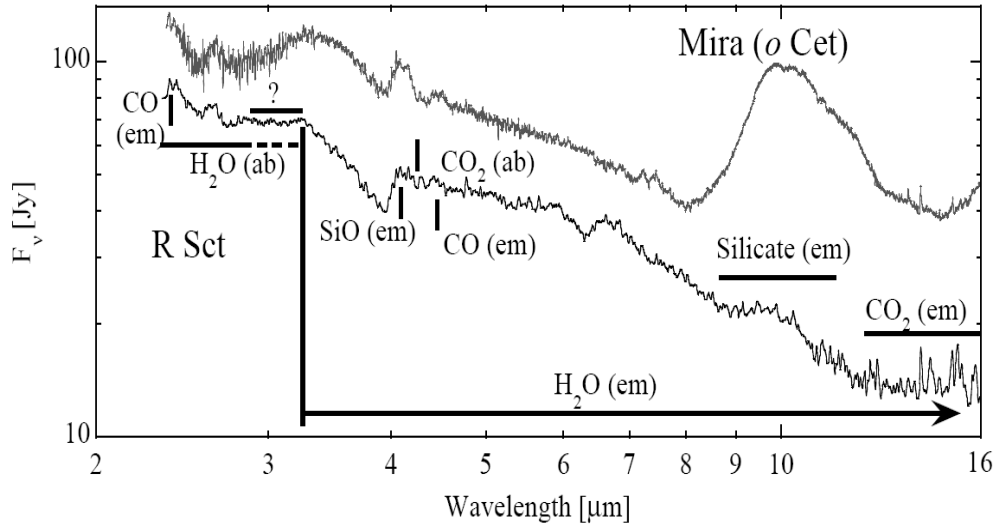


Figure 4.85: The presence of molecular features in the ISO/SWS spectra of R Sct compared to the oxygen-rich AGB star *o* Cet (Matsuura et al., 2002).

ering the expected mass loss rate at the end of the AGB phase, about $10^{-5} M_{\odot} \text{ yr}^{-1}$, the past mass loss rate of R Sct is much lower, about $10^{-7} M_{\odot} \text{ yr}^{-1}$ (Matsuura et al., 2002). The evolution of a star during its post-AGB phase suggests a decrease in period due to the reduction of stellar radius together with an increase in temperature. In the case of R Sct, the period did not change significantly over the last two hundred years. This in combination with a low abundance of s-process elements leads Matsuura et al. (2002) to the conclusion that R Sct might not be a post-AGB star after all.

Giridhar et al. (2000a) suggested that R Sct has not reached the tip of the AGB yet, and Matsuura et al. (2002) support this idea by presenting a theory that this star could be in the helium-burning phase of the thermal-pulse cycle. There are different indications for this proposition, for example a decrease in mass loss after a thermal pulse and a stillstand or reverse of period evolution during the helium-burning phase. The time scale of about 5000 years for this phase of evolution seems to fit the observed properties of R Sct quite well.

Szczerba et al. (2007) took the work of Matsuura et al. (2002) into consideration and decided to *disqualify* R Sct as a post-AGB star in *The Toruń catalogue of Galactic post-AGB and related objects*.

Chapter 5

Summary

Following the individual star description this general summary gives a résumé of the results, sorted by filter and variability class as far as possible. In this section I try to find properties and features which can be found in all of the stars of one type and to find dissimilarities, that can be assigned to specialities of the individual star observed. This overview is completed by a composition of comparison stars as well, the spectra for every single comparison star can be found in appendix B.

The J filter spectral region does not feature many lines, therefore the spectra observed in this filter are not as interesting as in e.g. the K filter. The spectra of the variable stars and those of the comparison stars are quite similar, so no conclusion about the properties or peculiarities of the estimated post-AGB objects can be drawn here.

In the H filter, most of the variable stars exhibit line-broadening and blending, but whether this can be assigned to their evolutionary phase or to peculiarities in the individual stars is not sure. The number of lines observable in this wavelength range can help estimate the ratio of metallic lines in comparison to molecular lines, especially the strength and presence of OH lines were very interesting.

The most promising filter seems to be the K filter, because in the three cases observations of variable stars in K were available, all of them showed emission lines as well as absorption lines in their spectra. This can lead to assumptions of the structure of the object, probably some kind of shell or detached component. This could be assigned to a post-AGB stage, where the envelope is removed and blown away from the star.

Due to the fact that AR Pup is the only star observed in another special region (named K*), this star was left out of the comparison done in this chapter. It is difficult to draw a scientific conclusion for the whole group of post-AGB candidate objects from a single spectrum of a possible post-AGB star taken in another wavelength range than the other programm star spectra. The analysis of this spectrum was made nonetheless because the spectral region seems promising, like the other K spectra.

5.1 J Filter

The first five stars presented here are of the variable type RVa, while the next two are either of unknown RV type or a not further specified variable class. The last two stars, α Boo and δ Oph were used as comparison stars/calibration stars.

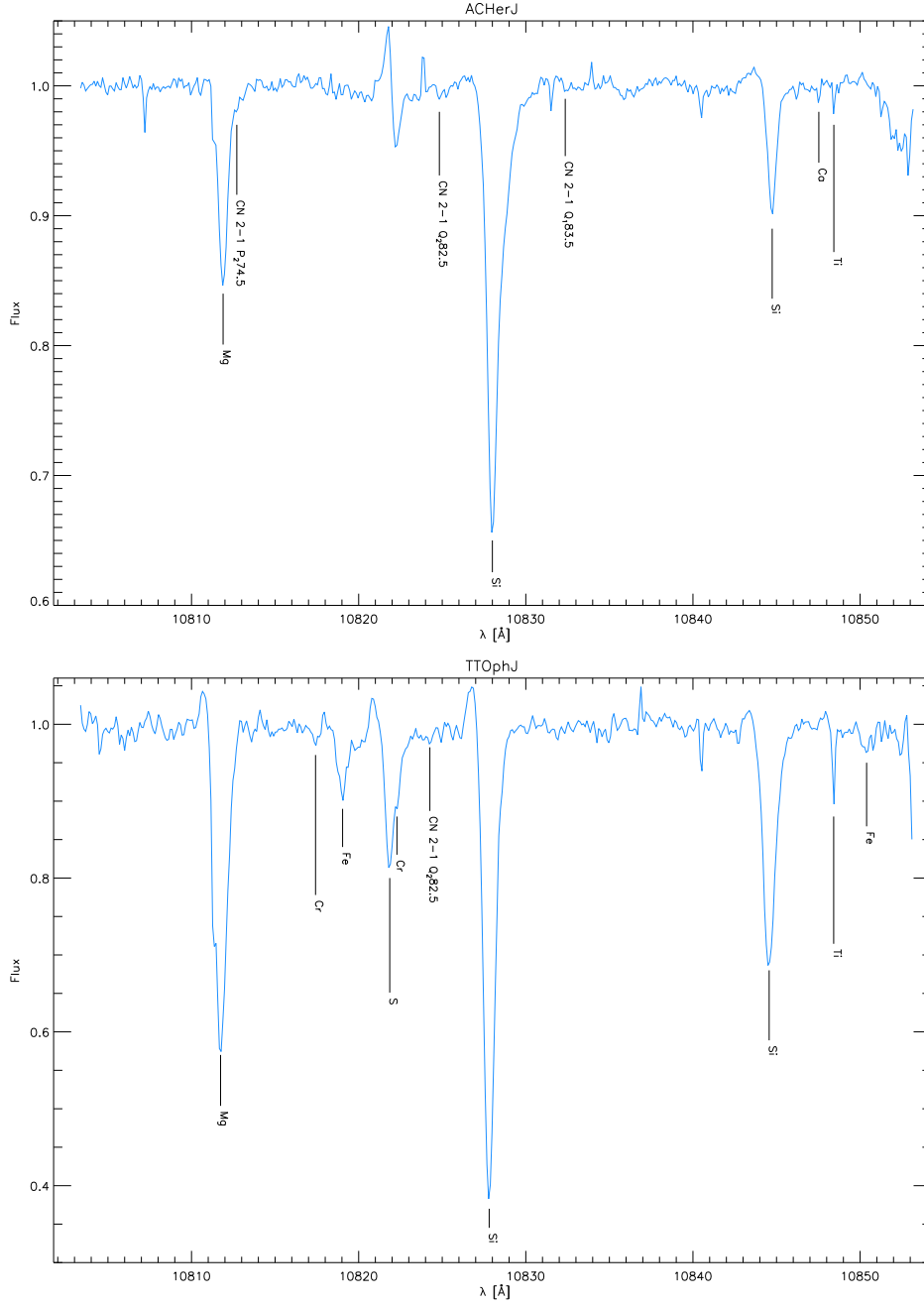


Figure 5.1: The two RVa stars AC Her and TT Oph in the J filter.

AC Her is a F4 Ib star that shows no Fe lines in this part of the spectrum. The CN lines are weak, the dominant features are the two Si lines and the Mg line. In the case of TT Oph, a F5 star, a inverse P-Cygni profile seems to be present. The atomic lines are rather strong while the only CN line identified is rather weak.

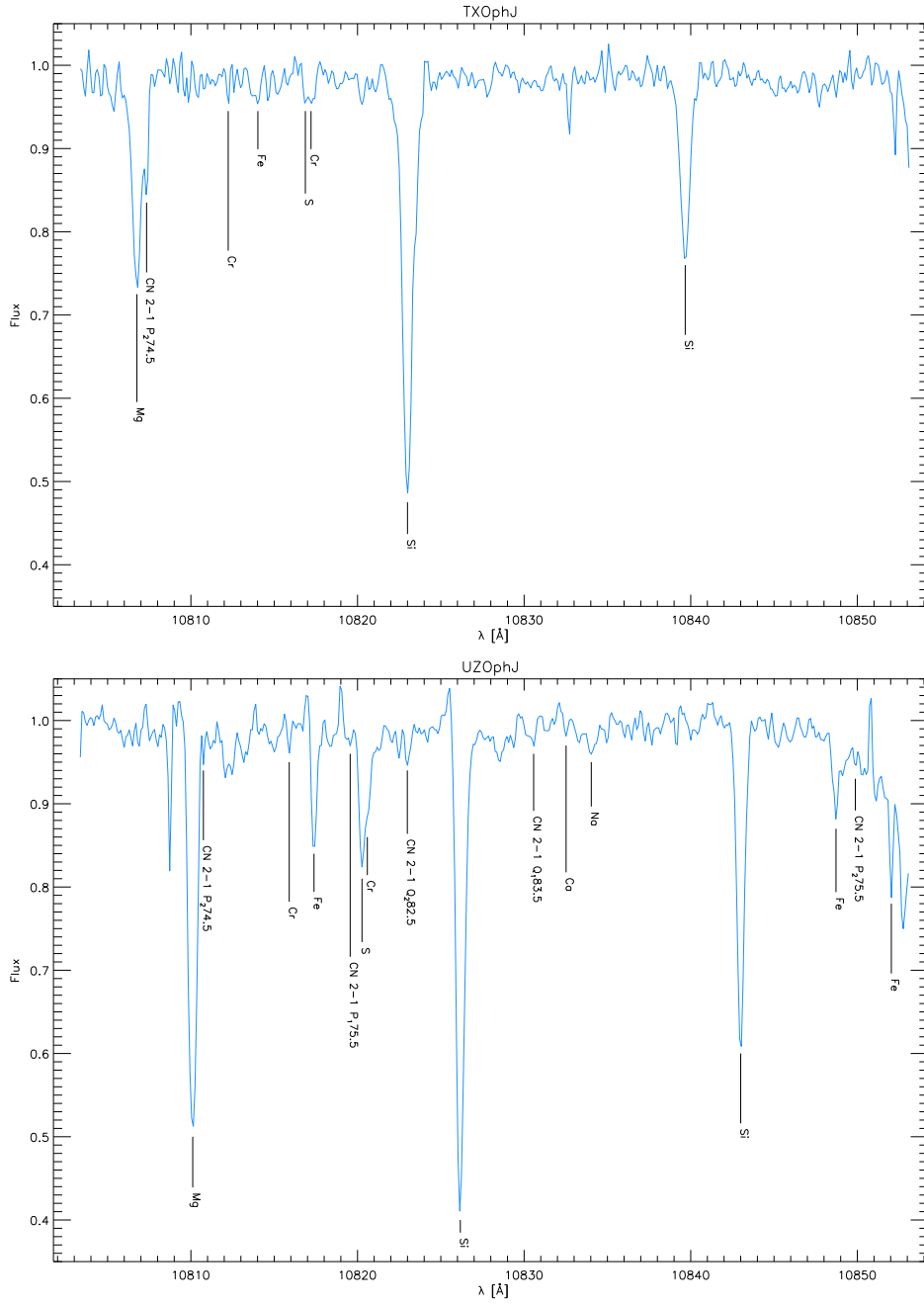


Figure 5.2: The two RVa stars TX Oph and UZ Oph in the J filter.

TX Oph belongs to spectral type G0 while UZ Oph is classified as a G2 type star. The strongest line by far in the first star is the Si line near 10823 \AA . The other lines seem to vanish in the rather uneven expected continuum. This kind of continuum can also be found in the latter star, UZ Oph. But here the atomic lines as well as the CN lines are better to define. There seems to be some kind of inverse P-Cygni profile, but the shaky continuum makes it hard to be sure.

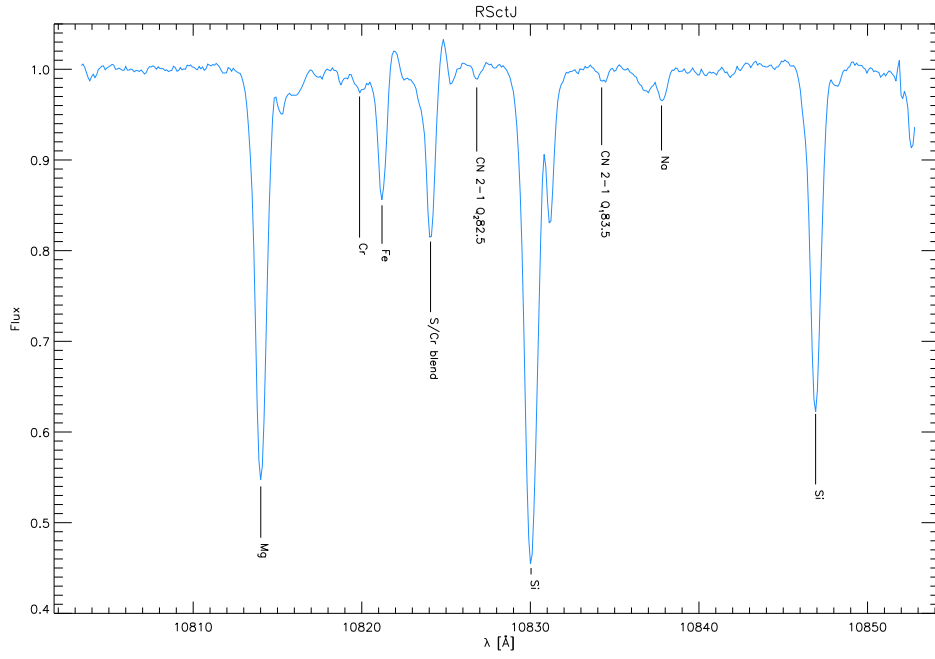


Figure 5.3: The RVa star R Sct in the J filter.

R Sct, a K0 Ib star, exhibits a smooth continuum with well defined lines in the spectrum. Emission components seem to be present, but it is difficult to assign them to an atomic or a molecular species.

The candidate stars in the J-filter seem to show emission sometimes in a P-Cygni-like profile. The atomic lines of Mg and Si are always the dominant features, while the presence of CN lines can be confirmed only for some stars and the CN lines present are not always the same.

HD 143352 is labeled as RV Tauri type variable uncertain, while θ Her was listed only as a variable star. One can see the difference in the spectra.

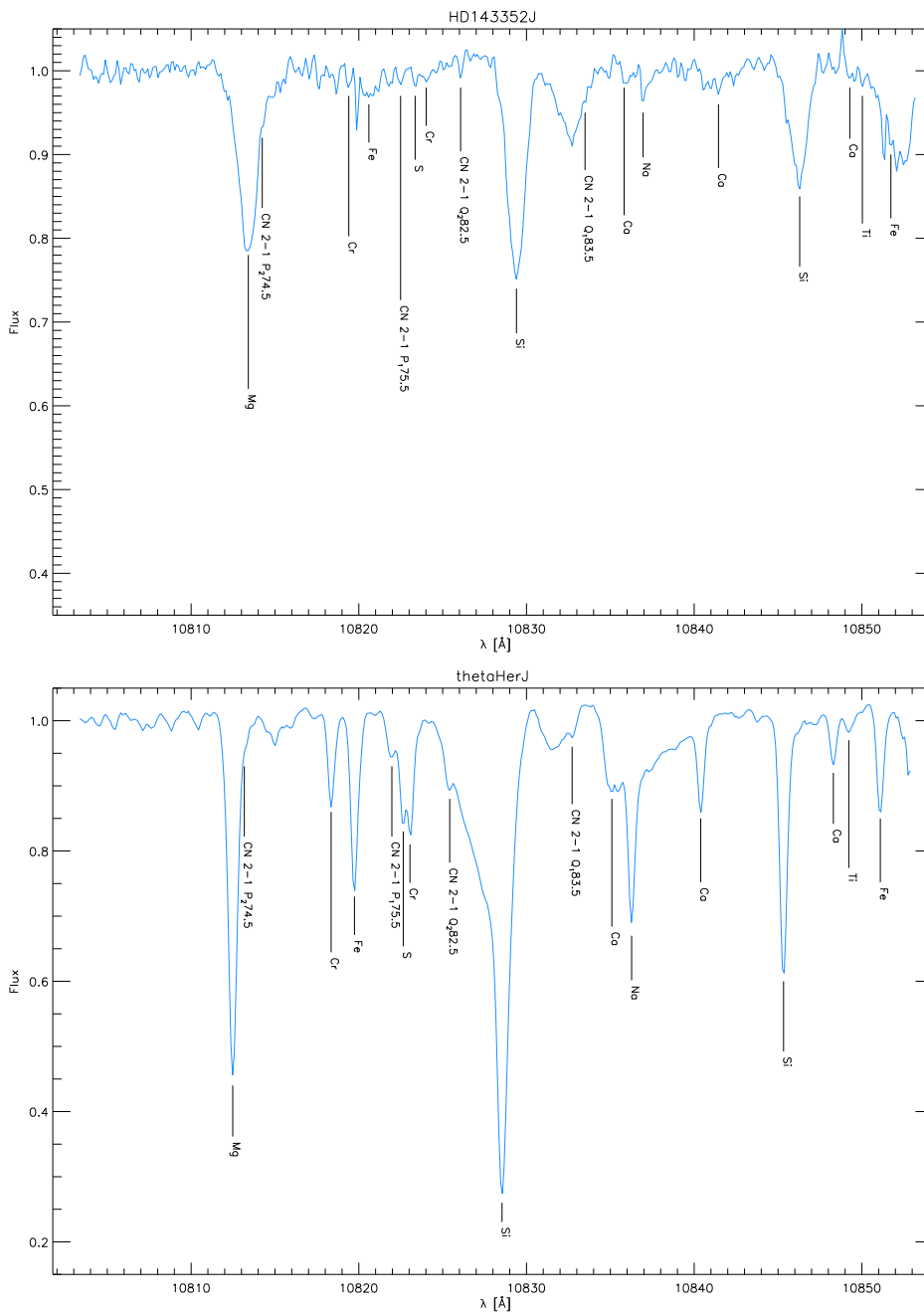


Figure 5.4: These two variable stars, HD 143352 and θ Her, are of unknown variable type.

These two stars of type F2 (HD 143352) and K1 IIa (θ Her), are quite different: HD 143352 shows very broad lines, probably broadened by macroturbulence, with an unknown feature at about 10833 Å. This spectrum looks totally different from the spectra of the other variable stars.

The same can be applied to the spectrum of θ Her. There is some kind of depression between the CN 2-1 Q₂82.5 line and the Si line at 10828.5 Å. All the atomic lines are present and of sharp and narrow shape.

The two comparison stars, α Boo and δ Oph.

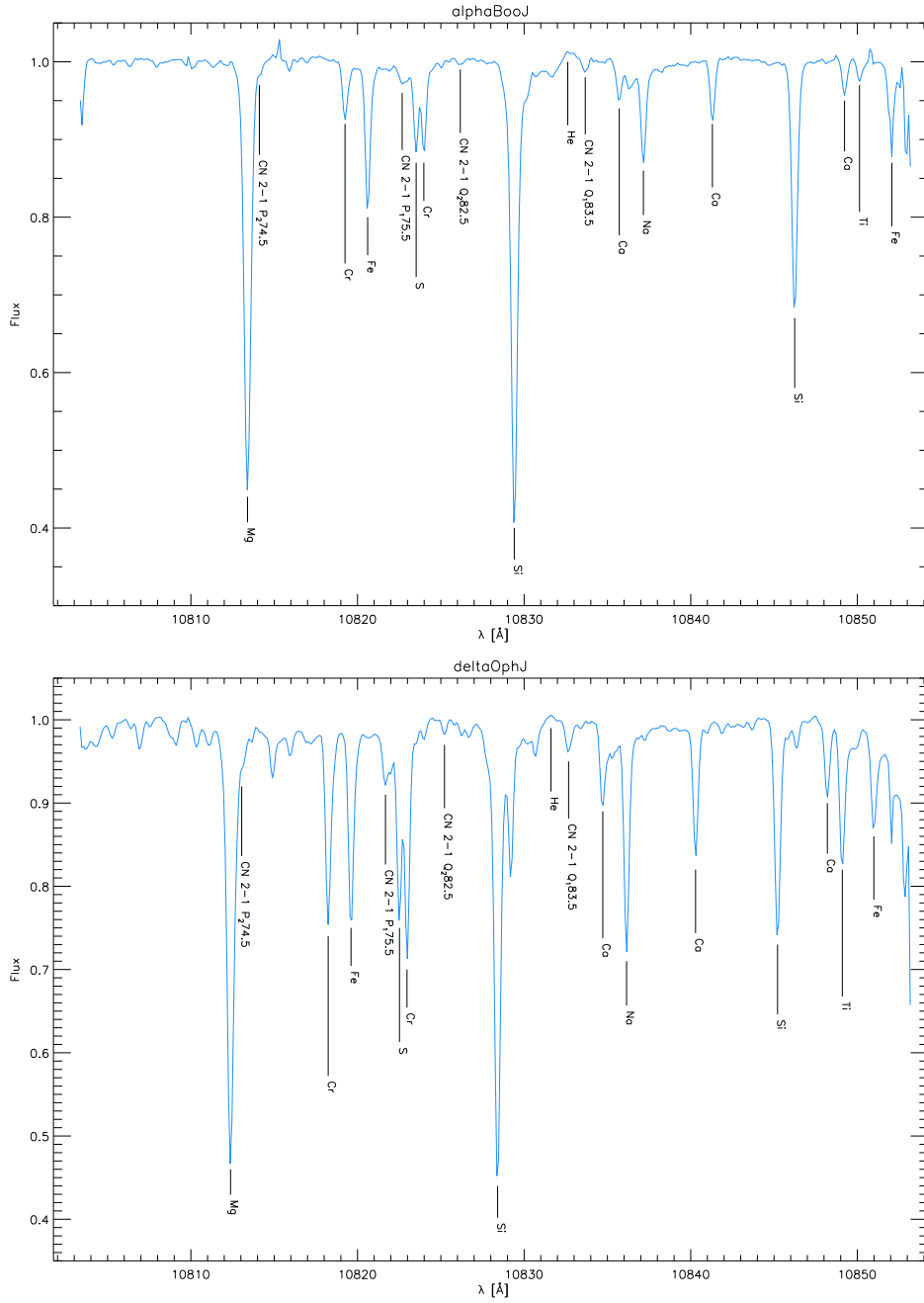


Figure 5.5: The two comparison stars α Boo and δ Oph in the J filter.

Both of these comparison stars are of luminosity class III. α Boo is a metal deficient K1.5 star with a rather flat continuum and well defined lines. The M0.5 star δ Oph has stronger metal lines than α Boo.

5.2 H Filter

The next three pages show the spectra of six variable stars of the SRd type in the H filter.

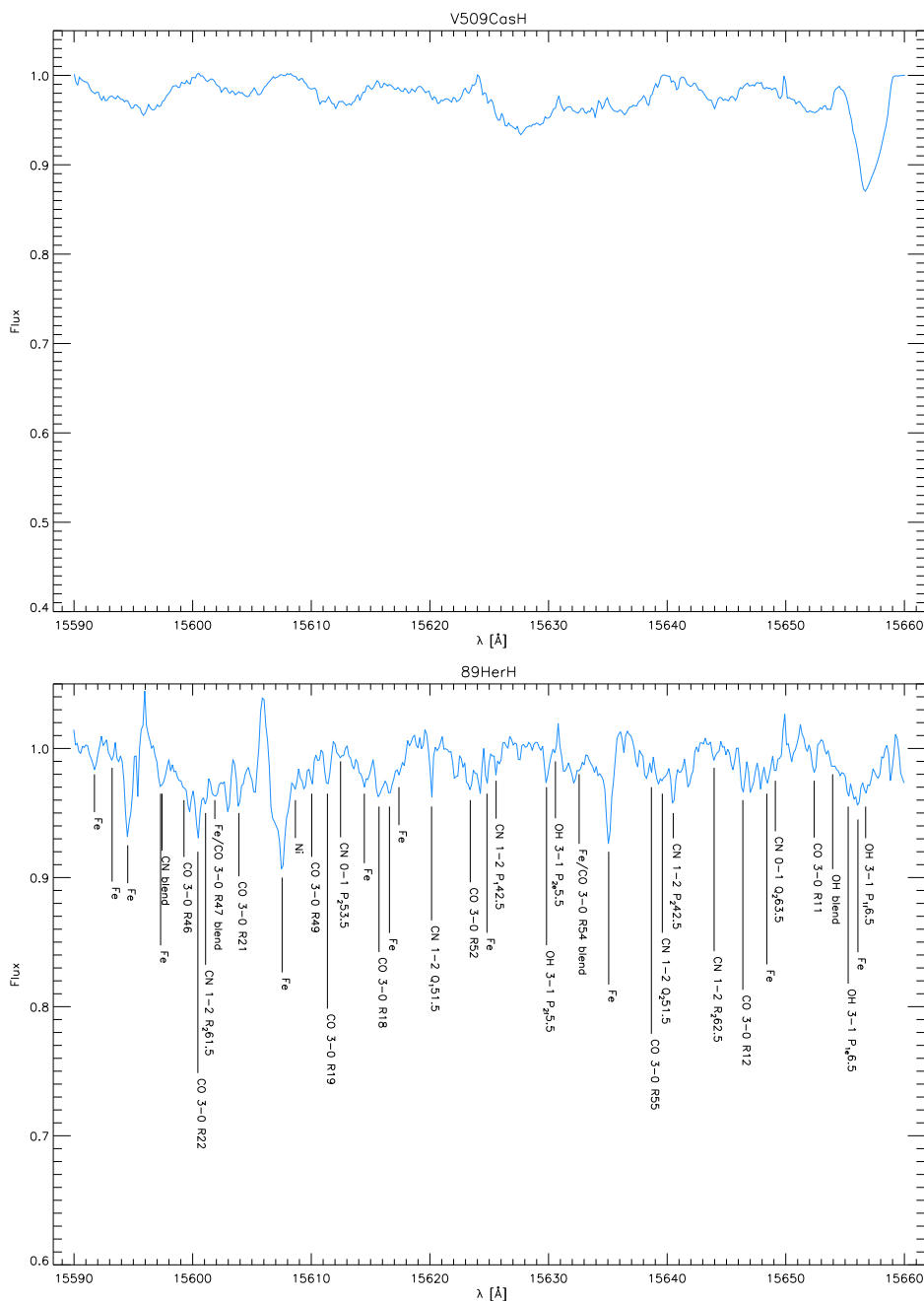


Figure 5.6: The two SRd stars V509 Cas and 89 Her in the H filter.

The first star of my sample, V509 Cas, is classified a SRd star with spectral type G0 and luminosity type Iab, but unfortunately there were no lines present in this spectral range to confirm this classification. If one has a look at the OH lines in the F2 Ib star 89 Her, they are very weak, almost not present.

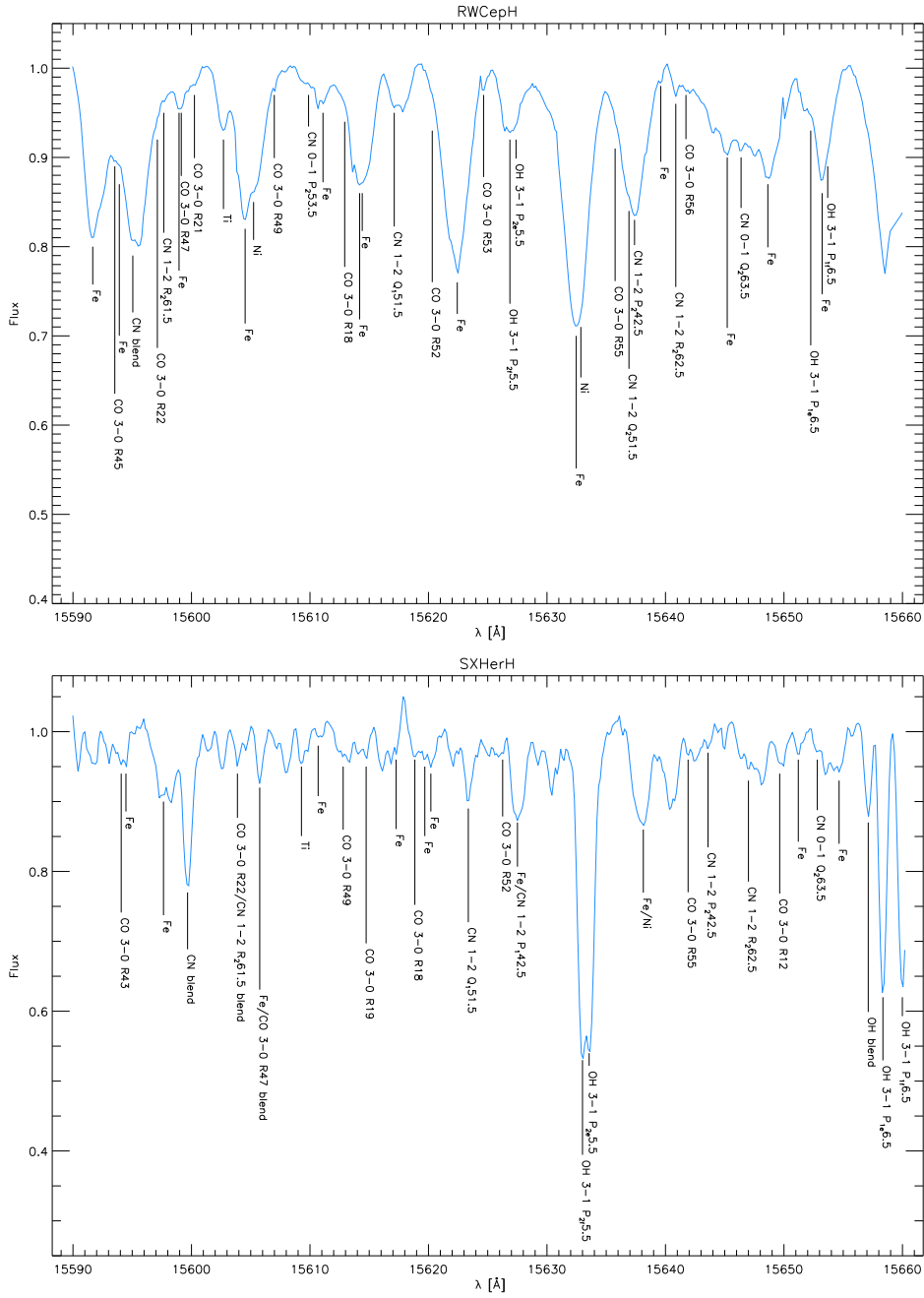


Figure 5.7: The two SRd stars RW Cep and SX Her in the H filter.

The most obvious difference between these two K2 type stars is the presence of such strong OH lines in SX Her. Compared to the other lines identified in this spectrum, the OH lines are the most dominant ones. The lines of RW Cep are broadened and blended, but still quite strong.

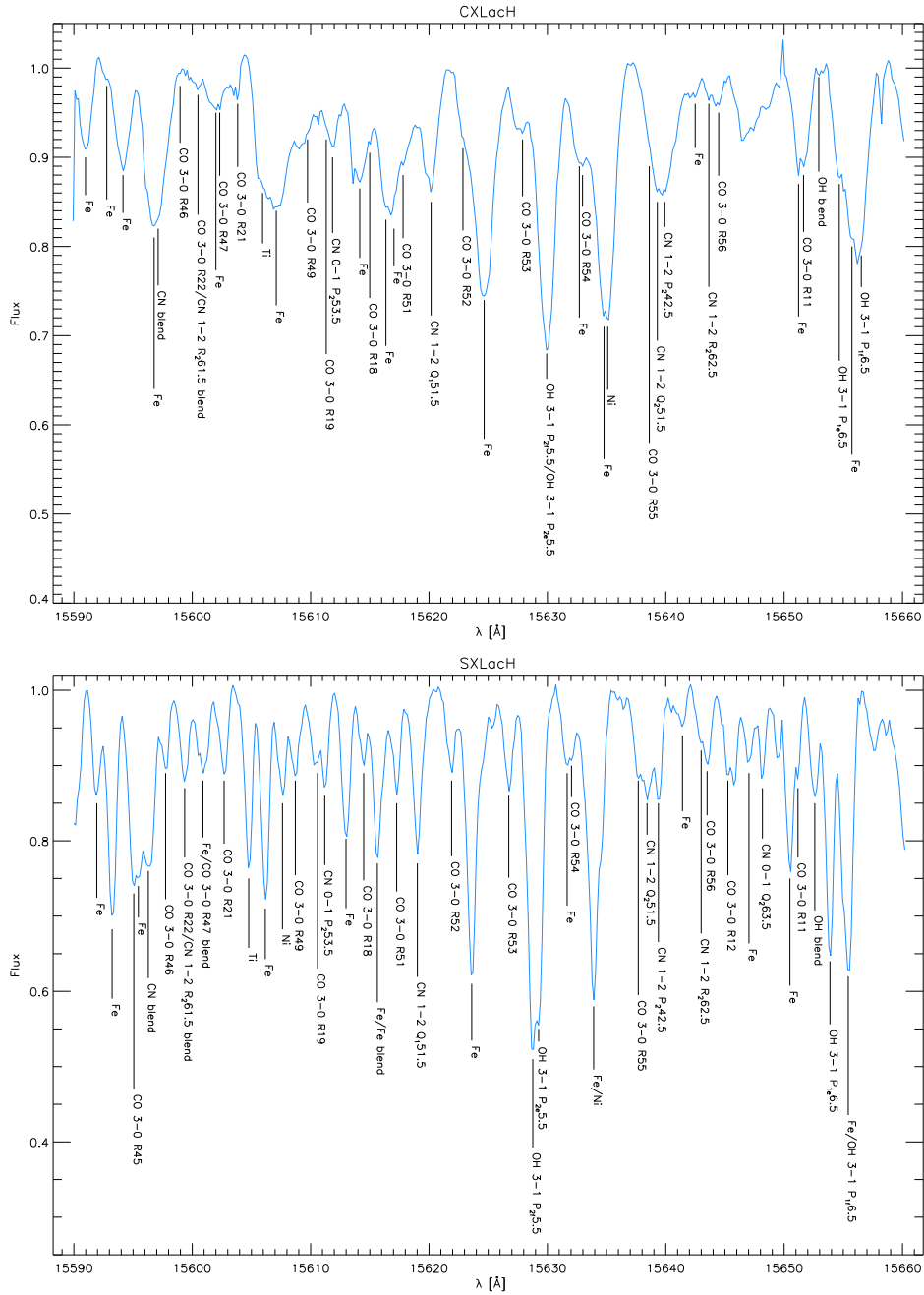
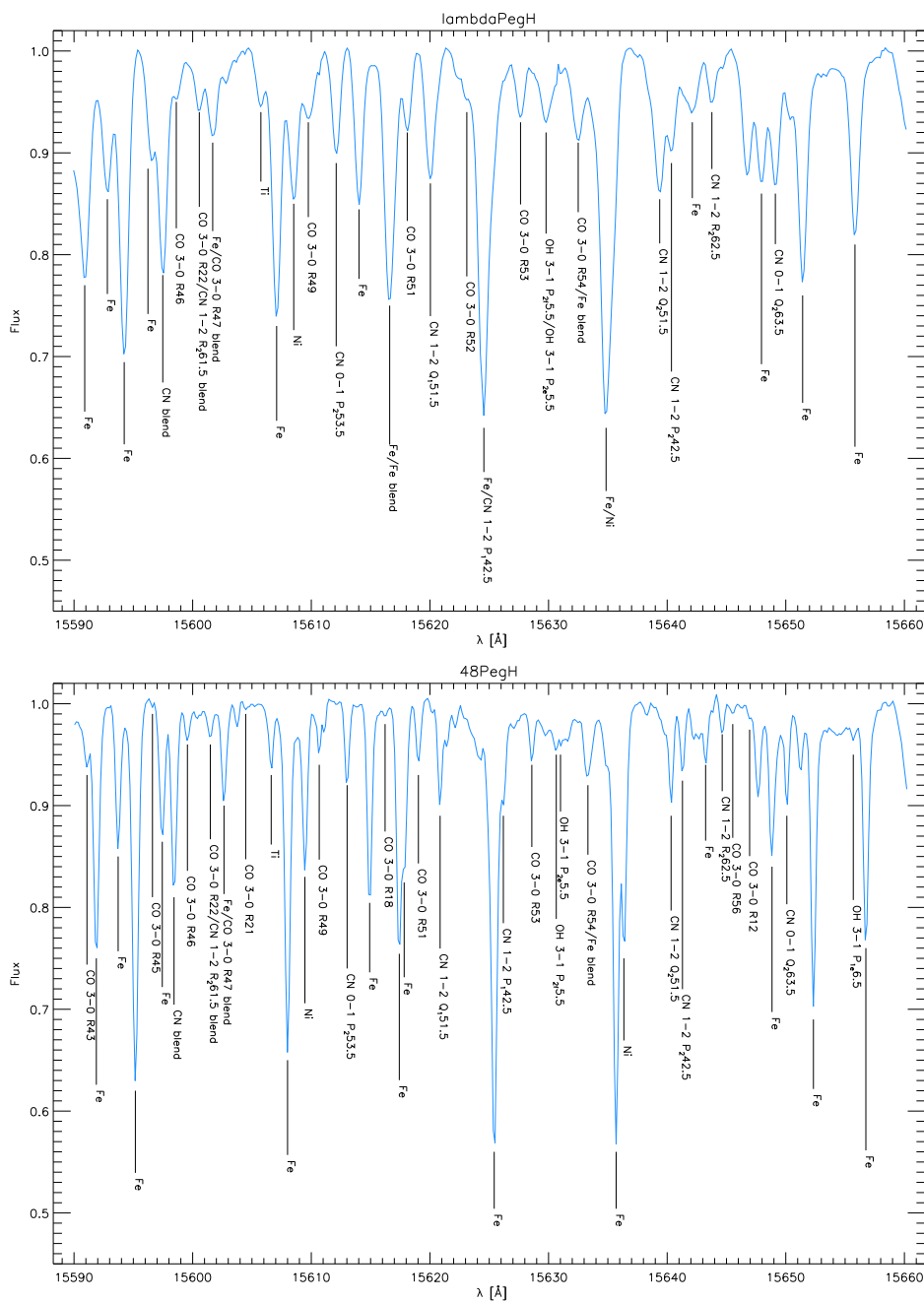


Figure 5.8: The two SRd stars CX Lac and SX Lac in the H filter.

SX Lac, a M0 star, on the bottom of the page exhibits small, sharp and well defined lines. The spectrum as such is in good agreement with the spectra of the comparison stars. CX Lac of spectral type K5 looks more like RW Cep mentioned above. The lines are broadened, there are often blends of lines and the continuum is difficult to locate due to the numerous declines in flux.

In the spectrum of the G8 Iab star λ Peg less lines have been identified than in the other comparison stars. As one can see, the lines are broadened here and most of the molecule lines are weak, e.g. the two OH lines that are blended with each other. The G8 III star μ Peg has strong metal lines, but there seems to be almost no OH in the spectrum.



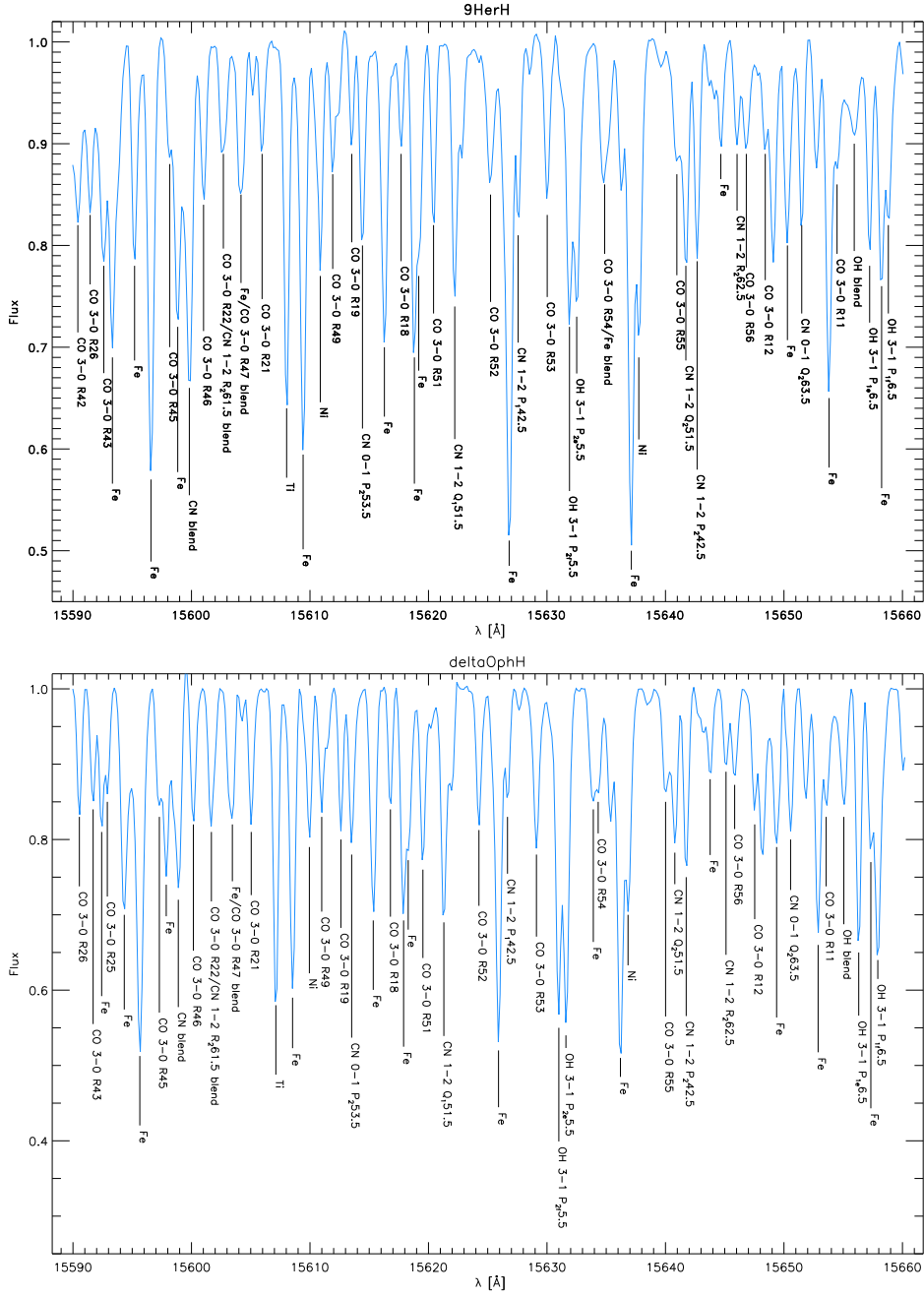


Figure 5.11: The two comparison stars 9 Her and δ Oph in the H filter.

The spectra of these two stars were used as calibration spectra and should therefore show no specialities. In fact they are quite similar, δ Oph, a M0.5 III star, at the bottom of the page, seems a bit enriched in OH compared to 9 Her, a K5 III star, because these lines are stronger in the former star. Another explanation is the difference in T_{eff} between the two stars, that can cause this effect. Metal lines are again the strongest lines in the spectra, and the lines are well separated from each other.

5.3 K Filter

All three RVa variable stars observed show a P-Cygni like structure in their spectra with strong emission lines.

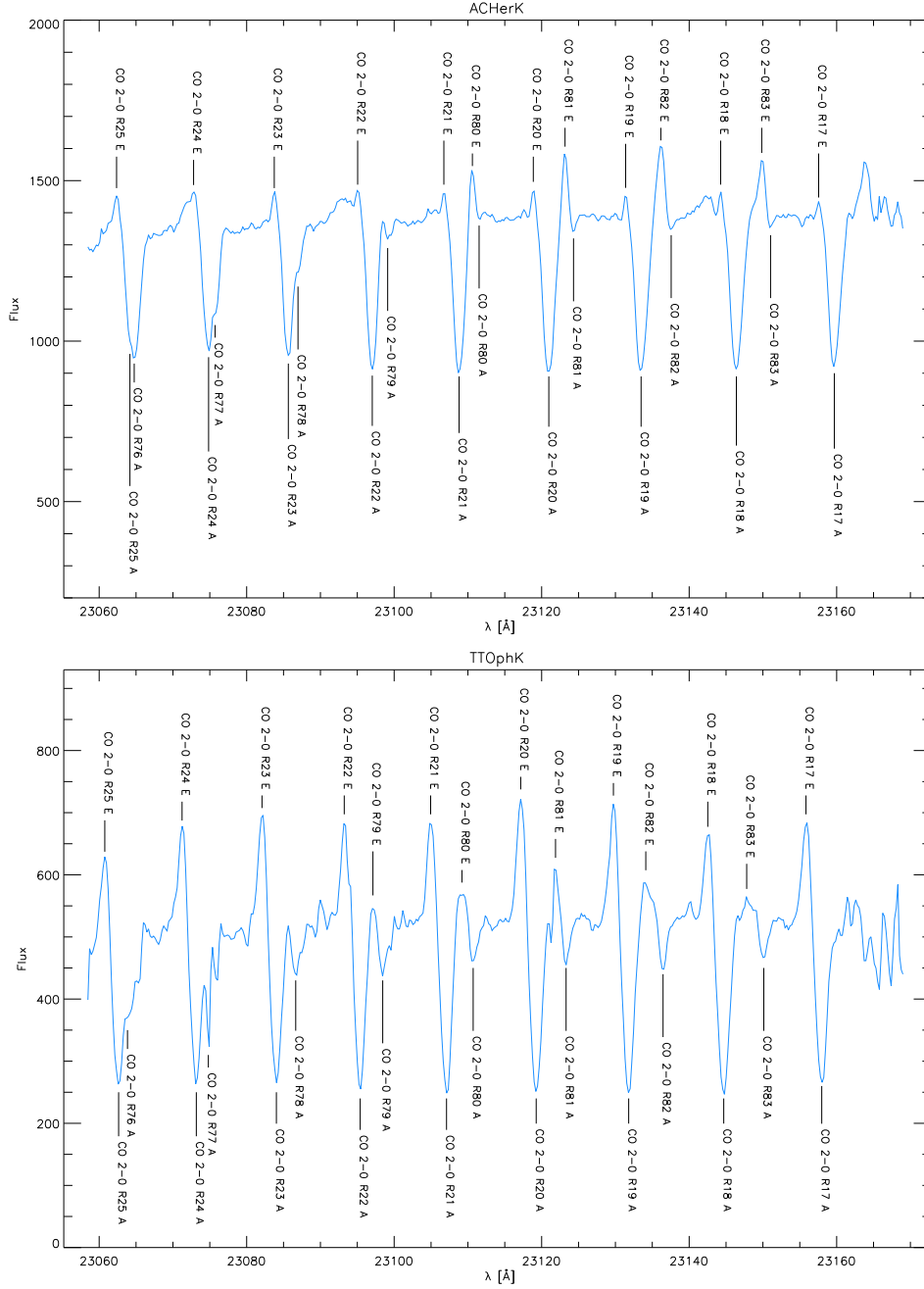


Figure 5.12: The two RVa variable stars AC Her and TT Oph in the K filter.

The upper panel shows AC Her, a F4 Ib type star, with absorption lines that are always stronger than the emission lines, which get stronger on the blueward side of the spectrum.

TT Oph below, a F5 type star, shows a more complicate spectrum with strong lines in emission and absorption. The strongest emission line seems to be the CO 2-0 R20 line followed by the emission component of the R19 line.

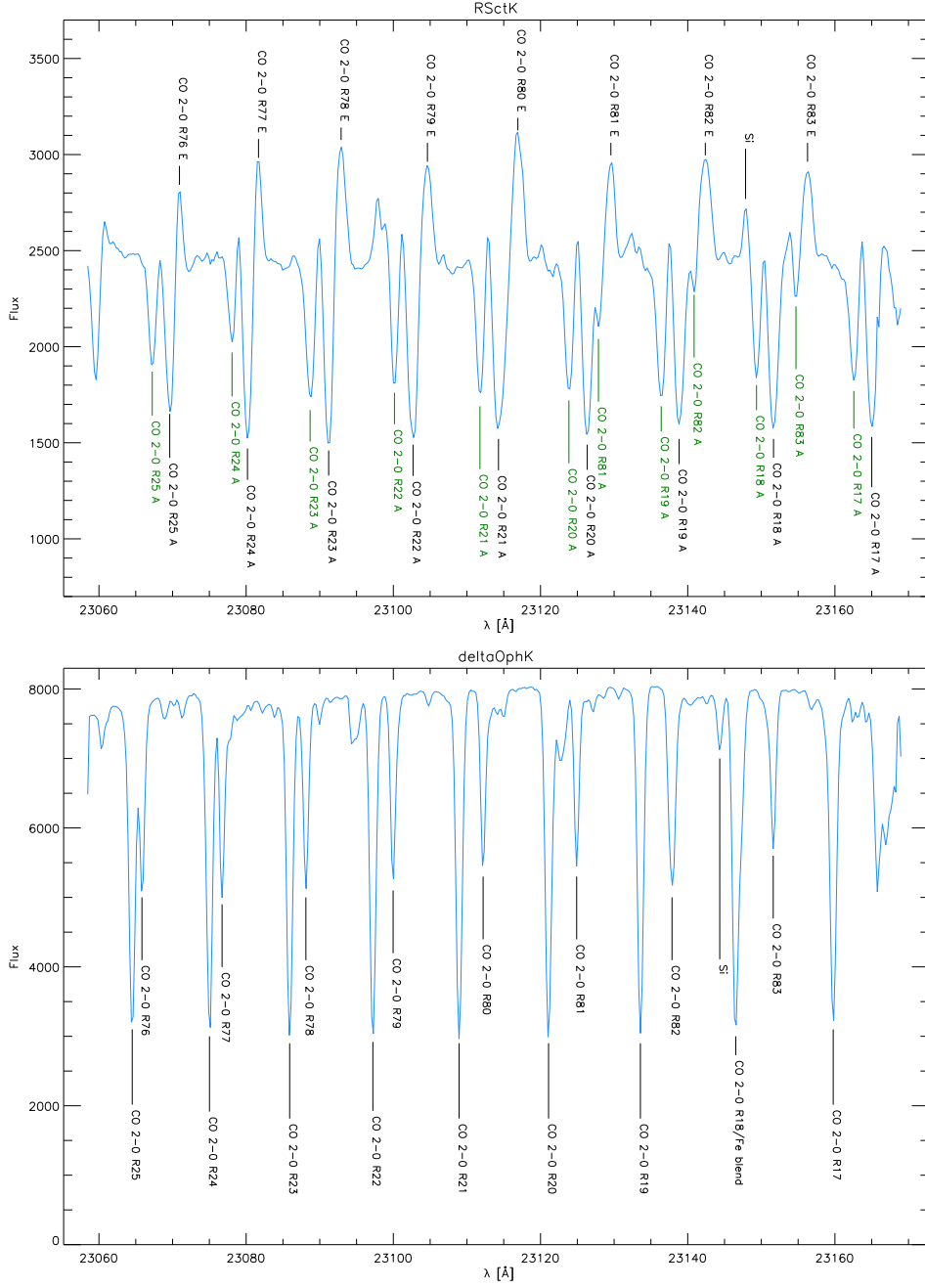


Figure 5.13: The RVa variable star R Sct and the comparison star delta Oph in the K filter.

R Sct on top exhibits the most interesting spectrum of the whole sample. This star belongs to spectral class K0 and luminosity class Ib. There seems to be a second component of the star, a hull or shell of some kind, that is responsible for the red-shifted absorption lines (labeled in green). Another component (labeled in black) shows all the high-excitation lines in emission and the low-excitation ones in absorption.

δ Oph is the only comparison star observed in this spectrum, a M0.5 III star. As one can see, there is only one metal line, namely Si, in this spectral range. The

low-excited absorption lines are stronger than the high-excited ones.

The spectra of AC Her and TT Oph seem to be quite similar, despite the fact that the lines in TT Oph seem stronger. Due to the fact that I was not able to draw a continuum through the spectra in this filter, the y-values are not really comparable to each other. It would be interesting to analyse more stars of the RV Tauri class in this spectral range as well as some SRd stars to be able to estimate if this is a characteristic of this group or just a coincidence.

The spectrum of R Sct also shows the well-known P-Cygni profile, but the existence of another component of this star that might be responsible for the second set of lines makes this spectrum a special case. The question is: can this appearance of another component be expected in other RV Tauri stars too or is R Sct no RVa star? In *The Toruń catalogue of Galactic post-AGB and related objects* by Szczerba et al. (2007) the post-AGB status of this star seems to be questionable. This decision is based on the work of Matsuura et al. (2002), who propose that R Sct could be in the helium-burning phase of the thermal-pulse cycle and not in the post-AGB phase.

Further observations in the K-filter might help to answer this question and could also help to find out more about the atmospheric structure of post-AGB stars.

Bibliography

- Acker, A., Marcout, J., Ochsenbein, F., Stenholm, B., & Tylanda, R. 1992, Strasbourg - ESO catalogue of galactic planetary nebulae. Part 1; Part 2 (Garching: European Southern Observatory, 1992)
- Aikawa, T. & Bruegman, O. 1987, *Astrophysics and Space Science*, 137, 115
- Alcolea, J. & Bujarrabal, V. 1991, *Astronomy and Astrophysics*, 245, 499
- Alcolea, J., Bujarrabal, V., & Planesas, P. 1993, in *Astronomical Society of the Pacific Conference Series*, Vol. 45, *Luminous High-Latitude Stars*, ed. D. D. Sasselov, 123
- Allamandola, L. J., Tielens, A. G. G. M., & Barker, J. R. 1989, *Astrophysical Journal*, Supplement, 71, 733
- Arellano Ferro, A. 1984, *Publications of the ASP*, 96, 641
- Arellano-Ferro, A. 1985, *Revista Mexicana de Astronomia y Astrofisica*, 11, 113
- Ayres, T. R. 2005, *Astrophysical Journal*, 618, 493
- Baird, S. R. 1981, *Astrophysical Journal*, 245, 208
- Barden, S. C. & Ramsey, L. W. 1980, *Publications of the ASP*, 92, 497
- Binney, J. & Merrifield, M. 1998, *Galactic astronomy* (Princeton, NJ : Princeton University Press, 1998. (Princeton series in astrophysics) QB857 .B522 1998)
- Bloecker, T. 1995a, *Astronomy and Astrophysics*, 299, 755
- . 1995b, *Astronomy and Astrophysics*, 297, 727
- Boothroyd, A. I. & Sackmann, I.-J. 1992, *Astrophysical Journal*, Letters, 393, L21
- Bowen, G. H. 1988, *Astrophysical Journal*, 329, 299
- Buchler, J. R., Kolláth, Z., & Cadmus, Jr., R. R. 2004, *Astrophysical Journal*, 613, 532
- Buchler, J. R. & Kovacs, G. 1987, *Astrophysical Journal*, Letters, 320, L57
- Bujarrabal, V., Gomez-Gonzalez, J., & Planesas, P. 1989, *Astronomy and Astrophysics*, 219, 256
- Bujarrabal, V., Van Winckel, H., Neri, R., Alcolea, J., Castro-Carrizo, A., & Deroo, P. 2007, *Astronomy and Astrophysics*, 468, L45

- Busso, M., Gallino, R., & Wasserburg, G. J. 1999, *Annual Review of Astronomy and Astrophysics*, 37, 239
- Busso, M., Palmerini, S., Maiorca, E., Cristallo, S., Straniero, O., Abia, C., Gallino, R., & La Cognata, M. 2010, *Astrophysical Journal, Letters*, 717, L47
- Cameron, A. G. W. & Fowler, W. A. 1971, *Astrophysical Journal*, 164, 111
- Cardelli, J. A. & Howell, S. B. 1989, *Astronomical Journal*, 98, 311
- Clayton, G. C. 1996, *Publications of the ASP*, 108, 225
- Climenhaga, J. L., Smoliński, J., Krempeć-Krygier, J., Krygier, B., & Krawczyk, S. 1987, in *IAU Symposium, Vol. 122, Circumstellar Matter*, ed. I. Appenzeller & C. Jordan, 329
- Dawson, D. W. 1979, *Astrophysical Journal, Supplement*, 41, 97
- Dawson, D. W. & Patterson, C. R. 1982, *Publications of the ASP*, 94, 574
- de Jager, C. & Nieuwenhuijzen, H. 1997, *Monthly Notices of the RAS*, 290, L50
- De Ruyter, S., Van Winckel, H., Maas, T., Lloyd Evans, T., Waters, L. B. F. M., & Dejonghe, H. 2006, *Astronomy and Astrophysics*, 448, 641
- Deupree, R. G. & Hodson, S. W. 1976, *Astrophysical Journal*, 208, 426
- Dickens, R. J., Croke, B. F. W., Cannon, R. D., & Bell, R. A. 1991, *Nature*, 351, 212
- Drake, S. A., Brown, A., & Linsky, J. L. 1984a, *Astrophysical Journal*, 284, 774
- Drake, S. A., Brown, A., & Linsky, J. L. 1984b, in *NASA Conference Publication, Vol. 2349, NASA Conference Publication*, ed. J. M. Mead, R. D. Chapman, & Y. Kondo, 472
- DuPuy, D. L. 1973, *Astrophysical Journal*, 185, 597
- DuPuy, D. L., Allwright, J. W. B., Dawson, D. W., & Africano, J. L. 1983, *Publications of the ASP*, 95, 427
- Eggen, O. J. 1974, *Publications of the ASP*, 86, 129
- Engvold, O. & Rygh, B. O. 1978, *Astronomy and Astrophysics*, 70, 399
- Evans, T. L. 1985, *Monthly Notices of the RAS*, 217, 493
- Feast, M. W., Woolley, R., & Yilmaz, N. 1972, *Monthly Notices of the RAS*, 158, 23
- Fernie, J. D. 1981, *Astrophysical Journal*, 243, 576
- Fokin, A. B. 1994, *Astronomy and Astrophysics*, 292, 133
- Fusi Pecci, F., Ferraro, F. R., Bellazzini, M., Djorgovski, S., Piotto, G., & Buonanno, R. 1993, *Astronomical Journal*, 105, 1145

- Gehrz, R. D. & Ney, E. P. 1972, *Publications of the ASP*, 84, 768
- Gehrz, R. D. & Woolf, N. J. 1970, *Astrophysical Journal, Letters*, 161, L213
- Gerasimovič, B. P. 1929, *Harvard College Observatory Circular*, 341, 1
- Gielen, C., Van Winckel, H., Waters, L. B. F. M., Min, M., & Dominik, C. 2007, *Astronomy and Astrophysics*, 475, 629
- Gillett, F. C., Hyland, A. R., & Stein, W. A. 1970, *Astrophysical Journal, Letters*, 162, L21
- Giridhar, S. 1988, in *IAU Symposium, Vol. 132, The Impact of Very High S/N Spectroscopy on Stellar Physics*, ed. G. Cayrel de Strobel & M. Spite, 407
- Giridhar, S., Lambert, D. L., & Gonzalez, G. 1998a, *Astrophysical Journal*, 509, 366
- . 1998b, *Publications of the ASP*, 110, 671
- . 1999, *Publications of the ASP*, 111, 1269
- . 2000a, *Astrophysical Journal*, 531, 521
- . 2000b, *Publications of the ASP*, 112, 1559
- Giridhar, S., Lambert, D. L., Reddy, B. E., Gonzalez, G., & Yong, D. 2005, *Astrophysical Journal*, 627, 432
- Giridhar, S., Rao, N. K., & Lambert, D. L. 1994, *Astrophysical Journal*, 437, 476
- Goebel, J. H. & Moseley, S. H. 1985, *Astrophysical Journal, Letters*, 290, L35
- Goldsmith, M. J., Evans, A., Albinson, J. S., & Bode, M. F. 1987, *Monthly Notice of the RAS*, 227, 143
- Gontcharov, G. A. 2006, *Astronomy Letters*, 32, 759
- Gonzalez, G., Lambert, D. L., & Giridhar, S. 1997, *The Astrophysical Journal*, 479, 427
- Guillois, O., Ledoux, G., & Reynaud, C. 1999, *Astrophysical Journal, Letters*, 521, L133
- Gustafsson, B., Bell, R. A., Eriksson, K., & Nordlund, A. 1975, *Astronomy and Astrophysics*, 42, 407
- Gustafsson, B. & Höfner, S. 2003, in *Asymptotic giant branch stars (Astronomy and astrophysics library, New York, Berlin: Springer, 2003)*, 149
- Habing, H. J. & Olofsson, H., eds. 2003a, *Asymptotic giant branch stars*
- Habing, H. J. & Olofsson, H. 2003b, in *Asymptotic giant branch stars (Astronomy and astrophysics library, New York, Berlin: Springer, 2003)*, 1
- Harper, G. M. 1992, *Monthly Notices of the RAS*, 256, 37

- Hartmann, L., Dupree, A. K., Jordan, C., & Brown, A. 1985, *Astrophysical Journal*, 296, 576
- Hertzsprung, E. 1911, *Publikationen des Astrophysikalischen Observatoriums zu Potsdam*, 63
- Herwig, F. 2005, *Annual Review of Astronomy and Astrophysics*, 43, 435
- Hinkle, K., Wallace, L., & Livingston, W. 1995, *Publications of the ASP*, 107, 1042
- Iben, Jr., I. 1984, *Astrophysical Journal*, 277, 333
- Iben, Jr., I., Kaler, J. B., Truran, J. W., & Renzini, A. 1983, *Astrophysical Journal*, 264, 605
- Iben, I. J. 1967, *Annual Review of Astronomy and Astrophysics*, 5, 571
- . 1991, *Astrophysical Journal, Supplement*, 76, 55
- Iben, I. J., Tutukov, A. V., & Yungelson, L. R. 1996, *Astrophysical Journal*, 456, 750
- Iliadis, C. 2007, *Nuclear Physics of Stars* (Wiley-VCH Verlag)
- Jaschek, C. & Jaschek, M. 1990, *The Classification of Stars* (The Classification of Stars, by Carlos Jaschek and Mercedes Jaschek, pp. 427. ISBN 0521389968. Cambridge, UK: Cambridge University Press, July 1990.)
- Jorgensen, U. G., Johnson, H. R., & Nordlund, A. 1992, *Astronomy and Astrophysics*, 261, 263
- Joy, A. H. 1952, *Astrophysical Journal*, 115, 25
- Joyce, R. R. 1992, in *Astronomical Society of the Pacific Conference Series*, Vol. 23, *Astronomical CCD Observing and Reduction Techniques*, ed. S. B. Howell, 258
- Jura, M. 1986, *Astrophysical Journal*, 309, 732
- Jura, M., Chen, C., & Werner, M. W. 2000, *The Astrophysical Journal*, 541, 264
- Kastner, J. H., Henn, L., Weintraub, D. A., & Gatley, I. 1999, in *IAU Symposium*, Vol. 191, *Asymptotic Giant Branch Stars*, ed. T. Le Bertre, A. Lebre, & C. Waelkens, 431
- Keenan, P. C. & McNeil, R. C. 1989, *Astrophysical Journal, Supplement*, 71, 245
- Khalilov, A. M., Samedov, Z. A., & Hasanova, A. R. 2008, *Astronomy Reports*, 52, 847
- Kurucz, R. L. 1979, *Astrophysical Journal, Supplement*, 40, 1
- Lambert, D. L. & Luck, R. E. 1978, *Monthly Notices of the RAS*, 184, 405
- Lattanzio, J. C. & Wood, P. R. 2003, in *Asymptotic giant branch stars* (*Astronomy and astrophysics library*, New York, Berlin: Springer, 2003), 23

- Lebzelter, T. & Hron, J. 2003, *Astronomy and Astrophysics*, 411, 533
- Likkel, L., Morris, M., Omont, A., & Forveille, T. 1987, *Astronomy and Astrophysics*, 173, L11
- Luck, R. E. 1975, *Astrophysical Journal*, 202, 743
- . 1981, *Publications of the ASP*, 93, 211
- Luck, R. E., Bond, H. E., & Lambert, D. L. 1990, *Astrophysical Journal*, 357, 188
- Luck, R. E. & Lambert, D. L. 1981, *Astrophysical Journal*, 245, 1018
- Mathis, J. S. & Lamers, H. J. G. L. M. 1992, *Astronomy and Astrophysics*, 259, L39
- Matsuura, M., Yamamura, I., Zijlstra, A. A., & Bedding, T. R. 2002, *Astronomy and Astrophysics*, 387, 1022
- McLaughlin, D. B. 1932, *Publications of Michigan Observatory*, 4, 135
- . 1939, *Publications of Michigan Observatory*, 7, 57
- McWilliam, A. 1990, *Astrophysical Journal, Supplement*, 74, 1075
- Merrill, P. W. & Wilson, O. C. 1956, *Astrophysical Journal*, 123, 392
- Molster, F. J., Waters, L. B. F. M., Trams, N. R., Van Winckel, H., Decin, L., van Loon, J. T., Jäger, C., Henning, T., Käufl, H., de Koter, A., & Bouwman, J. 1999, *Astronomy and Astrophysics*, 350, 163
- Morgenroth, O. 1939, *Astronomische Nachrichten*, 268, 273
- Mozurkewich, D., Gehrz, R. D., Hinkle, K. H., & Lambert, D. L. 1987, *Astrophysical Journal*, 314, 242
- Nuth, J. A., Moseley, S. H., Silverberg, R. F., Goebel, J. H., & Moore, W. J. 1985, *Astrophysical Journal, Letters*, 290, L41
- Oinas, V. 1977, *Astronomy and Astrophysics*, 61, 17
- Olofsson, H. 1999, in *IAU Symposium, Vol. 191, Asymptotic Giant Branch Stars*, ed. T. Le Bertre, A. Lebre, & C. Waelkens, 3
- Olofsson, H. 2003, in *Asymptotic giant branch stars (Astronomy and astrophysics library, New York, Berlin: Springer, 2003)*, 325
- Omont, A., Forveille, T., Moseley, S. H., Glaccum, W. J., Harvey, P. M., Likkel, L., Loewenstein, R. F., & Lisse, C. M. 1990, *Astrophysical Journal, Letters*, 355, L27
- Omont, A., Loup, C., Forveille, T., te Lintel Hekkert, P., Habing, H., & Sivagnanam, P. 1993, *Astronomy and Astrophysics*, 267, 515
- Ostlie, D. A. & Cox, A. N. 1986, *Astrophysical Journal*, 311, 864
- Oudmaijer, R. D., Waters, L. B. F. M., van der Veen, W. E. C. J., & Geballe, T. R. 1995, *Astronomy and Astrophysics*, 299, 69

- Paczynski, B. 1970, *Acta Astronomica*, 20, 47
- Parthasarathy, M. & Pottasch, S. R. 1986, *Astronomy and Astrophysics*, 154, L16
- Percy, J. R. & Kolin, D. L. 2000, *Journal of the American Association of Variable Star Observers (JAAVSO)*, 28, 1
- Peterson, R. C., Rood, R. T., & Crocker, D. A. 1995, *Astrophysical Journal*, 453, 214
- Pollard, K. R., Cottrell, P. L., Kilmartin, P. M., & Gilmore, A. C. 1996, *Monthly Notices of the RAS*, 279, 949
- Pollard, K. R., Cottrell, P. L., Lawson, W. A., Albrow, M. D., & Tobin, W. 1997, *Monthly Notices of the RAS*, 286, 1
- Preston, G. & Wallerstein, G. 1963, *Astrophysical Journal*, 138, 820
- Preston, G. W. 1962, *Astrophysical Journal*, 136, 866
- Preston, G. W., Krzeminski, W., Smak, J., & Williams, J. A. 1963, *Astrophysical Journal*, 137, 401
- Raveendran, A. V. 1989, *Monthly Notices of the RAS*, 238, 945
- . 1999, *Monthly Notices of the RAS*, 303, 595
- Rayner, J. T., Cushing, M. C., & Vacca, W. D. 2009, *Astrophysical Journal*, Supplement, 185, 289
- Rego, M. E., Williams, P. M., & Peat, D. W. 1972, *Monthly Notices of the RAS*, 160, 129
- Reimers, D. 1975, *Circumstellar envelopes and mass loss of red giant stars* (B. Baschek, W.H. Kegel, G. Traving (eds.), Springer, Berlin), 229
- . 1982, *Astronomy and Astrophysics*, 107, 292
- Rosenberg, H. 1911, *Astronomische Nachrichten*, 186, 71
- Sackmann, I., Boothroyd, A. I., & Kraemer, K. E. 1993, *Astrophysical Journal*, 418, 457
- Sackmann, I.-J. & Boothroyd, A. I. 1992, *Astrophysical Journal*, Letters, 392, L71
- Samus, N. N., Durlevich, O. V., & Kazarovets, R. V. 1997, *Baltic Astronomy*, 6, 296
- Sandage, A. & Wildey, R. 1967, *Astrophysical Journal*, 150, 469
- Sargent, W. L. W. 1965, *The Observatory*, 85, 33
- Sargent, W. L. W. & Osmer, P. S. 1969, in *Astrophysics and Space Science Library*, Vol. 13, *Mass Loss from Stars*, ed. M. Hack, 57
- Schoenberner, D. 1983, *Astrophysical Journal*, 272, 708

- Schoenberger, D. 1986, in *Astrophysics and Space Science Library*, Vol. 128, IAU Colloq. 87: Hydrogen Deficient Stars and Related Objects, ed. K. Hunger, D. Schoenberger, & N. Kameswara Rao, 471
- Searle, L., Sargent, W. L. W., & Jugaku, J. 1963, *Astrophysical Journal*, 137, 268
- Shapiro, L. 1972, *Astronomical Journal*, 77, 215
- Shokin, Y. A. & Samus, N. N. 1997, *Information Bulletin on Variable Stars*, 4429, 1
- Smith, G. 1998, *Astronomy and Astrophysics*, 339, 531
- Smith, V. V. & Lambert, D. L. 1990, *Astrophysical Journal, Supplement*, 72, 387
- Smolinski, J., Climenhaga, J., & Fletcher, J. M. 1986, in *IAU Symposium*, Vol. 116, *Luminous Stars and Associations in Galaxies*, ed. C. W. H. de Loore, A. J. Willis, & P. Laskarides, 89
- Smolinski, J., Climenhaga, J. L., Funakawa, H., & Fletcher, J. M. 1982, *Information Bulletin on Variable Stars*, 2229, 1
- Smolinski, J., Climenhaga, J. L., Huang, Y., Jiang, S., Schmidt, M., & Stahl, O. 1993, *Space Science Reviews*, 66, 231
- Smolinski, J., Feldman, P. A., & Higgs, L. A. 1977, *Astronomy and Astrophysics*, 60, 277
- Soubiran, C., Bienaymé, O., Mishenina, T. V., & Kovtyukh, V. V. 2008, *Astronomy and Astrophysics*, 480, 91
- Stanghellini, L., García-Lario, P., García-Hernández, D. A., Perea-Calderón, J. V., Davies, J. E., Manchado, A., Villaver, E., & Shaw, R. A. 2007, *The Astrophysical Journal*, 671, 1669
- Stickland, D. J. & Harmer, D. L. 1978, *Astronomy and Astrophysics*, 70, L53
- Suntzeff, N. B. 1981, *Astrophysical Journal, Supplement*, 47, 1
- Sylvester, R. J., Skinner, C. J., & Barlow, M. J. 1998, *Monthly Notices of the RAS*, 301, 1083
- Szczerba, R., Siódmiak, N., Stasińska, G., & Borkowski, J. 2007, *Astronomy and Astrophysics*, 469, 799
- Takeuti, M. & Petersen, J. O. 1983, *Astronomy and Astrophysics*, 117, 352
- Trams, N. R., Waters, L. B. F. M., Lamers, H. J. G. L. M., Waelkens, C., Geballe, T. R., & The, P. S. 1991, *Astronomy and Astrophysics, Supplement*, 87, 361
- Trams, N. R., Waters, L. B. F. M., Waelkens, C., Lamers, H. J. G. L. M., & van der Veen, W. E. C. J. 1989, *Astronomy and Astrophysics*, 218, L1
- Unsöld, A. & Baschek, B. 2002, *Der neue Kosmos. Einführung in die Astronomie und Astrophysik (Der neue Kosmos / Albrecht Unsöld, Bodo Baschek. 7. Auflage. Berlin, Germany: Springer, ISBN 3-540-42177-7, 2002, XIV + 575 pp.)*

- van der Veen, W. E. C. J. & Habing, H. J. 1988, *Astronomy and Astrophysics*, 194, 125
- Van Winckel, H. 1997, *Astronomy and Astrophysics*, 319, 561
- . 2003, *Annual Review of Astronomy and Astrophysics*, 41, 391
- Van Winckel, H., Waelkens, C., Fernie, J. D., & Waters, L. B. F. M. 1999, *Astronomy and Astrophysics*, 343, 202
- Van Winckel, H., Waelkens, C., Waters, L. B. F. M., Molster, F. J., Udry, S., & Bakker, E. J. 1998, *Astronomy and Astrophysics*, 336, L17
- Vassiliadis, E. & Wood, P. R. 1993, *Astrophysical Journal*, 413, 641
- von Helden, G., Tielens, A. G. G. M., van Heijnsbergen, D., Duncan, M. A., Hony, S., Waters, L. B. F. M., & Meijer, G. 2000, *Science*, 288, 313
- Waelkens, C. & Waters, L. B. F. M. 1993, in *Astronomical Society of the Pacific Conference Series*, Vol. 45, *Luminous High-Latitude Stars*, ed. D. D. Sasselov, 219
- Waelkens, C. & Waters, R. B. F. M. 2003, in *Asymptotic giant branch stars (Astronomy and astrophysics library*, New York, Berlin: Springer, 2003), 519
- Wahlgren, G. M. 1992, *Astronomical Journal*, 104, 1174
- Wahlgren, G. M., Wing, R. F., & White, N. M. 1984, in *Bulletin of the American Astronomical Society*, Vol. 16, *Bulletin of the American Astronomical Society*, 897
- Wallerstein, G., Iben, I. J., Parker, P., Boesgaard, A. M., Hale, G. M., Champagne, A. E., Barnes, C. A., Käppeler, F., Smith, V. V., Hoffman, R. D., Timmes, F. X., Sneden, C., Boyd, R. N., Meyer, B. S., & Lambert, D. L. 1997, *Reviews of Modern Physics*, 69, 995
- Waters, L. B. F. M., Molster, F. J., de Jong, T., Beintema, D. A., Waelkens, C., Boogert, A. C. A., Boxhoorn, D. R., de Graauw, T., Drapatz, S., Feuchtgruber, H., Genzel, R., Helmich, F. P., Heras, A. M., Huygen, R., Izumiura, H., Justantont, K., Kester, D. J. M., Kunze, D., Lahuis, F., Lamers, H. J. G. L. M., Leech, K. J., Loup, C., Lutz, D., Morris, P. W., Price, S. D., Roelfsema, P. R., Salama, A., Schaeidt, S. G., Tielens, A. G. G. M., Trams, N. R., Valentijn, E. A., Vandenbussche, B., van den Ancker, M. E., van Dishoeck, E. F., Van Winckel, H., Wesselius, P. R., & Young, E. T. 1996, *Astronomy and Astrophysics*, 315, L361
- Waters, L. B. F. M., Trams, N. R., & Waelkens, C. 1992, *Astronomy and Astrophysics*, 262, L37
- Waters, L. B. F. M., Waelkens, C., Mayor, M., & Trams, N. R. 1993, *Astronomy and Astrophysics*, 269, 242
- Weigert, A., J., W. H., & Wisotzki, L. 2005, *Astronomie und Astrophysik - Ein Grundkurs*. (Astronomie und Astrophysik - Ein Grundkurs., by Weigert, A.; Wendker, H. J.; Wisotzki, L. WILEY-VCH Verlagsgesellschaft, Weinheim, Germany, 2004, XVI+424 pp., ISBN 3-527-40358-2.)

- Wiescher, M., Görres, J., & Schatz, H. 1999, *Journal of Physics G Nuclear Physics*, 25, 133
- Williams, P. M. 1971a, *Monthly Notices of the RAS*, 155, 215
- . 1971b, *Monthly Notices of the RAS*, 153, 171
- . 1972, *Monthly Notices of the RAS*, 158, 361
- . 1975, *Monthly Notices of the RAS*, 170, 343
- Wilson, R. E. 1953, *Carnegie Institute Washington D.C. Publication*, 0
- Yamamuro, T., Nishimaki, Y., Motohara, K., Miyata, T., & Tanaka, M. 2007, *Publications of the ASJ*, 59, 973
- Yoshioka, K. 1979, *Publication of the ASJ*, 31, 23
- Zirin, H. 1976, *Astrophysical Journal*, 208, 414

Appendix A

Standard Stars

To make a proper data reduction, one needs some standard stars in the different filters used for telluric line correction and line identification.

For example in the H-filter, 9 Her was used for the line identification, because it is a non-pulsating star of spectral type K5. I used the Arcuturs Atlas by Hinkle et al. (1995) to find the correct wavelength range by searching for significant lines in both, the 9 Her and the Arcturus spectra in the H-filter.

Typically, a hot star with few to no spectral lines in the near infrared is used as a telluric standard, because hot stars only show absorptions lines due to the earth's atmosphere in this wavelength region.

In this thesis the correction for atmospheric lines was done by using the spectrum of α Cyg in the H-filter and α Aql in the J and K filters. Vega would also be suitable as a telluric standard but was not used during my data reduction because α Aql was sufficient.

Star	RA [h ' "]	DEC [° ' "]	Spectral Type	J [mag]	H [mag]	K [mag]	
α Aql	19 59 47.0	+08 52 06.0	A7 V	0.31	0.10	0.10	J,K
α Boo	14 15 39.7	+19 10 56.7	K1.5 III	-2.25	-2.81	-2.91	J
α Cyg	20 41 25.9	+45 16 49.2	A2 Ia	1.14	0.90	1.01	H
9 Her	16 13 15.4	+05 01 15.9	K5 III	3.04	2.30	2.08	H
δ Oph	16 14 20.7	-03 41 39.6	M0.5 III	-0.13	-1.03	-1.17	H,J,K
Vega	18 36 56.3	+38 47 01.3	A0 V	-0.18	-0.03	0.13	J,K

Table A.1: Stars used as telluric standards (early type stars) or for line identification (late type stars). The second column contains the right ascension, the third the declination. The spectral and luminosity type is given in column four, followed by the magnitudes measured in three near infrared bands (source: SIMBAD Astronomical Database, <http://simbad.u-strasbg.fr/simbad/>) and the observed wavelength ranges (see table 3.1 for further information).

Only the spectra of the stars used for line identification are presented here, because the spectra of the telluric standards are not for further use in this work.

A.1 α Boo

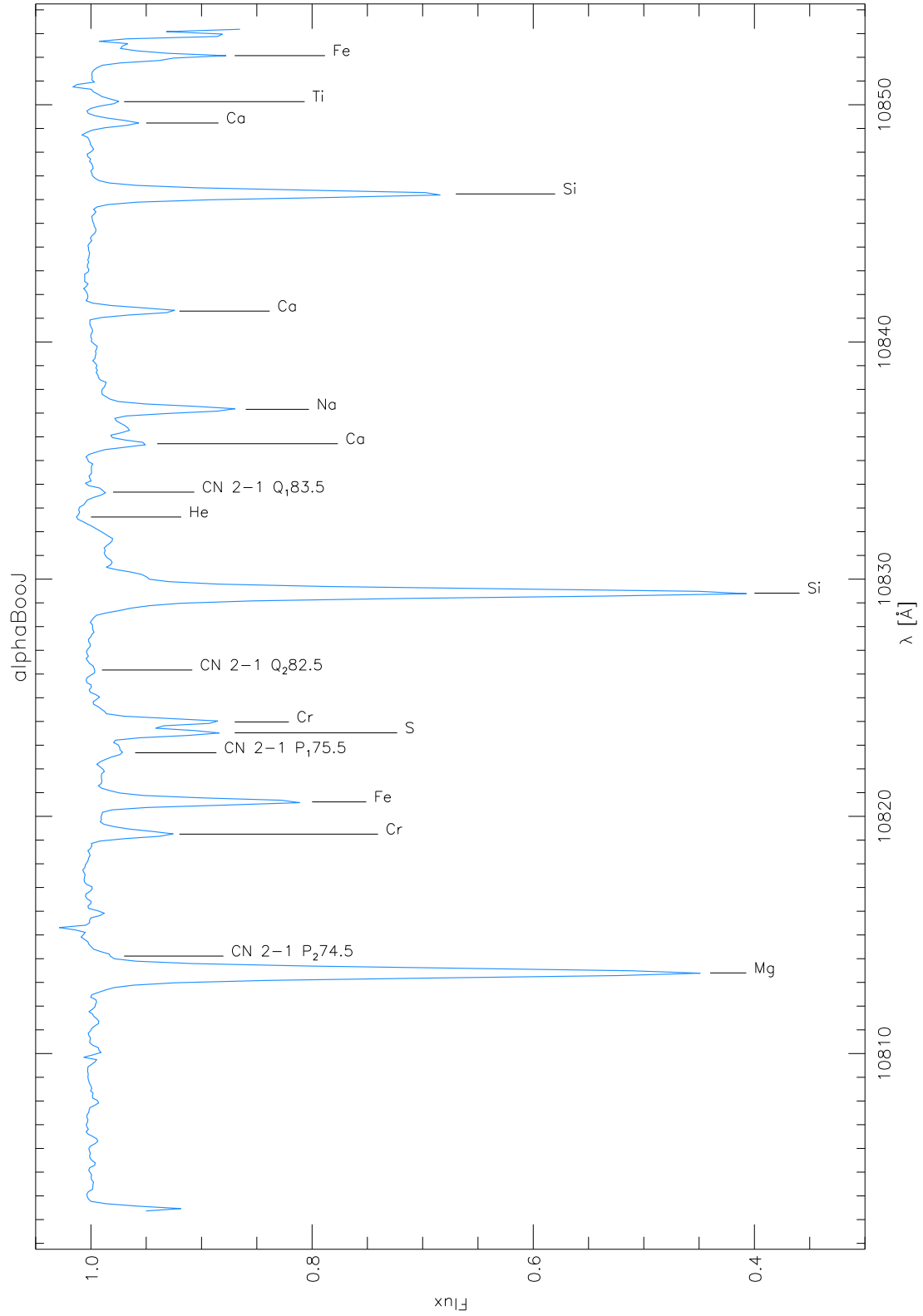


Figure A.1: The spectrum of α Bootis in the J-filter with identified and measured lines.

Wavelength [Å]	Atom/Molecule	EQW [mÅ]	Vacuum Pos.	Difference
10813.40	Mg	301.1	10814.05	0.65
10814.11	CN 2-1 P_2 74.5	7.3	10814.83	0.72
10819.25	Cr	28.4	10819.86	0.61
10820.61	Fe	82.2	10821.26	0.65
10822.68	CN 2-1 P_1 75.5	18.9	10823.43	0.75
10823.52	S	49.6	10824.17	0.65
10823.98	Cr	46.2	10824.58	0.60
10826.17	CN 2-1 Q_2 82.5	1.3	10826.84	0.67
10829.41	Si	345.2	10830.06	0.65
10832.62	He emission	- 5.7	10833.31	0.69
10833.67	CN 2-1 Q_1 83.5	5.5	10834.22	0.55
10835.71	Ca	22.1	10836.35	0.64
10837.16	Na	64.7	10837.84	0.68
10841.30	Ca	27.5	10841.94	0.64
10846.24	Si	150.2	10846.82	0.58
10849.23	Ca	14.3	10849.74	0.51
10850.13	Ti	8.3	10850.61	0.48
10852.07	Fe	46.1	10852.43	0.36

Table A.2: The equivalent widths for the lines in Fig. A.1 with the vacuum positions given by Hinkle et al. (1995). The mean difference between vacuum position and measured wavelength is 0.62 Å. The radial velocity derived from these measurements is -3.55 ± 2.51 km/s after heliocentric correction.

α Boo, or more commonly Arcturus, was observed by Hinkle et al. (1995), who published an *Infrared Atlas of the Arcturus Spectrum, 0.9-5.3 microns*, which was very helpful for identifying the elemental lines in the spectra of my programm stars.

As can be seen in Fig. A.2, the model spectrum does fit the observed spectrum quite well. There are lines present in the model spectrum that do not have a counterpart in the observed spectrum of α Boo.

This can be explained with the subsolar metallicity of Arcturus: the latest measurements by Soubiran et al. (2008) give $[\text{Fe}/\text{H}]=-0.55$. The stellar parameters derived by Soubiran et al. ($T_{\text{eff}}=4316$ K, $\log g=1.71$) are in good agreement with the values published earlier by Williams (1975): $T_{\text{eff}}=4339$ K and $\log g=2.1$.

The spectrum analysed in this work is in good agreement with the Arcturus Atlas (see Fig. A.3).

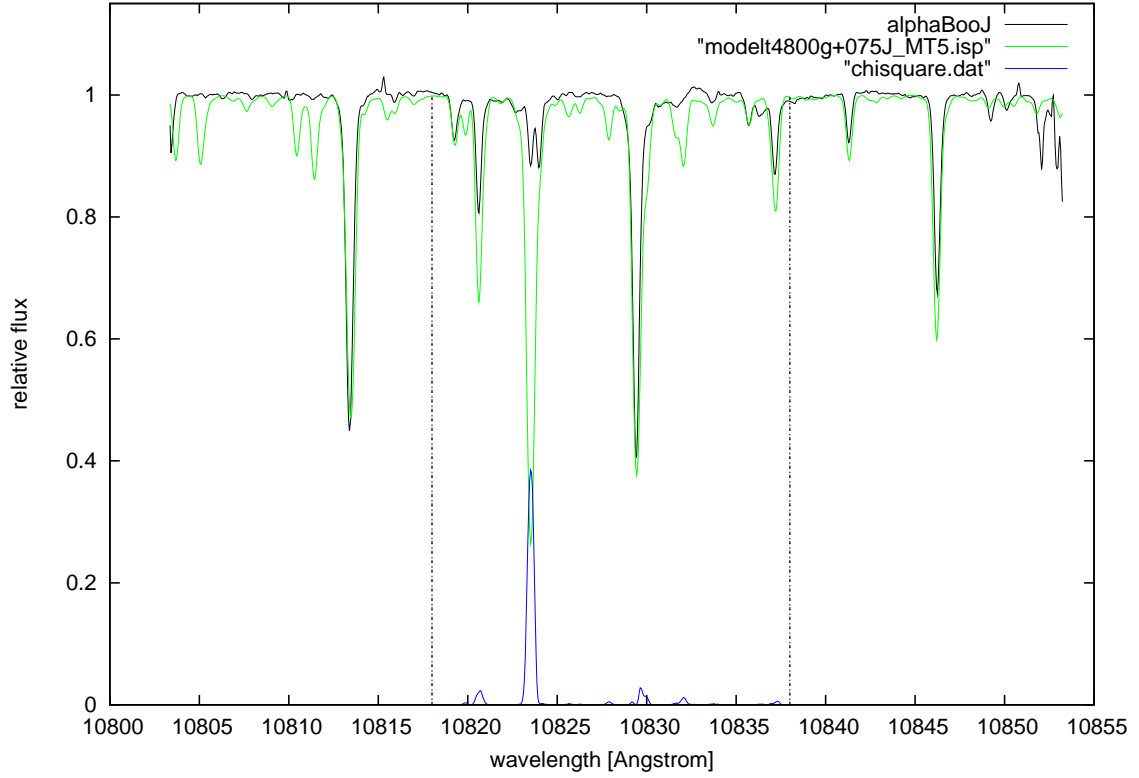


Figure A.2: The star α Boo overplotted by a MARCS model of 4200 K, $\log g=0.75$ and $\zeta=5$ km/s.

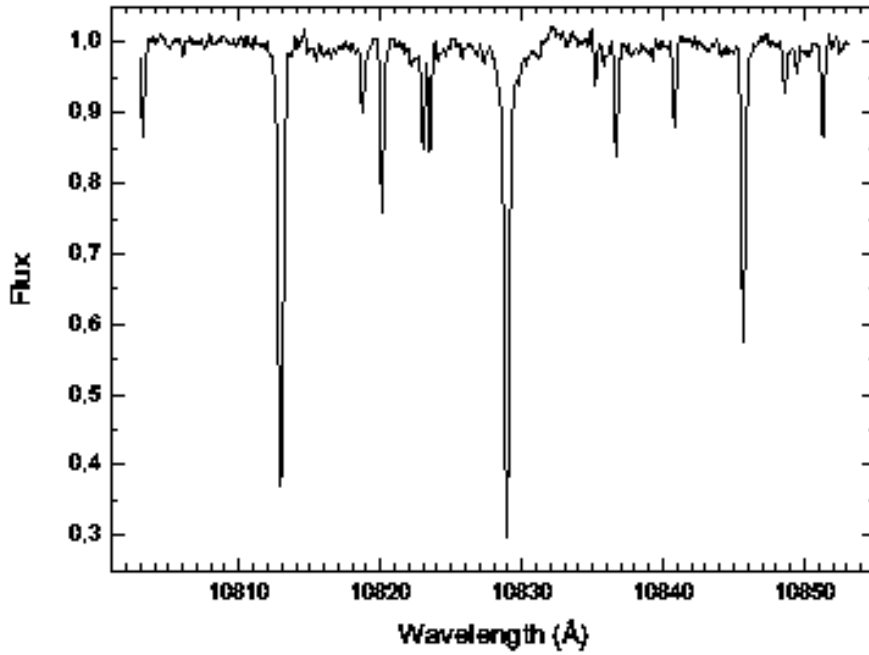


Figure A.3: Spectrum of Arcturus in the wavelength range from 10803 Å to 10853 Å. Data taken from Hinkle et al. (1995).

A.2 9Her

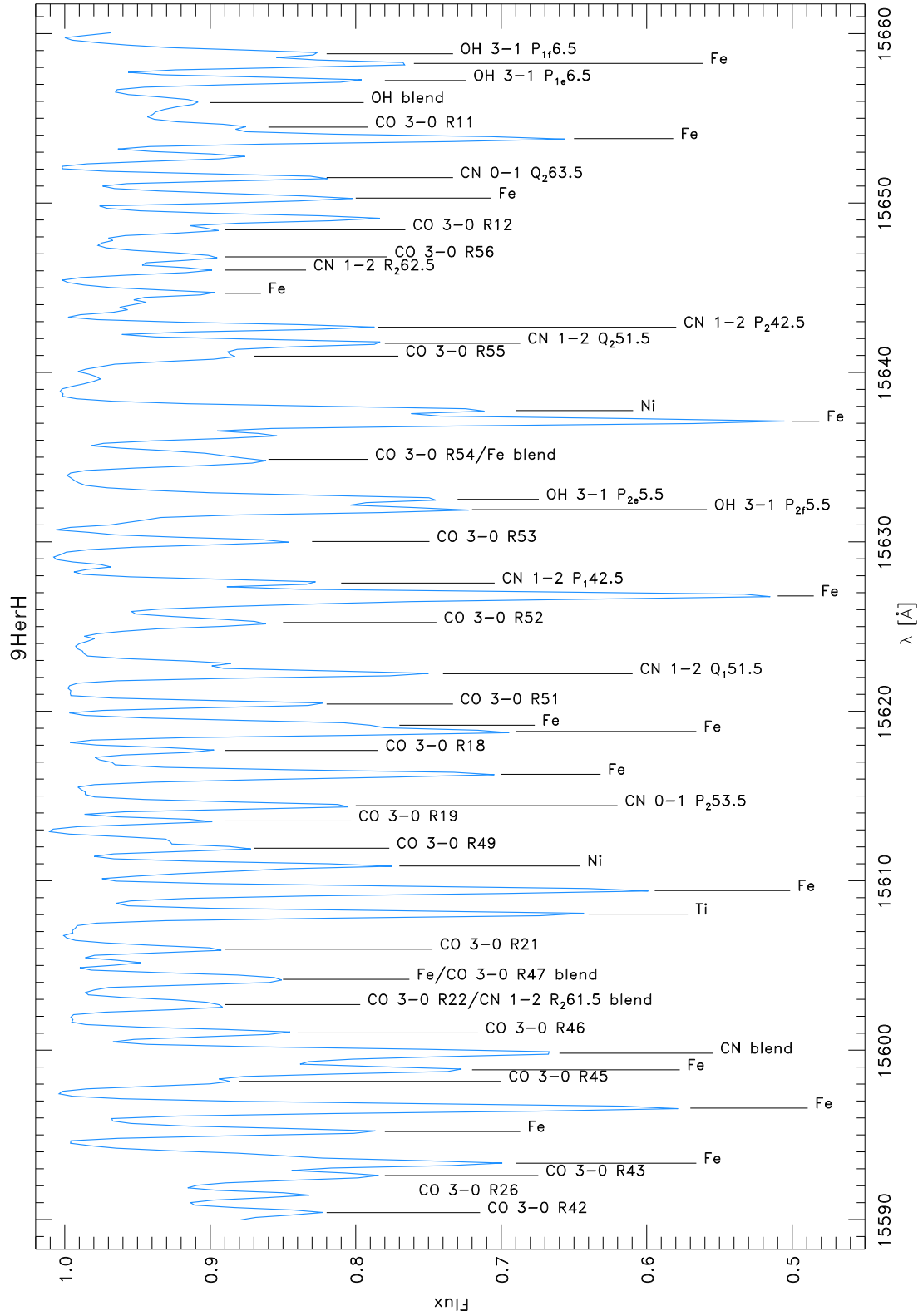


Figure A.4: The spectrum of 9Herculis in the H-filter with identified and measured lines.

Wavelength [Å]	Atom/Molecule	EQW [mÅ]	Vacuum Pos.	Difference
15590.41	CO 3-0 R42	244.6	15589.69	-0.72
15591.45	CO 3-0 R26	207.8	15590.70	-0.75
15592.60	CO 3-0 R43	311.4	15591.91	-0.69
15593.33	Fe	358.5	15592.52	-0.81
15595.20	Fe	126.1	15594.31	-0.89
15596.58	Fe	274.4	15595.75	-0.83
15598.16	CO 3-0 R45	70.7	15597.17	-0.99
15598.84	Fe	319.1	15598.01	-0.83
15601.02	CO 3-0 R46	105.5	15600.21	-0.81
15605.96	CO 3-0 R21	63.7	15605.00	-0.96
15608.03	Ti	211.0	15607.11	-0.92
15609.42	Fe	283.4	15608.48	-0.94
15610.87	Ni	127.0	15609.92	-0.95
15611.92	CO 3-0 R49	77.5	15610.97	-0.95
15613.53	CO 3-0 R19	44.5	15612.58	-0.95
15614.43	CN 0-1 P_2 53.5	115.7	15613.47	-0.96
15616.28	Fe	201.4	15615.40	-0.88
15617.69	CO 3-0 R18	49.9	15616.76	-0.93
15618.81	Fe	182.4	15617.89	-0.92
15619.18	Fe	143.9	15618.36	-0.82
15620.43	CO 3-0 R51	89.8	15619.52	-0.91
15622.22	CN 1-2 Q_1 51.5	141.5	15621.33	-0.89
15625.24	CO 3-0 R52	148.9	15624.21	-1.03
15626.81	Fe	495.2	15625.92	-0.89
15627.57	CN 1-2 P_1 42.5	100.1	15626.71	-0.86
15630.02	CO 3-0 R53	92.4	15629.18	-0.84
15631.90	OH 3-1 P_{2f} 5.5	183.7	15630.97	-0.93
15632.51	OH 3-1 P_{2e} 5.5	228.0	15631.68	-0.83
15637.12	Fe	441.0	15636.22	-0.90
15637.75	Ni	195.1	15636.89	-0.86
15640.96	CO 3-0 R55	90.7	15639.95	-1.01
15641.72	CN 1-2 Q_2 51.5	135.9	15640.86	-0.86
15642.67	CN 1-2 P_2 42.5	116.8	15641.80	-0.87
15644.67	Fe	69.0	15643.75	-0.92
15646.04	CN 1-2 R_2 62.5	59.9	15645.14	-0.90
15646.82	CO 3-0 R56	100.8	15645.76	-1.06
15648.42	CO 3-0 R12	79.2	15647.46	-0.96
15650.29	Fe	146.5	15649.29	-1.00
15651.50	CN 0-1 Q_2 63.5	103.8	15650.52	-0.98
15653.80	Fe	230.7	15652.79	-1.01
15654.48	CO 3-0 R11	102.2	15653.50	-0.98
15657.23	OH 3-1 P_{1e} 6.5	147.6	15656.17	-1.06
15658.24	Fe	159.0	15657.15	-1.09
15658.81	OH 3-1 P_{1f} 6.5	148.1	15657.75	-1.06

Table A.3: The equivalent widths for the lines in Fig. A.4 with the vacuum positions given by Hinkle et al. (1995). The mean difference between vacuum position and measured wavelength is -0.91 Å. The radial velocity derived from these measurements is -2.82 ± 1.70 km/s after heliocentric correction.

McWilliam (1990) published the stellar parameters of 9 Her to be $T_{\text{eff}}=4000$ K, $\log g=1.80$, $\xi=2.3$ km/s and $[\text{Fe}/\text{H}]=-0.13$. Based on these values I compared the observations to a model spectrum. A model with a temperature of 4000 K did not fit very well. Eventually I decided to use a synthetic spectrum with 4500 K and $\log g$ of 0.75 cm/s. The hotter model seems to be in good agreement with the observations, as can be seen in Fig. A.5.

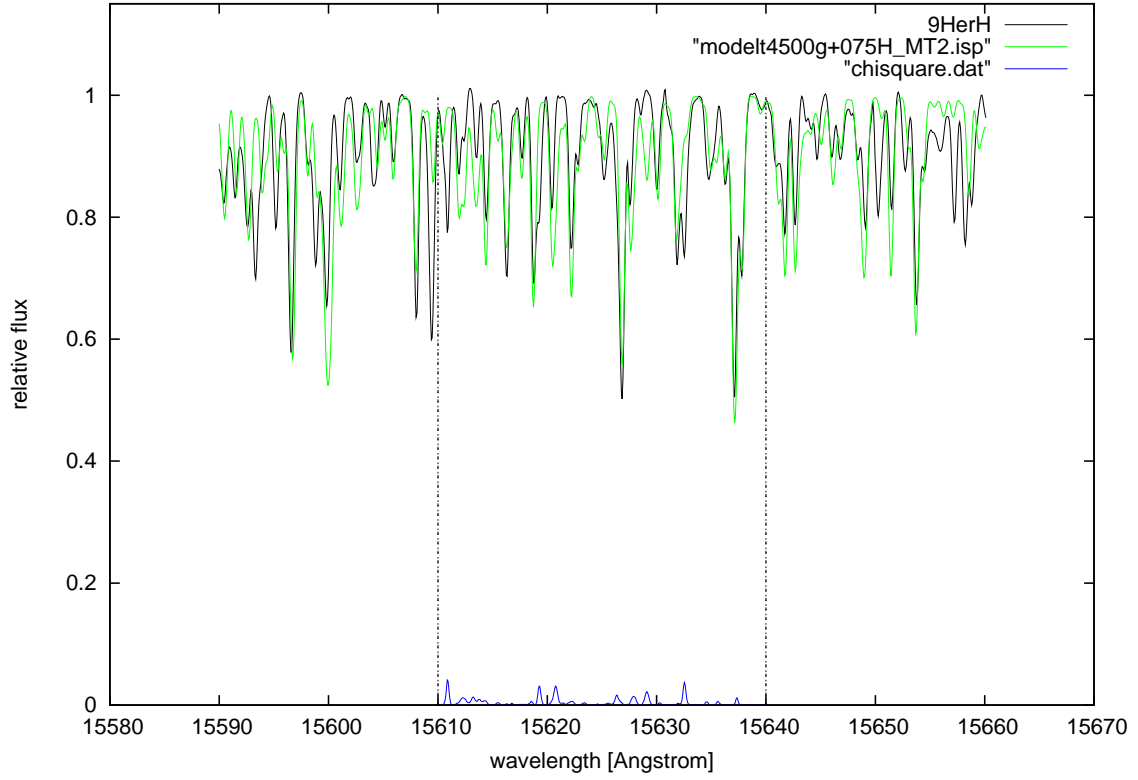


Figure A.5: The star 9 Her overplotted by a MARCS model of 4500 K, $\log g=0.75$ and $\zeta=2$ km/s.

A.3 δ Oph

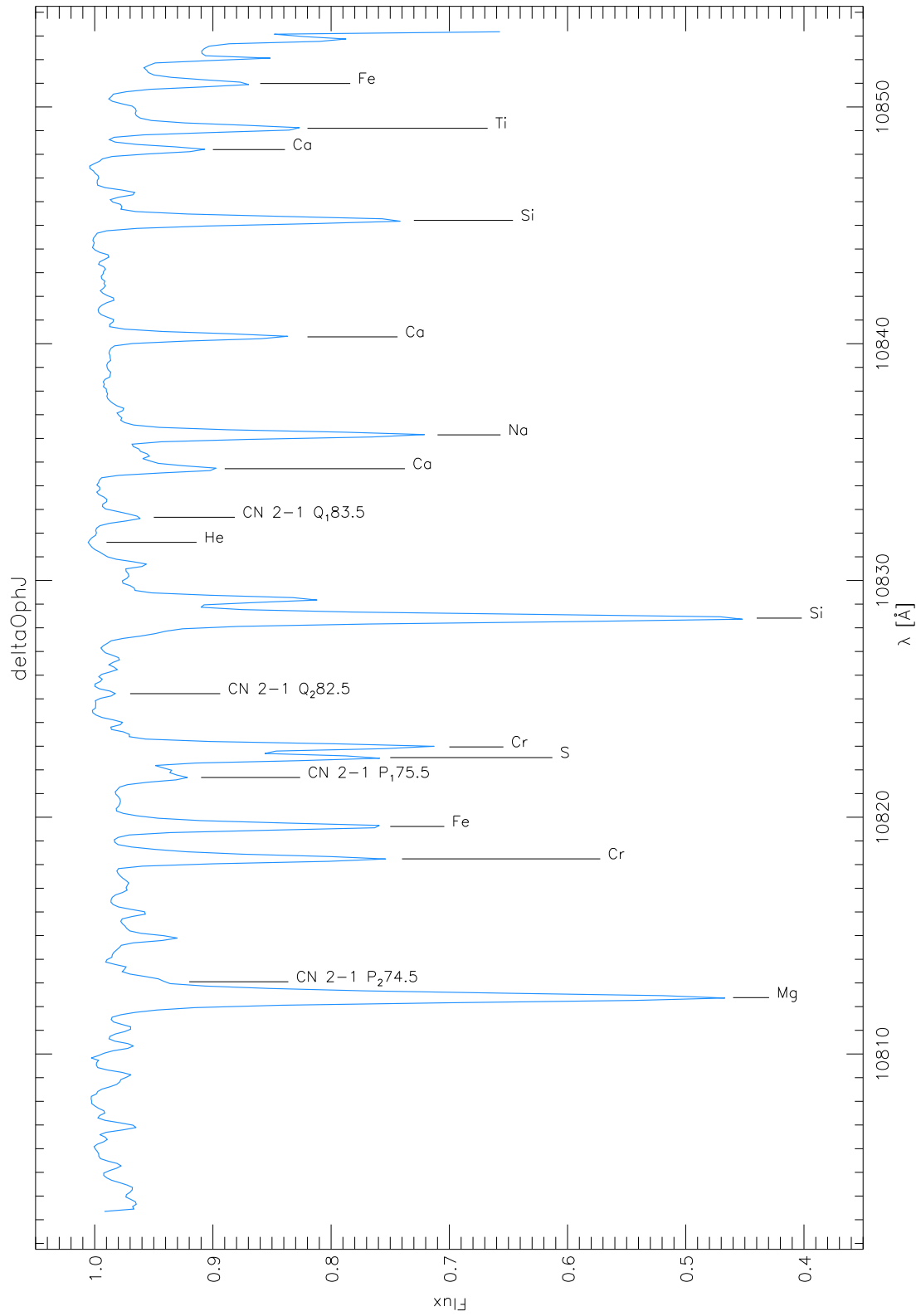


Figure A.6: The spectrum of δ Ophiuchi in the J-filter with identified and measured lines.

Wavelength [Å]	Atom/Molecule	EQW [mÅ]	Vacuum Pos.	Difference
10812.38	Mg	354.7	10814.05	1.67
10813.05	CN 2-1 P_2 74.5	41.5	10814.83	1.78
10818.24	Cr	98.9	10819.86	1.62
10819.61	Fe	120.2	10821.26	1.65
10821.68	CN 2-1 P_1 75.5	38.4	10823.43	1.75
10822.52	S	125.2	10824.17	1.65
10822.97	Cr	142.7	10824.58	1.61
10825.22	CN 2-1 Q_2 82.5	6.3	10826.84	1.62
10828.41	Si	321.9	10830.06	1.65
10831.61	He emission	- 2.1	10833.31	1.70
10832.67	CN 2-1 Q_1 83.5	18.4	10834.22	1.55
10834.72	Ca	42.6	10836.35	1.63
10836.15	Na	127.7	10837.84	1.69
10840.29	Ca	71.8	10841.94	1.65
10845.21	Si	124.9	10846.82	1.61
10848.20	Ca	35.7	10849.74	1.54
10849.10	Ti	75.4	10850.61	1.51
10850.99	Fe	63.9	10852.43	1.44

Table A.4: The equivalent widths for the lines in Fig. A.6 with the vacuum positions given by Hinkle et al. (1995). The mean difference between vacuum position and measured wavelength is 1.63 Å. The radial velocity derived from these measurements is -18.05 ± 2.21 km/s after heliocentric correction.

The stellar parameters derived by Engvold & Rygh (1978) are $T_{\text{eff}}=3300\text{K}$ and $\log g=1.30$. Oinas (1977) estimates a higher temperature for δ Oph ($T_{\text{eff}}=3670\text{K}$), with $\log g=1.4$ and $\xi=2.3\text{km/s}$.

δ Oph was used as a standard star and was the only star observed in all three filters. I decided to choose a model that fits the observations in all three wavelength ranges, this is the reason why the parameters I used ($T_{\text{eff}}=4200\text{K}$, $\log g=0.75$, $\xi=0.2\text{km/s}$) differ from the values mentioned above.

Wilson (1953) estimated a radial velocity of -19.9km/s , a value that is in good agreement with the measurements I made, giving velocities between -18.05km/s and -20.87km/s .

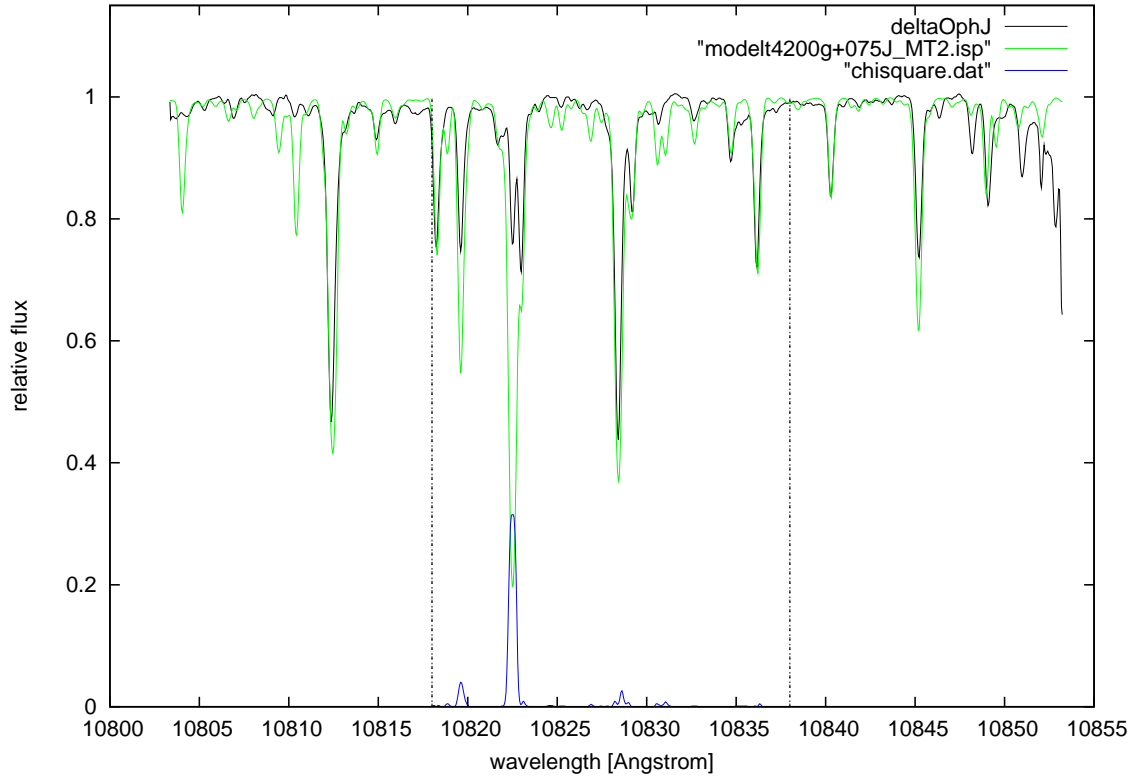


Figure A.7: The star δ Oph overplotted by a MARCS model of 4200 K, $\log g=0.75$ and $\zeta=2$ km/s.

The MARCS model chosen (4200 K, $\log g=0.75$, $\zeta=2$ km/s) does fit most of the lines quite well, especially the Si line at 10828.41 Å, the Cr line at 10818.24 Å, and the Ca line at 10840.29 Å.

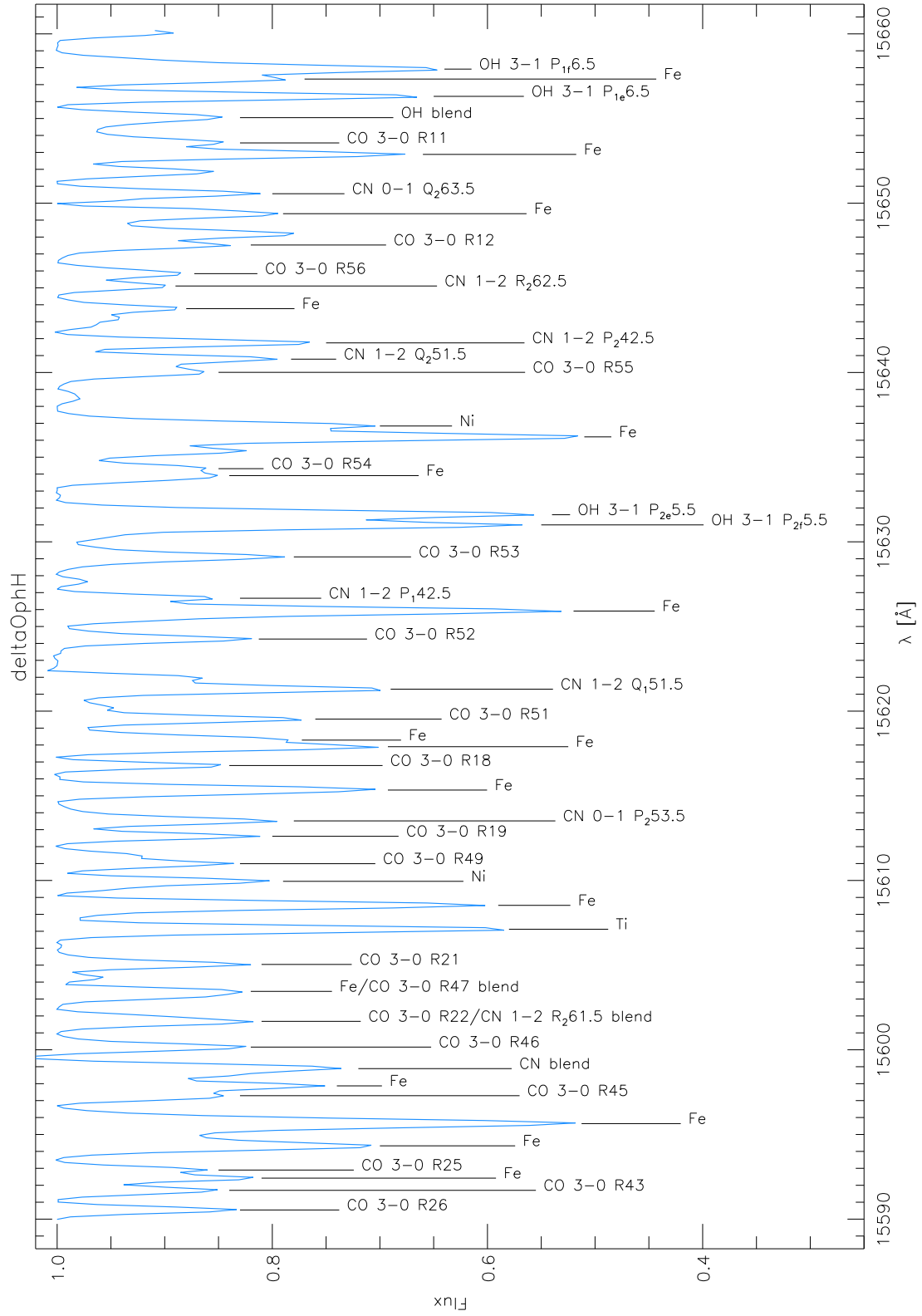


Figure A.8: The spectrum of δ Oph in the H-filter with identified and measured lines.

Wavelength [Å]	Atom/Molecule	EQW [mÅ]	Vacuum Pos.	Difference
15590.54	CO 3-0 R26	80.9	15590.70	0.16
15591.70	CO 3-0 R43	82.6	15591.91	0.21
15592.42	Fe	112.7	15592.52	0.10
15592.90	CO 3-0 R25	70.8	15593.03	0.13
15594.33	Fe	198.4	15594.31	-0.02
15595.64	Fe	424.5	15595.75	0.11
15597.29	CO 3-0 R45	113.3	15597.17	-0.12
15597.87	Fe	247.3	15598.01	0.14
15600.16	CO 3-0 R46	95.1	15600.21	0.05
15605.04	CO 3-0 R21	94.6	15605.00	-0.04
15607.12	Ti	234.3	15607.11	-0.01
15608.53	Fe	231.6	15608.48	-0.05
15609.95	Ni	143.4	15609.92	-0.03
15610.99	CO 3-0 R49	128.0	15610.97	-0.02
15612.61	CO 3-0 R19	96.4	15612.58	-0.03
15613.52	CN 0-1 P_2 53.5	140.2	15613.47	-0.05
15615.34	Fe	180.4	15615.40	0.06
15616.79	CO 3-0 R18	69.9	15616.76	-0.03
15617.90	Fe	176.5	15617.89	-0.01
15618.29	Fe	166.7	15618.36	0.07
15619.53	CO 3-0 R51	140.2	15619.52	-0.01
15621.30	CN 1-2 Q_1 51.5	194.7	15621.33	0.03
15624.26	CO 3-0 R52	110.3	15624.21	-0.05
15625.91	Fe	396.1	15625.92	0.01
15626.67	CN 1-2 P_1 42.5	76.9	15626.71	0.04
15629.11	CO 3-0 R53	161.9	15629.18	0.07
15631.00	OH 3-1 P_{2f} 5.5	273.9	15630.97	-0.03
15631.60	OH 3-1 P_{2e} 5.5	288.2	15631.68	0.08
15633.91	Fe	169.9	15633.89	-0.02
15634.32	CO 3-0 R54	93.7	15634.42	0.10
15636.20	Fe	395.3	15636.22	0.02
15636.84	Ni	190.7	15636.89	0.05
15640.01	CO 3-0 R55	87.2	15639.95	-0.06
15640.79	CN 1-2 Q_2 51.5	177.1	15640.86	0.07
15641.75	CN 1-2 P_2 42.5	127.1	15641.80	0.05
15643.77	Fe	94.6	15643.75	-0.02
15645.11	CN 1-2 R_2 62.5	57.9	15645.14	0.03
15645.84	CO 3-0 R56	87.0	15645.76	-0.08
15647.53	CO 3-0 R12	92.1	15647.46	-0.07
15649.38	Fe	206.2	15649.29	-0.09
15650.56	CN 0-1 Q_2 63.5	119.3	15650.52	-0.04
15652.88	Fe	186.7	15652.79	-0.09
15653.56	CO 3-0 R11	112.7	15653.50	-0.06
15656.31	OH 3-1 P_{1e} 6.5	180.0	15656.17	-0.14
15657.33	Fe	122.9	15657.15	-0.18
15657.92	OH 3-1 P_{1f} 6.5	356.4	15657.75	-0.17

Table A.5: The equivalent widths for the lines in Fig. A.8 with the vacuum positions given by Hinkle et al. (1995). The mean difference between vacuum position and measured wavelength is 0.00 Å. The radial velocity derived from these measurements is -20.87 ± 1.60 km/s after heliocentric correction.

The radial velocity derived in the J-band (-18.05 km/s) differs from the velocity estimated from the H-band measurements (-20.87 km/s). The observations were done on 8 months apart, so this could be an actual variation or an artificial due to data analysis.

The lines in the model are a bit stronger than in the observed spectrum, but in general the two spectra are in good agreement.

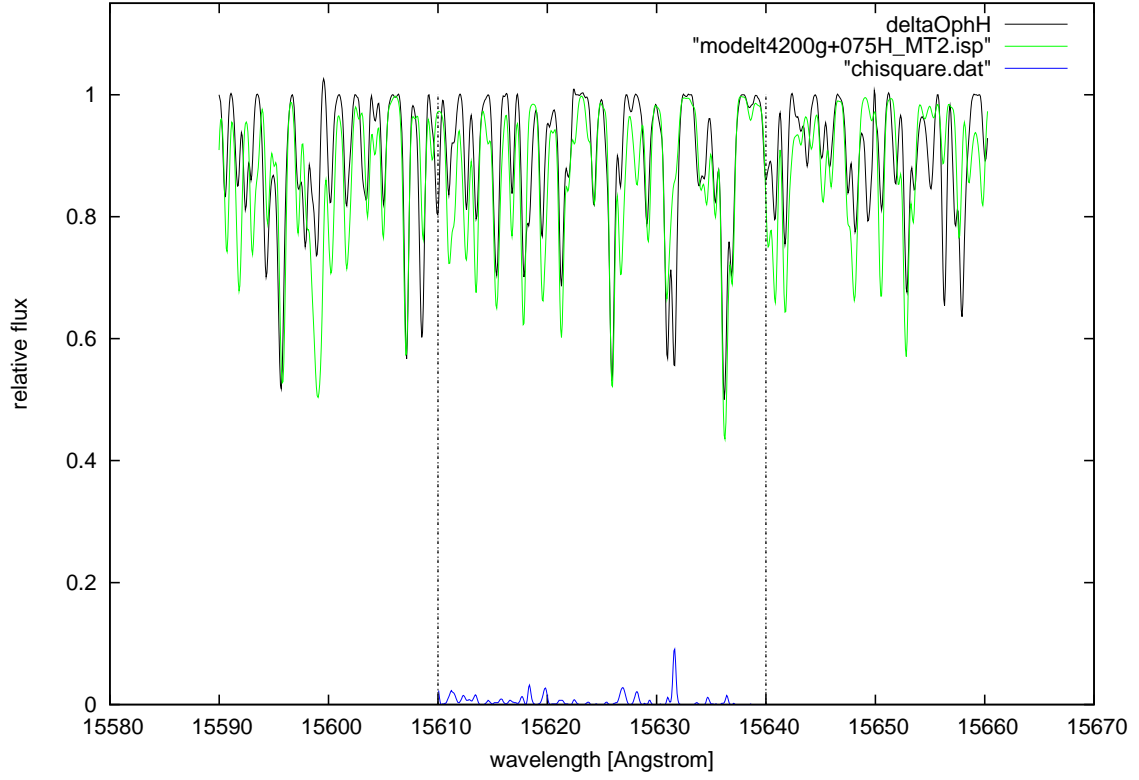


Figure A.9: The star δ Oph overplotted by a MARCS model of 4200 K, $\log g=0.75$ and $\zeta=2$ km/s.

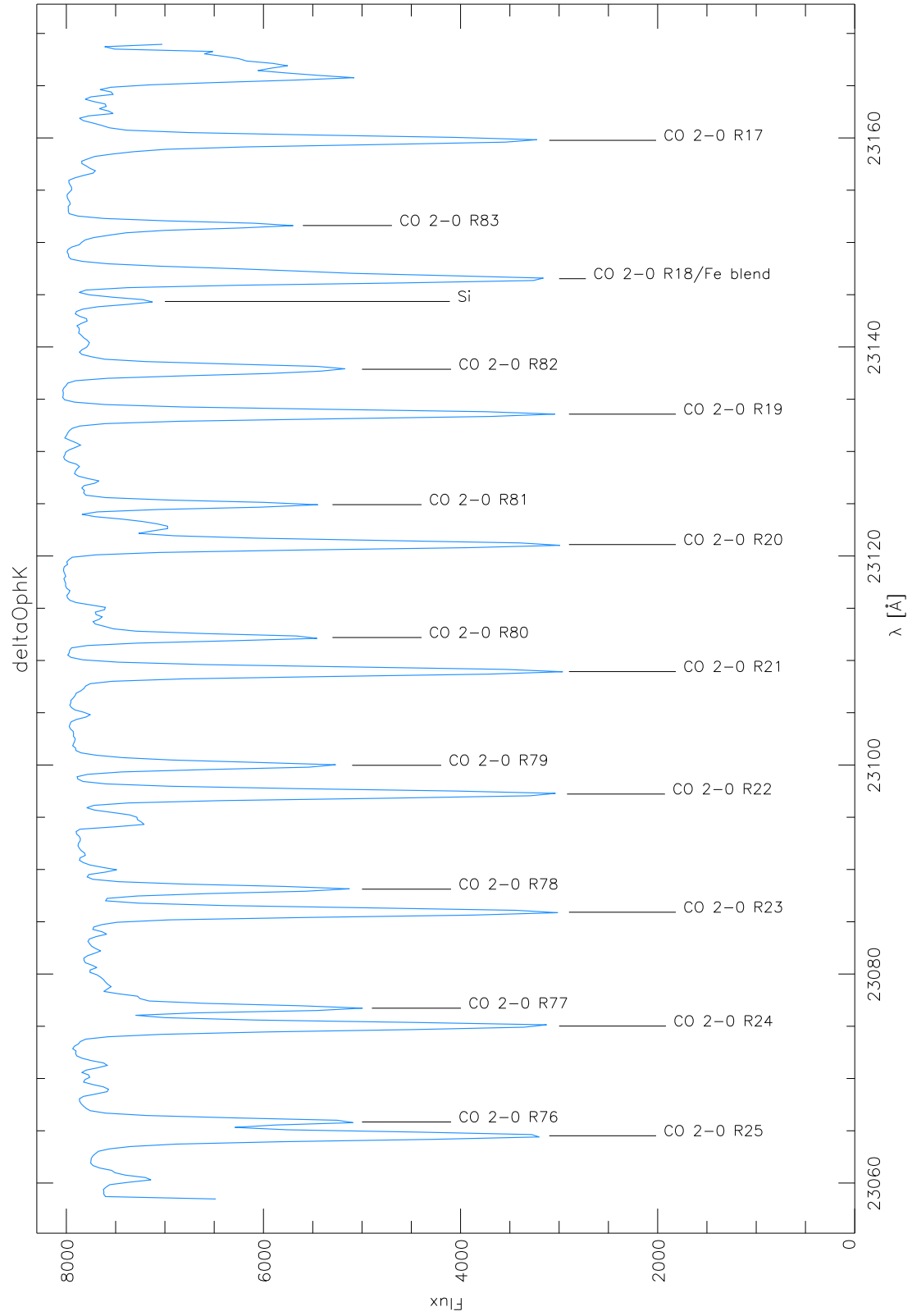


Figure A.10: The spectrum of δ Ophiuchi in the K-filter with identified and measured lines.

Wavelength [\AA]	Atom/Molecule	EQW [m\AA]	Vacuum Pos.	Difference
23064.52	CO 2-0 R25	782.4	23067.89	3.37
23065.84	CO 2-0 R76	403.7	23069.24	3.40
23075.02	CO 2-0 R24	749.8	23078.41	3.39
23076.73	CO 2-0 R77	421.0	23080.18	3.45
23085.91	CO 2-0 R23	721.4	23089.34	3.43
23088.12	CO 2-0 R78	400.3	23091.57	3.45
23097.22	CO 2-0 R22	683.5	23100.67	3.45
23099.97	CO 2-0 R79	398.2	23103.40	3.43
23108.94	CO 2-0 R21	673.2	23112.40	3.46
23112.20	CO 2-0 R80	302.6	23115.67	3.47
23121.09	CO 2-0 R20	706.0	23124.54	3.45
23124.91	CO 2-0 R81	300.2	23128.41	3.50
23133.57	CO 2-0 R19	636.8	23137.08	3.51
23137.87	CO 2-0 R82	431.2	23141.59	3.72
23144.35	Si	126.8	23147.94	3.59
23146.53	CO 2-0 R18/Fe blend	701.6	23150.03	3.50
23151.62	CO 2-0 R83	280.1	23155.23	3.61
23159.77	CO 2-0 R17	783.3	23163.38	3.61

Table A.6: The equivalent widths for the lines in Fig. A.10 with the vacuum positions given by Hinkle et al. (1995). The mean difference between vacuum position and measured wavelength is 3.49 \AA . The radial velocity derived from these measurements is $-18.64 \pm 1.14 \text{ km/s}$ after heliocentric correction.

Fig. A.11 illustrates a disagreement between the high-excitation lines of the model and the observed spectrum. My advisor suggested that the linelist used for the model spectrum is incorrect. Unfortunately, there was no time to calculate synthetic models with the rectified CO linelist.

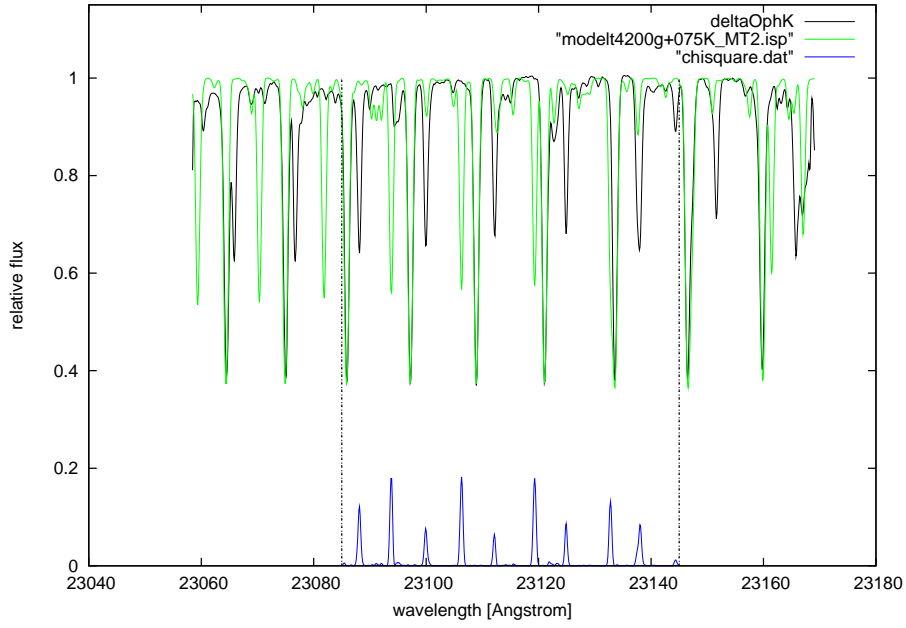


Figure A.11: The star δ Oph overplotted by a MARCS model of 4200 K, $\log g=0.75$ and $\zeta=2$ km/s.

Appendix B

Comparison Stars

The stars described in this section are used as comparison stars to the variable program objects. Together with the standard stars listed in appendix A, a sample of normal stars of different spectral classes is provided for comparison.

Star	RA	DEC	Spectral	J	H	K	
	[h ' "]	[° ' "]	Type	[mag]	[mag]	[mag]	
HD 148513	16 28 34.0	+00 39 54.0	K4 III	2.97	2.35	2.14	H
HD 210889	22 12 47.8	+34 36 16.5	K2 III	3.51	3.00	2.79	H
λ Peg	22 46 31.9	+23 33 56.4	G8 Iab	2.03	1.46	1.51	H
μ Peg	22 50 00.2	+24 36 05.7	G8 III	1.70	1.24	1.18	H

Table B.1: Stars without any specialities were used as comparison stars, to see the difference between the spectra of normal and variable stars within the same spectral class.

B.1 HD 148513

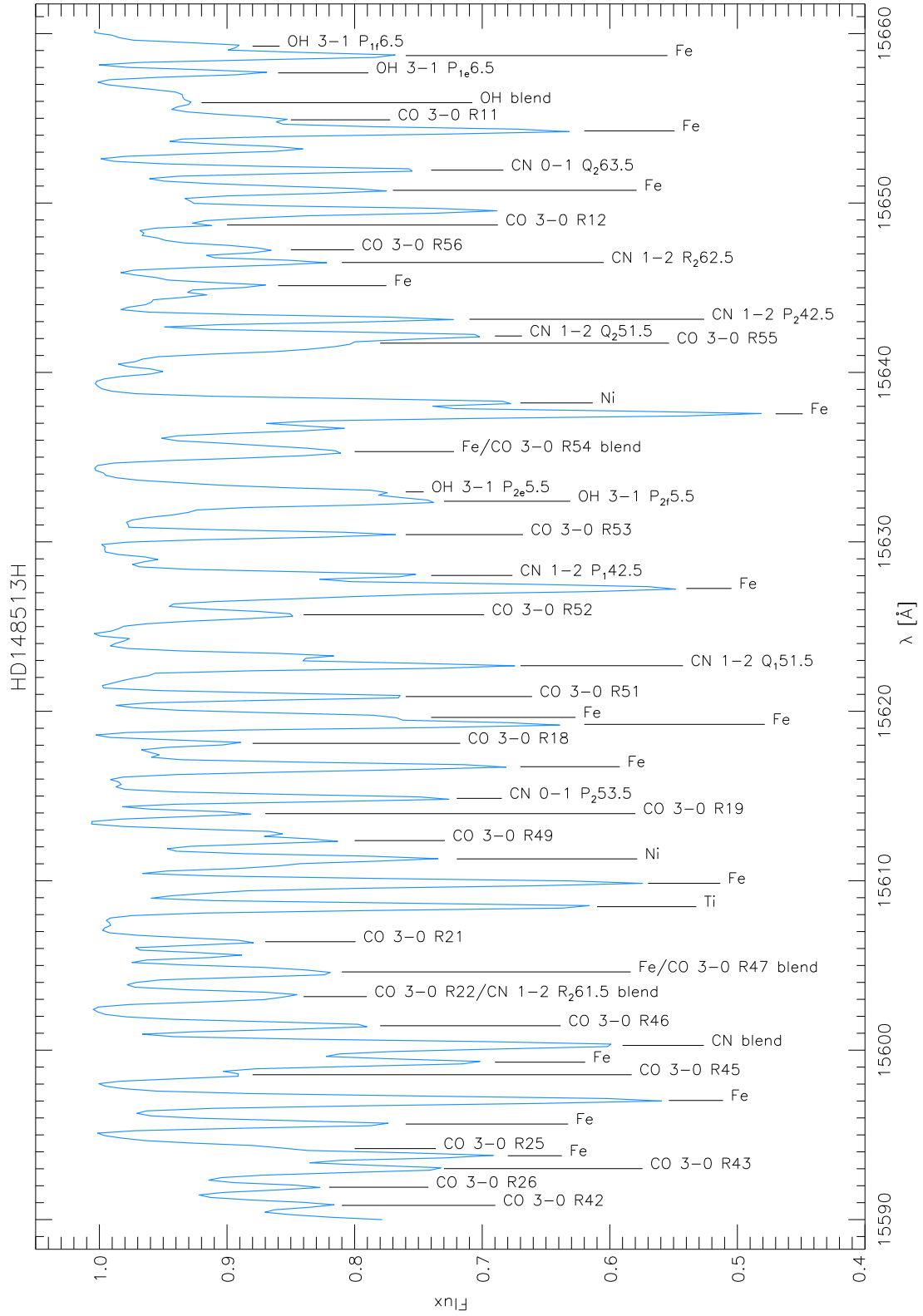


Figure B.1: The spectrum of HD 148513 in the H-filter with identified and measured lines.

Wavelength [Å]	Atom/Molecule	EQW [mÅ]	Vacuum Pos.	Difference
15590.84	CO 3-0 R42	263.8	15589.69	-1.15
15591.91	CO 3-0 R26	186.6	15590.70	-1.21
15593.01	CO 3-0 R43	316.0	15591.91	-1.10
15593.77	Fe	317.3	15592.52	-1.25
15594.19	CO 3-0 R25	101.7	15593.03	-1.16
15595.64	Fe	164.5	15594.31	-1.33
15597.03	Fe	298.1	15595.75	-1.28
15598.55	CO 3-0 R45	59.7	15597.17	-1.38
15599.29	Fe	288.4	15598.01	-1.28
15601.44	CO 3-0 R46	132.0	15600.21	-1.23
15606.40	CO 3-0 R21	81.2	15605.00	-1.40
15608.47	Ti	222.3	15607.11	-1.36
15609.85	Fe	317.0	15608.48	-1.37
15611.29	Ni	247.0	15609.92	-1.37
15612.37	CO 3-0 R49	142.6	15610.97	-1.40
15613.96	CO 3-0 R19	54.3	15612.58	-1.38
15614.86	CN 0-1 P_2 53.5	144.2	15613.47	-1.39
15616.73	Fe	278.2	15615.40	-1.33
15618.11	CO 3-0 R18	51.8	15616.76	-1.35
15619.23	Fe	203.2	15617.89	-1.34
15619.64	Fe	161.2	15618.36	-1.28
15620.87	CO 3-0 R51	123.9	15619.52	-1.35
15622.69	CN 1-2 Q_1 51.5	179.2	15621.33	-1.36
15625.70	CO 3-0 R52	131.5	15624.21	-1.49
15627.25	Fe	490.5	15625.92	-1.33
15628.02	CN 1-2 P_1 42.5	139.5	15626.71	-1.31
15630.43	CO 3-0 R53	122.2	15629.18	-1.25
15632.40	OH 3-1 P_{2f} 5.5	199.8	15630.97	-1.43
15632.95	OH 3-1 P_{2e} 5.5	248.4	15631.68	-1.27
15637.56	Fe	452.7	15636.22	-1.34
15638.20	Ni	209.0	15636.89	-1.31
15641.73	CO 3-0 R55	266.2	15639.95	-1.78
15642.15	CN 1-2 Q_2 51.5	201.3	15640.86	-1.29
15643.14	CN 1-2 P_2 42.5	157.2	15641.80	-1.34
15645.12	Fe	115.5	15643.75	-1.37
15646.49	CN 1-2 R_2 62.5	123.8	15645.14	-1.35
15647.24	CO 3-0 R56	162.8	15645.76	-1.48
15648.70	CO 3-0 R12	58.6	15647.46	-1.24
15650.75	Fe	212.6	15649.29	-1.46
15651.94	CN 0-1 Q_2 63.5	151.1	15650.52	-1.42
15654.26	Fe	259.1	15652.79	-1.47
15654.91	CO 3-0 R11	198.9	15653.50	-1.41
15657.68	OH 3-1 P_{1e} 6.5	61.1	15656.17	-1.51
15658.70	Fe	128.0	15657.15	-1.55
15659.26	OH 3-1 P_{1f} 6.5	62.7	15657.75	-1.51

Table B.2: The equivalent widths for the lines in Fig. B.1 with the vacuum positions given by Hinkle et al. (1995). The mean difference between vacuum position and measured wavelength is -1.35 Å. The radial velocity derived from these measurements is 6.70 ± 2.21 km/s after heliocentric correction.

This star is also known as HR 6136 and belongs to the Wolf 630 group. The work of Eggen (1974) about the G-type giants also includes the Wolf 630 group and the author indicates that the members of this group have only 70% of the solar metal abundance. Eggen (1974) assigned HD 148513 to a spectral type of K4IIIp with strong CN lines.

The stellar parameters I used as a basic estimate for my model spectrum where published by McWilliam (1990): $T_{\text{eff}}=4000$ K, $\log g=1.77$, and $\xi=2.3$ km/s. Wilson (1953) derived a radial velocity of 7.3 km/s, which is in good agreement with the radial velocity of 6.7 km/s estimated in this thesis.

The model I chose eventually fits the observed spectrum of HD 148513 quite well (see Fig. B.2).

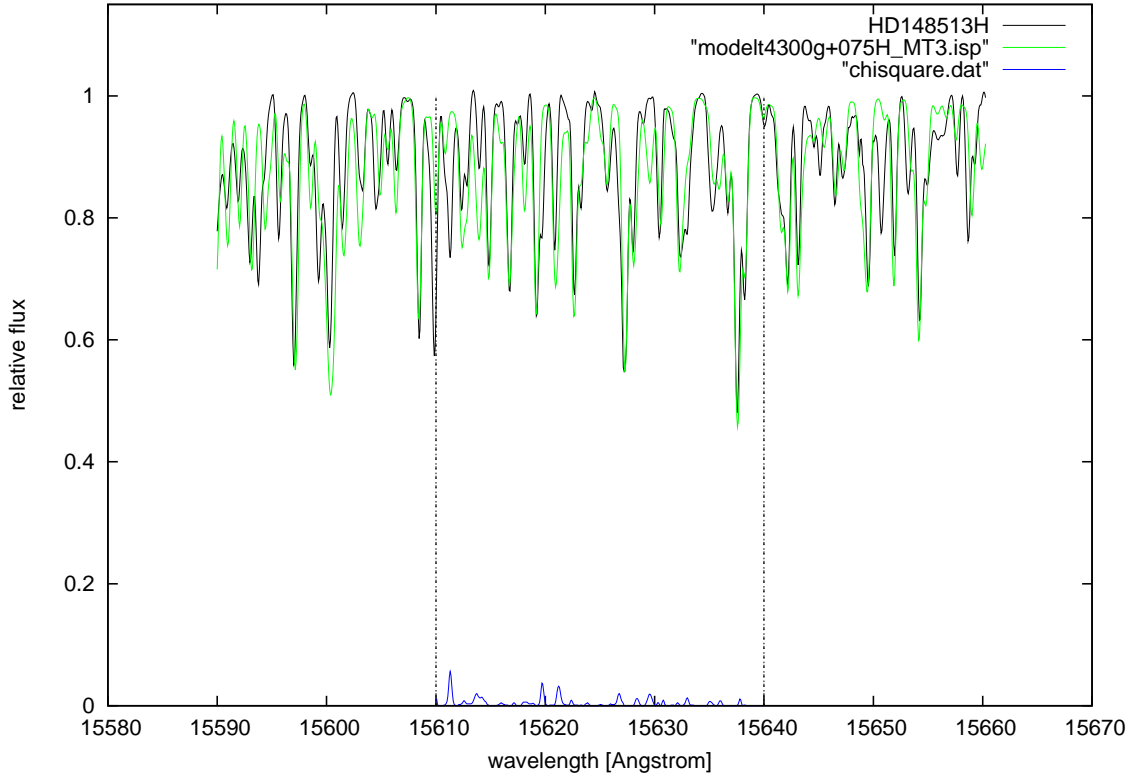


Figure B.2: The star HD 148513 overplotted by a MARCS model of 4300 K, $\log g=0.75$ and $\zeta=3$ km/s.

B.2 HD 210889

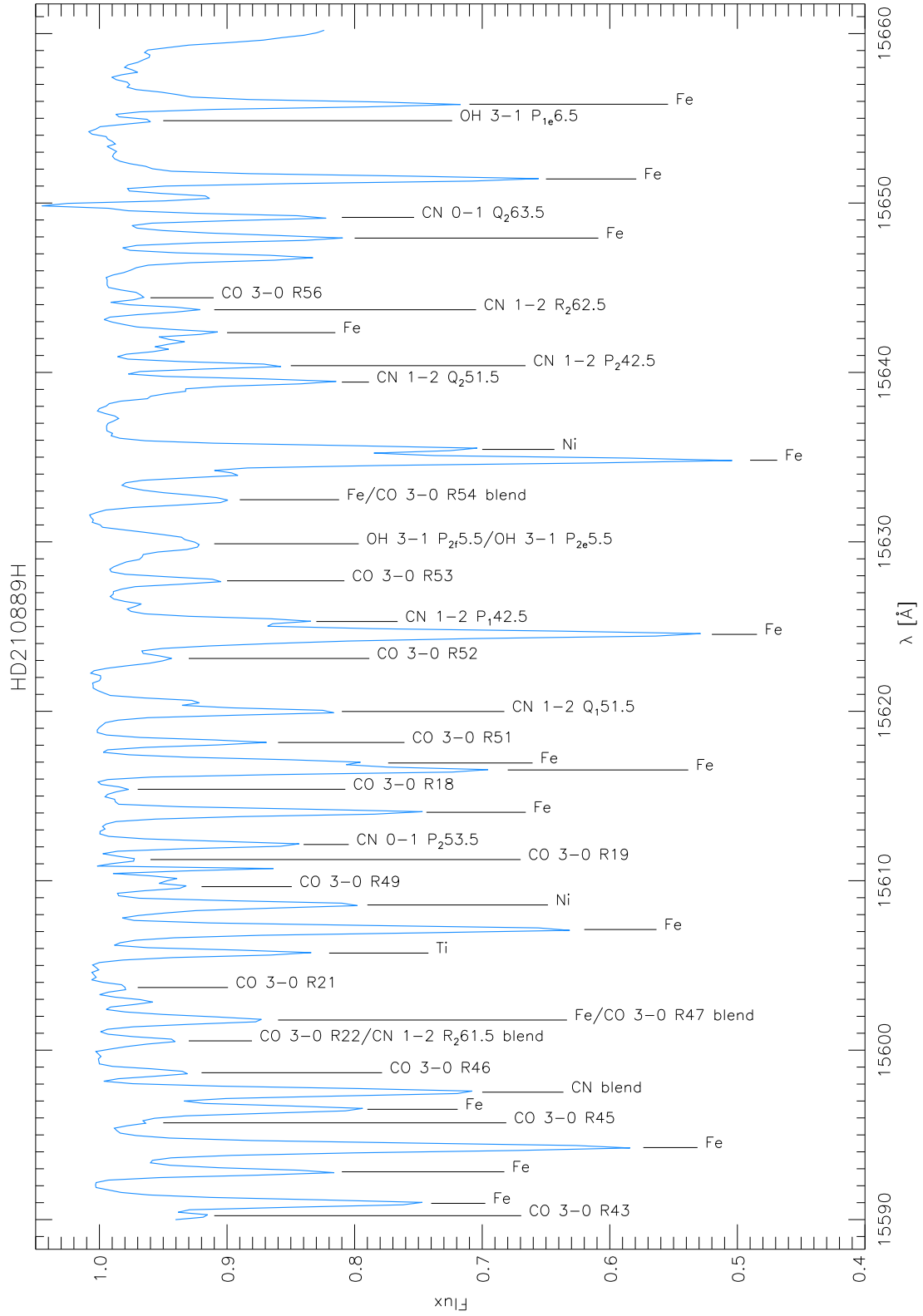


Figure B.3: The spectrum of HD 210889 in the H-filter with identified and measured lines.

Wavelength [\AA]	Atom/Molecule	EQW [$\text{m}\text{\AA}$]	Vacuum Pos.	Difference
15590.23	CO 3-0 R43	91.0	15591.91	1.68
15590.96	Fe	177.2	15592.52	1.56
15592.82	Fe	114.9	15594.31	1.49
15594.25	Fe	325.9	15595.75	1.50
15595.71	CO 3-0 R45	21.5	15597.17	1.46
15596.51	Fe	169.7	15598.01	1.50
15598.67	CO 3-0 R46	38.0	15600.21	1.54
15603.70	CO 3-0 R21	11.3	15605.00	1.30
15605.73	Ti	80.0	15607.11	1.38
15607.12	Fe	236.9	15608.48	1.36
15608.57	Ni	112.5	15609.92	1.35
15609.65	CO 3-0 R49	38.4	15610.97	1.32
15611.25	CO 3-0 R19	12.7	15612.58	1.33
15612.14	CN 0-1 P_2 53.5	76.9	15613.47	1.33
15614.04	Fe	138.4	15615.40	1.36
15615.40	CO 3-0 R18	8.7	15616.76	1.36
15616.54	Fe	180.4	15617.89	1.35
15616.95	Fe	123.6	15618.36	1.41
15618.16	CO 3-0 R51	60.5	15619.52	1.36
15619.99	CN 1-2 Q_1 51.5	105.0	15621.33	1.34
15623.12	CO 3-0 R52	59.6	15624.21	1.09
15624.54	Fe	473.4	15625.92	1.38
15625.30	CN 1-2 P_1 42.5	101.4	15626.71	1.41
15627.70	CO 3-0 R53	53.3	15629.18	1.48
15634.82	Fe	385.6	15636.22	1.40
15635.46	Ni	183.2	15636.89	1.43
15639.43	CN 1-2 Q_2 51.5	105.8	15640.86	1.43
15640.40	CN 1-2 P_2 42.5	79.7	15641.80	1.40
15642.35	Fe	69.3	15643.75	1.40
15643.70	CN 1-2 R_2 62.5	45.1	15645.14	1.44
15644.41	CO 3-0 R56	22.5	15645.76	1.35
15647.93	Fe	136.5	15649.29	1.36
15649.89	Emission Feature	- 10.4		
15649.15	CN 0-1 Q_2 63.5	95.8	15650.52	1.37
15651.42	Fe	213.1	15652.79	1.37
15654.86	OH 3-1 P_{1e} 6.5	17.7	15656.17	1.31
15655.83	Fe	164.6	15657.15	1.32

Table B.3: The equivalent widths for the lines in Fig. B.3 with the vacuum positions given by Hinkle et al. (1995). The mean difference between vacuum position and measured wavelength is 1.39 \AA . The radial velocity derived from these measurements is $-7.88 \pm 1.82 \text{ km/s}$ after heliocentric correction.

The star shows an emission feature at 15649.89 \AA which was produced most likely during data reduction, while applying a synthetic continuum.

For my model spectrum, I used the stellar parameters derived by McWilliam (1990), who found $T_{\text{eff}}=4520$ K, $\log g=2.53$, and $\xi=2.5$ km/s.

Based on these values, I chose a model with a higher temperature ($T_{\text{eff}}= 4700$ K) and the highest $\log g$ value available in my model grid ($\log g=0.75$). The resulting synthetic spectrum turns out to be in good agreement with the observed spectrum (see Fig. B.4).

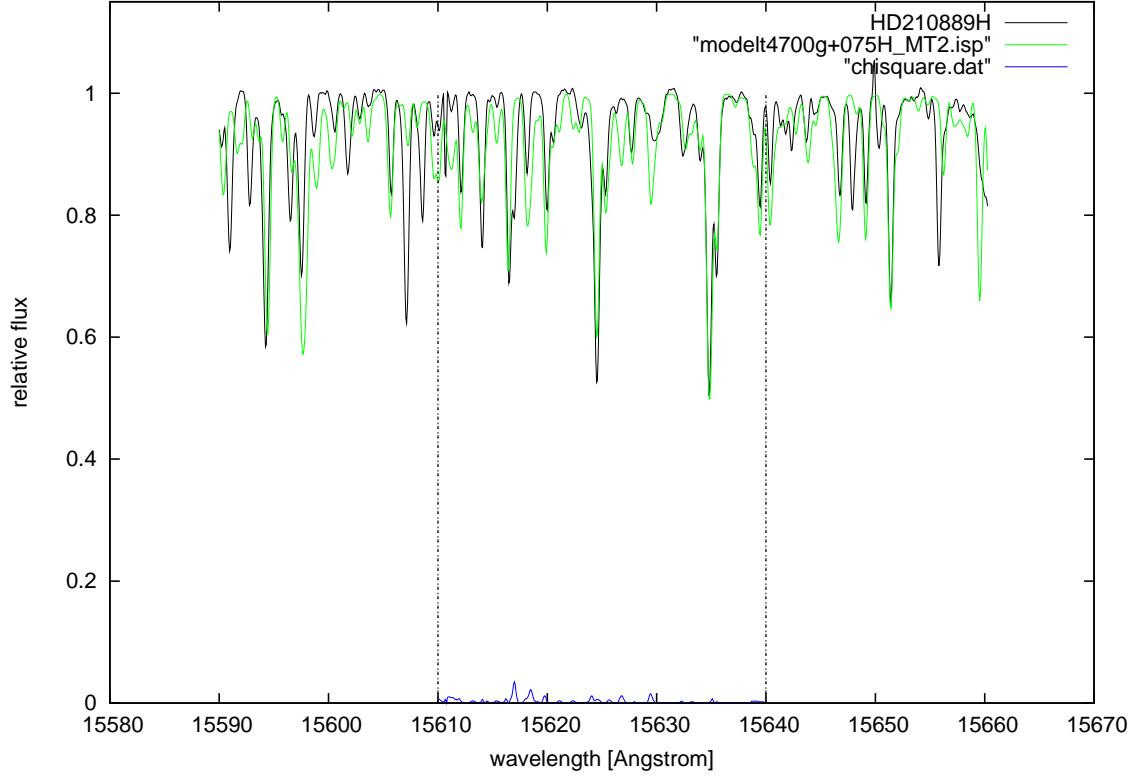


Figure B.4: The star HD 210889 overplotted by a MARCS model of 4700 K, $\log g=0.75$ and $\zeta=2$ km/s.

B.3 λ Peg

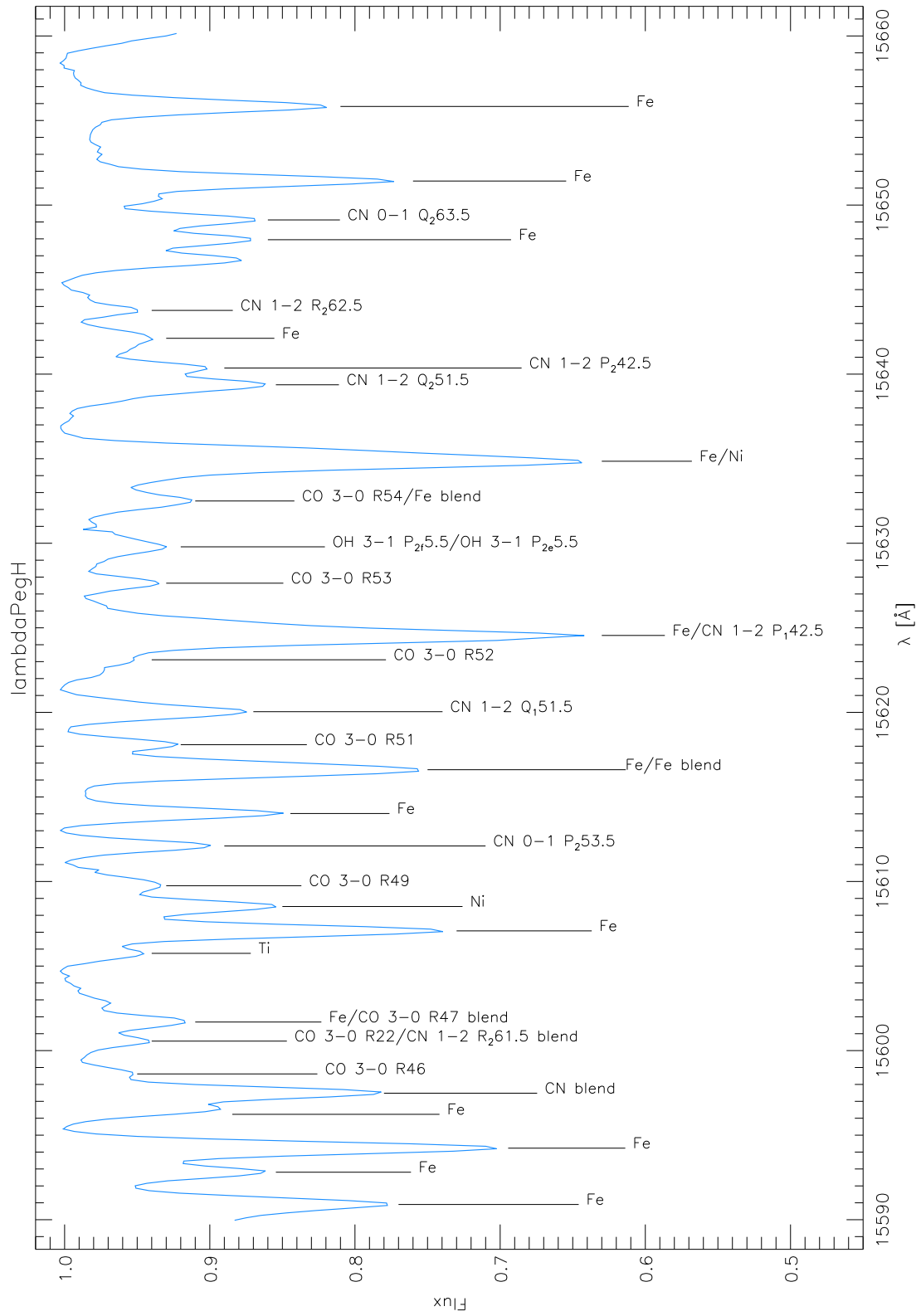


Figure B.5: The spectrum of λ Pegasi in the H-filter with identified and measured lines.

Wavelength [Å]	Atom/Molecule	EQW [mÅ]	Vacuum Pos.	Difference
15590.90	Fe	328.4	15592.52	1.62
15592.81	Fe	239.9	15594.31	1.50
15594.23	Fe	284.7	15595.75	1.52
15596.60	Fe	114.5	15598.01	1.41
15598.62	CO 3-0 R46	63.5	15600.21	1.59
15605.75	Ti	52.6	15607.11	1.36
15607.08	Fe	284.9	15608.48	1.40
15608.52	Ni	206.3	15609.92	1.40
15609.75	CO 3-0 R49	93.9	15610.97	1.22
15612.10	CN 0-1 P_2 53.5	84.0	15613.47	1.37
15614.02	Fe	140.1	15615.40	1.38
15618.09	CO 3-0 R51	66.4	15619.52	1.43
15620.04	CN 1-2 Q_1 51.5	191.5	15621.33	1.29
15623.11	CO 3-0 R52	75.2	15624.21	1.10
15627.64	CO 3-0 R53	70.7	15629.18	1.54
15639.37	CN 1-2 Q_2 51.5	174.7	15640.86	1.49
15640.36	CN 1-2 P_2 42.5	137.0	15641.80	1.44
15642.12	Fe	84.3	15643.75	1.63
15643.77	CN 1-2 R_2 62.5	57.7	15645.14	1.37
15647.95	Fe	230.0	15649.29	1.34
15649.12	CN 0-1 Q_2 63.5	201.4	15650.52	1.40
15651.42	Fe	263.6	15652.79	1.37
15655.83	Fe	211.1	15657.15	1.32

Table B.4: The equivalent widths for the lines in Fig. B.5 with the vacuum positions given by Hinkle et al. (1995). The mean difference between vacuum position and measured wavelength is 1.41 Å. The radial velocity derived from these measurements is -4.25 ± 2.32 km/s after heliocentric correction.

The atmospheric parameters computed by Smith (1998) (see table B.5) are in good agreement with the values published by Williams (1972), who found an effective temperature T_{eff} of 4678 K with a gravity value ($\log g$) of 2.8 and derived the iron abundance $[\text{Fe}/\text{H}]$ to be -0.26.

	$\lambda \text{ Peg}$
$T_{\text{eff}}(\text{K})$	4800 ± 50
$\log g$ (g in cm s^{-2})	1.7 ± 0.1
$[\text{M}/\text{H}]$	-0.1 ± 0.05
Microturbulence, ξ (km s^{-1})	1.8 ± 0.2
Macroturbulence, ζ (km s^{-1})	7.6 ± 0.5

Table B.5: The parameters from Smith (1998) for the star $\lambda \text{ Peg}$.

The radial velocity measured by Eggen (1974) is -3.9 km/sec and is assigned a spectral type of G8II-III. This is in good agreement with the radial velocity derived in this thesis: -4.25 km/s.

The effect of higher macroturbulence in the case of $\lambda \text{ Peg}$ causes the lines to get broader and less deep than they would be without macroturbulence.

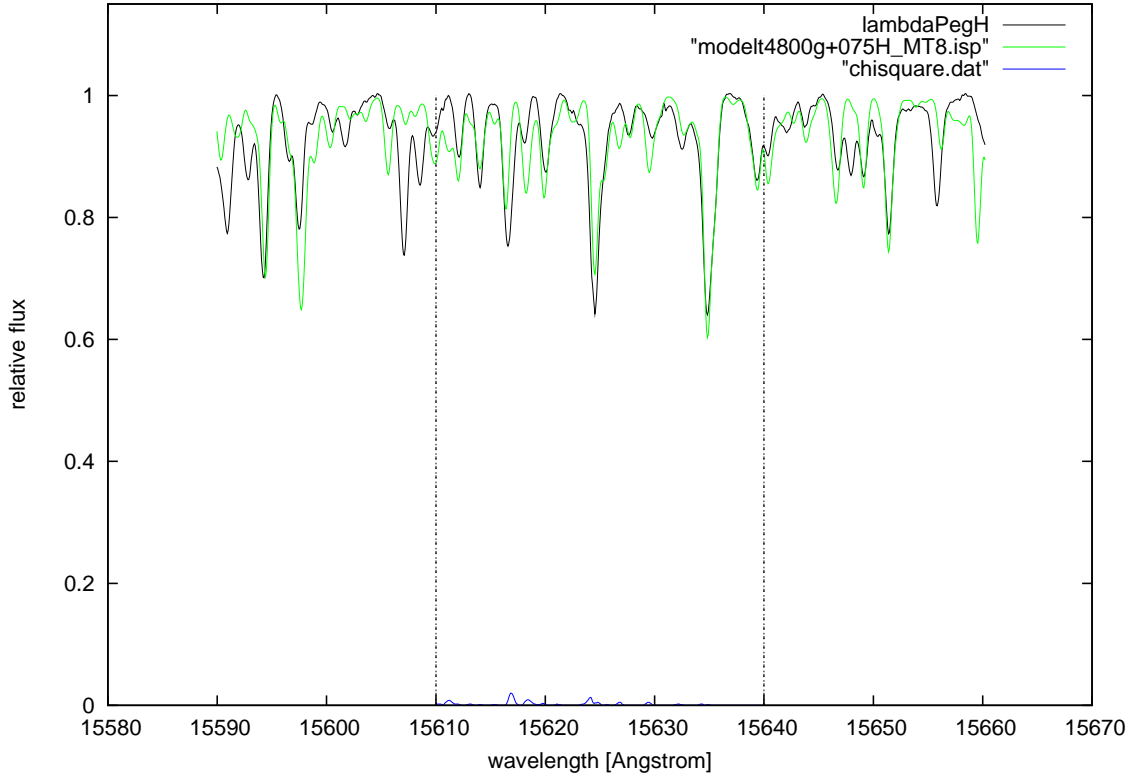


Figure B.6: The star $\lambda \text{ Peg}$ overplotted by a MARCS model of 4800 K, $\log g=0.75$ and $\zeta=8 \text{ km/s}$.

B.4 μ Peg

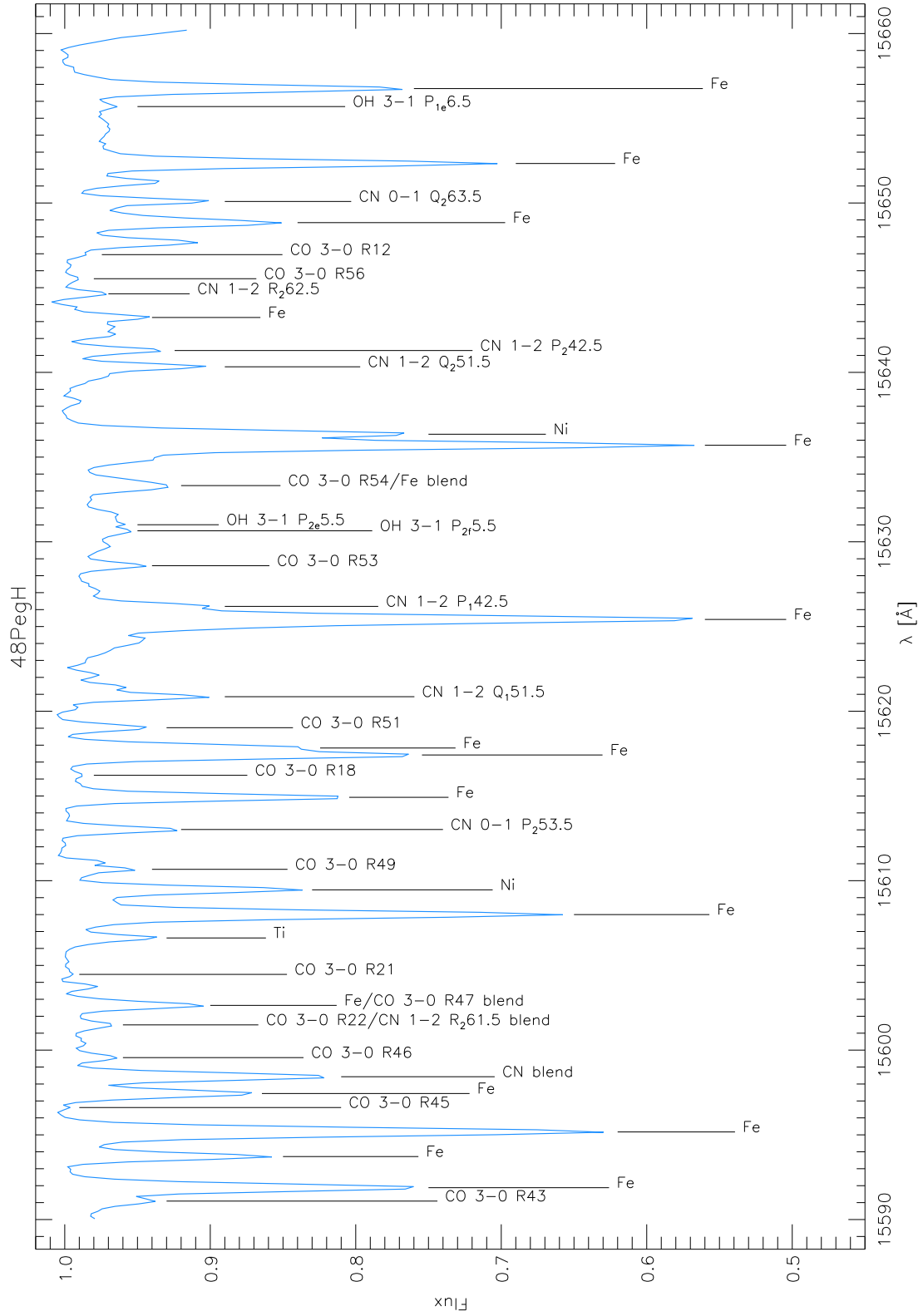


Figure B.7: The spectrum of μ Pegasi in the H-filter with identified and measured lines.

Wavelength [Å]	Atom/Molecule	EQW [mÅ]	Vacuum Pos.	Difference
15591.09	CO 3-0 R43	68.8	15591.91	0.82
15591.88	Fe	178.4	15592.52	0.64
15593.72	Fe	75.8	15594.31	0.59
15595.17	Fe	256.8	15595.75	0.58
15596.61	CO 3-0 R45	0.7	15597.17	0.56
15597.44	Fe	84.8	15598.01	0.57
15599.56	CO 3-0 R46	20.4	15600.21	0.65
15604.47	CO 3-0 R21	2.3	15605.00	0.53
15606.62	Ti	44.5	15607.11	0.49
15608.00	Fe	235.4	15608.48	0.48
15609.46	Ni	112.2	15609.92	0.46
15610.67	CO 3-0 R49	18.9	15610.97	0.30
15613.02	CN 0-1 P_2 53.5	39.3	15613.47	0.45
15614.92	Fe	104.8	15615.40	0.48
15616.22	CO 3-0 R18	10.8	15616.76	0.54
15617.42	Fe	137.3	15617.89	0.47
15617.83	Fe	96.1	15618.36	0.53
15619.03	CO 3-0 R51	31.1	15619.52	0.49
15620.86	CN 1-2 Q_1 51.5	50.3	15621.33	0.47
15625.42	Fe	428.9	15625.92	0.50
15626.19	CN 1-2 P_1 42.5	68.5	15626.71	0.52
15628.59	CO 3-0 R53	40.5	15629.18	0.59
15630.65	OH 3-1 P_2 _f 5.5	68.8	15630.97	0.32
15631.01	OH 3-1 P_2 _e 5.5	40.1	15631.68	0.67
15635.70	Fe	324.2	15636.22	0.52
15636.35	Ni	145.7	15636.89	0.54
15640.33	CN 1-2 Q_2 51.5	71.6	15640.86	0.53
15641.29	CN 1-2 P_2 42.5	41.6	15641.80	0.51
15643.24	Fe	47.2	15643.75	0.51
15644.64	CN 1-2 R_2 62.5	12.2	15645.14	0.50
15646.95	CO 3-0 R12	6.6	15647.46	0.51
15648.84	Fe	100.0	15649.29	0.45
15650.09	CN 0-1 Q_2 63.5	63.9	15650.52	0.43
15652.33	Fe	186.9	15652.79	0.46
15655.69	OH 3-1 P_1 _e 6.5	35.0	15656.17	0.48
15656.75	Fe	157.7	15657.15	0.40

Table B.6: The equivalent widths for the lines in Fig. B.7 with the vacuum positions given by Hinkle et al. (1995). The mean difference between vacuum position and measured wavelength is 0.51 Å. The radial velocity derived from these measurements is 13.12 ± 1.76 km/s after heliocentric correction.

In The Perkins Catalog of revised MK types for the cooler stars by Keenan & McNeil (1989), μ Pegasi is labeled as a standard-type star with V 3.48 mag, a spectral type G8 and luminosity class III. This star was subject to a research done by Smith (1998) to find stellar atmospheric parameters for the giant stars μ Pegasi and λ Pegasi. The results for μ Pegasi are:

	μ Peg
$T_{\text{eff}}(\text{K})$	5000 ± 50
$\log g$ (g in cm s^{-2})	2.6 ± 0.1
[M/H]	-0.1 ± 0.05
Microturbulence, ξ (km s^{-1})	1.4 ± 0.1
Macroturbulence, ζ (km s^{-1})	3.00 ± 0.13

Table B.7: The parameters from Smith (1998) for the star μ Peg.

The star μ Peg was included in the sample of Williams (1972), whose aim it was to derive iron abundances of evolved stars. For μ Peg, the following stellar parameters were published: $T_{\text{eff}}=4968$ K, $\log g=3.0$, $[\text{Fe}/\text{H}]=0.09$. These values do not differ too much from the ones listed in table B.7. The model spectrum I compared to the observation of μ Peg was based on the values mentioned above and fits the data quite well (see Fig. B.8).

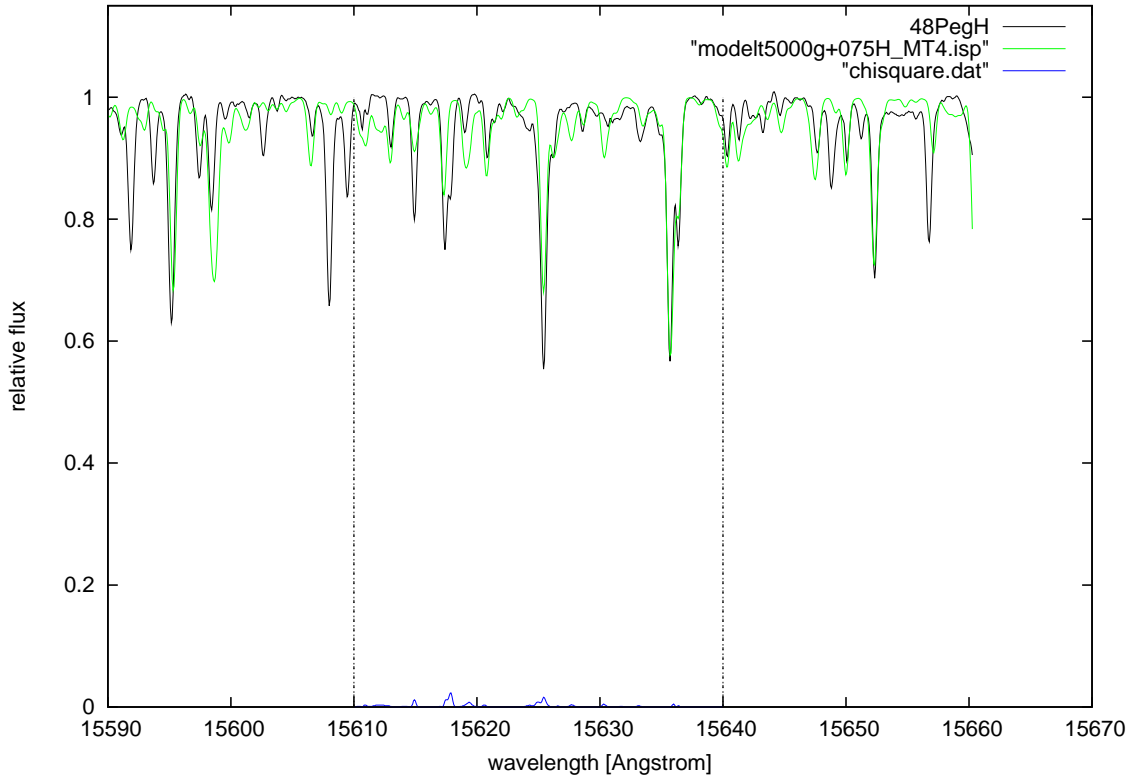


Figure B.8: The star μ Peg overplotted by a MARCS model of 5000 K, $\log g=0.75$ and $\zeta=4$ km/s.

The star μ Pegasi is an old-disk-population giant and a possible member of the solar group. The radial velocity measured by Eggen (1974) is 13.9 km/s and is assigned a G8III spectral type. This radial velocity is in good agreement with mine: 13.12 km/s.

Danksagung

Ich möchte mich an dieser Stelle bei allen bedanken, die mich durch mein Studium begleitet und unterstützt haben.

- An erster Stelle gilt mein Dank meinem Betreuer Dr. Thomas Lebzelter, für seine Unterstützung und vorbildliche Betreuung, und dafür, dass er seine Begeisterung für Astronomie an seine Studenten weitergibt.
- Weiters möchte ich mich bei Ken Hinkle und Michael Lederer bedanken für die Unterstützung bei der Gewinnung der Daten.
- Danke auch an alle meine Studienkollegen, allen voran Elisabeth Füllenhals und Angela Baier, die mir mit Rat und Tat zur Seite standen und deren Humor meine Freude am Studium noch verdoppelt hat.
- Meinen Eltern möchte ich dafür danken, dass sie mich all die Jahre sowohl auf finanzieller als auch auf menschlicher Ebene unterstützt haben. Ohne sie wäre diese Arbeit nicht möglich gewesen.
- Ich bedanke mich auch bei meinem Ehemann Gerald Jungwirth, den ich Dank dieses Studiums kennengelernt habe und der mich immer wieder motiviert und tatkräftig unterstützt hat.
- Mein Dank gilt auch all jenen, die hier nicht erwähnt wurden, aber ohne die diese Diplomarbeit nicht zu Stande gekommen wäre.

Acknowledgements

This research has made use of the SIMBAD database, operated at CDS, Strasbourg, France.

Erklärung

Hiermit erkläre ich, die vorliegende Arbeit selbstständig und nur unter Verwendung der angegebenen Quellen und Hilfsmittel angefertigt zu haben.

Wien, November 2010

Marianne Jungwirth

Curriculum Vitae

Marianne Jungwirth

Personal	Birthday:	25. January 1983, Tulln Austria, Austrian citizenship
	Address:	Kriemhildengasse 39 3424 Zeiselmauer
	e-mail:	jungwirth_marianne@yahoo.com
	Languages:	German (native), English
Education	1989 - 1993	Elementary school
	1993 - 1997	Secondary school focussing on music
	1997 - 2002	Higher Secondary School for Art and Fashion
	18. June 2002	School leaving examination (Matura)
	2002 - 2006	Bachelor study of Astronomy at the University of Vienna
	29. March 2006	Bachelor rer.nat
	2006 - 2010	Master study of Astronomy at the University of Vienna
	2006 - 2010	Master thesis: Near Infrared Spectra of post-AGB Variables
Employment	2003 - now	Diploma study of Physics at the University of Vienna
	Sept. 2005 - Dec. 2005	Catering BA-CA
	Sept. 2006 - May 2008	Gartenbau Lederleitner
	Oct. 2008 - Feb. 2009	Tutor Beobachtungsorientiertes Praktikum Part II
	March 2009 - Aug. 2009	Tutor Anfängerpraktikum
	Sept. 2009	Internship IT-Support VAV
Interests	Sept. 2010	Internship IT-Support VAV
		Astronomy, Music, Art